



Space engineering

Space environment

Published by: ESA Publications Division
ESTEC, P.O. Box 299,
2200 AG Noordwijk,
The Netherlands

ISSN: 1028-396X

Price: € 30

Printed in The Netherlands

Copyright 2000 © by the European Space Agency for the members of ECSS

Foreword

This Standard is one of the series of ECSS Standards intended to be applied together for the management, engineering and product assurance in space projects and applications. ECSS is a cooperative effort of the European Space Agency, national space agencies and European industry associations for the purpose of developing and maintaining common standards.

Requirements in this Standard are defined in terms of what shall be accomplished, rather than in terms of how to organize and perform the necessary work. This allows existing organizational structures and methods to be applied where they are effective, and for the structures and methods to evolve as necessary without re-writing the standards.

The formulation of this Standard takes into account the existing ISO 9000 family of documents.

This Standard has been prepared by the ECSS Working Group on ECSS-E-10-04 Space Environment Standard, reviewed by the ECSS Technical Panel and approved by the ECSS Steering Board.

(This page is intentionally left blank)

Introduction

This Standard is of level 3 in the ECSS hierarchy. It forms part of the System engineering branch (ECSS-E-10) of the Engineering area of the ECSS system (ECSS-E). As such it is intended to assist in the consistent application of space environment engineering to space products through specification of required or recommended methods, data and models to the problem of ensuring best performance, problem-avoidance or survivability of a product in the space environment.

The space environment can cause severe problems for space systems. Proper assessment of the potential effects is part of the system engineering process as defined in ECSS-E-10. This is performed in the early phases of a mission when consideration is given to e.g. orbit selection, mass budget, thermal protection, and component selection policy. As the design of a space system is developed, further engineering iteration is normally necessary with more detailed analysis.

In this Standard, each component of the space environment is treated separately, although synergies and cross-linking of models are specified. Extensive informative annexes are provided as explanatory background information associated with each clause.

(This page is intentionally left blank)

Contents

Foreword	3
Introduction	5
1 Scope	15
2 Normative references	17
3 Terms, definitions and abbreviated terms	19
3.1 Terms and definitions	19
3.2 Abbreviated terms	26
4 Gravitation	29
4.1 Introduction	29
4.2 Model presentation	32
4.3 Reference data	32
4.4 References	34
5 Geomagnetic fields	35
5.1 Introduction – Overview of the geomagnetic field and effects	35

5.2	Reference data on the geomagnetic field	36
5.3	Geomagnetic field models and analysis methods	36
5.4	Tailoring guidelines	41
5.5	Figures	42
5.6	References	43
6	Solar and Earth electromagnetic radiation and indices	45
6.1	Introduction	45
6.2	Solar electromagnetic radiation	46
6.3	Earth electromagnetic radiation	47
6.4	Solar and geomagnetic indices	47
6.5	Figures	52
6.6	References	53
7	The neutral Earth atmosphere	55
7.1	Introduction	55
7.2	Recommended reference model	55
7.3	Structure of the Earth atmosphere	55
7.4	Atmospheric state parameters	56
7.5	Temperature, composition, and density model of the Earth heterosphere .	57
7.6	Temperature, composition, and density model of the Earth homosphere . .	66
7.7	Reference model output	67
7.8	Wind model of the Earth homosphere and heterosphere	67
7.9	Simple density models of planetary atmospheres	68
7.10	Aerodynamics in the Earth atmosphere	69
7.11	Figures	71
7.12	References	77
8	Plasmas	79
8.1	Introduction	79
8.2	The ionosphere	80
8.3	The plasmasphere	83
8.4	The outer magnetosphere	84
8.5	The solar wind	86
8.6	Induced environments	87
8.7	Tailoring guidelines	89
8.8	References	90

9	Energetic particle radiation	91
9.1	Introduction – Overview of energetic particle radiation environment and effects	91
9.2	Quantification of effects and related environments	93
9.3	Energetic particle radiation environment reference data, models and analysis methods	94
9.4	Analysis methods for derived quantities	101
9.5	Tailoring guidelines: Orbital and mission regimes	104
9.6	Preparation of a radiation environment specification	105
9.7	Figures	106
9.8	References	121
10	Particulates	123
10.1	Introduction	123
10.2	Analysis techniques	124
10.3	Model presentation	125
10.4	Reference data	128
10.5	Figures	133
10.6	References	137
11	Contamination	139
11.1	Introduction	139
11.2	Molecular contamination	140
11.3	Particulate contamination	141
11.4	Effect of contamination	142
11.5	Models	142
11.6	References	146
Annex A (informative)		147
Annex B (informative) Gravitation		149
B.1	Related tools	149
B.2	Effects	149
B.3	Gravitational field at the surface of a planet	151
B.4	Uncertainties	152
B.5	References	153

Annex C (informative) Geomagnetic field 155

C.1	Description of magnetosphere	155
C.2	Derivation of dipole strength from field model coefficients	155
C.3	Incompatibilities and inconsistencies	156
C.4	IGRF model details and availability	156
C.5	References	157

Annex D (informative) Solar and Earth electromagnetic radiation and indices 159

D.1	Solar spectrum details	159
D.2	Albedo and infrared variability	159
D.3	Activity indices information	160
D.4	Radio noise	160
D.5	Solar radiation pressure	160
D.6	Figures	161
D.7	References	165

Annex E (informative) The neutral Earth atmosphere 167

E.1	Overview of atmosphere models	167
E.2	Accessibility of the MSISE-90 model	168
E.3	References	168

Annex F (informative) Plasma 169

F.1	Surface charging	169
F.2	Charging in LEO	170
F.3	NASCAP charging code	171
F.4	POLAR charging code	172
F.5	Other charging codes	173
F.6	NASA worst case charging environment	173
F.7	Ram and wake effects	173
F.8	Current collection effects	174
F.9	Sputtering	174
F.10	Ionospheric propagation effects	175
F.11	Availability of the IRI95 model	175
F.12	References	176

Annex G (informative) Radiation 177

G.1	Links with radiation testing	177
G.2	Future models	178
G.3	Sources of models	179
G.4	Internal electrostatic charging analysis tools	179
G.5	Further information	180
G.6	References	180

Annex H (informative) Particulates 181

H.1	Space debris flux models	181
H.2	Model uncertainties	183
H.3	Damage assessment	184
H.4	Analysis tools	185
H.5	Lunar dust simulant	186
H.6	References	186

Annex I (informative) Contamination 187

I.1	Existing Tools	187
I.2	ESABASE: OUTGASSING, PLUME-PLUMFLOW and CONTAMINE modules	187
I.3	JMC3D	188
I.4	CONTAM 3.2 or CONTAM III	189
I.5	TRICONTAM	190
I.6	SOCRATES	190
I.7	SPACE II	191
I.8	MOLFLUX	191
I.9	ISEM	192
I.10	OPT	192
I.11	CAP	192
I.12	Databases	192
I.13	References	193

Figures

Figure 1:	Geomagnetic field strength at 400 km altitude based on IGRF-1995	42
Figure 2:	Output from geomagnetic field models showing the diurnal distortion to the field and seasonal variations in the distortion [RD5.8]	42
Figure 3:	Variation of the geomagnetic field as a function of altitude	43
Figure 4:	Standard predictions of solar and geomagnetic activity during a cycle ...	52
Figure 5:	Variation of the MSISE-90 mean temperature with altitude for extremely low activities, for mean activities and for extremely high activities	71

Figure 6:	Variation of the MSISE-90 mean air density with altitude for low activities, for mean activities and for extremely high activities	71
Figure 7:	Variation of the MSISE-90 mean atomic oxygen with altitude for extremely low activities, for mean activities and for extremely high activities	72
Figure 8:	Variation of the MSISE-90 mean concentration profile of the atmosphere constituents N ₂ , O, O ₂ , He, Ar, H, and N with altitude for mean activities ..	72
Figure 9:	Diurnal (a) and seasonal-latitudinal (b) variations of the MSISE-90 local temperature at altitude h = 400 km	73
Figure 10:	Diurnal (a) and seasonal-latitudinal (b) variations of the MSISE-90 air density at altitude h = 400 km for mean atmospheric conditions	74
Figure 11:	Diurnal (a) and seasonal latitudinal (b) variations of the MSISE-90 atomic oxygen concentration at altitude h = 400 km for mean atmospheric conditions ..	75
Figure 12:	Diurnal (a) and seasonal-latitudinal (b) variations of wind magnitude and direction according to HWM-93 at altitude h = 400 km for mean atmospheric conditions	76
Figure 13:	Mean ranges of protons and electrons in aluminium	106
Figure 14:	Contour plots of the electron and proton radiation belts	107
Figure 15:	Electron (a) and proton (b) omnidirectional fluxes, integral in energy, on the geomagnetic equator for various energy thresholds	108
Figure 16:	Integral omnidirectional fluxes of protons (> 10 MeV) and electrons (> 1 MeV) at 400 km altitude showing the inner radiation belt's "South Atlantic anomaly" and, in the case of electrons, the outer radiation belt encountered at high latitudes	109
Figure 17:	The flux anisotropy in low Earth orbit averaged over an orbit of the space station for protons > 100 MeV energy	110
Figure 18:	Solar proton fluence spectra for various statistical confidence levels (99 %, 95 %, 90 %, 75 % and 50 %, from top to bottom in each panel) for various mission durations (data from JPL-1991 Model)	111
Figure 19:	Cosmic ray LET spectra for typical missions	113
Figure 20:	SHIELDOSE dataset for computing doses for arbitrary spectra:	114
Figure 21:	Annual doses behind 4 mm spherical shielding on circular equatorial orbits in the radiation belts, as a function of orbit height	117
Figure 22:	Typical doses predicted for typical missions	118
Figure 23:	Typical dose-depth curves for Earth-orbits	119
Figure 24:	Quality factors for use in dose equivalent calculations for radio-biological effect purposes, as defined by the ICRP	120
Figure 25:	The NIEL curve: (a) energy lost by protons in non-ionizing interactions (bulk, displacement damage); (b) NIEL relative to 10 MeV giving damage-equivalence of other energies	120
Figure 26:	Time evolution of the number of trackable objects in orbit	133
Figure 27:	Altitude distribution of trackable objects in LEO orbits	133
Figure 28:	Distribution of trackable objects as function of their inclination	134
Figure 29:	Cumulative number of impacts, N from 1 side to a randomly oriented plate for a range of minimum particle sizes	134
Figure 30:	Activity ratio factor versus period of activity for major meteoroid streams ..	135
Figure C-1:	Schematic of the magnetosphere showing the current flows and magnetic field lines	156

Figure D-1:	Normally incident solar radiation at sea level on very clear days, solar spectral irradiance outside the Earth atmosphere at 1 AU, and black body spectral irradiance curve at T=5762 K.	161
Figure D-2:	Daily solar and geomagnetic activity indices over the last two solar cycles.	162
Figure D-3:	Monthly mean solar and geomagnetic activity indices over the last two solar cycles.	163
Figure D-4:	Power flux levels for various frequency ranges of naturally occurring electromagnetic and plasma waves (from [RDD.2]).	164
Figure F-1:	Spectrograms showing electron and ion fluxes during a charging event ..	170
Figure F-2:	Satellite potential and electron integral number flux above 30 eV and 14 keV [RDF.1]	171
Figure F-3:	Surface potential vs. electron temperature for a number of materials	172

Tables

Table 1:	Mandatory model parameters	32
Table 2:	Values of normalized coefficients Cnm from JGM-2 model to degree (n) and order (m) 9	33
Table 3:	Values of normalized coefficients Snm from JGM-2 model to degree (n) and order (m) 9	33
Table 4:	Predicted orbit error associated with use of the JGM-2 gravity model	33
Table 5:	Changes in dipole moments 1945-1995	36
Table 6:	The IGRF-95 Model: Coefficients and their secular variations to degree and order 3	38
Table 7:	Changes in dipole-terms and derived dipole moments of IGRF models ...	38
Table 8:	Sibeck et al. [RD5.17] Magnetopause model	41
Table 9:	High-energy solar electromagnetic flux	46
Table 10:	Conversion from Kp to ap	48
Table 11:	Maximum, mean, and minimum values of the 13-month smoothed 10.7 cm solar radio flux and geomagnetic activity index over the mean solar cycle	48
Table 12:	Reference index values	52
Table 13:	MSISE-90 altitude profiles of temperature T, total density r, pressure p, mean molecular weight M and density scale height H for low activities	60
Table 14:	MSISE-90 altitude profiles of temperature T, total density r, pressure p, mean molecular weight M and density scale height H for mean activities	62
Table 15:	MSISE-90 altitude profiles of temperature T, total density r, pressure p, mean molecular weight M and density scale height H for extremely high activities ...	64
Table 16:	Main engineering concerns due to space plasmas	80
Table 17:	Parameters for the USAF diffuse aurora model	81
Table 18:	Ionospheric electron density profiles derived from IRI95 [RD8.2]	82
Table 19:	Electron density vs. L-shell for the Carpenter and Anderson [RD8.7] model, ignoring seasonal and solar cycle effects	84
Table 20:	Typical plasma parameters at geostationary orbit	86
Table 21:	Standard worst-case bi-Maxwellian environment	86

Table 22:	Solar wind parameters (from RD8.14)	87
Table 23:	Typical magnetosheath plasma parameters (from RD8.14)	87
Table 24:	Some solar UV photoionization rates at 1 AU (from RD8.17)	89
Table 25:	Photoelectron sheath parameters	89
Table 26:	Examples of appropriate plasma environments for different missions	89
Table 27:	Parameters for quantification of radiation effects	93
Table 28:	Characteristics of typical radiation belt particles	94
Table 29:	Standard field models to be used with radiation-belt models	95
Table 30:	Fluence levels for energy, mission duration and confidence levels from the JPL-1991 model	97
Table 31:	Standard probability (confidence) levels to be applied for various mission durations	97
Table 32:	Cumulative number of impacts, N, from one side to a randomly oriented plate for a range of minimum particle sizes using the ORDEM 96 debris model	129
Table 33:	Cumulative number of impacts, N, from one side to a randomly oriented plate for a range of minimum particle sizes using the ORDEM 96 model	130
Table 34:	Cumulative number of impacts, N, from 1 side to a randomly oriented plate for a range of minimum particle sizes using the MASTER debris model	131
Table B-1:	Planetary gravitational characteristics	152
Table B-2:	Covariance errors in normalized coefficients C_{nm} (units of 10^{-6}) from JGM-2 model to degree (n) and order (m) 9	152
Table B-3:	Covariance errors in normalized coefficients S_{nm} (units of 10^{-6}) from JGM-2 model to degree (n) and order (m) 9	152
Table D-1:	Running mean (averaged over 90 minutes) albedo percentile data	159
Table D-2:	Running mean (averaged over 90 minutes) Earth infrared radiation percentile values in units of W/m^2	160
Table F-1:	NASA worst-case environment	173
Table G-1:	Radiation tests	177
Table H-1:	Nominal and worst case debris model parameters and mass densities ..	182
Table H-2:	Uncertainty of 90 % confidence level for debris flux	184

Scope

This Standard applies to all product types which exist or operate in space and defines the natural environment for all space regimes. It also defines general models and rules for determining the local induced environment.

Project-specific or project-class-specific acceptance criteria, analysis methods or procedures are not defined.

The natural space environment of a given item is that set of environmental conditions defined by the external physical world for the given mission (e.g. atmosphere, meteoroids and energetic particle radiation). The induced space environment is that set of environmental conditions created or modified by the presence or operation of the item and its mission (e.g. contamination, secondary radiations and spacecraft charging). The space environment also contains elements which are induced by the execution of other space activities (e.g. debris and contamination).

(This page is intentionally left blank)

2

Normative references

The following normative documents contain provisions which, through reference in this text, constitute provisions of this ECSS Standard. For dated references, subsequent amendments to, or revisions of any of these publications do not apply. However, parties to agreements based on this ECSS Standard are encouraged to investigate the possibility of applying the most recent editions of the normative documents indicated below. For undated references the latest edition of the publication referred to applies.

ECSS-P-001	Glossary of terms
ECSS-E-10	Space engineering - System engineering
ECSS-Q-70-01 ¹⁾	Space product assurance - Contamination and cleanliness control

Normative references for the specific components of the space environment are provided in the respective component clauses.

NOTE Informative references for the specific components of the space environment are provided in the respective component clauses.

1) To be published.

(This page is intentionally left blank)

Terms, definitions and abbreviated terms

3.1 Terms and definitions

The following terms and definitions are specific to this Standard in the sense that they are complementary or additional with respect to those contained in ECSS-P-001.

3.1.1

A_p , K_p indices

geomagnetic activity indices to describe fluctuations of the geomagnetic field

NOTE Values of A_p range from 0 to 400 and they are expressed in units of 2 nT (nanotesla). K_p is essentially the logarithm of A_p

3.1.2

absorbed dose

energy absorbed locally per unit mass as a result of radiation exposure which is transferred through ionization and excitation

NOTE A portion of the energy absorption can result in damage to the lattice structure of solids through displacement of atoms, and this is now commonly referred to as Non-Ionizing Energy Loss (NIEL).

3.1.3

accommodation coefficient

measure for the amount of energy transfer between a molecule and a surface

3.1.4

albedo

fraction of sunlight which is reflected off a planet

3.1.5

bremsstrahlung

high-energy electromagnetic radiation in the X- γ energy range emitted by charged particles slowing down by scattering off atomic nuclei

NOTE The primary particle is ultimately absorbed while the bremsstrahlung can be highly penetrating. In space, the

most common source of bremsstrahlung is electron scattering.

3.1.6

contaminant

foreign (or unwanted) molecular or particulate matter that can affect or degrade the performance of any component when being in line of sight with that component or when residing onto that component

3.1.7

contaminant environment

molecular and particulate environment in the vicinity of and created by the presence of a spacecraft

3.1.8

current

often used in the discussion of radiation transport to refer to the rate of transport of particles through a boundary

NOTE In contrast to flux, current is dependent on the direction in which the particle crosses the boundary (it is a vector integral). An isotropic omnidirectional flux, f , incident on a plane gives rise to a current of $1/4f$ normally in each direction across the plane.

3.1.9

direct flux

free stream or outgassing molecules that directly impinge onto a critical surface, i.e. without prior collisions with other gas species or any other surface

3.1.10

distribution function $f(\mathbf{x}, \mathbf{v})$

function describing the particle density of a plasma in 6-D space made up of the three spatial vectors and the three velocity vectors, with units $\text{s}^3 \text{m}^{-6}$

NOTE For distributions that are spatially uniform and isotropic, it is often quoted as $f(v)$, a function of scalar velocity, with units s m^{-4} , or $f(E)$ a function of energy, with units $\text{J}^{-1} \text{m}^{-3}$. This can be converted to flux as follows:

$$Flux = \int v f(v) dv \quad \text{or}$$

$$Flux = \int \frac{f(E)}{m} dE$$

where

v is the scalar velocity;

E is the energy;

m is the particle mass.

3.1.11

dose

quantity of radiation delivered at a position

NOTE In its broadest sense this can include the flux of particles, but in the context of space energetic particle radiation ef-

fects, it usually refers to the energy absorbed locally per unit mass as a result of radiation exposure.

3.1.12

dose equivalent

quantity normally applied to biological effects and includes scaling factors to account for the more severe effects of certain kinds of radiation

3.1.13

dust

particulates which have a direct relation to a specific solar system body and which are usually found close to the surface of this body (e.g. Lunar, Martian or Cometary dust)

3.1.14

Earth infrared

Earth emitted thermal radiation

NOTE It is also called outgoing long wave radiation.

3.1.15

energetic particle

particles which, in the context of space systems radiation effects, can penetrate outer surfaces of spacecraft

NOTE For electrons, this is typically above 100 keV, while for protons and other ions this is above 1 MeV. Neutrons, gamma rays and X-rays are also considered energetic particles in this context.

3.1.16

equivalent fluence

quantity which attempts to represent the damage at different energies and from different species

EXAMPLE For example, for solar cell degradation it is often taken that one 10 MeV proton is “equivalent” to 3000 1 MeV electrons. This concept also occurs in consideration of Non-ionizing Energy Loss effects (NIEL).

NOTE Damage coefficients are used to scale the effect caused by particles to the damage caused by a standard particle and energy.

3.1.17

exosphere

part of the Earth atmosphere above the thermosphere which extends into space

NOTE *H* and *He* atoms can attain escape velocities at the outer rim of the exosphere.

3.1.18

$F_{10,7}$ flux

solar flux at a wavelength of 10,7 cm in units of 10^4 Jansky (one Jansky equals $10^{-26} \text{ W m}^{-2} \text{ Hz}^{-1}$)

3.1.19

fluence

time-integration of the flux

3.1.20

flux

amount of radiation crossing a surface per unit of time, often expressed in “integral form” as particles per unit area per unit time (e.g. electrons $\text{cm}^{-2} \text{s}^{-1}$) above a certain threshold energy

NOTE The directional flux is the differential with respect to solid angle (e.g. particles $\text{cm}^{-2} \text{steradian}^{-1} \text{s}^{-1}$) while the “differential” flux is differential with respect to energy (e.g. particles $\text{cm}^{-2} \text{MeV}^{-1} \text{s}^{-1}$). In some cases fluxes are also treated as a differential with respect to Linear Energy Transfer (see 3.1.28).

3.1.21

free molecular flow regime

mean free path of a molecule is greater than compared to the dimensions of the volume of interest (characteristic length)

3.1.22

geocentric solar magnetospheric coordinates (GSM)

elements of a right-handed Cartesian coordinate system (X,Y,Z) with the origin at the centre of the Earth

NOTE X points towards the Sun; Z is perpendicular to X, lying in the plane containing the X and geomagnetic dipole axes; Y points perpendicular to X and Z and points approximately towards dusk magnetic local time (MLT).

3.1.23

heterosphere

Earth atmosphere above 105 km altitude where species-wise neutral concentration profiles are established due to a diffusive equilibrium, with N_2 dominance below 200 km, O dominance from 200 km to 600 km, and He dominance as of 600 km altitude

3.1.24

homosphere

Earth atmosphere below 105 km altitude where complete vertical mixing yields a near-homogeneous composition of about 78,1 % N_2 , 20,9 % O_2 , 0,9 % Ar, and 0,1 % CO_2 and trace constituents; the homopause (or turbopause) marks the ceiling of the homosphere

3.1.25

indirect flux

molecules impinging on a critical surface, after collision with, or collision and sojourn on other surfaces

3.1.26

isotropic

property of a distribution of particles where the flux is constant over all directions

3.1.27

L or L shell

parameter of the geomagnetic field, often used to describe positions in near-Earth space

NOTE L or L shell has a complicated derivation based on an invariant of the motion of charged particles in the terrestrial magnetic field (see clause 5). However, it is useful in defining plasma regimes within the magnetosphere because, for a dipole magnetic field, it is equal to the geocentric altitude in

Earth-radii of the local magnetic field line where it crosses the equator.

3.1.28

linear energy transfer (LET)

rate of energy deposit from a slowing energetic particle with distance travelled in matter, the energy being imparted to the material

NOTE Normally used to describe the ionization track caused by passage of an ion. LET is material-dependant and is also a function of particle energy. For ions involved in space radiation effects, it increases with decreasing energy (it also increases at high energies, beyond the minimum ionizing energy). LET allows different ions to be considered together by simply representing the ion environment as the summation of the fluxes of all ions as functions of their LETs. This simplifies single-event upset calculation. The rate of energy loss of a particle, which also includes emitted secondary radiations, is the stopping power.

3.1.29

magnetic local time (MLT)

parameter analogous to longitude, often used to describe positions in near-Earth space

NOTE Pressure from the solar wind distorts the Earth magnetic field into a comet-like shape. This structure remains fixed with its nose towards the Sun and the tail away from it as the Earth spins within it. Hence longitude, which rotates with the Earth, is not a useful way of describing position in the magnetosphere. Instead, magnetic local time is used. This has value 0 (midnight) in the anti-sunward direction, 12 (noon) in the sunward direction and 6 (dawn) and 18 (dusk) perpendicular to the sunward/anti-sunward line. This is basically an extension of the local solar time on Earth, projected vertically upwards into space although allowance is made for the tilt of the dipole.

3.1.30

mass flow rate

mass (g) of molecular species crossing a specified plane per unit time and unit area ($\text{g cm}^{-2} \text{s}^{-1}$)

3.1.31

Maxwellian distribution

in thermal equilibrium, plasma distribution functions can be described in terms of scalar velocity, v , by the Maxwellian distribution below:

$$f(v) = 4\pi n \left(\frac{m}{2\pi kT} \right)^{3/2} v^2 \exp \left(- \frac{v^2 m}{2kT} \right)$$

where

n is the density;
 k is the Boltzmann constant;
 T is the temperature.

NOTE The complete distribution is therefore described by a pair of numbers for density and temperature. Even non-equilibrium distributions can often be usefully described by a combination of two Maxwellians.

3.1.32

meteoroids

particles in space which are of natural origin; nearly all meteoroids originate from asteroids or comets

3.1.33

molecular column density (MCD)

integral of the number density (number of molecules of a particular species per unit volume) along a specified line of sight originating from a (target, critical, measuring, reference) surface

3.1.34

molecular contaminant

contaminant without observable dimensions

3.1.35

omnidirectional flux

scalar integral of the flux over all directions

NOTE This implies that no consideration is taken of the directional distribution of the particles which can be non-isotropic. The flux at a point is the number of particles crossing a sphere of unit cross-sectional surface area (i.e. of radius $1/\sqrt{\pi}$). An omnidirectional flux is not to be confused with an isotropic flux.

3.1.36

outgassing rate

mass of molecular species evolving from a material per unit time and unit surface area ($\text{g cm}^{-2} \text{s}^{-1}$)

NOTE Outgassing rates can also be given in other units, such as in relative mass unit per time unit: (g s^{-1}), ($\% \text{s}^{-1}$) or ($\% \text{s}^{-1} \text{cm}^{-2}$).

3.1.37

particulate contaminant

solid or liquid contaminant particles

3.1.38

permanent molecular deposition (PMD)

molecular matter that permanently sticks onto a surface (non-volatile under the given circumstances) as a result of reaction with surface material, UV-irradiation or residual atmosphere induced reactions (e.g. polymerization, formation of inorganic oxides)

3.1.39

plasma

partly or wholly ionized gas whose particles exhibit collective response to magnetic and electric fields

NOTE The collective motion is brought about by the electrostatic Coulomb force between charged particles. This causes the particles to rearrange themselves to counteract electric fields within a distance of the order of the Debye length. On spatial scales larger than the Debye length plasmas are electrically neutral.

3.1.40**radiation**

transfer of energy by means of a particle (including photons)

NOTE In the context of this Standard, electromagnetic radiation below the X-ray band is excluded. This therefore excludes UV, visible, thermal, microwave and radio-wave radiation.

3.1.41**return flux**

molecules returning to (in the direction of) the source or a surface not in direct view; the cause can be:

- collisions with other residual natural atmospheric species (ambient scatter) or with other identical or different contaminant species (self scatter) before reaching the critical surface;
- ionization or dissociative ionization of the molecules under radiation (e.g. UV or particles) and subsequent attraction to a charged surface

3.1.42**single-event upset (SEU), single-event effect (SEE), single-event latch-up (SEL)**

these effects are the result of the highly localized deposition of energy by single particles or their reaction products: the energy deposition is sufficient to cause observable effects

3.1.43**space debris**

man-made objects or parts thereof in space which do not serve any useful purpose

NOTE 1 The term space debris is used here exclusively for man-made objects in space.

NOTE 2 In some NASA documents these man-made particles are referred to as “orbital debris” and the term space debris is used to denote both, natural meteoroids and man-made objects.

3.1.44**solar constant**

electromagnetic radiation from the Sun that falls on a unit area of surface normal to the line from the Sun, per unit time, outside the atmosphere, at one astronomical unit (1 AU = average Earth-Sun distance)

3.1.45**solar flare**

emission of optical, UV and X-radiation from an energetic event on the Sun

NOTE There is some controversy about the causal relationship between solar flares and the arrival of large fluxes of energetic particles at Earth. Therefore, it is more consistent to refer to the latter as Solar Energetic Particle Events (SEPEs).

3.1.46**sticking coefficient**

parameter defining the probability that a molecule, colliding with a surface, stays onto that surface for a time long compared to the phenomena under investigation

NOTE It is a function of parameters such as contamination/surface material pairing, temperature, photo-polymerization, reactive interaction with atomic oxygen.

3.1.47

surface accommodation

situation which occurs when a molecule becomes attached to a surface long enough to come into a thermal equilibrium with that surface

3.1.48

thermosphere

Earth atmosphere between 120 km and 250 km to 400 km (depending on the activity level), where temperature has an exponential increase up to a limiting value T_{∞} at the thermopause (where T_{∞} is the exospheric temperature)

3.1.49

VCN-test

screening thermal vacuum test to determine the outgassing properties of materials

NOTE The test is described in ECSS-Q-70-04 and ASTM-E595 [RD11.1, RD11.2]. The test results are:

- TML - Total Mass Loss, measured ex-situ as a difference of mass before and after exposure to a vacuum under the conditions specified in the outgassing test, normally expressed in % of initial mass of material.
- CVCN - Collected Volatile Condensable Material, measured ex-situ on a collector plate after exposure (to a vacuum) under the conditions specified in the outgassing test, normally expressed in % of initial mass of material.

3.2 Abbreviated terms

The following abbreviated terms are defined and used within this Standard.

Abbreviation	Meaning
ASTM	American Society for Testing and Materials
AE	auroral electrojet
AO	atomic oxygen
BIRA	Belgisch Instituut voor Ruimte-Aeronomie
CIRA	COSPAR International Reference Atmosphere
COSPAR	Committee on Space Research
CVCN	collected volatile condensable material
DISCOS	ESA's database and information system characterizing objects in space
DTM	density and temperature model
e.m.f.	electro-motive force
GCR	galactic cosmic ray
GEO	geostationary Earth orbit
GRAM	global reference atmosphere model
GSM	geocentric solar magnetospheric co-ordinates
HEO	high eccentric orbit
HWM	horizontal wind model
IASB	Institute d'Aeronomie Spatiale de Belgique
IDES	integrated debris evolution suite
IECM	in-flight experiment for contamination monitoring
LDEF	long duration exposure facility

LEO	low Earth orbit
LET	linear energy transfer
MAH	model of the high atmosphere
MASTER	meteoroid and space debris terrestrial environment reference model
MCD	molecular column density
MEO	medium (altitude) Earth orbit
MET	Marshall engineering thermosphere model
MLT	magnetic local time
MSIS	mass spectrometer and incoherent scatter
NIEL	non-ionizing energy loss
PMD	permanent molecular deposition
R	Sunspot number
r.m.s.	root-mean-square
RTG	radioisotope thermo-electric generator
SEU	single-event upset
SEE	single-event effect
SEL	single-event latch-up
SEPs	solar energetic particles
SEPE	solar energetic particle events
SPE	solar particle events
SRP	solar radiation pressure
TML	total mass loss
TD	total density model
USSA	US standard atmosphere
VCM	volatile condensable material
VUV	vacuum ultra violet

(This page is intentionally left blank)

Gravitation

4.1 Introduction

4.1.1 Newton's law of gravitation

Gravity models are necessary to define the motion of a satellite in orbit about a central body. The gravitational field influences the motion both, of the centre of mass (trajectory), and about the centre of mass (attitude) of the satellite. Newton's Law of Gravitation states that any two bodies attract each other with a force proportional to the product of their masses, and inversely proportional to the square of the distance between them. This relationship is used to define the force of a central body acting on a satellite (and vice versa). This can be expressed as:

$$F = - \frac{GMm}{r^2}$$

where

- F is the gravitational force;
- G is the factor of proportionality in Newton's Law of Gravitation, the so-called universal gravitational constant;
- m is the mass of the satellite;
- M is the mass of the central body;
- r is the distance between their centres of mass.

If the central body is spherical and isolated from other bodies, then in the absence of an atmosphere, the orbit of a satellite about this body is an ellipse of constant size and shape, in a plane whose direction remains fixed in space. The moment due to the gravitational force acting on the different mass elements of the satellite is termed the gravity gradient torque. In the absence of other disturbance torques, this moment causes the longitudinal axis of the satellite to align with the centre of the body. As its name implies, the gravity gradient torque decreases with the cube of the distance between the masses.

4.1.2 Departures from the point-mass model

The Earth is not a perfect sphere, nor is it isolated in space. Thus the motion of a satellite in orbit about the Earth departs from the simple behaviour described above. Depending upon the nature of the application, a more complex model of the Earth gravitational field can be required. For preliminary engineering analyses, simple analytic expressions exist which characterize the dominant perturbations to a satellite orbit due to Earth gravitational anomalies. These relations are derived from the more comprehensive spherical harmonic representations of the Earth gravitational field that are presented in subclause 4.3.1, but assume that the Earth is symmetric about its polar axis and consider only the dominant terms in the harmonic expansions. These expressions are given in annex B. Gravity gradient stabilization is normally used where only coarse Earth pointing accuracy is required ($>1^\circ$) and thus the point-mass model given above is applicable for most applications. A comprehensive treatise on gravity gradient stabilization is given by Regan and Anandakrishnan [RD4.1] and Wiesel [RD4.2]. When considering the gravitational attraction for an Earth-orbiting satellite due to the Sun and Moon, point mass models are normally sufficient. Mass values for these bodies and the other planets within the solar system are presented in annex B.

4.1.3 Accurate representation of the geopotential

For orbit prediction or trajectory determination purposes an accurate representation of the gravity field of the Earth is necessary. As the Earth is not a perfect sphere it is necessary to represent the geopotential field in terms of a central force augmented by a series of spherical harmonics²⁾ satisfying Laplace's equation in empty space ($\nabla^2 U = 0$). The geopotential can be expressed as:

$$U(r, \phi, \lambda) = \frac{GM_\oplus}{\gamma} \left(1 + \sum_{n=2}^{\infty} \sum_{m=0}^n \left(\frac{a}{r} \right)^n P_{nm}(\sin \phi) [C_{nm} \cos(m\lambda) + S_{nm} \sin(m\lambda)] \right)$$

where

- G is the constant of gravitation;
- M_\oplus is the mass of the Earth;
- r is the radial distance from the Earth's centre of mass;
- a is the semimajor axis of the reference ellipsoid (normally taken as the equatorial radius of the Earth, R_\oplus);
- n is the degree of the harmonic term;
- m is the order of the harmonic term;
- ϕ is the geocentric latitude;
- λ is the geocentric longitude;
- C_{nm}, S_{nm} are spherical harmonic coefficients;
- $P_{nm}(\sin \phi)$ are associated Legendre functions of the first kind where:

$$P_{nm}(\sin \phi) = \frac{(\cos \phi)^m}{2^n n!} \frac{d^{n+m}(\sin^2 \phi - 1)^n}{d^{n+m}(\sin \phi)}$$

are Legendre polynomials.

²⁾ Other forms of the potential, expressed in terms of ellipsoidal coordinates have also been developed but result in a more complex representation requiring use of elliptic Legendre polynomials of the second kind. The development of the potential in terms of spherical harmonics is a natural one to adopt in the analysis of satellite orbits because the symmetry properties of the harmonics correspond to the division of the potential according to the type of change in the classical orbital elements.

For computational purposes these expressions and their corresponding coefficients are used in their normalized form \bar{P}_{nm} , \bar{C}_{nm} , and \bar{S}_{nm} where:

$$\bar{P}_{nm} = \left[\frac{(2n+1)k(n-m)!}{(n+m)!} \right]^{1/2} P_{nm}$$

$$\bar{C}_{nm} = \left[\frac{(n+m)!}{(2n+1)k(n-m)!} \right]^{1/2} C_{nm}$$

$$\bar{S}_{nm} = \left[\frac{(n+m)!}{(2n+1)k(n-m)!} \right]^{1/2} S_{nm}$$

where $k = 1$ when $m = 0$, $k = 2$ when $m \neq 0$.

Depending upon its degree n and order m a Legendre function is referred to as:

1. a *zonal* harmonic when $m = 0$
2. a *sectorial* harmonic when $m = n$
3. a *tesseral* harmonic when $m \neq n$.

A zonal harmonic corresponds geometrically to a particular shape of the geopotential surface [RD4.3]. The second zonal harmonic ($m = 0$, $n = 2$) which expresses the main effect of the Earth flattening, makes a north-south slice through the Earth appear elliptical; the third zonal harmonic ($m = 0$, $n = 3$) provides a profile with a tendency to a triangle; the fourth harmonic relating to a square, the fifth to a pentagon, and so on.

A similar representation can be envisaged for longitudinal variation. Thus at any fixed latitude ϕ , the variation of geoid height with longitude λ is a sinusoidal oscillation having a wavelength $2\pi/m$, e.g. each harmonic of order 15 produces *bulges* every 24° in longitude.

The evaluation of spherical harmonic coefficients is a non-trivial task. Models are based on analyses of satellite observations, either photographic, Doppler or laser in nature, together with terrestrial gravity measurements and data from satellite altimeters.

The development of gravity models and evaluation of the geopotential coefficients is a constantly evolving process [RD4.4]. The first gravity models were based on the analysis of Transit satellite Doppler tracking data and Baker-Nunn camera observations and were produced by John Hopkins University's Applied Physics Laboratory and the Smithsonian Astrophysical Observatory. These were complete to degree and order 8.

At the present time there are five contemporary gravity models being used within the astrodynamics community. These are WGS-84 developed by the United States of America's Department of Defence, TEG-2B developed by the University of Texas (UT), OSU-91A developed by Ohio State University (OSU), GRIM4 developed by the European community, and JGM-2 developed by NASA, UT, CNES, and OSU. All of the models provide metre-level accuracy for orbit computation purposes. Use of the JGM-2 model is recommended as it represents the best long wavelength representation of the Earth that is currently available, and can provide centimetre-level accuracy. The JGM-2 model comprises results from OSU-91A [RD4.5] and TEG-2B [RD4.6] in its formulation. The WGS-84 and GRIM4 models are discussed briefly in the annex. A new model EGM-96 has recently been developed by the National Imagery and Mapping Agency, Goddard Space Flight Center and OSU. Although not yet established within the community, this is a possible candidate for a future successor to JGM-2 as the ESA standard model (see annex B).

4.2 Model presentation

4.2.1 Model

JGM-2 (Joint Gravity Model) [RD4.7] was developed from a combination of satellite tracking data, surface gravimetry and satellite altimetry observations. It is complete to degree and order 70 in spherical harmonics.

4.2.2 Mandatory model parameters

Table 1: Mandatory model parameters

Parameter	Value	Units
Constant of Gravitation, G	$6,67259 \times 10^{-11}$	$\text{m}^3 \text{kg}^{-1} \text{s}^{-2}$
Earth equatorial radius, R_{\oplus}	6378136,3	m
Geocentric Mass, M_{\oplus}	$5,97370 \times 10^{24}$	kg
$G M_{\oplus}$	398600,4415	$\text{km}^3 \text{s}^{-2}$

4.2.3 Guidelines for use

Three models were developed within the JGM-2 family. JGM-2S contains only the satellite tracking data used in JGM-2. JGM-2S is complete to degree 70. A further version JGM-2G was developed to accommodate geophysicists. The principal cause of uncertainty in the JGM-2 model is the sparsity of tracking data from satellites in different inclination bands and the lack of precise tracking data for satellites in very low orbits. The portion of the model up to degree 70 is well known, due principally to tracking data from the LAGEOS satellite. The short wavelengths of the JGM-2 model were predominantly determined using altimeter and surface gravity data, and thus are inherently less accurate. However, the JGM-2 model is more than adequate for most astrodynamics and engineering applications, while oceanographers performing precise altimeter computations are advised to use the JGM-2G version of the model. The coefficients for all these models can be obtained over the Science Internet via anonymous file transfer protocol (ftp) from geodesy@gsfc.nasa.gov. If a truncated set of coefficients is used, validation of the data set should be established for the particular application.

4.3 Reference data

4.3.1 Model output

Tables 2 and 3 give the values of the normalized spherical harmonic coefficients \bar{C}_{nm} and \bar{S}_{nm} to degree and order 9. Their associated 1σ errors are given in annex B.

4.3.2 Results for typical missions

Table 4 provides an estimate of the predicted orbit error in the radial, cross-track and along-track directions for representative missions associated with use of the full JGM-2 gravity model.

Table 2: Values of normalized coefficients \bar{C}_{nm} from JGM-2 model to degree (n) and order (m) 9

	n							
	2	3	4	5	6	7	8	9
0	-484,1654663	0,9571224	0,5401433	0,0684645	-0,1500030	0,0909460	0,0493049	0,0267036
1	-0,0001870	2,0283997	-0,5363680	-0,0591214	-0,0761294	0,2758256	0,0232834	0,1462664
2	2,4390838	0,9044086	0,3503493	0,6533875	0,0486483	0,3278766	0,0787560	0,0245294
3		0,7211539	0,9902582	-0,4519017	0,0579537	0,2508965	-0,0208114	-0,1619243
4			-0,1884885	-0,2950801	-0,0862993	-0,2755462	-0,2448369	-0,0085254
5				0,1749710	-0,2671890	0,0018128	-0,0251488	-0,0166623
6					0,0098855	-0,3590382	-0,0651558	0,0626750
7						0,0012547	0,0671575	-0,1184886
8							-0,1238923	0,1884251
9								-0,0481248

Units of 10^{-6}

Table 3: Values of normalized coefficients \bar{S}_{nm} from JGM-2 model to degree (n) and order (m) 9

	n							
	2	3	4	5	6	7	8	9
1	0,0011953	0,2488066	-0,4734226	-0,0955327	0,0265588	0,0967770	0,0591996	0,0206503
2	-1,4001093	-0,6192306	0,6628689	-0,3237786	-0,3737880	0,0940337	0,0662488	-0,0337777
3		1,4140369	-0,2010099	-0,2150966	0,0090304	-0,2166254	-0,0866613	-0,0751423
4			0,3088453	0,0496700	-0,4716700	-0,1238634	0,0702875	0,0192064
5				-0,6696502	-0,5365234	0,0177164	0,0892490	-0,0543111
6					-0,2370946	0,1517702	0,3092402	0,2224258
7						0,0244337	0,0746269	-0,0965854
8							0,1204626	-0,0031477
9								0,0966002

Units of 10^{-6}

Table 4: Predicted orbit error associated with use of the JGM-2 gravity model

Satellite	Semimajor axis (km)	Eccentricity	Inclination (°)	Predicted orbit error (cm)		
				Radial	Cross-track	Along-track
ERS-1	7153	0,001	98,8	8,0	15,1	160,4
Ajisai	7870	0,001	50,0	2,6	3,6	13,2
Starlette	7331	0,020	49,8	5,2	7,2	16,1
GEOS 3	7226	0,001	114,9	6,6	9,6	72,5
GEOS 1	8075	0,073	59,3	2,3	3,0	45,1
GEOS 2	7711	0,031	105,8	3,3	5,1	63,8
Peole	7006	0,016	15,0	981,0	106,7	353,5
BE-C	7507	0,025	41,2	9,2	11,4	60,0
DI-C	7341	0,053	40,0	14,5	16,9	70,7
DI-D	7622	0,084	39,5	10,1	11,2	88,9
NOVA	7559	0,001	90,0	9,6	21,7	397,0

4.4 References

- RD4.1 Regan F.J. and S.M. Anandakrishnan, "Dynamics of Atmospheric Re-entry", ISBN 1-56347-048-9, 1993.
- RD4.2 Wiesel, W.E., "Space Dynamics", McGraw-Hill, Hightstown, NJ, 1989.
- RD4.3 King-Hele D.G., "Satellite Orbits in an Atmosphere", ISBN 0-216-92252-6, Published by Blackie and Son Ltd, Glasgow, 1987.
- RD4.4 "Recommended Practice: Astrodynamics - Concepts, Terms, and Symbols - Part 1", BSR/AIAA R-064-1994.
- RD4.5 Rapp, R.H., Y.M. Wang, and N.K. Pavlis, "The Ohio State 1991 Geopotential and Sea Surface Topography Harmonic Coefficient Models", Report 410, Depart of Geodetic Science and Surveying, Ohio State University, Columbus, Ohio, USA, 1991.
- RD4.6 Tapley, B.D., C.K. Shum, D.N. Yuan, J.C. Ries, R.J. Eanes, M.M. Watkins and B.E. Schutz, "The University of Texas Earth Gravity Model", Paper presented at IUGG XX General Assembly, IAG Symp. G3, Gravity Field Determination from Space and Airborne Measurements, Vienna, Austria, August 12-24, 1991.
- RD4.7 Nerem R.S., F.J. Lerch, J.A. Marshall, E.C. Pavlis, B.H. Putney, B.D. Tapley, R.J. Eanes, J.C. Ries, B.E. Schutz, C.K. Shum, M.M. Watkins, S.M. Losko, J.C. Chan, S.B. Luthcke, G.B. Patel, N.K. Pavlis, R.G. Williamson, R.H. Rapp, R. Biancale, and F. Nouel, "Gravity Model Development for TOPEX/POSEIDON: Joint Gravity Models 1 and 2", J. Geophys. Res., Vol. 99, No. C12, Pages 24,421-24,447, December 15, 1994.

Geomagnetic fields

5.1 Introduction – Overview of the geomagnetic field and effects

At low altitude, the Earth field is approximately that of a magnetic dipole while at high altitude it is strongly distorted by the interactions with the solar wind.

Models of the Earth magnetic field are required by models of trapped (radiation-belt), solar and cosmic ray particle environments. Trapped particle morphologies are described in terms of location in idealized geomagnetic dipole space (B , L coordinates), while the field is needed in order to include magnetic shielding effects for solar energetic particle and cosmic ray environments. Field models are also used for magnetospheric physics studies, such as tracing the trajectories of particles through the magnetosphere.

Spacecraft motion across the geomagnetic field results in an induced motional e.m.f. given by $\underline{E} = \underline{v} \times \underline{B}$ in the spacecraft. If a current path can be completed, a current flows through the spacecraft and the surrounding plasma. These phenomena can lead to generation of a few volts potential differences on large spacecraft in LEO. The effect is also used or studied in tethered satellite missions where the length of the tether perpendicular to \underline{B} can lead to large currents and potentials.

Interaction between the magnetic field and an on-board magnetic moment \underline{m} gives rise to a force:

$$\underline{F} = (\underline{m} \cdot \nabla) \underline{B}$$

which can be used for attitude control where an on-board magnetic torquer provides \underline{m} .

This clause deals largely with quasi-static geomagnetic fields, data which are needed for the most common applications. However, the magnetosphere is a dynamic system and, especially in the outer parts, is characterized by large fluctuations in plasma populations, electric fields and magnetic fields. It is through the induced disturbances to the main geomagnetic field that the onset of geomagnetic sub-storms at high altitude can be monitored. These disturbances are quantified by observations on the surface of the Earth of the familiar K_p , A_p , D_{st} and other geomagnetic indices (see clause 6 for more detail on geomagnetic activity indices). The disturbed plasma environment which often accompanies such sub-storms can lead to electrostatic charging (see clause 8 for details).

5.2 Reference data on the geomagnetic field

The total field strength in an ideal dipole is given by

$$B = MR^{-3}[1 + 3 \sin^2 \lambda]^{1/2}$$

where λ is the magnetic latitude and R is the radial coordinate (R, λ constituting a polar coordinate system). M is the magnetic dipolar moment. In a dipole approximation for the Earth field, M currently has a value of about $7,9 \times 10^{30} \text{ nT} \cdot \text{cm}^3$ or $30400 \text{ nT} \cdot R_E^3$ where R_E is the mean radius of the Earth. The dipole which approximates the Earth field is both tilted and offset with respect to the Earth's rotation axis, so that the geomagnetic poles do not coincide with the geographic poles and the field strength is not independent of longitude. This configuration is called an eccentric dipole [RD5.1]. Furthermore, the geomagnetic field is slowly changing. The 1990 value for the displacement of the eccentric dipole is 515 km, increasing at 2,6 km per year in the direction of $15,6^\circ \text{ N}$, $150,9^\circ \text{ E}$. An eccentric dipole has axial poles but also dip poles where the field lines are normal to the Earth's surface [RD5.1]. The 1985 axial northern pole (geomagnetic south) was at $82,05^\circ \text{ N}$, $270,2^\circ \text{ E}$. Reference RD5.1 contains an extensive discussion of the geomagnetic dipole and its variations. Table 5 shows the slow decay in the dipole moment.

**Table 5: Changes in dipole moments
1945-1995**

Year	$M_E \text{ (nT} \cdot R_E^3 \text{)}$	$M \text{ (nT} \cdot \text{cm}^3 \text{)}$
1945	31259,7	$8,0844 \times 10^{30}$
1955	31125,9	$8,0498 \times 10^{30}$
1965	30951,6	$8,0047 \times 10^{30}$
1975	30696,4	$7,9387 \times 10^{30}$
1985	30438,0	$7,8719 \times 10^{30}$
1995	30207,7	$7,8123 \times 10^{30}$

5.3 Geomagnetic field models and analysis methods

5.3.1 Dipole model

Many scoping estimates of geomagnetic field effects can be made with the assumption of a dipole model for the Earth's field, as given above. However, account should be taken of the tilt and displacement of the dipole axis described in 5.2.

The radial and latitudinal components of the field are given in polar coordinates by:

$$B_R = -\frac{M}{R^3} 2 \sin \lambda$$

$$B_\lambda = \frac{M}{R^3} \cos \lambda$$

and in Cartesian coordinates by:

$$B_x = 3xz M R^{-5}$$

$$B_y = 3yz M R^{-5}$$

$$B_z = (3z^2 - R^2) M R^{-5}$$

where

M can be taken from the table above;

R is the radius of the location in units consistent with the units of M .
The z axis is along the dipole axis.

5.3.2 Internal-source field models

Although to a first approximation the Earth internally-generated magnetic field is dipolar, the non-dipolar contributions are important and are best described by numerical models of the field which also account for the offset and tilt of the geomagnetic axis with respect to the Earth's rotation axis.

The standard numerical models of the geomagnetic field in general use describe the internal field and its secular variations by spherical harmonic expansions of the scalar potential V [RD5.2]:

$$\mathbf{B} = -\nabla V$$

Although a number of geomagnetic field models are available, the main internationally accepted standard ones are those in the International Geomagnetic Reference Field (IGRF) series [RD5.3]. These shall be used as the standard except for special reasons given elsewhere in this clause and in clause 9. The potential expansion is:

$$V = a \sum_{n=1}^k \left\{ \left(\frac{a}{R} \right)^{n+1} \sum_{m=0}^n [g_n^m \cos(m\phi) + h_n^m \sin(m\phi)] P_n^m(\cos\theta) \right\} \quad (5.1)$$

where a is the radius of a reference sphere and has a value of 6371,2 km for the IGRF models, corresponding to the mean Earth radius. The position of a point of interest is specified with R , θ and ϕ , the geocentric distance, co-latitude (measured from the geographic north pole) and longitude respectively; g_n^m and h_n^m are the model coefficients and P_n^m are Schmidt normalised associated Legendre functions.

The IGRF models released since 1960 have had 120 spherical harmonic coefficients (to degree and order 10) and a further 80 (to degree and order 8) describing the secular variations of the corresponding main field coefficients in a linear fashion.

5.3.3 Eccentric dipole model

For the IGRF-95 model [RD5.4], the first 15 coefficients and their secular variations are shown in Table 6 below. Note that the first 3 terms represent contributions to a centred (tilted) dipole from dipoles along the three Cartesian axes while the first 8 terms define an eccentric (offset and tilted) dipole. Fraser-Smith [RD5.1] describes how the eccentricity, tilt and axial poles can be computed from these terms.

Figure 1 shows the total field strength at an altitude of 400 km super-imposed on a world-map.

As described in annex C, the total dipole strength (moment) can be derived from the first three terms as follows:

$$M = a^3 [(g_0^0)^2 + (g_1^1)^2 + (h_1^1)^2]^{1/2}$$

So given field model, it is possible to extract a value of dipole moment which includes, through the secular variations to g and h , changes with time. Table 7 shows how the first 3 model coefficients of the IGRF series models have been changed with time, and the consequent changes in geomagnetic dipole moment.

**Table 6: The IGRF-95 Model:
Coefficients and their secular
variations to degree and order 3**

	<i>m</i>	<i>n</i>	Coefficient (nT)	Secular variation (nT/y)
<i>g</i>	0	1	-29682	17,6
<i>g</i>	1	1	-1789	13,0
<i>h</i>	1	1	5318	-18,3
<i>g</i>	0	2	-2197	-13,2
<i>g</i>	1	2	3074	3,7
<i>h</i>	1	2	-2356	-15,0
<i>g</i>	2	2	1685	-0,8
<i>h</i>	2	2	-425	-8,8
<i>g</i>	0	3	1329	1,5
<i>g</i>	1	3	-2268	-6,4
<i>h</i>	1	3	-263	4,1
<i>g</i>	2	3	1249	-0,2
<i>h</i>	2	3	302	2,2
<i>g</i>	3	3	769	-8,1
<i>h</i>	3	3	-406	-12,1

**Table 7: Changes in dipole-terms and derived dipole
moments of IGRF models**

IGRF model	Model coefficients			M_E (nT. R_E^3)	M (nT.cm ³)
	g_0^1	g_1^1	h_1^1		
1945	-30634,	-2240,	5806,	31259,7	$8,0844 \times 10^{30}$
1955	-30507,	-2134,	5796,	31125,9	$8,0498 \times 10^{30}$
1965	-30334,	-2119,	5776,	30951,6	$8,0047 \times 10^{30}$
1975	-30100,	-2013,	5675,	30696,4	$7,9387 \times 10^{30}$
1985	-29877,	-1903,	5497,	30438,0	$7,8719 \times 10^{30}$
1990	-29775,	-1851,	5411,	30319,2	$7,8412 \times 10^{30}$
1995	-29682,	-1789,	5318,	30207,7	$7,8123 \times 10^{30}$

5.3.4 Geomagnetic coordinates – *B* and *L*

Geomagnetic coordinates are useful or necessary for a number of applications where charged particle morphology or behaviour needs to be described in the magnetosphere. The most important application is in models of the Earth radiation-belt environment (see clause 9). These particle models give fluxes of trapped energetic particles as functions of particle energy and of McIlwain's geomagnetic co-ordinates *L* and *B/B*₀. *L* is the radial distance of the field line from the axis at the geomagnetic equator in an ideal dipole field and *B* is the magnetic field strength, determining the position along a field line from the minimum *B*₀ at the geomagnetic equator. For many applications the pair *B*, *L* (or equivalently, *B/B*₀, *L*) is sufficient to define a location in the field because of its azimuthal symmetry and the azimuthal symmetry in particle populations.

In the true geomagnetic field, which is only quasi-dipolar, L is formally defined by means of a function of the adiabatic integral invariant I [RD5.5]:

$$I = \int_{l_1}^{l_2} \left(1 - \frac{B}{B_m} \right)^{1/2} dl$$

where the integral is evaluated along the field line between the two conjugate mirror points l_1 and l_2 and B_m is the field at the mirror points. I is a constant on a field line or drift shell. The definition of L is then written as [RD5.5, RD5.6]:

$$L^3 \left(\frac{B}{M} \right) = f \left(\frac{I^3 B}{M} \right) \quad (5.2)$$

where M is the geodipole moment (McIlwain used a constant value $M = 31165,3$ nT.R_E). The function f is evaluated using values for I and B derived from the true geomagnetic field via a model. Hilton [RD5.7] provided a simple approximation for the function f :

$$f(x) = 1 + a_1 x^{1/3} + a_2 x^{2/3} + a_3 x \quad (5.3)$$

where

$$\begin{aligned} x &= I^3 B / M; \\ a_1 &= 1,35047; \\ a_2 &= 0,456376; \\ a_3 &= 0,0475455. \end{aligned}$$

L is found to be nearly constant on a field-line or “drift shell”. A charged particle in the geomagnetic field has three basic components of motion: a gyration about field-lines, a bouncing motion between magnetic mirrors at higher-field parts of the field-lines and an azimuthal drift around the Earth, tracing out a drift shell. By transforming orbital locations into the B, L coordinate system and accessing the radiation environment models throughout the orbit, predictions can be made of satellite radiation exposures (see clause 9).

It is clear from this that computation of L at a point involves an integration along a field line, making use of a magnetic field model. It is important that the method of integration and the parameters M and a_1, a_2, a_3 are consistent when preparing particle environment models and accessing them. For the purposes of radiation belt models, McIlwain’s value was used, un-updated for magnetic moment changes, and this value shall be used in access routines for the AE-8 and AP-8 models specified in clause 9. Furthermore, only the magnetic field models specified in clause 9 shall be used for the generation of B, L coordinates for employing these particle models.

At the geomagnetic equator, which corresponds to the position on a field line with the minimum B ,

$$B = B_0 = ML^{-3}$$

where M is the geomagnetic dipole moment.

Polar coordinates in idealized dipole space are related to B and L by:

$$R = L \cos^2 \lambda$$

and the field strength given by

$$B = \frac{M}{R^3} (1 + 3 \sin^2 \lambda)^{1/2}$$

where λ is the magnetic latitude and R is the radial coordinate which clearly has a value $R_0 = L$ at the magnetic equator.

5.3.5 External-source field models

The models described above only describe the field generated by processes within the Earth. At high altitudes most of the higher-order terms become negligible and the dipole approximation is often adequate to describe this contribution. However, the solar wind causes large diurnal distortions of the field at high altitude (see Figure 2 [RD5.8]). This effect, together with the ring current from azimuthally drifting particles, and other current systems means that the internal field is a poor representation of the total field. The effects of the other current systems are to introduce diurnal variations into the magnetic field and a perturbation from the external current systems varying with solar and geomagnetic activity (solar wind pressure, ring current intensity, K_p variations).

Various models for the external contributions to the field have been developed by Tsyganenko [RD5.9, RD5.10], Olsen and Pfitzer [RD5.11] and Mead and Fairfield [RD5.12]. No internationally recognized standard has yet appeared although progress is being made in that direction [RD5.13]. Since these models include the diurnal asymmetry of the field and depend on geomagnetic activity indices, they are attractive for use in mapping energetic particle fluxes and their responses to activity variations. The post-flight data analysis programme for the CRRES mission makes use of external field models [RD5.14]. However, the effect of the high-altitude distortions is to make the equatorial radius of the drift-shell of a particle dependent on the particle's pitch-angle, so that populations are separated and merged azimuthally in a way that complicates the modelling of their morphologies.

External-source models should not be used in conjunction with current standard radiation-belt environment models described in clause 9.

No particular external source model is required as standard.

The field magnitudes involved in the external sources are very small and it is emphasized that only in special circumstances do they need to be considered. Bass and Jordan [RD5.15] inter-compared various models and show the magnitudes of the errors with various models and also compared with CRRES magnetometer data can be large, but it should be re-emphasized that the fields are themselves relatively weak here.

One of the areas where an external model of the geomagnetic field is useful is for improved B , L coordinate calculation for trapped radiation-belt models. Using an internal-only field results in an error compared to an internal-plus-external model of up to one Earth-radius at high altitudes. Such improved methods shall be consistently applied as mentioned previously: the model generation and access routines shall use the same methods for B and L calculation.

The field at geostationary orbit is of approximately 100 nT strength with an approximately 50 % modulation due to the diurnal asymmetry. During severe geomagnetic storm events, the field strength can completely reverse and reach -200 nT. In the geomagnetic tail (anti-sunward direction) the direction of the field can be far from parallel to the Earth geomagnetic or rotation axes. Data on magnetic field fluctuations at geostationary orbit are available from the GOES satellite space environment data archive [RD5.16].

Figure 3 shows the variation of the total geomagnetic field as a function of altitude, as derived from a combined internal and external source model. Various local time and activity conditions are shown. The error bar at geostationary altitude qualitatively represents the variability.

5.3.6 Magnetospheric boundaries

Some simple expressions can be used to estimate basic locations of magnetospheric boundaries for mission planning. The stand-off radial distance of the magnetopause in the sunward direction is given by:

$$L_{mp} = 107,4 (n_{sw} u_{sw}^2)^{-1/6}$$

where L_{mp} is in units of Earth-radii, n_{sw} , the solar wind proton number density is in units of cm^{-3} and the solar wind bulk velocity is in units of km/s. Typical values for n_{sw} and u_{sw} are 8 cm^{-3} and 450 km/s respectively, leading to a stand-off distance of about 10 Earth-radii.

For modelling the full magnetopause position, the following model of Sibeck et al. [RD5.17] shall be used. This represents the magnetopause position as the function:

$$R^2 + A x^2 + B x + C = 0$$

where

$$R^2 = y^2 + z^2;$$

x , y , and z are GSM coordinates, in Earth-radii;

A , B and C are fit parameters dependent on the solar wind pressure as given in Table 8.

Table 8: Sibeck et al. [RD5.17] Magnetopause model

Solar wind pressure range (nPa)	A	B	C	Sub-solar point (R_E)	Dawn meridian (R_E)
0,54-0,87	0,19	19,3	-272,4	12,6	16,5
0,87-1,47	0,19	19,7	-243,9	11,7	15,6
1,47-2,60	0,14	18,2	-217,2	11,0	14,7
2,60-4,90	0,15	17,3	-187,4	10,0	13,7
4,90-9,90	0,18	14,2	-139,2	8,8	11,8

5.4 Tailoring guidelines

As has already been mentioned, careful consideration should be given to application needs before selecting a model. A low-fidelity dipole model (aligned, eccentric or tilted dipoles) can suffice for many engineering applications. Most engineering applications never have need of the external-source model augmentation. These can only be necessary for mission planning for magnetospheric missions or if data on high latitude or high altitude variability of the fields with respect to local time and solar-geomagnetic activity is required. They can also be necessary where magnetic torquing is used at high altitudes such as in geostationary orbit, although the dynamic variability of the field at high altitudes shall be taken in to account.

For radiation belt modelling applications consistence shall be assured between the model's construction field model and the users access field model (e.g. Jensen-Cain and GSFC models for AE and AP series models - see clause 9).

5.5 Figures

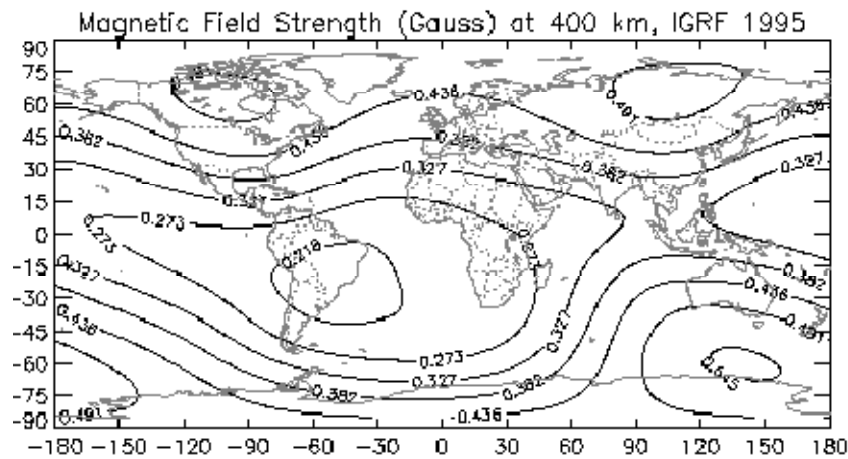


Figure 1: Geomagnetic field strength at 400 km altitude based on IGRF-1995

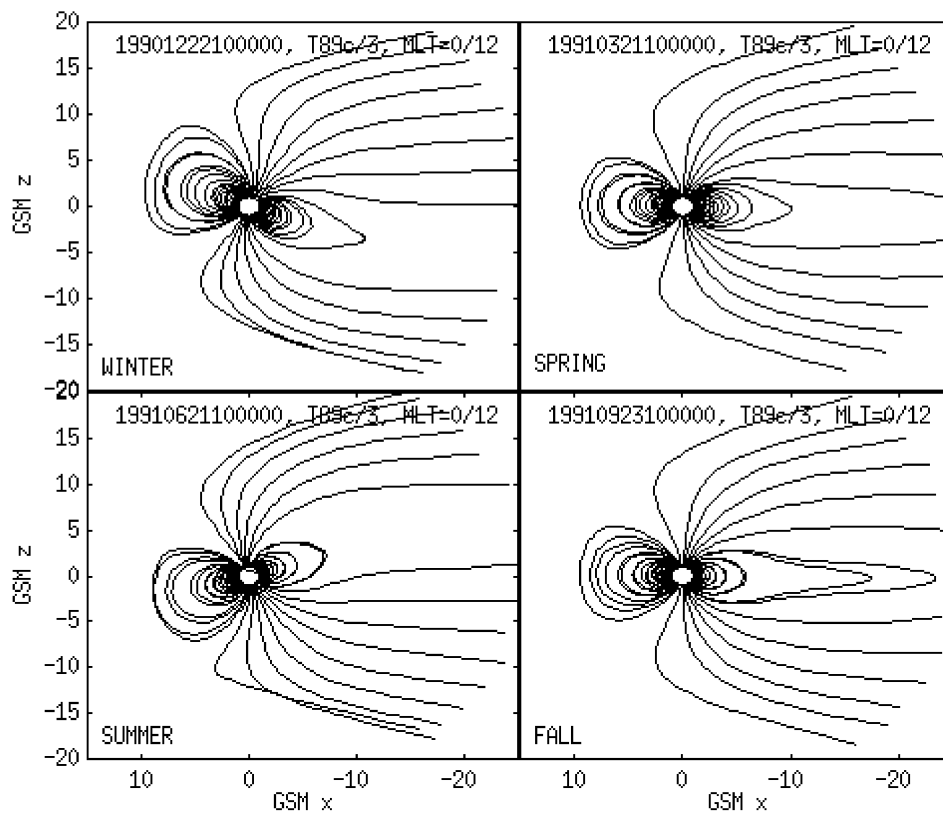
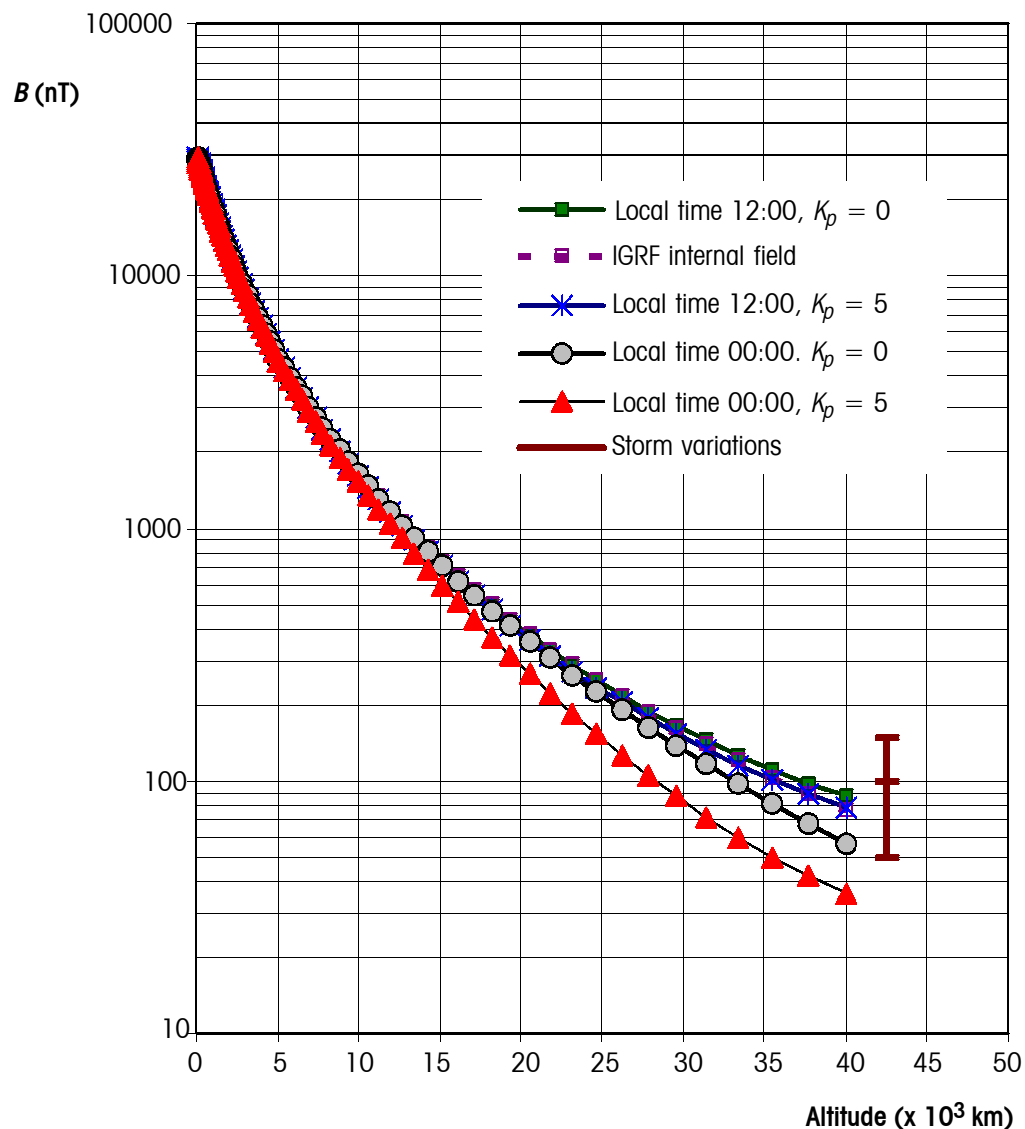


Figure 2: Output from geomagnetic field models showing the diurnal distortion to the field and seasonal variations in the distortion [RD5.8]



Field models include internal-only (IGRF) and external-source models for various conditions. Also shown is the typical dynamic variation at geostationary orbit during disturbed periods.

Figure 3: Variation of the geomagnetic field as a function of altitude

5.6 References

- RD5.1 Fraser-Smith, A.C., "Centered and Eccentric Geomagnetic Dipoles and Their Poles, 1600–1985", *Rev. Geophys.*, 25, 1–16, 1987.
- RD5.2 Stern D. "Representation of Magnetic Fields in Space", *Rev. Geophys. and Space Phys.* 14, 199, 1976.
- RD5.3 Peddie, N.W., "International Geomagnetic Reference Field: The Third Generation", *J. Geomag. Geoelectr.* 34, 309–326, 1982.
- RD5.4 Barton C.E., "Revision of International Geomagnetic Reference Field Released", *EOS Transactions of the AGU* 77, 16, April 16, 1996.
- RD5.5 Hess W.N., "The Radiation Belt and the Magnetosphere", Blaisdell Publ. Co. New York, 1968.
- RD5.6 McIlwain C.E., "Co-ordinates for Mapping the Distribution of Geomagnetically Trapped Particles", *J. Geophys. Res.*, 66, 3681, 1961.
- RD5.7 Hilton H.H., "L Parameter - A New Approximation", *J. Geophys. Res.*, 76, 6952, 1971. (Note that this paper contains a typographical error in its expression for a_3 of Equation 5.3).

- RD5.8 Rasinkangas R., K. Mursula, T. Ulich, and J. Kangas, "Magnetic field models" in "Space Physics Textbook", <http://www oulu.fi/~spaceweb/textbook/bmodels.html>, Oulu University, 1998.
- RD5.9 Tsyganenko N.A., "A Magnetospheric Magnetic Field Model with a Warped Tail Current Sheet", Planet. Space Sci. 37, 5-20, 1989.
- RD5.10 Tsyganenko N.A. and D.P. Stern, "Modeling the Global Magnetic Field of the Large-Scale Birkeland Current Systems", J. Geophys. Res., 101, 27187-27198, 1996.
- RD5.11 Olsen W.P. and K.A. Pfitzer, "A Quantitative Model of the Magnetospheric Magnetic Field", J. Geophys. Res., 79, 3739, 1974.
- RD5.12 Mead G.D. and D.H. Fairfield, "Magnetospheric Mapping with a Quantitative Geomagnetic Field Model", J. Geophys. Res. 80, 523, 1975.
- RD5.13 Stern D.P. and N.A. Tsyganenko, "Uses and Limitations of the Tsyganenko Magnetic Field Models", EOS, Transactions, American Geophysical Union, 73, no. 46, 489, 17 November 1992.
- RD5.14 Pfitzer K.A., "Improved Models of the Inner and Outer Radiation Belts", Phillips Lab Scientific Report PL-TR-91-2187, US Air Force Systems Command, PLGD, Hanscom AFB, Ma., 1991.
- RD5.15 Bass, J.N. and C.E. Jordan, "Models of the External Source Contribution to Magnetospheric Magnetic Fields for CRRES Data Analysis, Scientific Report No. 2", GL-TR-90-0009, Geophysics Laboratory, AFSC, 1990.
- RD5.16 National Geophysical Data Center, "Space Environment Data from NOAA's GOES Satellites", National Geophysical Data Center, Code E/GC2, Dept. 946, 325 Broadway Boulder Co 80303 3328 USA., also Space Physics Interactive Data Resource at <http://www.ngdc.noaa.gov:8080/>.
- RD5.17 Sibeck D.G., R.E.Lopez and E.C.Roelof, "Solar Wind Control of the Magnetopause Shape, Location and Motion", J. Geophys. Res, 96, p. 5489, 1991.

Solar and Earth electromagnetic radiation and indices

6.1 Introduction

A spacecraft in LEO receives electromagnetic radiation from three primary external sources. The largest source is the direct solar flux. The mean value of this solar flux at the mean Sun-Earth distance is called the “solar constant”. It is not really a constant but varies by about 3,4 % during each year because of the slightly elliptical orbit of the Earth about the Sun. In addition the amount of radiation emitted by the Sun varies slightly (by about $\pm 0,1$ %) throughout the 11-year solar cycle.

The fraction of incident sunlight that is reflected off a planet is termed albedo. For an orbiting spacecraft the albedo value depends mainly on the sunlit part of the Earth which it can see. Albedo radiation has approximately the same spectral distribution as the Sun and in this Standard albedo refers to the total solar spectrum albedo. Albedo is highly variable across the globe and depends on surface properties and cloud cover. It also depends on the solar zenith angle.

The third source is the Earth infrared radiation. The Earth-emitted thermal radiation has a spectrum of a black body with a characteristic average temperature of 288 K. The Earth infrared radiation also varies across the globe but less than the albedo. It also shows a diurnal variation which is small over the ocean but can amount to 20 % for desert areas.

Solar and geomagnetic activities are often described by indices. The UV radiation of the Sun, which strongly effects the Earth atmosphere, cannot be directly measured from the ground. But it was found to be strongly correlated with e.g. the sunspot number and the cm wavelength Sun radiation. The widely used 10,7 cm radio flux index ($F_{10,7}$) gives a good measure of the solar UV radiation output which is highly variable over a solar cycle.

Geomagnetic indices typically describe the variation of the geomagnetic field over a certain time period. They provide a measure of the disturbance of the magnetosphere which has direct consequences for the charged particle space environment.

Solar and geomagnetic indices are required as input for upper atmosphere and other models of the near Earth space environment. They are provided for short durations or as long time averages. Predictions for future index values are

usually provided at different confidence levels and they are available for complete solar cycles.

The given data are mainly average values. For detailed thermal analyses or certain special applications more detailed data and models are required which are outside the scope of this Standard. Requirements for thermal analyses are specified in ECSS-E-30: part 1 [RD6.1].

6.2 Solar electromagnetic radiation

6.2.1 Solar constant

The solar constant is defined as the radiation that falls on a unit area of surface normal to the line from the Sun, per unit time, outside the atmosphere, at one astronomical unit (1 AU = average Earth-Sun distance).

The solar constant has an uncertainty of about $\pm 10 \text{ W/m}^2$ [RD6.2]. The following values for the electromagnetic radiation shall be used:

Solar constant at 1 AU	1371 W/m^2
Maximum solar energy flux (winter solstice)	1428 W/m^2
Minimum solar energy flux (summer solstice)	1316 W/m^2
Solar radiation pressure (100 % reflecting plate)	$9,02 \times 10^{-6} \text{ N/m}^2$.

6.2.2 Solar spectrum

The solar spectrum shall be approximated by a black body curve with a characteristic temperature of 5762 K. A space sink temperature of 3 K shall be assumed.

The UV portion (wavelength, $\lambda < 300 \text{ nm}$) of the electromagnetic spectrum is of particular importance in determining effects of solar radiation on the upper atmosphere and on material properties. The integrated irradiance of the near UV electromagnetic radiation flux ($180 \text{ nm} < \lambda < 400 \text{ nm}$) is approximately 118 W/m^2 . The far UV portion ($\lambda < 180 \text{ nm}$) contributes about $0,023 \text{ W/m}^2$.

The solar constant changes by only about $\pm 0,1 \%$ around the mean value over one solar cycle [RD6.3] and is largest during the period of maximum solar activity.

Certain parts of the spectrum are much more variable, both, over the 27-day solar rotation period and over the 11-year solar cycle. This variation ranges from about 50 % for the near UV part to a factor 2 for the UV and far UV portions and can reach orders of magnitude for flare X-rays.

Average and worst case irradiance levels for the high-energy spectrum are summarized in Table 9. The average values were taken from RD6.2.

For design purposes the worst case values of Table 9 shall be used. The fluxes given for flare X-rays are peak values of large flares. For design, one such X-ray flare per week, lasting one hour, shall be assumed.

Annex D contains more details on the solar spectrum.

Table 9: High-energy solar electromagnetic flux

Type	Wavelength (nm)	Average flux (W/m^2)	Worst-case flux (W/m^2)
Near UV	180-400	118	177
UV	< 180	$2,3 \times 10^{-2}$	$4,6 \times 10^{-2}$
UV	100-150	$7,5 \times 10^{-3}$	$1,5 \times 10^{-2}$
EUV	10-100	2×10^{-3}	4×10^{-3}
X-rays	1-10	5×10^{-5}	1×10^{-4}
Flare X-rays	0,1-1	1×10^{-4}	1×10^{-3}

6.3 Earth electromagnetic radiation

6.3.1 Earth albedo

Albedo is the fraction of sunlight which is reflected off a planet.

The average albedo of the Earth is about 0,3. For short periods the albedo can vary considerably between about 0,05 and 0,6.

For albedo radiation the same spectral shape as for sunlight shall be assumed.

Albedo values are only applicable when a portion of the Earth that is seen by the satellite is sunlit. Albedo values vary with solar zenith angle. The sunlit part of the Earth and the solar zenith angle shall be considered for albedo analyses.

Average albedo values have sometimes to be used with care, e.g. for short duration analyses or for Sun-synchronous orbits where albedo is from specific local times.

Additional information on the variability of the albedo is given in annex D.

6.3.2 Earth infrared

The Earth-emitted thermal radiation is also called “Earth infrared” or “outgoing long wave radiation”.

For the Earth infrared radiation a black body spectrum with a characteristic temperature of 288 K shall be assumed.

The average infrared radiation emitted by Earth is 230 W/m². On a short time scale it can vary between 150 W/m² to 350 W/m².

The diurnal variations can amount to about 20 % over desert areas while it is small over oceans.

Additional information on the variability of the Earth infrared radiation is given in annex D.

6.4 Solar and geomagnetic indices

6.4.1 General

Solar and geomagnetic indices are used to describe the activity levels of the Sun and the disturbance of the geomagnetic field. Most activity indices are given for short periods and as long duration averages. They are also used for long range predictions of solar activities. Many space environment models require activity index values as input parameters.

6.4.2 Description of indices

6.4.2.1 Solar activity indices

The most frequently used solar activity indices are the sunspot number, R , and the 10,7 cm wavelength radio flux, $F_{10,7}$. These values, which can be measured at the ground, were found to have a strong correlation with the UV radiation of the Sun, which has a strong influence on the Earth atmosphere.

The $F_{10,7}$ solar activity index gives the flux at a wavelength of 10,7 cm in units of 10⁴ Jansky (one Jansky equals 10⁻²⁶ W m⁻² Hz⁻¹).

The $F_{10,7}$ index and the sunspot number, R , are correlated. Averaged (over one month or longer) values can be converted by the following expression:

$$F_{10,7} = 63,7 + 0,728 R + 8,9 \cdot 10^{-4} R^2.$$

6.4.2.2 Geomagnetic activity indices

Geomagnetic activity indices are used to describe fluctuations of the geomagnetic field. Most widely used planetary indices are K_p and a_p . They are based on 3-hour measurements from 12 ground stations. Values of a_p range from 0 to 400 and they are expressed in units of 2 nT. K_p is essentially the logarithm of a_p . The conversion from K_p to a_p is given in Table 10 (taken from RD6.4). A daily index, A_p , is obtained by averaging the eight values of a_p for each day.

Besides K_p and a_p several other activity indices are used to describe different aspects of the geomagnetic field activity. An overview of the various activity indices and their definitions is given in RD6.5.

Table 10: Conversion from K_p to a_p

K_p	0	0+	1-	10	1+	2-	20	2+	3	30	3+	4-	40	4+
a_p	0	2	3	4	5	6	7	9	12	15	18	22	27	32
K_p	5-	50	5+	6-	60	6+	7-	70	7+	8-	80	8+	9-	90
a_p	39	48	56	67	80	94	111	132	154	179	207	236	300	400

6.4.3 Solar cycle dependence

Table 11 lists the minimum, mean and maximum 13-month smoothed values for $F_{10,7}$ and A_p throughout a mean 11-year solar cycle. These values are taken from RD6.2. The minimum and maximum values are the historical extremes for each point in the cycle and were obtained after the data have been 13-month smoothed and constrained to the mean duration cycle. The standard deviation of the mean cycle length is 1,23 years over the historical record. Figure 4 shows these data graphically.

Table 11: Maximum, mean, and minimum values of the 13-month smoothed 10,7 cm solar radio flux and geomagnetic activity index over the mean solar cycle

Month of cycle	$F_{10,7}$			A_p		
	Max	Mean	Min	Max	Mean	Min
1	73,3	69,6	67,0	11,5	9,5	7,6
2	73,4	69,7	67,0	11,7	9,6	7,7
3	74,0	70,0	67,0	11,8	9,7	7,7
4	74,5	70,4	67,0	11,9	9,7	7,6
5	74,9	70,7	67,0	11,9	9,7	7,4
6	76,2	71,1	67,1	12,2	9,9	7,3
7	78,4	71,6	67,2	12,5	10,0	7,2
8	79,8	72,2	67,3	12,9	10,3	7,2
9	81,5	72,8	67,4	13,3	10,6	7,8
10	84,1	73,6	67,5	14,1	10,9	8,1
11	87,7	74,5	67,7	15,1	11,2	8,2
12	93,4	75,7	67,9	15,7	11,5	8,3
13	97,9	77,0	68,0	15,9	11,8	8,3
14	101,7	78,4	68,0	16,4	12,0	8,3
15	107,7	80,1	68,0	17,4	12,3	8,5
16	114,5	82,0	68,0	18,4	12,7	8,4
17	121,1	84,0	68,1	18,7	12,9	8,5

Table 11: Maximum, mean, and minimum values of the 13-month smoothed 10,7 cm solar radio flux and geomagnetic activity index over the mean solar cycle (*continued*)

Month of cycle	$F_{10,7}$			A_p		
	Max	Mean	Min	Max	Mean	Min
18	129,1	86,2	68,4	18,8	13,1	8,7
19	137,6	88,5	68,5	18,6	13,2	9,0
20	143,4	91,0	68,6	18,3	13,2	9,3
21	147,6	93,7	68,8	18,1	13,2	9,7
22	151,7	96,3	68,7	18,4	13,4	9,5
23	155,7	98,9	68,8	18,4	13,5	9,3
24	160,1	101,6	69,2	17,6	13,5	9,1
25	164,8	104,4	69,7	17,1	13,6	9,0
26	169,1	107,2	70,1	17,4	13,6	9,1
27	173,0	110,2	70,6	17,4	13,6	9,4
28	177,1	113,2	70,7	18,5	13,8	9,8
29	186,1	116,2	71,3	19,9	14,0	10,0
30	191,5	119,3	72,2	19,9	14,1	10,0
31	194,3	122,0	72,6	19,9	14,1	10,1
32	196,9	124,3	73,3	20,1	14,1	10,4
33	199,6	126,5	73,9	20,4	14,2	10,2
34	204,2	128,6	74,1	20,8	14,2	10,3
35	210,6	131,0	74,4	20,9	14,1	10,6
36	214,8	133,3	74,5	21,0	14,0	10,6
37	217,2	135,6	74,6	21,2	14,0	10,5
38	221,6	137,6	74,5	21,6	14,1	10,4
39	226,9	139,6	74,1	22,1	14,1	10,6
40	229,9	141,4	73,6	22,2	14,0	10,8
41	231,7	143,2	73,5	21,0	13,7	10,7
42	233,7	144,6	73,6	20,1	13,4	10,4
43	235,6	145,6	74,0	19,8	13,3	10,5
44	238,8	146,7	75,1	19,3	13,3	10,7
45	242,8	147,2	75,8	19,2	13,3	10,8
46	245,2	147,7	76,5	19,0	13,4	11,0
47	244,5	148,1	78,1	18,8	13,3	10,7
48	243,3	148,4	80,1	18,6	13,4	10,8
49	244,7	148,7	82,5	18,6	13,4	10,6
50	245,7	148,2	84,0	18,3	13,4	10,2
51	243,3	146,8	85,5	18,2	13,5	10,6
52	239,4	145,7	87,9	18,7	13,8	11,3
53	235,0	145,1	89,5	19,2	14,1	11,4
54	232,9	144,9	92,2	19,6	14,2	11,3
55	233,3	144,9	93,8	20,3	14,4	11,3
56	233,1	144,7	94,9	21,0	14,6	11,5
57	231,2	144,2	95,0	21,4	14,8	11,6
58	229,1	143,5	94,7	21,2	14,8	11,6
59	228,1	142,7	94,9	20,4	14,7	11,8

Table 11: Maximum, mean, and minimum values of the 13-month smoothed 10,7 cm solar radio flux and geomagnetic activity index over the mean solar cycle (*continued*)

Month of cycle	$F_{10,7}$			A_p		
	Max	Mean	Min	Max	Mean	Min
60	227,6	142,3	96,5	20,7	14,8	12,1
61	226,7	142,1	97,3	21,9	15,1	12,2
62	225,6	141,3	96,8	22,7	15,2	12,0
63	223,0	140,1	96,0	22,7	15,1	11,6
64	218,6	138,4	96,0	22,3	15,1	11,2
65	215,3	136,8	96,6	21,7	15,1	11,2
66	212,0	135,5	96,7	21,5	15,1	11,2
67	206,9	134,3	95,1	22,1	15,1	11,2
68	204,0	133,0	95,0	23,1	15,5	11,3
69	203,6	131,6	96,3	23,5	15,6	11,3
70	200,4	129,8	96,5	23,4	15,6	11,2
71	196,8	128,3	94,7	23,3	15,7	11,1
72	195,7	127,3	93,6	23,1	15,5	10,8
73	194,8	126,5	93,5	22,2	15,7	10,9
74	191,5	125,1	91,9	22,1	15,6	11,1
75	187,4	123,5	88,7	22,2	15,6	11,7
76	182,9	122,3	86,6	22,5	15,8	11,6
77	178,6	121,5	87,8	22,6	15,9	11,5
78	176,3	120,5	86,5	22,5	15,8	11,3
79	174,9	119,5	85,9	21,6	15,7	11,3
80	171,1	117,9	85,0	21,0	15,4	11,3
81	164,5	116,3	83,6	21,1	15,2	11,2
82	158,1	114,6	82,3	21,6	15,2	11,2
83	154,4	112,9	81,6	22,2	15,4	11,4
84	152,7	111,1	81,5	22,0	15,3	11,3
85	150,8	109,5	81,9	22,0	15,2	11,4
86	148,1	108,0	81,6	22,2	15,0	11,3
87	145,0	106,4	81,4	22,5	14,9	11,3
88	141,1	104,9	80,2	22,8	14,7	11,2
89	137,0	103,4	80,3	23,5	14,7	11,1
90	132,4	101,9	80,0	24,2	14,7	11,0
91	125,4	100,3	78,9	24,7	14,8	11,3
92	119,5	98,9	77,6	25,0	14,8	11,3
93	118,4	97,7	76,6	24,9	14,8	11,2
94	118,7	96,6	74,8	24,5	14,8	11,4
95	119,4	95,6	74,0	23,6	14,7	11,6
96	119,8	94,8	73,4	22,8	14,7	11,3
97	119,0	93,9	73,2	22,1	14,7	11,1
98	117,7	92,8	73,1	21,8	14,8	11,1
99	116,4	91,8	72,7	21,4	14,8	11,2
100	114,6	90,6	71,7	21,1	14,8	11,2
101	110,8	89,6	71,1	20,5	14,7	10,5

Table 11: Maximum, mean, and minimum values of the 13-month smoothed 10,7 cm solar radio flux and geomagnetic activity index over the mean solar cycle (*continued*)

Month of cycle	$F_{10,7}$			A_p		
	Max	Mean	Min	Max	Mean	Min
102	105,4	88,4	70,6	19,7	14,4	9,9
103	103,2	87,3	70,1	19,7	14,3	9,5
104	102,0	86,5	69,9	19,8	14,1	9,2
105	100,0	85,7	70,0	19,5	14,0	9,0
106	98,2	84,8	69,9	19,1	13,8	8,9
107	96,6	83,6	69,7	18,6	13,8	8,8
108	94,6	82,5	69,5	17,9	13,8	8,7
109	93,8	81,8	69,4	17,0	13,7	8,7
110	92,7	81,1	69,3	16,5	13,6	8,8
111	92,0	80,3	69,0	16,7	13,5	8,9
112	91,8	79,6	68,8	16,9	13,4	9,0
113	91,4	78,9	68,5	17,1	13,3	9,0
114	90,8	78,2	68,2	17,4	13,3	9,0
115	90,1	77,5	68,2	17,4	13,1	9,0
116	89,1	76,9	68,2	17,6	12,9	9,2
117	88,2	76,4	68,2	17,4	12,7	9,3
118	87,0	75,9	68,3	16,9	12,5	9,2
119	85,4	75,3	68,3	16,1	12,2	9,1
120	83,2	74,8	68,3	14,7	11,8	9,1
121	80,5	74,2	68,3	13,6	11,5	9,1
122	78,5	73,5	67,9	13,7	11,2	8,9
123	77,6	72,9	67,6	13,4	10,9	8,5
124	77,1	72,3	67,4	13,0	10,6	8,1
125	76,9	72,0	67,4	12,7	10,5	8,0
126	76,7	71,6	67,2	12,4	10,3	8,0
127	76,5	71,3	67,1	11,7	10,1	8,0
128	76,2	70,9	67,0	11,2	9,9	8,0
129	75,2	70,6	67,0	11,0	9,8	7,9
130	74,2	70,3	67,0	10,9	9,1	7,2
131	74,0	70,1	67,0	11,1	9,2	7,4
132	73,5	69,9	67,0	11,4	9,4	7,6

6.4.4 Reference index values

The reference index values shown in Table 12 for low, mean and high solar and geomagnetic activities shall be used. The long-term values apply for monthly mean or longer term averaged values. They shall also be used for periods between 1 day and 1 month.

The short duration high values apply for periods of 1 day or less. They shall be used to assess the maximum short-term variations of environmental properties (e.g. atmospheric density fluctuations). Annex D contains some historical data on the variability of these indices.

Table 12: Reference index values

	Long-term			Short-term
	Low	Mean	High	High
$F_{10,7}$	70	140	250	380
A_p	0	15	25	300

6.4.5 Tailoring guidelines

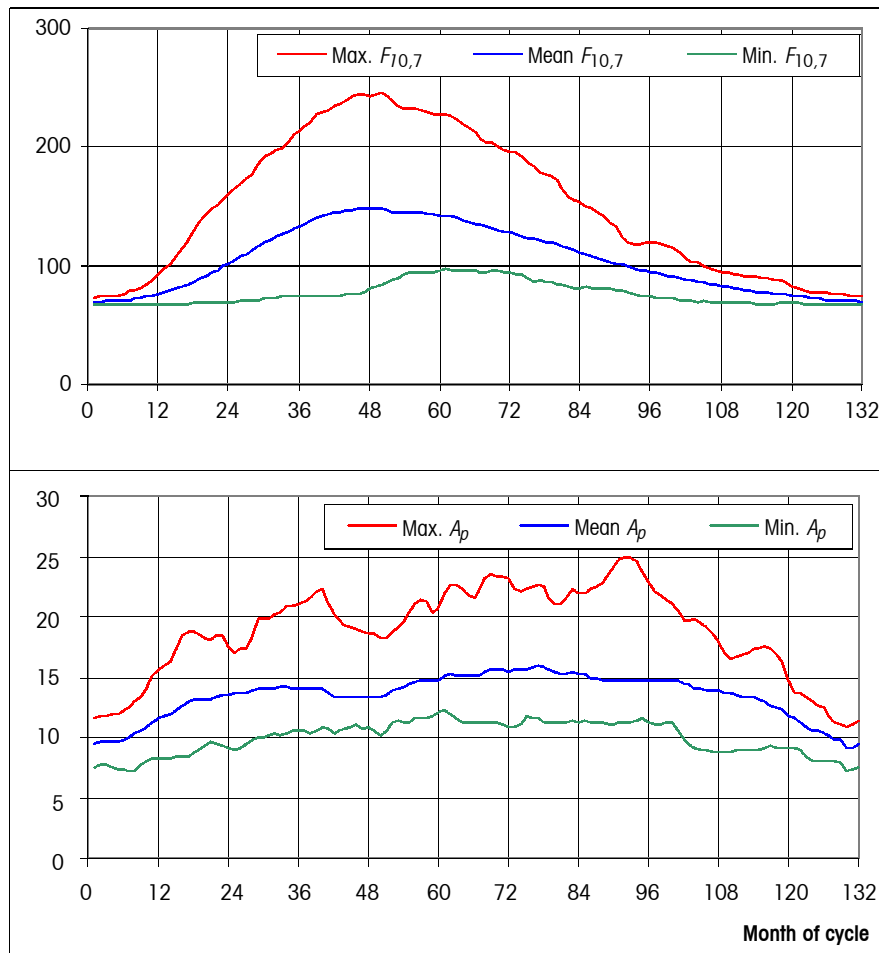
For design purposes the worst case activity values shall be used. These can be the high or low values, depending on the effect to be studied.

Depending on the case to be analysed either the constant reference data in sub-clause 6.4.4 (to get a typical or maximum value) or the solar cycle data in 6.4.3 (to analyse a longer mission or to obtain the activity prediction for a specific future date) shall be used.

The solar cycle activity in Table 11 can be extended by repetition of the 11-year cycle.

August 1996 shall be assumed as start of cycle 23 (month 1 of Table 11).

6.5 Figures



See description in text.

Figure 4: Standard predictions of solar and geomagnetic activity during a cycle

6.6 References

- RD6.1 “European Cooperation for Space Standardization, Mechanical Engineering - Thermal Control”, ECSS-E-30 part 1.
- RD6.2 “Natural Orbital Environment Guidelines for Use in Aerospace Vehicle Development”, B.J. Anderson, editor and R.E. Smith, compiler; NASA TM 4527, chapters 6 and 9, June 1994.
- RD6.3 Willson R.C. and H.S. Hudson, “The Sun’s luminosity over a complete solar cycle”, *Nature*, Vol. 351, pp 42-44, May 1991.
- RD6.4 Menvielle M. and A. Berthelier, “The K-derived Planetary Indices: Description and Availability”, *Rev. Geophys.*, 29, 3, pp 415-432, August 1991.
- RD6.5 “SESC Glossary of Solar-Terrestrial Terms”, NOAA-USAF Space Environment Services Center, Boulder, 1988 (revised 1992).

(This page is intentionally left blank)

The neutral Earth atmosphere

7.1 Introduction

A good knowledge of temperature, total density, concentrations of gas constituents, and pressure can be important for many space missions in the low-Earth orbit regime (LEO), below 1000 km altitude. Aerodynamic forces due to the orbital motion of a satellite through a rarefied gas with superimposed winds are required to be known for orbit maintenance planning, for sizing of the propulsion system, for attitude controller design, and for the estimation of accelerations acting on sensitive payloads.

Also surface corrosion due to atomic oxygen impingement shall be assessed to predict the degradation of sensitive coatings. Atomic oxygen reactions around a spacecraft can also lead to “vehicle glow”.

7.2 Recommended reference model

Due to the large underlying set of supporting measurement data, the large temporal and spatial distribution of these data, the good fit of these data, and the flexible mathematical formulation of the model, the MSISE-90 atmosphere [RD7.1] shall be adopted as reference (corresponding to CIRA-86, the COSPAR International Reference Atmosphere, described in RD7.2 for altitudes above 120 km).

MSISE-90 determines temperature, density, and number concentrations of the major constituents from ground to exospheric altitudes as a function of seven atmospheric state parameters. Other current and historic atmosphere models are mentioned in the informative annex. For horizontal winds the HWM-93 model shall be adopted (Horizontal Wind Model 1993, based on RD7.3). It provides north and east wind components as a function of the same parameters used by MSISE-90.

Annex E contains information on other models.

7.3 Structure of the Earth atmosphere

The Earth atmosphere can be broadly divided into three distinct regimes:

- the homosphere which comprises the troposphere (0 km to 12 km altitude), the stratosphere (12 km to 50 km), and the mesosphere (50 km to 90 km);
- the thermosphere which extends from about 90 km altitude to 250 km or 400 km (depending on solar and geomagnetic activity levels);
- the exosphere which begins at the top of the thermosphere and extends into space.

The homosphere, due to vertical winds and turbulent mixing, has a nearly uniform composition of about 78,1 % N₂, 20,9 % O₂, and 0,9 % Ar. Its temperature profile shows alternating gradients with a local minimum at the tropopause (218 K), a local maximum at the stratopause (280 K), and another local minimum at the mesopause (≈ 150 K).

In the thermosphere, starting at the turbopause near 105 km, vertical mixing processes become less significant, and diffusion under the influence of gravitation and temperature gradients determines the concentration profiles with altitude of the major constituents N₂, N, O₂, O, He, H, and Ar. The thermospheric temperature profile starts off with a nearly constant value at the turbopause and attains an asymptotic limit T_{∞} at the thermopause (between 250 km and 400 km). Both the thermopause altitude and the thermospheric temperature T_{∞} are depending on the energy input into the heterosphere. These inputs are primarily due to EUV radiation from the Sun and its absorption by atomic oxygen, due to Joule heating caused by charged particles which precipitate into the atmosphere at auroral zones, due to photo dissociation, and due to re-combination processes. Locally, T_{∞} can attain values between 600 K and 2000 K for extremely low and extremely high solar activity levels. Upwards from 400 km the mean free path length of molecules increases to a level at which the light constituent H (which is a major contributor at these altitudes) may exceed the Earth escape velocity and exit the system (hence the term “exosphere”).

7.4 Atmospheric state parameters

Satellite drag data from orbit determinations, on-orbit mass spectrometers, accelerometers, sounding rockets, and ground-based incoherent scatter radars provide a wealth of information on the composition, temperature, and variability of the heterosphere, particularly between 150 km and 700 km altitude. Measurement data reveal that temperature, composition, pressure, and total density of the Earth atmosphere change with the following parameters:

- h , in km, geodetic altitude;
- ϕ , in $^{\circ}$ or rad, geodetic latitude;
- t_{ls} , in h, local solar time;
- t_{ut} , in h, universal time, or alternatively θ , in $^{\circ}$ or rad, geographic longitude;
- t_d , in d, day of the current year (counting from Jan. 1);
- $F_{10,7}$, in 10^{-22} W m⁻² Hz⁻¹ ($= 10^4$ Jansky) the daily 10,7 cm solar flux index (mostly used from the previous day);
- $(F_{10,7})_{avg}$, in 10^{-22} W m⁻² Hz⁻¹, a mean solar flux index (mostly a running mean over the previous three rotations of the Sun, corresponding to 81 days);
- $A_p \in [0, 400]$, daily mean geomagnetic index, or alternatively $K_p \in [0, 10]$, quasi-logarithmic daily mean geomagnetic index, or alternatively $k_p \in [0, 10]$, 3-hourly quasi-logarithmic geomagnetic indices for one day.

The parameters t_{ls} , t_{ut} , and θ are interrelated. In order to be consistent, they shall obey the relation

$$\theta (^{\circ}) = 15 \times [t_{ls} (\text{h}) - t_{ut} (\text{h})].$$

The solar activity in terms of the 10,7 cm radio flux $F_{10,7}$ and the corresponding Sun-spot number (R) follow a long-periodic 11-year solar cycle with a superimposed 27-day cycle due to the rotation of the Sun. Data histories of solar and geomagnetic activities are shown in clause 6 and annex D. The forecast of the actual level of the daily $F_{10,7}$ and geomagnetic A_p index is difficult and associated with considerable uncertainties.

If the atmospheric state parameters are well known, then the total air density, comprising activity dependent variations (with $(F_{10,7})_{avg}$, $F_{10,7}$ and A_p or k_p), diurnal variations (with t_{ls} and ϕ), longitudinal-latitudinal variations (with t_{ut} and ϕ) and seasonal-latitudinal variations (with t_d and ϕ) of the heterosphere can be modelled with an r.m.s. accuracy of $\pm 10\%$ to 15% for the MSISE-90 atmosphere model [RD7.1] which shall be the adopted ECSS reference for both homospheric and heterospheric altitudes.

7.5 Temperature, composition, and density model of the Earth heterosphere

In the heterosphere, well above 90 km, one can assume that the constituents are in diffusive equilibrium with no vertical mixing, and that concentration profiles develop for each constituent independently under the influence of the Earth gravity and thermal diffusion.

$$\frac{1}{n_i} \frac{dn_i}{dh} + \frac{1}{H_i} + \frac{1 + \alpha_i}{T} \frac{dT}{dh} = 0 \quad (7.1)$$

where

- i = 1, ... , 7 refers to N_2 , O_2 , Ar , O , He , H , and N ;
- h is the geodetic altitude, km;
- T is the local atmospheric temperature, K;
- n_i is the particle concentration (number density) of species i , $1/m^3$;
- H_i is the concentration scale height of species i , km;
- α_i is the thermal diffusion coefficient for species i ($\alpha_i = -0,4$ for H and He , and $0,0$ otherwise).

The altitude profile of the temperature $T(h)$, which is required in equation (7.1), can be well approximated by an exponential function which reaches an asymptotic limit T_∞ (exospheric temperature) at the thermopause.

$$T = T_\infty - (T_\infty - T_{120}) \exp[-s(h - h_{120})] \quad (7.2)$$

where

- $()_\infty$ are the conditions at the thermopause (start of the exosphere);
- $()_{120}$ are the conditions at geodetic altitude 120 km;
- s is the temperature gradient parameter, $1/km$.

Using expansions in the parameter c , equations (7.1) and (7.2) can be rewritten as explicit, analytical approximations of the altitude profiles in terms of the following expressions.

$$n_i = n_{i,120} \exp(-\sigma \gamma_i z) \left[\frac{(1 - c)}{(1 - c \exp(-\sigma z))} \right]^{1 + \alpha_i + \gamma_i} \quad (7.3)$$

$$T = T_\infty [1 - c \exp(-\sigma z)] \quad (7.4)$$

where

- z = $(h - h_{120})(R_E + h_{120}) / (R_E + h)$, geopotential altitude parameter, km;
- c = $1 - T_{120} / T$;
- T_∞ = $T_\infty(h, \phi, t_{ls}, t_{ut}, t_d, (F_{10,7})_{avg}, F_{10,7}, A_p)$;
- T_{120} = $T_{120}(h, \phi, t_{ls}, t_{ut}, t_d, (F_{10,7})_{avg}, F_{10,7}, A_p)$;
- $n_{i,120}$ = $n_{i,120}(h, \phi, t_{ls}, t_{ut}, t_d, (F_{10,7})_{avg}, F_{10,7}, A_p)$;
- σ = $s + (R_E + h_{120})^{-1}$, temperature gradient parameter, $1/km$;
- s = $s(h, \phi, t_{ls}, t_{ut}, t_d, (F_{10,7})_{avg}, F_{10,7}, A_p)$;
- γ_i = $1 / (H_i \sigma)$, dimensionless diffusion parameter;

H_i	$= RT/(M_i g)$, the concentration scale height of species i , m ;
M_i	$= 28, 32, 40, 16, 4, 1$, and 14 for N_2, O_2, Ar, O, He, H and N , molar masses, respectively, $kg/kmol$;
R_E	$= 6357$ km, normalizing Earth radius;
g	$= 9,806$ m/s^2 , reference gravity acceleration constant;
R	$= 8314$ $J\ kmol^{-1}K^{-1}$, the universal gas constant.

The air density is then determined from the mass-weighted, normalized concentrations, and the total pressure can be expressed as the sum of the partial pressures of the constituents.

$$\rho = \frac{1}{N_A} \sum_{i=1}^7 n_i M_i \quad (7.5)$$

$$p = \sum_{i=1}^7 p_i = kT \sum_{i=1}^7 n_i \quad (7.6)$$

where

ρ	is the total density, kg/m^3 ;
p	is the pressure, N/m^2 ;
k	$= 1,3807 \times 10^{-23}$ J/K , the Boltzmann constant;
N_A	$= \approx 6,022 \times 10^{23}$ mol^{-1} , Avogadro's number.

For aerodynamic calculations in a rarefied gas, in particular below altitudes of 200 km, the mean free path length, the speed of sound, and the dynamic viscosity are important. They can be approximated with good accuracy from

$$\frac{1}{L} = \sqrt{2} \pi d_{avg}^2 \frac{p}{kT} \quad (7.7)$$

$$a = \sqrt{\kappa \frac{p}{\rho}} \quad (7.8)$$

$$\mu = \frac{2}{3} L \rho a \sqrt{\frac{2}{\pi \kappa}} \quad (7.9)$$

where

L	is the mean free path of a molecule, m ;
μ	is the dynamic viscosity, $kg\ s^{-1}\ m^{-1}$;
a	is the speed of sound, m/s ;
κ	$= 1,44$, the ratio of specific heats (in an N_2 dominated environment);
d_{avg}	$= 3,62 \times 10^{-10}$ m , the mean collision diameter (for N_2).

All quantities on the right-hand sides of equations (7.3) and (7.4) are functions of the above listed seven atmospheric state parameters, with model coefficients which need to be fitted to measurement data. For the quality of a model it is essential that an adequate spatial and temporal distribution of measurement data is available in order to fit altitude profiles and their variation with daily, seasonal, and solar cycle periods. Due to sparse measurement data atmosphere models tend to be less reliable at altitudes below 150 km, above 700 km, and for extreme excursions of solar and geomagnetic activities.

According to equations (7.1) and (7.3), the changes of the number densities n_i with altitude are mainly driven by the hydrostatic equation which yields an exponential decrease. The logarithmic slope of this decrease, which is described by H_i^{-1} , becomes steeper with higher molar masses M_i and lower exospheric temperatures T_∞ (see Figure 8). The dominant constituents with increasing altitude are consequently N_2, O, He , and H , with varying altitude regions of dominance

according to activity levels (which mainly determine T_{∞}). Also the position of the diurnal density maximum is governed by the molar masses. Maxima occur near the sub-solar position with a time lag of 3,5 hrs for N_2 and O , and with a time lag of up to 12 hrs for the light weight species He and H . Due to the maximum EUV absorption by atomic oxygen, the diurnal density variation reaches its highest amplitudes of $\rho_{max}(h)/\rho_{min}(h) \approx 10$ near $h = 600$ km, where O is the dominant species. At these altitudes the density variation with solar activity also attains its maximum amplitude with changes by up to two orders of magnitude between extremes of the solar cycle (see Tables 13 to 15 and Figures 5 to 7, discussed later).

Table 13: MSISE-90 altitude profiles of temperature T , total density ρ , pressure p , mean molecular weight M and density scale height H for low activities

h (km)	T (K)	ρ (kg/m ³)	p (N/m ²)	M (kg/mol)	H (km)	n_{N_2} (/m ³)	n_O (/m ³)	n_{O_2} (/m ³)	n_{He} (/m ³)	n_{Ar} (/m ³)	n_H (/m ³)	n_N (/m ³)
0	300,2511	1,17E+00	1,01E+05	28,9502	11,4737	1,90E+25	-	5,09E+24	1,27E+20	2,27E+23	-	-
20	206,2085	9,48E-02	5,62E+03	28,9502	5,5843	1,54E+24	-	4,14E+23	1,03E+19	1,84E+22	-	-
40	257,6979	4,07E-03	3,01E+02	28,9502	7,2030	6,62E+22	-	1,78E+22	4,44E+17	7,91E+20	-	-
60	244,1212	3,31E-04	2,32E+01	28,9502	8,1940	5,38E+21	-	1,44E+21	3,61E+16	6,44E+19	-	-
80	203,1065	1,69E-05	9,81E-01	29,1353	6,1010	2,62E+20	3,93E+18	7,04E+19	7,21E+13	1,36E+19	1,27E+12	1,20E+16
100	168,7219	5,77E-07	2,89E-02	28,0036	5,0095	1,00E+19	6,58E+17	1,64E+18	4,92E+13	1,18E+17	1,25E+12	2,57E+15
120	356,8669	1,70E-08	1,92E-03	26,3948	7,9781	2,92E+17	6,34E+16	3,22E+16	2,11E+13	1,05E+15	7,23E+11	3,02E+14
140	545,8594	2,96E-09	5,37E-04	25,0665	15,2801	4,79E+16	1,88E+16	4,33E+15	1,34E+13	9,48E+13	5,33E+11	9,88E+13
160	630,0652	9,65E-10	2,13E-04	23,7884	20,2988	1,44E+16	8,89E+15	1,12E+15	1,06E+13	1,80E+13	4,71E+11	5,03E+13
180	667,8662	3,90E-10	9,62E-05	22,5037	23,7416	5,19E+15	4,85E+15	3,52E+14	8,91E+12	4,32E+12	4,39E+11	2,94E+13
200	684,9187	1,75E-10	4,70E-05	21,2516	26,3234	2,02E+15	2,80E+15	1,20E+14	7,70E+12	1,14E+12	4,19E+11	1,81E+13
220	692,6487	8,47E-11	2,43E-05	20,0935	28,6112	8,17E+14	1,66E+15	4,28E+13	6,73E+12	3,13E+11	4,03E+11	1,15E+13
240	696,1697	4,31E-11	1,31E-05	19,0789	30,7226	3,36E+14	9,97E+14	1,55E+13	5,91E+12	8,82E+10	3,89E+11	7,33E+12
260	697,7811	2,30E-11	7,31E-06	18,2300	32,6731	1,40E+14	6,03E+14	5,70E+12	5,21E+12	2,52E+10	3,77E+11	4,72E+12
280	698,5220	1,27E-11	4,20E-06	17,5402	34,6129	5,87E+13	3,67E+14	2,11E+12	4,60E+12	7,29E+09	3,65E+11	3,06E+12
300	698,8644	7,22E-12	2,47E-06	16,9830	36,3499	2,48E+13	2,24E+14	7,88E+11	4,07E+12	2,13E+09	3,54E+11	1,99E+12
320	699,0233	4,21E-12	1,48E-06	16,5214	37,6859	1,05E+13	1,37E+14	2,96E+11	3,60E+12	6,26E+08	3,43E+11	1,29E+12
340	699,0973	2,50E-12	9,01E-07	16,1147	39,0274	4,49E+12	8,44E+13	1,12E+11	3,19E+12	1,85E+08	3,33E+11	8,45E+11
360	699,1320	1,51E-12	5,57E-07	15,7219	40,0512	1,92E+12	5,20E+13	4,25E+10	2,82E+12	5,53E+07	3,23E+11	5,53E+11
380	699,1483	9,20E-13	3,50E-07	15,3028	40,9778	8,30E+11	3,22E+13	1,63E+10	2,50E+12	1,66E+07	3,13E+11	3,63E+11
400	699,1561	5,68E-13	2,23E-07	14,8185	41,9519	3,60E+11	2,00E+13	6,25E+09	2,22E+12	5,04E+06	3,04E+11	2,39E+11
420	699,1597	3,54E-13	1,45E-07	14,2332	42,8975	1,57E+11	1,24E+13	2,42E+09	1,97E+12	1,54E+06	2,95E+11	1,58E+11
440	699,1615	2,23E-13	9,61E-08	13,5181	43,8193	6,86E+10	7,74E+12	9,40E+08	1,75E+12	4,72E+05	2,87E+11	1,04E+11
460	699,1623	1,42E-13	6,54E-08	12,6581	45,1370	3,02E+10	4,84E+12	3,68E+08	1,56E+12	1,46E+05	2,78E+11	6,92E+10
480	699,1627	9,20E-14	4,59E-08	11,6594	46,6954	1,33E+10	3,04E+12	1,45E+08	1,39E+12	4,55E+04	2,70E+11	4,60E+10
500	699,1629	6,03E-14	3,32E-08	10,5547	48,3084	5,92E+09	1,91E+12	5,72E+07	1,24E+12	1,43E+04	2,63E+11	3,07E+10

* Concentrations of n_O , n_H , and n_N are computed for $h \geq 80$ km

Table 13: MSISE-90 altitude profiles of temperature T , total density ρ , pressure p , mean molecular weight M and density scale height H for low activities (*continued*)

h (km)	T (K)	ρ (kg/m ³)	p (N/m ²)	M (kg/mol)	H (km)	n_{N_2} (/m ³)	n_O (/m ³)	n_{O_2} (/m ³)	n_{He} (/m ³)	n_{Ar} (/m ³)	n_H (/m ³)	n_N (/m ³)
520	699,1630	4,03E-14	2,49E-08	9,4006	50,8992	2,64E+09	1,20E+12	2,27E+07	1,10E+12	4,50E+03	2,55E+11	2,05E+10
540	699,1630	2,75E-14	1,94E-08	8,2657	53,8186	1,18E+09	7,61E+11	9,09E+06	9,82E+11	1,43E+03	2,48E+11	1,37E+10
560	699,1631	1,93E-14	1,55E-08	7,2141	58,2364	5,33E+08	4,83E+11	3,65E+06	8,76E+11	4,58E+02	2,41E+11	9,21E+09
580	699,1631	1,39E-14	1,28E-08	6,2904	63,5906	2,41E+08	3,07E+11	1,48E+06	7,82E+11	1,48E+02	2,34E+11	6,19E+09
600	699,1631	1,03E-14	1,09E-08	5,5149	71,0934	1,10E+08	1,95E+11	5,99E+05	6,99E+11	4,78E+01	2,28E+11	4,18E+09
620	699,1631	7,90E-15	9,40E-09	4,8864	79,7750	5,01E+07	1,25E+11	2,45E+05	6,25E+11	1,56E+01	2,22E+11	2,82E+09
640	699,1631	6,24E-15	8,27E-09	4,3891	90,0817	2,30E+07	8,00E+10	1,00E+05	5,59E+11	5,12E+00	2,15E+11	1,91E+09
660	699,1631	5,06E-15	7,36E-09	4,0012	102,0265	1,06E+07	5,14E+10	4,14E+04	5,00E+11	1,69E+00	2,10E+11	1,30E+09
680	699,1631	4,21E-15	6,62E-09	3,6999	115,2614	4,89E+06	3,31E+10	1,72E+04	4,48E+11	5,63E-01	2,04E+11	8,82E+08
700	699,1631	3,58E-15	6,00E-09	3,4648	129,9408	2,27E+06	2,13E+10	7,15E+03	4,02E+11	1,89E-01	1,98E+11	6,01E+08
720	699,1631	3,09E-15	5,48E-09	3,2789	142,8583	1,06E+06	1,38E+10	2,99E+03	3,60E+11	6,35E-02	1,93E+11	4,11E+08
740	699,1631	2,70E-15	5,02E-09	3,1289	156,2294	4,98E+05	8,96E+09	1,26E+03	3,23E+11	2,15E-02	1,88E+11	2,81E+08
760	699,1631	2,39E-15	4,63E-09	3,0049	168,9813	2,34E+05	5,82E+09	5,32E+02	2,90E+11	7,33E-03	1,83E+11	1,93E+08
780	699,1631	2,13E-15	4,28E-09	2,8996	181,3580	1,11E+05	3,80E+09	2,26E+02	2,61E+11	2,52E-03	1,78E+11	1,33E+08
800	699,1631	1,91E-15	3,96E-09	2,8075	188,1991	5,26E+04	2,48E+09	9,65E+01	2,35E+11	8,68E-04	1,73E+11	9,15E+07
820	699,1631	1,73E-15	3,68E-09	2,7249	199,7376	2,51E+04	1,62E+09	4,14E+01	2,11E+11	3,01E-04	1,69E+11	6,32E+07
840	699,1631	1,56E-15	3,43E-09	2,6492	208,2405	1,20E+04	1,07E+09	1,78E+01	1,90E+11	1,05E-04	1,65E+11	4,37E+07
860	699,1631	1,42E-15	3,21E-09	2,5784	212,0086	5,77E+03	7,02E+08	7,72E+00	1,71E+11	3,69E-05	1,60E+11	3,03E+07
880	699,1631	1,30E-15	3,00E-09	2,5113	221,2246	2,79E+03	4,63E+08	3,36E+00	1,54E+11	1,31E-05	1,56E+11	2,11E+07
900	699,1631	1,18E-15	2,81E-09	2,4470	223,6053	1,35E+03	3,06E+08	1,47E+00	1,39E+11	4,64E-06	1,52E+11	1,47E+07

* Concentrations of n_O , n_H , and n_N are computed for $h \geq 80$ km

Table 14: MSISE-90 altitude profiles of temperature T , total density ρ , pressure p , mean molecular weight M and density scale height H for mean activities

h (km)	T (K)	ρ (kg/m ³)	p (N/m ²)	M (kg/mol)	H (km)	n_{N_2} (/m ³)	n_O (/m ³)	n_{O_2} (/m ³)	n_{He} (/m ³)	n_{Ar} (/m ³)	n_H (/m ³)	n_N (/m ³)
0	300,2511	1,17E+00	1,01E+05	28,9502	11,4721	1,90E+25	-	5,09E+24	1,27E+20	2,27E+23	-	-
20	206,2085	9,49E-02	5,62E+03	28,9502	5,5842	1,54E+24	-	4,14E+23	1,04E+19	1,85E+22	-	-
40	257,6979	4,07E-03	3,02E+02	28,9502	7,2029	6,62E+22	-	1,78E+22	4,44E+17	7,92E+20	-	-
60	244,1212	3,31E-04	2,32E+01	28,9502	8,1933	5,38E+21	-	1,44E+21	3,61E+16	6,44E+19	-	-
80	196,3636	1,68E-05	9,45E-01	29,0175	6,1281	2,66E+20	5,36E+18	6,30E+19	9,51E+13	1,40E+19	4,65E+11	2,81E+16
100	184,0160	5,08E-07	2,81E-02	27,7137	5,3926	8,87E+18	7,88E+17	1,28E+18	6,02E+13	1,05E+17	4,27E+11	5,30E+15
120	374,9715	1,80E-08	2,17E-03	25,8745	7,7281	3,02E+17	8,43E+16	2,98E+16	2,69E+13	1,14E+15	2,53E+11	6,86E+14
140	635,5703	3,26E-09	7,03E-04	24,5349	16,3411	5,12E+16	2,44E+16	4,22E+15	1,64E+13	1,13E+14	1,76E+11	2,17E+14
160	787,5532	1,18E-09	3,31E-04	23,4225	23,3363	1,72E+16	1,19E+16	1,25E+15	1,27E+13	2,61E+13	1,50E+11	1,13E+14
180	877,6729	5,51E-10	1,80E-04	22,4106	29,0312	7,29E+15	6,97E+15	4,76E+14	1,07E+13	8,04E+12	1,37E+11	6,96E+13
200	931,2806	2,91E-10	1,05E-04	21,4734	33,5804	3,46E+15	4,44E+15	2,05E+14	9,36E+12	2,85E+12	1,29E+11	4,66E+13
220	963,2701	1,66E-10	6,44E-05	20,6108	37,3389	1,75E+15	2,96E+15	9,42E+13	8,35E+12	1,09E+12	1,24E+11	3,25E+13
240	982,4191	9,91E-11	4,09E-05	19,8292	40,5638	9,12E+14	2,02E+15	4,50E+13	7,55E+12	4,33E+11	1,20E+11	2,33E+13
260	993,9173	6,16E-11	2,66E-05	19,1337	43,3273	4,87E+14	1,41E+15	2,20E+13	6,86E+12	1,78E+11	1,16E+11	1,69E+13
280	1000,8427	3,94E-11	1,77E-05	18,5256	45,9808	2,63E+14	9,87E+14	1,09E+13	6,26E+12	7,40E+10	1,13E+11	1,24E+13
300	1005,0267	2,58E-11	1,20E-05	18,0015	48,3416	1,44E+14	6,97E+14	5,46E+12	5,74E+12	3,13E+10	1,10E+11	9,14E+12
320	1007,5620	1,72E-11	8,20E-06	17,5537	50,2822	7,91E+13	4,95E+14	2,76E+12	5,26E+12	1,33E+10	1,08E+11	6,77E+12
340	1009,1030	1,16E-11	5,69E-06	17,1721	52,2731	4,38E+13	3,53E+14	1,40E+12	4,83E+12	5,73E+09	1,06E+11	5,03E+12
360	1010,0423	7,99E-12	3,98E-06	16,8449	53,9613	2,43E+13	2,52E+14	7,18E+11	4,44E+12	2,48E+09	1,03E+11	3,75E+12
380	1010,6166	5,55E-12	2,81E-06	16,5597	55,6560	1,36E+13	1,81E+14	3,69E+11	4,08E+12	1,08E+09	1,01E+11	2,80E+12
400	1010,9688	3,89E-12	2,01E-06	16,3044	57,1177	7,62E+12	1,30E+14	1,90E+11	3,76E+12	4,72E+08	9,91E+10	2,10E+12
420	1011,1853	2,75E-12	1,44E-06	16,0669	58,4012	4,29E+12	9,35E+13	9,87E+10	3,46E+12	2,08E+08	9,71E+10	1,57E+12
440	1011,3188	1,96E-12	1,04E-06	15,8360	59,4317	2,42E+12	6,74E+13	5,14E+10	3,19E+12	9,18E+07	9,51E+10	1,18E+12
460	1011,4014	1,40E-12	7,55E-07	15,6008	60,4864	1,37E+12	4,87E+13	2,69E+10	2,94E+12	4,08E+07	9,32E+10	8,90E+11
480	1011,4526	1,01E-12	5,53E-07	15,3508	61,5528	7,80E+11	3,53E+13	1,41E+10	2,71E+12	1,82E+07	9,13E+10	6,71E+11

* Concentrations of n_O , n_H , and n_N are computed for $h \geq 80$ km

Table 14: MSISE-90 altitude profiles of temperature T , total density ρ , pressure p , mean molecular weight M and density scale height H for mean activities (*continued*)

h (km)	T (K)	ρ (kg/m ³)	p (N/m ²)	M (kg/mol)	H (km)	n_{N_2} (/m ³)	n_O (/m ³)	n_{O_2} (/m ³)	n_{He} (/m ³)	n_{Ar} (/m ³)	n_H (/m ³)	n_N (/m ³)
500	1011,4845	7,30E-13	4,07E-07	15,0760	62,4024	4,45E+11	2,56E+13	7,42E+09	2,51E+12	8,16E+06	8,95E+10	5,07E+11
520	1011,5043	5,31E-13	3,03E-07	14,7669	63,4137	2,55E+11	1,86E+13	3,92E+09	2,31E+12	3,68E+06	8,77E+10	3,83E+11
540	1011,5168	3,88E-13	2,27E-07	14,4148	63,9820	1,46E+11	1,36E+13	2,08E+09	2,14E+12	1,67E+06	8,60E+10	2,91E+11
560	1011,5245	2,85E-13	1,71E-07	14,0125	65,3319	8,43E+10	9,90E+12	1,11E+09	1,98E+12	7,58E+05	8,43E+10	2,21E+11
580	1011,5294	2,11E-13	1,31E-07	13,5547	66,4024	4,88E+10	7,24E+12	5,92E+08	1,83E+12	3,46E+05	8,27E+10	1,68E+11
600	1011,5325	1,56E-13	1,01E-07	13,0389	68,1361	2,83E+10	5,30E+12	3,18E+08	1,69E+12	1,59E+05	8,11E+10	1,28E+11
620	1011,5345	1,17E-13	7,89E-08	12,4665	69,7510	1,64E+10	3,89E+12	1,71E+08	1,56E+12	7,33E+04	7,96E+10	9,74E+10
640	1011,5357	8,79E-14	6,24E-08	11,8428	70,9524	9,59E+09	2,86E+12	9,24E+07	1,45E+12	3,40E+04	7,80E+10	7,44E+10
660	1011,5365	6,65E-14	5,01E-08	11,1779	72,9834	5,61E+09	2,11E+12	5,01E+07	1,34E+12	1,58E+04	7,66E+10	5,69E+10
680	1011,5370	5,08E-14	4,07E-08	10,4854	74,8578	3,30E+09	1,55E+12	2,72E+07	1,24E+12	7,38E+03	7,51E+10	4,36E+10
700	1011,5374	3,91E-14	3,36E-08	9,7818	78,5188	1,94E+09	1,15E+12	1,49E+07	1,15E+12	3,46E+03	7,37E+10	3,35E+10
720	1011,5375	3,04E-14	2,82E-08	9,0847	81,5376	1,15E+09	8,49E+11	8,15E+06	1,07E+12	1,63E+03	7,23E+10	2,57E+10
740	1011,5377	2,39E-14	2,39E-08	8,4111	84,7760	6,79E+08	6,30E+11	4,48E+06	9,92E+11	7,73E+02	7,10E+10	1,98E+10
760	1011,5377	1,90E-14	2,06E-08	7,7753	89,4495	4,03E+08	4,68E+11	2,47E+06	9,21E+11	3,67E+02	6,97E+10	1,53E+10
780	1011,5378	1,53E-14	1,79E-08	7,1884	95,5420	2,40E+08	3,48E+11	1,37E+06	8,55E+11	1,75E+02	6,84E+10	1,18E+10
800	1011,5378	1,25E-14	1,58E-08	6,6572	101,1751	1,44E+08	2,59E+11	7,59E+05	7,94E+11	8,40E+01	6,72E+10	9,10E+09
820	1011,5378	1,03E-14	1,40E-08	6,1849	108,3571	8,61E+07	1,93E+11	4,23E+05	7,38E+11	4,04E+01	6,59E+10	7,05E+09
840	1011,5379	8,64E-15	1,26E-08	5,7711	117,4539	5,17E+07	1,45E+11	2,36E+05	6,87E+11	1,95E+01	6,48E+10	5,46E+09
860	1011,5379	7,32E-15	1,14E-08	5,4132	126,1862	3,12E+07	1,08E+11	1,32E+05	6,39E+11	9,48E+00	6,36E+10	4,24E+09
880	1011,5379	6,28E-15	1,04E-08	5,1066	135,5045	1,89E+07	8,12E+10	7,45E+04	5,94E+11	4,62E+00	6,25E+10	3,30E+09
900	1011,5379	5,46E-15	9,47E-09	4,8460	146,5578	1,14E+07	6,10E+10	4,20E+04	5,53E+11	2,26E+00	6,14E+10	2,57E+09

* Concentrations of n_O , n_H , and n_N are computed for $h \geq 80$ km

Table 15: MSISE-90 altitude profiles of temperature T , total density ρ , pressure p , mean molecular weight M and density scale height H for extremely high activities

h (km)	T (K)	ρ (kg/m ³)	p (N/m ²)	M (kg/mol)	H (km)	n_{N_2} (/m ³)	n_O (/m ³)	n_{O_2} (/m ³)	n_{He} (/m ³)	n_{Ar} (/m ³)	n_H (/m ³)	n_N (/m ³)
0	300,2511	1,16E+00	9,98E+04	28,9502	11,4728	1,88E+25	-	5,05E+24	1,26E+20	2,25E+23	-	-
20	206,2085	9,41E-02	5,57E+03	28,9502	5,5843	1,53E+24	-	4,10E+23	1,03E+19	1,83E+22	-	-
40	257,6979	4,04E-03	2,99E+02	28,9502	7,2035	6,56E+22	-	1,76E+22	4,40E+17	7,85E+20	-	-
60	244,1212	3,28E-04	2,30E+01	28,9502	8,1920	5,34E+21	-	1,43E+21	3,58E+16	6,38E+19	-	-
80	172,2146	1,68E-05	8,42E-01	28,5290	6,1265	2,80E+20	1,43E+19	4,32E+19	2,20E+14	1,62E+19	1,38E+10	5,75E+17
100	297,3338	2,78E-07	2,63E-02	26,1997	7,3856	4,74E+18	1,10E+18	4,42E+17	9,58E+13	6,03E+16	8,77E+09	5,69E+16
120	430,8385	2,34E-08	3,55E-03	23,6456	6,5809	3,48E+17	2,11E+17	2,35E+16	5,57E+13	1,69E+15	6,48E+09	1,28E+16
140	875,9174	4,93E-09	1,61E-03	22,3209	20,0481	6,52E+16	5,98E+16	3,84E+15	3,17E+13	2,10E+14	4,09E+09	3,89E+15
160	1143,5426	2,23E-09	9,90E-04	21,4577	31,2463	2,69E+16	3,22E+16	1,45E+15	2,47E+13	6,63E+13	3,41E+09	2,19E+15
180	1314,3427	1,28E-09	6,76E-04	20,7706	41,2666	1,41E+16	2,09E+16	7,07E+14	2,12E+13	2,80E+13	3,08E+09	1,48E+15
200	1423,6469	8,28E-10	4,86E-04	20,1836	49,7766	8,27E+15	1,49E+16	3,89E+14	1,89E+13	1,35E+13	2,89E+09	1,09E+15
220	1493,7864	5,69E-10	3,60E-04	19,6664	56,8205	5,16E+15	1,12E+16	2,29E+14	1,73E+13	7,05E+12	2,76E+09	8,38E+14
240	1538,9154	4,08E-10	2,72E-04	19,2046	62,8153	3,35E+15	8,61E+15	1,40E+14	1,60E+13	3,84E+12	2,68E+09	6,65E+14
260	1568,0294	3,00E-10	2,08E-04	18,7901	67,5214	2,22E+15	6,75E+15	8,77E+13	1,50E+13	2,15E+12	2,61E+09	5,36E+14
280	1586,8613	2,25E-10	1,61E-04	18,4178	71,6228	1,49E+15	5,36E+15	5,59E+13	1,41E+13	1,23E+12	2,56E+09	4,37E+14
300	1599,0743	1,71E-10	1,26E-04	18,0839	75,3036	1,02E+15	4,29E+15	3,60E+13	1,33E+13	7,11E+11	2,51E+09	3,59E+14
320	1607,0154	1,32E-10	9,93E-05	17,7852	78,1849	6,95E+14	3,45E+15	2,34E+13	1,26E+13	4,15E+11	2,47E+09	2,97E+14
340	1612,1920	1,03E-10	7,86E-05	17,5186	80,8340	4,79E+14	2,78E+15	1,53E+13	1,19E+13	2,44E+11	2,43E+09	2,46E+14
360	1615,5751	8,05E-11	6,26E-05	17,2812	83,4085	3,31E+14	2,25E+15	1,00E+13	1,13E+13	1,44E+11	2,40E+09	2,04E+14
380	1617,7916	6,35E-11	5,01E-05	17,0699	85,6516	2,30E+14	1,83E+15	6,61E+12	1,07E+13	8,56E+10	2,36E+09	1,70E+14
400	1619,2476	5,04E-11	4,02E-05	16,8818	87,5157	1,60E+14	1,48E+15	4,37E+12	1,01E+13	5,11E+10	2,33E+09	1,42E+14
420	1620,2062	4,02E-11	3,25E-05	16,7142	89,5633	1,12E+14	1,21E+15	2,90E+12	9,63E+12	3,06E+10	2,30E+09	1,18E+14
440	1620,8390	3,23E-11	2,63E-05	16,5643	90,8765	7,82E+13	9,85E+14	1,93E+12	9,15E+12	1,84E+10	2,27E+09	9,91E+13
460	1621,2577	2,60E-11	2,13E-05	16,4297	92,6589	5,49E+13	8,04E+14	1,29E+12	8,70E+12	1,11E+10	2,24E+09	8,30E+13
480	1621,5354	2,10E-11	1,73E-05	16,3079	94,5872	3,86E+13	6,57E+14	8,59E+11	8,27E+12	6,69E+09	2,22E+09	6,96E+13
500	1621,7200	1,70E-11	1,42E-05	16,1967	96,3381	2,72E+13	5,38E+14	5,76E+11	7,87E+12	4,06E+09	2,19E+09	5,84E+13

* Concentrations of n_O , n_H , and n_N are computed for $h \geq 80$ km

Table 15: MSISE-90 altitude profiles of temperature T , total density ρ , pressure p , mean molecular weight M and density scale height H for extremely high activities (*continued*)

h (km)	T (K)	ρ (kg/m ³)	p (N/m ²)	M (kg/mol)	H (km)	n_{N_2} (/m ³)	n_O (/m ³)	n_{O_2} (/m ³)	n_{He} (/m ³)	n_{Ar} (/m ³)	n_H (/m ³)	n_N (/m ³)
520	1621,8430	1,38E-11	1,16E-05	16,0940	97,6136	1,92E+13	4,41E+14	3,87E+11	7,49E+12	2,47E+09	2,16E+09	4,91E+13
540	1621,9253	1,13E-11	9,50E-06	15,9980	98,0937	1,36E+13	3,62E+14	2,61E+11	7,13E+12	1,51E+09	2,13E+09	4,13E+13
560	1621,9803	9,21E-12	7,81E-06	15,9067	99,3060	9,63E+12	2,97E+14	1,76E+11	6,78E+12	9,22E+08	2,11E+09	3,47E+13
580	1622,0172	7,55E-12	6,44E-06	15,8187	100,6720	6,84E+12	2,45E+14	1,19E+11	6,46E+12	5,66E+08	2,08E+09	2,93E+13
600	1622,0421	6,20E-12	5,31E-06	15,7321	102,6271	4,87E+12	2,01E+14	8,07E+10	6,15E+12	3,48E+08	2,06E+09	2,47E+13
620	1622,0588	5,10E-12	4,40E-06	15,6457	103,0355	3,47E+12	1,66E+14	5,49E+10	5,86E+12	2,15E+08	2,03E+09	2,09E+13
640	1622,0702	4,20E-12	3,65E-06	15,5578	104,1285	2,48E+12	1,37E+14	3,74E+10	5,59E+12	1,33E+08	2,01E+09	1,76E+13
660	1622,0778	3,47E-12	3,03E-06	15,4672	104,9730	1,78E+12	1,13E+14	2,55E+10	5,33E+12	8,24E+07	1,99E+09	1,49E+13
680	1622,0830	2,88E-12	2,52E-06	15,3725	106,0742	1,28E+12	9,37E+13	1,75E+10	5,08E+12	5,13E+07	1,96E+09	1,26E+13
700	1622,0865	2,38E-12	2,11E-06	15,2723	108,0038	9,16E+11	7,76E+13	1,20E+10	4,85E+12	3,20E+07	1,94E+09	1,07E+13
720	1622,0890	1,98E-12	1,76E-06	15,1653	108,4682	6,60E+11	6,43E+13	8,22E+09	4,63E+12	2,00E+07	1,92E+09	9,09E+12
740	1622,0906	1,65E-12	1,48E-06	15,0503	108,7983	4,76E+11	5,33E+13	5,66E+09	4,41E+12	1,26E+07	1,89E+09	7,72E+12
760	1622,0918	1,37E-12	1,24E-06	14,9260	110,3542	3,44E+11	4,43E+13	3,91E+09	4,21E+12	7,90E+06	1,87E+09	6,57E+12
780	1622,0925	1,15E-12	1,05E-06	14,7912	112,2861	2,49E+11	3,68E+13	2,70E+09	4,02E+12	4,98E+06	1,85E+09	5,59E+12
800	1622,0930	9,59E-13	8,84E-07	14,6447	111,8358	1,81E+11	3,07E+13	1,87E+09	3,84E+12	3,15E+06	1,83E+09	4,76E+12
820	1622,0934	8,04E-13	7,48E-07	14,4854	113,5786	1,31E+11	2,56E+13	1,30E+09	3,67E+12	1,99E+06	1,81E+09	4,06E+12
840	1622,0936	6,74E-13	6,36E-07	14,3123	115,0666	9,56E+10	2,13E+13	9,04E+08	3,51E+12	1,27E+06	1,79E+09	3,46E+12
860	1622,0939	5,67E-13	5,42E-07	14,1244	115,8021	6,97E+10	1,78E+13	6,30E+08	3,36E+12	8,07E+05	1,77E+09	2,96E+12
880	1622,0940	4,77E-13	4,63E-07	13,9210	117,5788	5,09E+10	1,49E+13	4,40E+08	3,21E+12	5,16E+05	1,75E+09	2,53E+12
900	1622,0940	4,03E-13	3,97E-07	13,7015	118,1314	3,73E+10	1,24E+13	3,08E+08	3,07E+12	3,30E+05	1,73E+09	2,16E+12

* Concentrations of n_O , n_H , and n_N are computed for $h \geq 80$ km

7.6 Temperature, composition, and density model of the Earth homosphere

At altitudes below about 85 km the Earth atmosphere can be assumed of uniform composition (78,1 % N₂, 20,9 % O₂, 0,9 % Ar, and 0,1 % CO₂ and trace constituents), at equilibrium conditions, with properties of a perfect gas. For each constituent i altitude profiles of partial pressures p_i evolve according to the law of hydrostatic equilibrium.

$$\frac{dp_i}{p_i} = -\frac{gM_i}{RT}dh \quad (7.10)$$

p_i can be integrated from equation (7.10) for piecewise linear temperature profile segments.

The US Standard Atmosphere 1976 (USSA-76 [RD7.4]) defines the homospheric temperature as a function of altitude:

starting from $T_0 = T(h=0) = 288,15$ K,
with $dT/dh =$
 $-6,5$ °/km for $h \in [0 \text{ km}, 11 \text{ km}]$,
 $0,0$ °/km for $h \in [11 \text{ km}, 20 \text{ km}]$,
 $+1,0$ °/km for $h \in [20 \text{ km}, 32 \text{ km}]$,
 $+2,8$ °/km for $h \in [32 \text{ km}, 47 \text{ km}]$,
 $0,0$ °/km for $h \in [47 \text{ km}, 51 \text{ km}]$,
 $-2,8$ °/km for $h \in [51 \text{ km}, 71 \text{ km}]$, and
 $-2,0$ °/km for $h \in [71 \text{ km}, 85 \text{ km}]$.

For a given temperature $T(h)$ the partial pressures p_i translate into number densities according to

$$n_i = \frac{p_i}{kT} \quad (7.11)$$

Based on the known quantities p_i , n_i , and T , the total density ρ , total pressure p , mean free path length L , and speed of sound a can be computed as outlined in equations (7.5) to (7.9).

At altitudes below about 85 km, for objects of diameters larger than or similar to the mean free path length ($d > L$) the dynamic viscosity and kinematic viscosity of the ambient gas is given by the following semi-empirical relations:

$$\mu = \beta \frac{T^{3/2}}{T + S} \quad (7.12)$$

$$\eta = \frac{\mu}{\rho} \quad (7.13)$$

where

μ is the dynamic viscosity, $\text{kg s}^{-1} \text{m}^{-1}$;
 η is the kinematic viscosity, $\text{s}^{-1} \text{m}^2$;
 $\beta = 1,458 \times 10^{-6} \text{ kg s}^{-1} \text{m}^{-1} \text{K}^{-1/2}$;
 $S = 110,4 \text{ K}$, Sutherland constant.

Non-static homosphere models, such as MSISE-90, allow for variations of temperature profiles and resulting densities with diurnal, longitudinal-latitudinal, seasonal-latitudinal, and solar/geomagnetic activity effects. The activity influence, however, diminishes with decreasing altitude below the turbopause. MSISE-90 and the underlying MAP 16 model [RD7.5] consider activity related effects only down to 90 km and diurnal effects only down to 72 km altitude.

Variations in total density according to MSISE-90 can have amplitudes of ± 40 % due to seasonal-latitudinal effects (with maxima at 50 km and 110 km in June and December).

7.7 Reference model output

MSISE-90 altitude profiles of temperature, number densities (concentrations), pressure, total density, mean molecular weight, and density scale height are listed in Tables 13, 14, and 15 for low activity levels ($F_{10,7} = (F_{10,7})_{avg} = 70, A_p = 0$), mean activities ($F_{10,7} = (F_{10,7})_{avg} = 140, A_p = 15$), and extremely high activity levels ($F_{10,7} = (F_{10,7})_{avg} = 380, A_p = 300$), respectively. The tables cover both homospheric and heterospheric altitudes from ground level up to 900 km, averaged over diurnal and seasonal latitudinal variations. Figures 5 through 7 illustrate the corresponding altitude profiles of temperature, total density, and atomic oxygen number density at minimum, maximum, and mean activity conditions. For mean activity levels Figure 8 shows the logarithmic number concentration profiles of the main atmospheric constituents. Figures 9 through 11 display diurnal and seasonal latitudinal variations of temperature, total density, and atomic oxygen concentrations at 400 km altitude. Local minima/maxima can be lower/higher than indicated here.

MSISE-90, the recommended ECSS standard atmosphere model, determines total densities at thermospheric altitudes with an r.m.s. accuracy of $\pm 10\%$ to $\pm 15\%$ at mean activity conditions. Especially for very high solar or geomagnetic activities these uncertainties can considerably increase due to the lack of corresponding measurement data.

For its homosphere part (below 90 km) MSISE-90 determines densities with an rms error well below 5%. Standard deviations in temperature and pressure are on the order of 3 K and 2%, respectively. The MSISE-90 homosphere temperature and concentration profiles are merged with those of the lower thermosphere to obtain smooth transitions in the vicinity of the turbopause (between 85 km and 120 km).

7.8 Wind model of the Earth homosphere and heterosphere

The knowledge of wind patterns in the Earth atmosphere is largely based on satellite data (mainly AE-E and DE-2), providing wind and temperature spectroscopy (WATS), and Fabry-Perot interferometry (FPI). At lower altitudes ground-based incoherent scatter radar, FPI data, and meteor observations prevail in the data set.

Existing wind models, including the recommended standard HWM-93 (Horizontal Wind Model 1993, based on RD7.3) as well as GRAM-88 (Global Reference Atmosphere Model 1988 [RD7.6]) and MAH-96 (High Atmosphere Model 1996 [RD7.7]), mainly restrict themselves to a prediction of the meridional component V_x (positive towards north) and zonal component V_y (positive towards East) of the horizontal motion. The mean wind velocity in the vertical direction V_z is generally less than 1 cm/s, and can be neglected for most applications.

Much of the horizontal wind can be attributed to the flow due to the local pressure gradient, under the influence of the Coriolis acceleration. These geostrophic winds can be determined from

$$V_x = \frac{1}{2\rho\omega_e \sin \phi} \frac{\partial p}{\partial x} \quad (7.14)$$

$$V_y = \frac{1}{2\rho\omega_e \sin \phi} \frac{\partial p}{\partial y} \quad (7.15)$$

where

- p is the local pressure, N/m²;
- V_x is the northward meridional wind component, m/s;
- V_y is the eastward zonal wind component, m/s;
- ρ is the local air density, kg/m³;

ω_e = $7,292 \times 10^{-5}$ rad/s, Earth rotation rate;
 ϕ is the geodetic latitude, ° (degrees).

In equatorial regions (i.e. for $\phi \in [-15^\circ, +15^\circ]$) these assumptions are not valid, and results for such latitudes should be determined from linear interpolation between $\phi = \pm 15^\circ$. The concept of geostrophic winds is applied by GRAM-88 in the altitude range 0 km to 20 km and above 90 km. MAH-96 uses geostrophic winds from underlying MSISE-90 pressure gradients over its entire altitude range from 0 km to 120 km.

Considering its close relationship with the MSISE-90 atmosphere model and its compatibility with the stochastic MAH-96 wind model, HWM-93 is adopted as deterministic horizontal wind model for homospheric and heterospheric altitudes. Below 120 km, for the analysis of small scale perturbation spectra, the MSISE-90 based MAH-96 model [RD7.7] is recommended.

An empirical horizontal wind model in terms of vector spherical harmonic expansions is used by HWM-93 for altitudes from 0 km to 2000 km. The HWM 93 model has a similar structure and the same parameters as the atmosphere model MSISE-90, with equally unconstrained applicability from ground level to exospheric altitudes. Geostrophic wind contributions are embedded in the harmonic expansions of HWM-93. The horizontal wind directions and magnitudes are found to change with a diurnal period at thermospheric altitudes and with a semi-diurnal period in the homosphere. The effect of solar activity indices (though included in the model) is small. Apart from (semi-)diurnal variations, mainly seasonal-latitudinal effects dominate, with amplitudes which are largely driven by geomagnetic activity. Since A_p effects focus on the vicinity of the magnetic poles, and since the related dynamics is not totally predictable, wind models tend to be most reliable at moderate and low latitudes. The wind directions and velocities provided by HWM-93 closely correlate with pressure distributions according to MSISE-90. Hence, highest velocities are noted along the dawn-dusk region, especially towards the night hemisphere across the poles. Here, wind speeds of up to 1 km/s can be reached at moderate thermospheric altitudes (e.g. around 300 km). Diurnal and seasonal-latitudinal variation patterns of HWM-93 winds in 400 km altitude at mean activity conditions are shown in Figures 12(a) and 12(b).

7.9 Simple density models of planetary atmospheres

For the major planets and for the Saturn moon Titan (the largest moon in the solar system) simple atmosphere models are available, which mostly restrict themselves to uniform, mean density profiles based on the hydrostatic equilibrium of an isothermal atmosphere.

The planetary atmosphere densities as a function of altitude can be approximated as:

$$\rho(h) = \rho_0 \exp\left[\frac{-(h - h_0)}{H_0}\right] \quad (7.16)$$

with model parameters selected according to the following list:

Venus (C. Sagan et al., 1971, [RD7.8])

h_0 = 285 km, reference altitude
 ρ_0 = $7,1 \times 10^{-9}$ kg/m³, reference density
 H_0 = 44,8 km, reference density scale height

Mars (A. Seiff and D.B. Kirk, 1977, [RD7.9])

h_0 = 140,0 km, reference altitude
 ρ_0 = $7,25 \times 10^{-10}$ kg/m³, reference density
 H_0 = 11,127 km, reference density scale height

Jupiter (R.J. Newburn and S. Gulkis, 1973, [RD7.10])	
h_o	= 314,4 km, reference altitude
ρ_o	= $3,86 \times 10^{-8}$ kg/m ³ , reference density
H_o	= 21,0 km, reference density scale height
Saturn (R.J. Newburn and S. Gulkis, 1973, [RD7.10])	
h_o	= 536,1 km, reference altitude
ρ_o	= $2,32 \times 10^{-8}$ kg/m ³ , reference density
H_o	= 40,0 km, reference density scale height
Titan (R.J. Newburn and S. Gulkis, 1973, [RD7.10])	
h_o	= 0,0 km, reference altitude
ρ_o	= 5,53 kg/m ³ , reference density
H_o	= 24,3 km, reference density scale height

More detailed constituent-wise models and day/night hemisphere models are available for some planets.

For rough calculations equation (7.16) can also be applied to model the Earth atmosphere. The density scale height H_o shall then be obtained from Tables 13, 14, or 15 (depending on the activity level), for an altitude of interest h_o .

7.10 Aerodynamics in the Earth atmosphere

The aerodynamic perturbation acting on a spacecraft during its orbital motion or atmospheric descent can be described by the drag component (D) and lift component (L) of the aerodynamic force.

$$\alpha_D = \frac{1}{2} \rho \frac{A}{m} V^2 c_D \quad (7.17)$$

$$\alpha_L = \frac{1}{2} \rho \frac{A}{m} V^2 c_L \quad (7.18)$$

where

α_D	is the aerodynamic drag, parallel to free-stream velocity, m/s ² ;
α_L	is the aerodynamic lift, perpendicular to free-stream velocity, m/s ² ;
c_D	is the drag coefficient, dimensionless;
c_L	is the lift coefficient, dimensionless;
V	is the free-stream aerodynamic velocity, m/s;
ρ	is the local air density, kg/m ³ ;
A	is the aerodynamic reference cross-section, m ² ;
m	is the spacecraft mass, kg.

Due to the energy dissipating character of the drag deceleration, natural orbital motion below altitudes of 120 km cannot be sustained in the Earth atmosphere.

The values of the drag and lift coefficient are depending on the spacecraft shape and dimensions, and on the flow conditions which can be characterized by the dimensionless Mach number M_a , Reynolds number R_e , and Knudsen number K_n .

$$M_a = \frac{V}{a} \quad (7.19)$$

$$R_e = \frac{\rho V d}{\mu} \quad (7.20)$$

$$K_n = \frac{L}{d} \quad (7.21)$$

where

a	is the speed of sound, m/s;
d	is the characteristic spacecraft dimension, m;

μ is the dynamic viscosity, $\text{kg s}^{-1}\text{m}^{-1}$;

L is the mean free path length of molecules, m.

The relevant aerodynamic theories to be used to derive c_D and c_L depend on the flow regimes which are identified via the Mach and Reynolds number. Three main regimes can be distinguished:

$M_a/R_e > 3$: free molecular flow

$M_a/R_e < 3$ and $M_a/R_e > 0,01$: transitional flow

$M_a/R_e < 0,01$: continuum flow.

Within the free molecular regime the incident flow is undisturbed by the body moving through it. This is also referred to as a collisionless flow. The momentum exchange is dominated by the gas-surface interaction mechanisms. Closed form analytical solutions exist in this regime, particularly for simple, convex body shapes. For simplified engineering analyses it is often adequate to use $c_D = 2,2$ and $c_L = 0,0$ (assuming the cross-section A to be the projected body surface perpendicular to the flow).

The transitional flow regime is not well understood, and no closed form solutions exist which cover the conditions from free-molecular flow to intermolecular collision flow. Numerical DSMC (Direct Simulation Monte Carlo) Methods can closely simulate the transitional flow conditions, but they are computationally intensive. For most engineering applications bridging methods are used to join the easily obtainable results of the free-molecular regime (above altitudes of transitional flow), and the continuum regime (below altitudes of transitional flow).

$$\frac{(c_D - c_{D,c})}{(c_{D,f} - c_{D,c})} = f_D(K_n) \quad (7.22)$$

$$\frac{(c_L - c_{L,c})}{(c_{L,f} - c_{L,c})} = f_L(K_n) \quad (7.23)$$

where

$()_c$ are the continuum flow results;

$()_f$ are the free-molecular flow results;

$f_{D,L}$ are the bridging function for drag and lift coefficient, dimensionless.

The continuum regime dominates the aerodynamic characteristics of re-entry vehicles. It can be categorized as follows:

$M_a \leq 0,3$: incompressible flow

$0,3 < M_a < 1,0$: compressible flow

$0,8 < M_a < 1,2$: transonic flow

$M_a > 1,0$: supersonic flow

$M_a > 5,0$: hypersonic flow.

In the most general case, complete solutions of the Navier-Stokes equations shall be used to characterize the aerodynamic behaviour of a vehicle in the continuum regime. For simplified engineering applications, however, a constrained Newtonian solution can be applied (assuming only pressure, but no shear stress forces acting on the vehicle). In this case, for simple, convex bodies, analytical expressions can be derived which depend on the body shape and on the angle of attack. For a sphere the continuum drag coefficient results in $c_D = 1,0$.

7.11 Figures

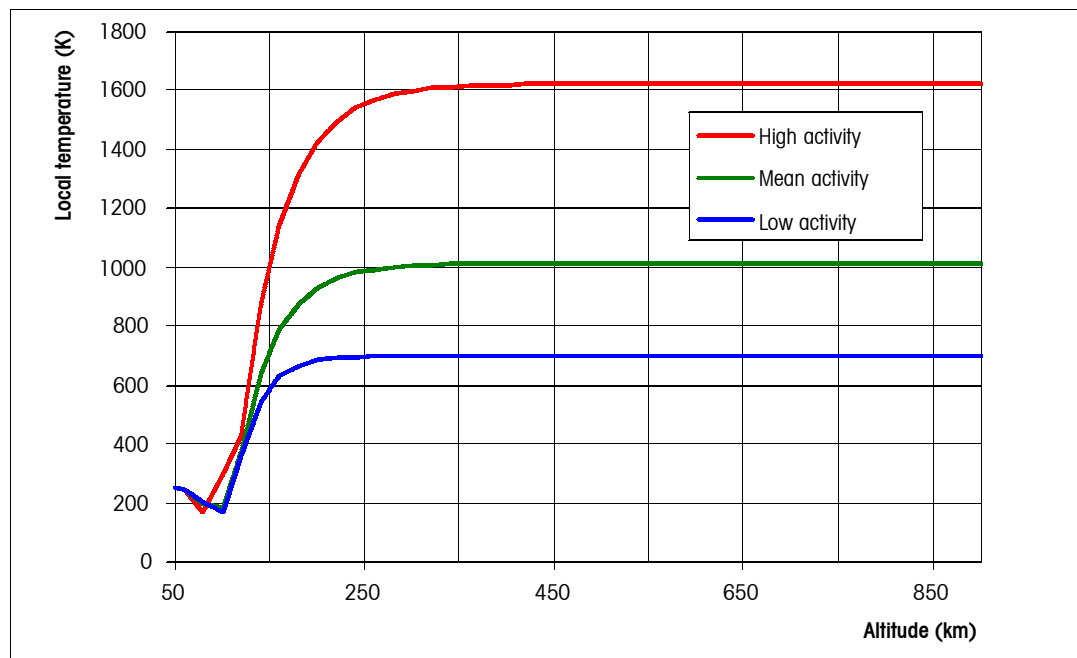


Figure 5: Variation of the MSISE-90 mean temperature with altitude for extremely low activities, for mean activities and for extremely high activities

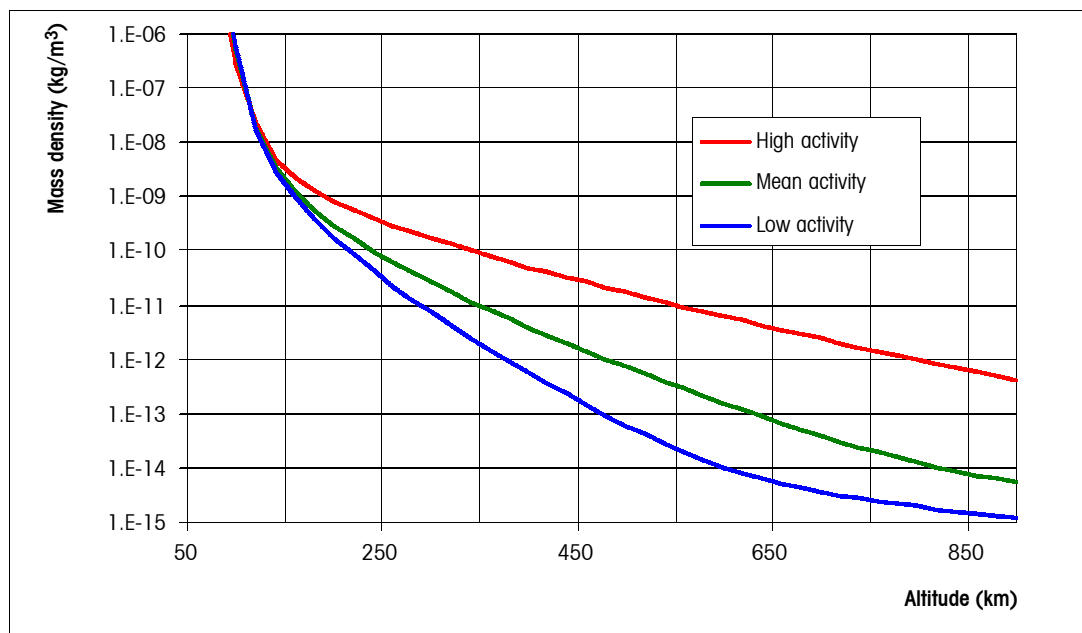


Figure 6: Variation of the MSISE-90 mean air density with altitude for low activities, for mean activities and for extremely high activities

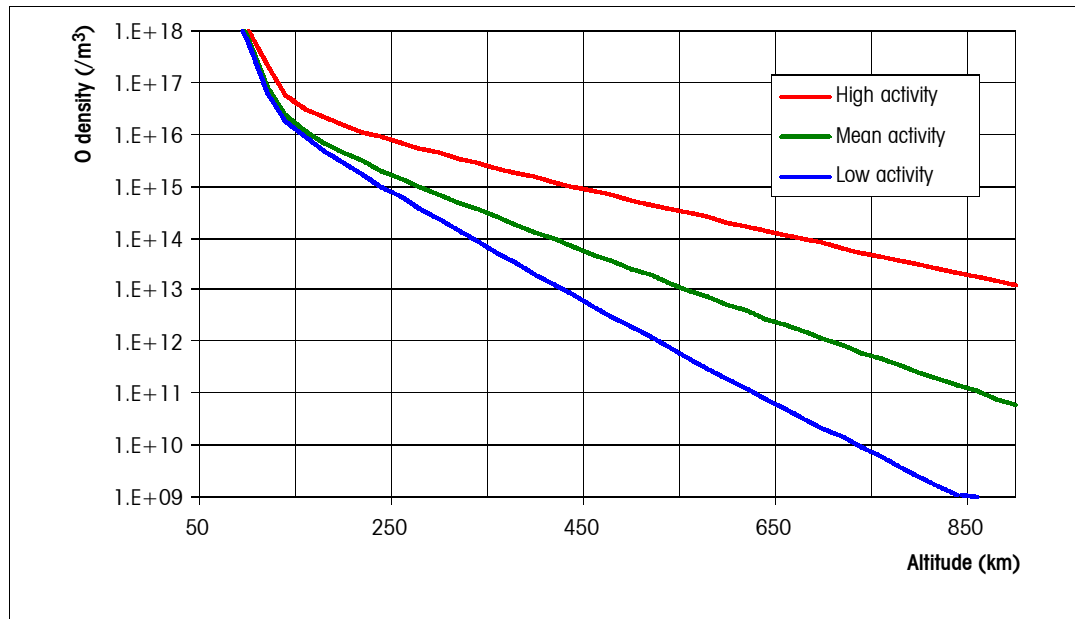


Figure 7: Variation of the MSISE-90 mean atomic oxygen with altitude for extremely low activities, for mean activities and for extremely high activities

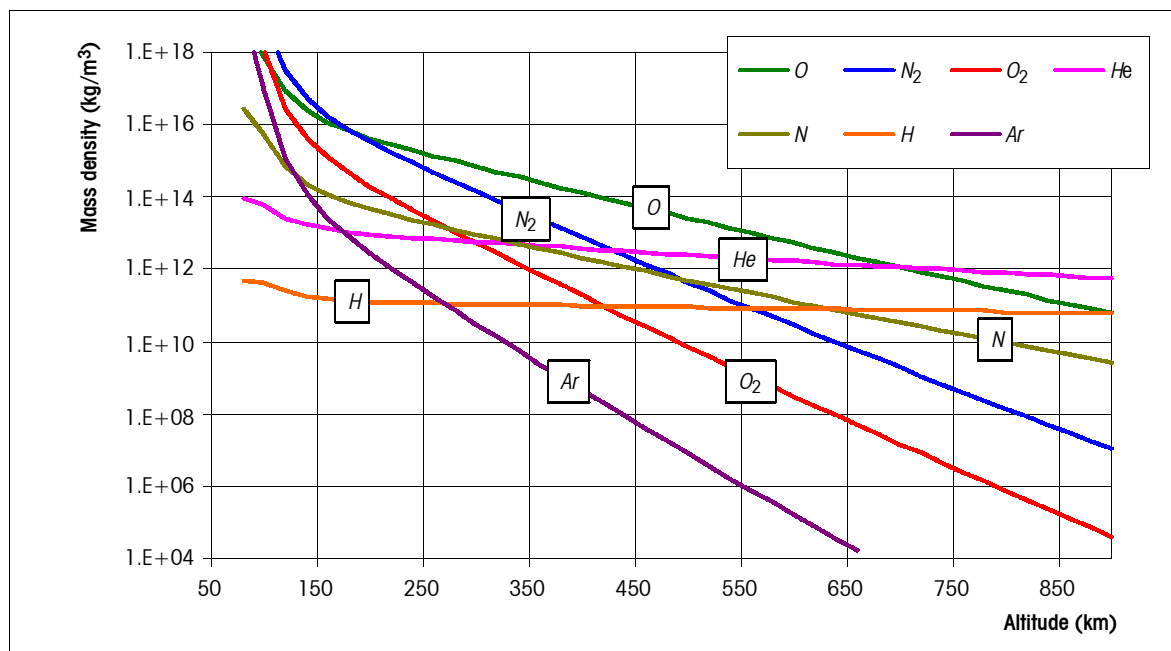
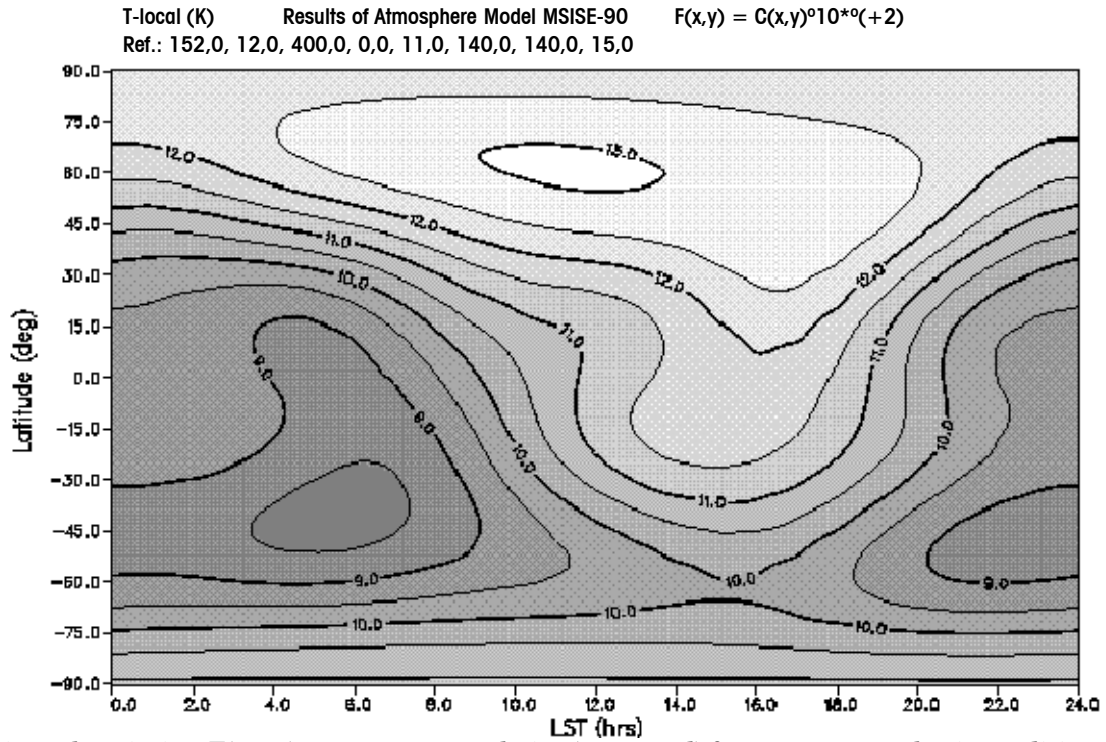
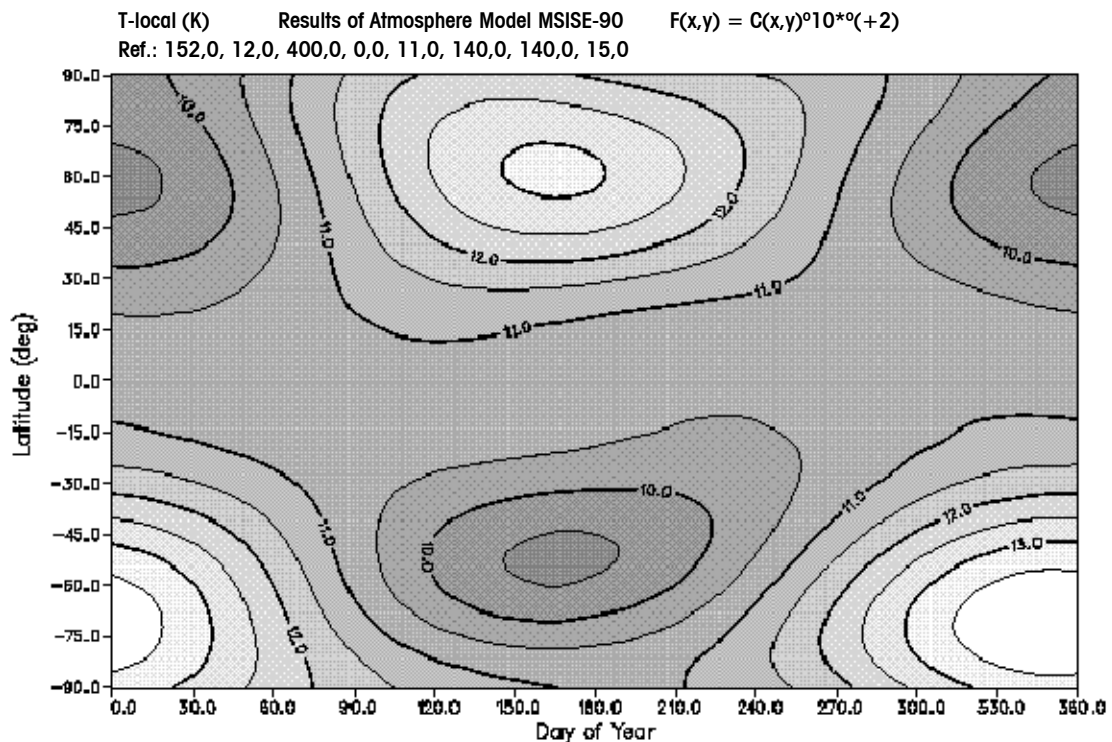


Figure 8: Variation of the MSISE-90 mean concentration profile of the atmosphere constituents N_2 , O , O_2 , He , Ar , H , and N with altitude for mean activities

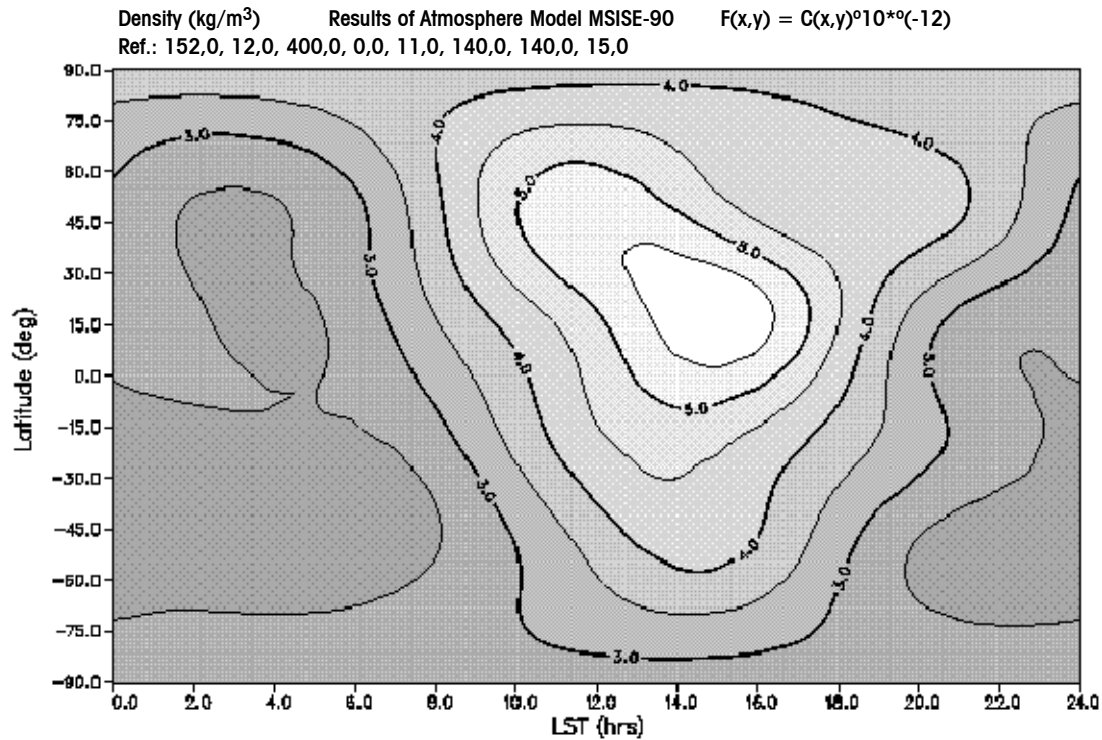


(a) Diurnal variation $T(\phi, t_{ls})$ near summer solstice ($t_d = 152$ d) for mean atmospheric conditions. The level lines indicate temperatures T in units of 100 K.

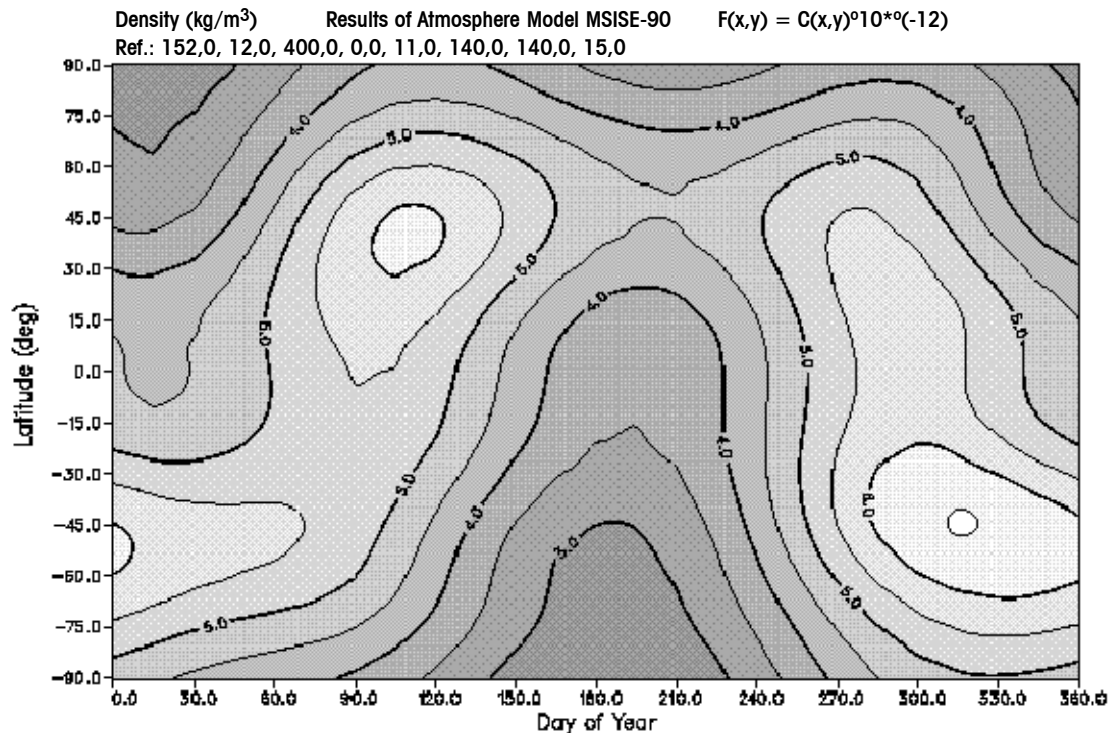


(b) Seasonal-latitudinal variation $T(\phi, t_{ls})$ near noon ($t_{ls} = 11$ h) for mean atmospheric conditions. The level lines indicate temperatures T in units of 100 K.

Figure 9: Diurnal (a) and seasonal-latitudinal (b) variations of the MSISE-90 local temperature at altitude $h = 400$ km

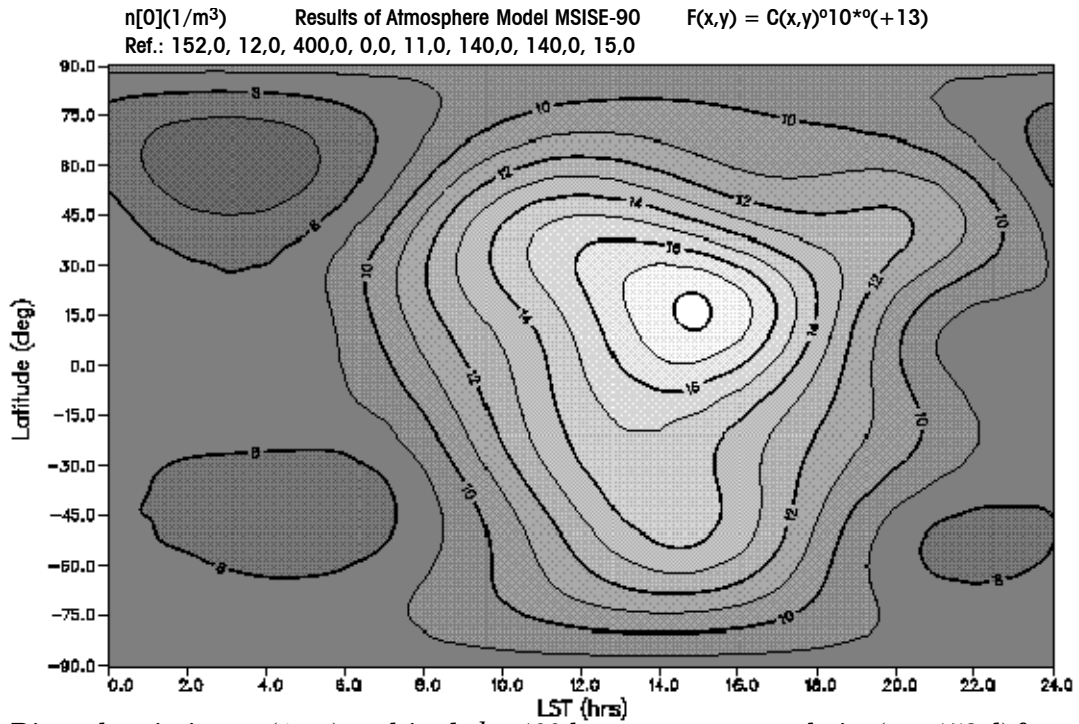


(a) Diurnal variation $\rho(\phi, t_{ls})$ at altitude $h = 400$ km near summer solstice ($t_d = 152$ d) for mean atmospheric conditions. The level lines indicate air densities in units of 10^{-12} kg/m³.

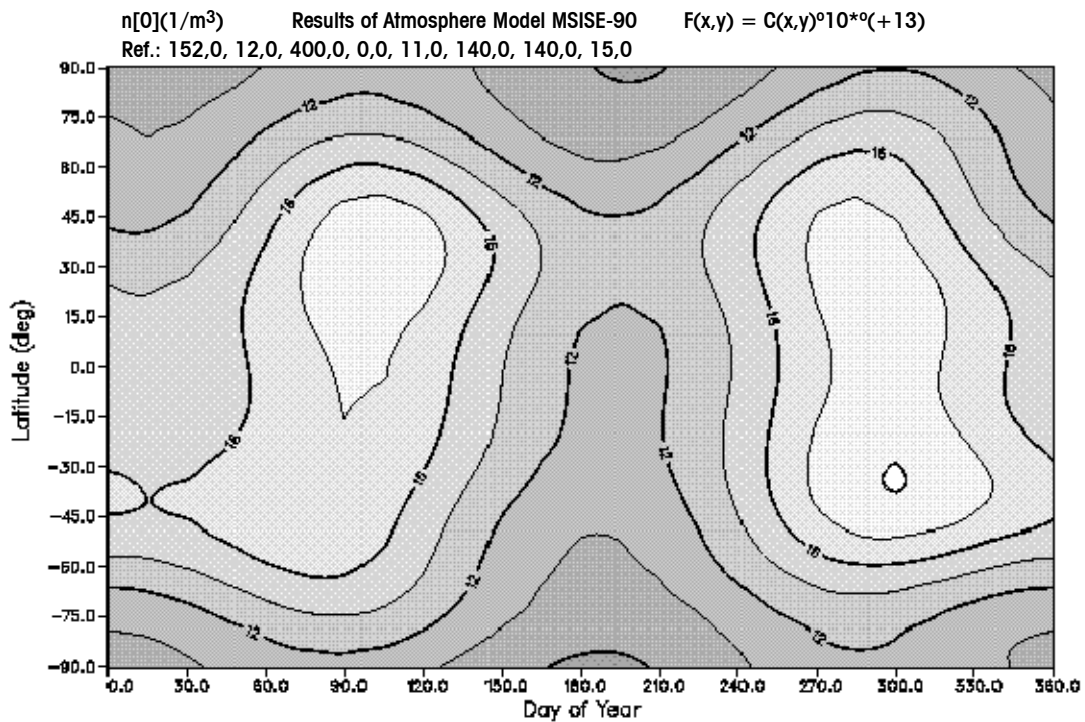


(b) Seasonal-latitudinal variation $\rho(\phi, t_d)$ at altitude $h = 400$ km near noon ($t_{ls} = 11$ h) for mean atmospheric conditions. The level lines indicate air densities in units of 10^{-12} kg/m³.

Figure 10: Diurnal (a) and seasonal-latitudinal (b) variations of the MSISE-90 air density at altitude $h = 400$ km for mean atmospheric conditions

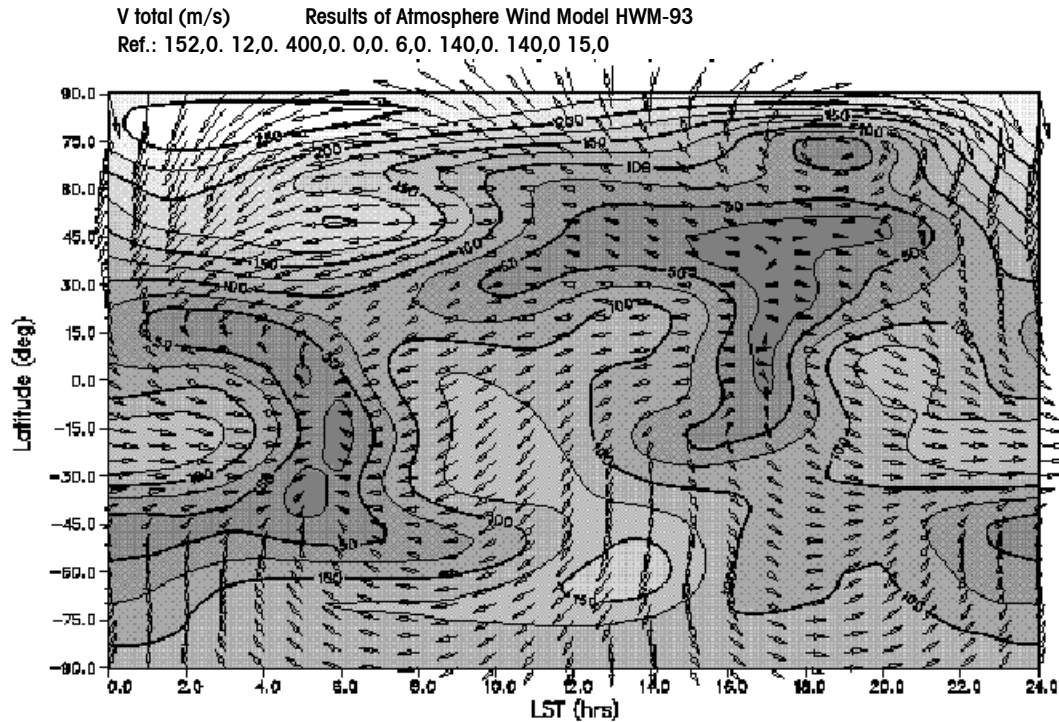


(a) Diurnal variation $n_O(\phi, t_{ls})$ at altitude $h = 400$ km near summer solstice ($t_d = 152$ d) for mean atmospheric conditions. The level lines indicate atomic oxygen concentrations n_O in units of 10^{+13} 1/m^3 .

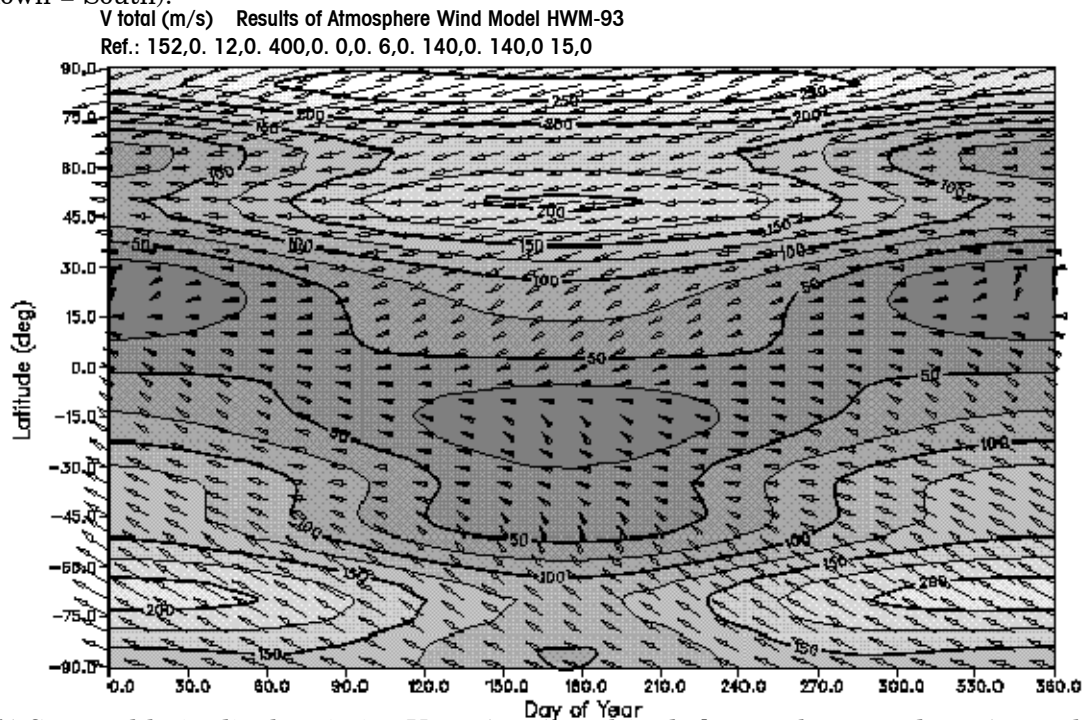


(b) Seasonal latitudinal variation $n_O(\phi, t_d)$ at altitude $h = 400$ km near noon ($t_{ls} = 11$ h) for mean atmospheric conditions. The level lines indicate atomic oxygen concentrations n_O in units of 10^{+13} 1/m^3 .

Figure 11: Diurnal (a) and seasonal latitudinal (b) variations of the MSISE-90 atomic oxygen concentration at altitude $h = 400$ km for mean atmospheric conditions



(a) Diurnal variation $V_{wind}(\phi, t_{ls})$ at altitude $h = 400$ km near summer solstice ($t_d = 152$ d) for mean atmospheric conditions ($F_{10,7} = (F_{10,7})_{avg} = 140$, $A_p = 15$, $t_{ut} = 12$ h). The level lines indicate horizontal wind magnitudes in m/s. They connect the footpoints of wind vectors of the same length. Wind directions are indicated by the orientation of the wind vectors (left = West, right = East, up = North, down = South).



(b) Seasonal-latitudinal variation $V_{wind}(\phi, t_d)$ at altitude $h = 400$ km near dawn ($t_{ls} = 6$ h) for mean atmospheric conditions ($F_{10,7} = (F_{10,7})_{avg} = 140$, $A_p = 15$, $t_{ut} = 12$ h). The level lines indicate horizontal wind magnitudes in m/s. They connect the footpoints of wind vectors of the same length. Wind directions are indicated by the orientation of the wind vectors (left = West, right = East, up = North, down = South).

Figure 12: Diurnal (a) and seasonal-latitudinal (b) variations of wind magnitude and direction according to HWM-93 at altitude $h = 400$ km for mean atmospheric conditions

7.12 References

- RD7.1 Hedin A.E., "Extension of the MSIS Thermosphere Model into the Middle and Lower Atmosphere" J. Geophys. Res., Vol. 96, No. A2, pp. 1159-1172, Feb.1, 1991.
- RD7.2 Hedin A.E., "MSIS-86 Thermospheric Model" J. Geophys. Res., Vol. 92, No. A5, pp 4649 4662, May 1, 1987.
- RD7.3 Hedin A.E. et al., "Revised Global Model of Thermosphere Winds Using Satellite and Ground-based Observations", J. Geophys. Res., Vol.96, No. A5, pp 7657-7688, May 1, 1991.
- RD7.4 Anon., "U.S. Standard Atmosphere, 1976", U.S. Government Printing Office, Washington/DC, 1976.
- RD7.5 Barnett J. and M. Corney, "Middle Atmosphere Reference Model Derived from Satellite Data Handbook MAP 16", Eds. K. Labitzke, J. Barnett, and B. Edwards, pp. 47 85, Sci. Comm. for Sol.-Terr. Phys. Secr., Univ. of Illinois/Urbana, 1985.
- RD7.6 Justus C.G., F.N. Alyea, D.M. Cunnold, R.S. Blocker and D.L. Johnson, "GRAM 88, Improvements to the Perturbation Simulation of the Global Reference Atmospheric Model", NASA MSFC memorandum ES-44-11-9-88.
- RD7.7 Didier C. and A. Maillard, "High Atmosphere Model" Final Report of ESA contract no. RFP/3 8126/F/FB, June 1996.
- RD7.8 Sagan C., Ed. Planetary Atmospheres, D. Reidel, Dordrecht, The Netherlands, 1971.
- RD7.9 Seiff A., B.D. Kirk, "Structure of the Atmosphere of Mars in Summer at Mid-Latitudes", J. Geophys. Res., Vol. 82, No. 28, pp. 4634, Sep. 30, 1997.
- RD7.10 Newburn R.L. and S. Gulkis, "A Survey of the Outer Planets Jupiter, Uranus, Neptune, Pluto, and their Satellites", Space Sci. Rev., Vol. 3, pp. 179, 1973.

(This page is intentionally left blank)

Plasmas

8.1 Introduction

A plasma is a partly or wholly ionized gas whose particles exhibit a collective response to magnetic and electric fields. The collective motion is brought about by the electrostatic Coulomb force between charged particles. This causes the particles to rearrange themselves to counteract electric fields within a distance of the order of λ , the Debye length.

$$\lambda = \left(\frac{\epsilon_0 k T_e}{n e^2} \right)^{1/2}$$

where

- λ is the Debye length expressed in m;
- T_e is electron temperature in expressed in K;
- e is electron charge expressed in C;
- n is density in expressed in, m^{-3} ;
- k is the Boltzmann constant;
- ϵ_0 is the permittivity of free space.

On spatial scales larger than λ plasmas are electrically neutral.

Spacecraft in Earth orbit can experience a number of distinct plasma regimes:

- The ionosphere, the cold plasma regime at the top of the atmosphere.
- The magnetosphere, the area above the ionosphere dominated by the Earth magnetic field and bounded by the magnetopause. This can be usefully divided into the cold low altitude regime, or plasmasphere and the hot high altitude regime.
- The solar wind, surrounding the magnetosphere, originating on the Sun and blowing throughout interplanetary space.

Within the magnetosphere, plasma flows freely up and down magnetic field lines but only slowly across it. Hence, two spacecraft observe similar plasmas if they are on the same field line, even if far apart. These spacecraft share the same L -shell and magnetic local time.

The principal spacecraft engineering concerns caused by space plasmas are outlined in Table 16 (see annex F for further details).

Table 16: Main engineering concerns due to space plasmas

Scenario	Problem
High altitudes	Surface charging - possibly harmful electrostatic discharges.
High-voltage systems at low altitudes	Power leakage, possible discharges, high spacecraft ground potential, sputtering.
Large spacecraft at low altitudes	Spacecraft wake creation.
Polar orbiting spacecraft	Surface charging - sputtering and possible discharges.
All spacecraft	Ionospheric barrier to ground-space communications below a threshold frequency. Perturbation of signals at higher frequencies.
Radar/navigation	Ionospheric propagation delays to beams.
Electric propulsion	Interactions between generated plasma, ambient plasma, and the spacecraft.
Scientific spacecraft	Low level charging and photoelectrons which interfere with plasma measurements. Plasma entry into sensitive detectors.

8.2 The ionosphere

8.2.1 Description

The ionosphere is the ionized plasma at the top of the atmosphere, produced by the dissociation of atmospheric atoms, mainly by sunlight. A good general description of this environment can be found in NASA TM-4527 [RD8.1], page 4-3. Here a less detailed summary of ionospheric characteristics is given.

It is generally divided into layers D, E and F1 at low altitudes and F2 at higher altitude. The low altitude layers are significant only during daylight hours. F2 is permanent and the most dense, peaking at around 300 km altitude. Ion composition varies between the different layers but, for most space applications, it is the electron density which is the most important characteristic. Immediately above the F2 peak, density falls off nearly exponentially with height. At mid to low latitudes, the density fall-off slows down at higher altitudes as the magnetic field traps plasma to form the plasmasphere.

In the auroral region, between 60° and 70° latitude, ionospheric density can become irregular on the scale of metres to kilometres vertically and metres to hundreds of kilometres horizontally. This is caused through heating by energetic electrons and plasma drift due to electric fields in the magnetosphere. The energetic electrons have energies of 10s of keV and travel to the ionosphere from the outer magnetosphere along magnetic field lines. Plasma density in this region can suddenly increase by a factor of up to 100 during magnetically active periods.

In the Polar Cap, above 70°, density fluctuations are less severe but because of the tilt of the Earth, there is a strong winter-summer asymmetry. Strong drift motion occurs due to electric fields. In winter, density is maintained by this drift and by “polar rain”, a weak electron flux from the solar wind with energy around 100 eV. When both these processes are depressed, ionospheric density in this region can become very low.

8.2.2 Effects

High plasma densities in the ionosphere cause reflection of radio beams below a critical frequency, as well as refraction and other effects. Hence the ionosphere acts as a barrier to satellite-ground communications and complicates satellite radar altimetry, satellite navigation systems and the radio tracking of satellites.

The high velocity of an orbiting spacecraft relative to ion velocity in this region leads to a plasma void in its immediate wake. In the auroral zone, where there are energetic electrons, this can permit surface charging to occur on wake surfaces.

For high potential surfaces, the abundance of cold ions and electrons allows current to flow through the plasma, because ions and electrons are drawn to negative and positive regions respectively. This acts as a current drain on high voltage systems, such as solar arrays and necessitates the covering of otherwise exposed surfaces. The greater mobility of electrons over ions means that a solar array tends to float with the positive end near space potential. If the negative end is selected to be spacecraft ground, this can result in the spacecraft body being significantly negative relative to space.

8.2.3 Models

The International Reference Ionosphere 1995 (IRI95) [RD8.2] shall be used for scoping studies of ionospheric parameters, although it should be stressed that it is not suitable for real-time calculations. This model calculates ionospheric plasma parameters below 60° latitude. It provides monthly mean plasma density, composition and temperature for magnetically quiet conditions in the altitude range 60km to 3000km. It is described in detail in RD8.2 and is obtainable from NSSDC via the Internet. See annex F for details.

IRI95 contains a number of options suitable for different applications. Recommended choices are indicated when the code is run. Error bars in the model at quiet times are a factor of 2 to 4 below the F2 peak. Above the F2 peak errors can be up to a factor 10 [RD8.1].

In the auroral zone, the USAF MIL-STD-1809 model [RD8.3] shall be used to represent precipitating electrons. However, a typographical error means it is printed incorrectly in RD8.3. For diffuse aurorae:

- Intensity distribution:
Gaussian with full width at half maximum of 3°.
- Energy distribution:

$$\text{Gaussian i.e. } Flux(E) = \left[\frac{Q}{2(E_m)^3} \right] E \exp\left(-\frac{E}{E_m}\right)$$

where

$Flux(E)$ is expressed in $\text{cm}^{-2} \text{s}^{-1} \text{keV}^{-1}$;

E is the energy in keV;

E_m is the characteristic energy in keV;

Q is the integral energy flux in $\text{ergs cm}^{-2} \text{s}^{-1}$.

Table 17: Parameters for the USAF diffuse aurora model

	Minimum	Typical	Nominal	Maximum
Q	0,25	1,0	3,0	12,0
E_m	0,40	1,15	3,0	9,0

For discrete aurorae the USAF MIL-STD-1809 [RD8.3] model shall be used:

- Intensity distribution: Gaussian with full width at half maximum of 0,1°.
- Energy distribution: Gaussian.
- $Flux(E)$ ten times higher than for the diffuse aurora, shown above.

8.2.4 Typical and worst case parameters

Table 18 shows an altitude profile of electron density, as calculated by IRI95, at 0° longitude and latitude, on 1st January, for a near-average sunspot number of 100, at 0 h and 12 h local time, using otherwise default options.

Table 18: Ionospheric electron density profiles derived from IRI95 [RD8.2]

Height (km)	Midnight electron density (cm ⁻³)	Noon electron density (cm ⁻³)
100	2900	157974
200	64987	204147
300	777138	469115
400	860340	1438307
500	465137	1212265
600	246060	554271
700	162271	296707
800	129393	212067
900	115569	181719
1000	109497	170067

For auroral charging assessment, the following worst-case electron distribution function shall be used. (This standard comes from RD8.3 and is based on work described in RD8.4. Unfortunately, it is printed in RD8.3 with a typographical error.)

For $E \leq 17,44$ keV:

$$f(E) = 3,9 \times 10^{-30}$$

For $E > 17,44$:

$$f(E) = \frac{[N_0(m_e)^{3/2} \exp\{-(E - E_0)/kT_0\}]}{(2\pi kT_0)^{3/2}}$$

where

$f(E)$ is the distribution function in sec³ cm⁻⁶;

N_0 is the density = 1,13 cm⁻³;

kT_0 is the “temperature” = 3,96 keV;

E_0 = 17,44 keV;

m_e is the electron mass.

For auroral charging assessment, thermal ion density of 125 cm⁻³ shall be used to represent a severely low density ion population. This comes from a severe charging case seen on the DMSP spacecraft by RD8.5. Measuring ionospheric thermal ion density during a strong charging event is potentially prone to errors because of the way the charged satellite alters ion trajectories, so there is a degree of uncertainty in this measurement.

The above worst-case environment shall be used to predict spacecraft surface potential using the POLAR [RD8.6] charging code or an equivalent code or calculations, applicable to the low Earth orbit environment. POLAR accepts inputs as Maxwellian, Power Law or Gaussian distributions.

8.3 The plasmasphere

8.3.1 Description

The plasmasphere is a region of cold dense plasma originating in the ionosphere and trapped by the Earth magnetic field.

Two magnetospheric electric fields, the co-rotation and cross-tail fields, cause particles, spiralling up and down field lines, to undergo drift perpendicular to the magnetic field. At low L -shells, the co-rotation field dominates and drift trajectories form closed paths. This allows ions, escaping from the ionosphere, to accumulate to form the dense plasmasphere. At higher L -shells, the cross-tail field dominates and drift trajectories carry particles sunwards to the magnetopause, where they are lost from the magnetosphere. The boundary between closed and open drift paths is highly variable and the outer regions of the plasmasphere are continually being lost and refilled over a period of days. Typically, the magnetopause, the outer edge of the plasmasphere, lies at an L -shell of 3 to 6, with a bulge in the dusk region of magnetic local time.

8.3.2 Effects

Because the plasmasphere contains a dense plasma, it contributes to the radio propagation effects that affect ground-space communications with satellites at high altitude. However, densities here are far below ionospheric density, so the effect is not large.

Plasmaspheric ions play a moderating role in spacecraft charging because any strong negative potential attracts ions and is neutralized. Effectively, hazardous surface charging can be said not to occur in the plasmasphere.

8.3.3 Models

Because the plasmasphere is quite variable and yet does not present major engineering concerns, it has not been considered necessary to define a standard model for this region. Nevertheless, where a model is required for scoping studies of typical plasmasphere parameters, the empirical model of Carpenter and Anderson [RD8.7] is recommended. This model is particularly comprehensive and includes terms to describe solar cycle variation and annual and semi-annual variations. Density is described as:

$$\log(n_e) = (-0,34145L + 3,9043) + \left[0,15 \left(\cos\left(\frac{2\pi(d+9)}{365}\right) - 0,5 \cos\left(\frac{4\pi(d+9)}{365}\right) \right) + 0,00127\bar{R} - 0,0635 \right] \times \exp\left(-\frac{(L-2)}{1,5}\right)$$

where

n_e is the electron density in cm^{-3} ;

d is the day of year;

\bar{R} is the 13-month average sunspot number, centred on day d .

For purposes such as estimating the likelihood of charging, the plasmaspheric density is not as important as the position of the plasmapause. In the Carpenter and Anderson model, the inner edge of the plasmapause is given as follows:

$$L_{\text{ppi}} = 5,6 - 0,46 K_{p\text{max}}$$

where

L_{ppi} is the inner plasmapause boundary in units of Earth-radii;

$K_{p\max}$ is the maximum K_p in the preceding 24 h, except that for MLT intervals 06-09, 09-12 and 12-15, one, two and three immediately preceding K_p values are omitted.

8.3.4 Typical parameters

Typical ion and electron temperatures, throughout the plasmasphere are of the order of 1 eV and 0,5 eV, respectively. The electron temperature is thus far too low to produce hazardous charging effects.

Table 19: Electron density vs. L -shell for the Carpenter and Anderson [RD8.7] model, ignoring seasonal and solar cycle effects

L -Shell (Earth-radii)	Electron density (cm ⁻³)
2,5	1312
3,0	913
3,5	636
4,0	442
4,5	308
5,0	214

8.4 The outer magnetosphere

8.4.1 Description

Beyond the plasmopause and within the magnetopause, the magnetospheric plasma environment is characterized by high temperatures and low densities. Plasma here is principally of solar wind origin. It enters mainly through the magnetosphere's tail and drifts sunwards to the near-Earth region under the influence of the cross-tail electric field. Some plasma also enters on the day side when the solar wind and terrestrial magnetic field merge in a process called re-connection. As plasma moves sunwards from the tail, it is heated adiabatically because it moves to regions of higher magnetic field strength and onto shorter magnetic field lines. In addition, sudden re-connection events in the tail can transfer large amounts of magnetic energy to the plasma which is injected into the near-Earth region. These active periods are called substorms and are detectable on the ground as magnetic disturbances. Hence there is a strong link between hot plasma and high K_p and AE (Auroral Electrojet) indices. The injected plasma drifts from the region around midnight MLT, westwards (towards dusk) for the ions and eastwards (towards dawn) for the electrons.

Like the plasmopause, the magnetopause is a dynamic boundary. Its location is controlled by the balance between the ram pressure of the flowing solar wind and the magnetic pressure of the terrestrial magnetic field. Along the Earth-Sun line, the magnetopause is closest to the Earth and its position can be expressed approximately [RD8.8] as:

$$L_m = \left(\frac{B_0^2}{\mu_0 n m V^2} \right)^{1/6}$$

where

L_m is the distance from the centre of the Earth to the magnetopause, at the subsolar point, in Earth-radii;

B_0 is the strength of the terrestrial internal magnetic field, at surface of the Earth, on the equator = 3×10^4 nT;

μ_o	is the permeability of free space;
n	is the density of the solar wind;
m	is the mass of the proton;
V	is the velocity of the solar wind.

L_m is typically 10 Earth-radii away from the subsolar point, the magnetopause flares out on the flanks and is effectively infinite in length in the anti-solar direction. This boundary is described in more detail in clause 5.

8.4.2 Effects

Magnetospheric electrons accumulate on exposed spacecraft surfaces, causing a net current which makes the surface charge negatively. Opposing currents exist which usually prevent significant charging levels, but if these are not sufficient, the spacecraft can charge to hundreds or thousands of volts. Different spacecraft surfaces can charge to different levels and so the possibility of damaging electrostatic discharges exists. A discussion of the factors contributing to charging is contained in annex F, along with typical charging levels associated with various materials. Because the intense, high-temperature electrons produced in substorms are usually required, conditions conducive to hazardous charging levels occur mainly in the midnight to dawn quadrant of local time and preferentially around the equinoxes. The regularity with which a spacecraft experiences charging depends on its electrical, geometric and surface composition characteristics. For the geostationary ATS-5 and -6 satellites, the probability of charging to greater than -10 kV during one pass from 00 LT to 06 LT was between 6 % and 12 % [RD8.9]. NASA has defined a severe charging environment [RD8.10] based on the 90th percentile of severe environments. However, this is not the one adopted as the ECSS Standard. (See annex F for more details.)

Internal, or deep dielectric charging, is discussed in clause 9 since it is due to energetic electrons not normally considered as part of the plasma population.

8.4.3 Models

The injection of heated plasma during substorms makes the outer magnetosphere highly dynamic. There are no standard models to describe this region and the standard approach for most engineering purposes is to use worst-case environments.

Garret and DeForest [RD8.11] created a comprehensive model of electron and ion and electron plasma parameters for geostationary orbit. This is not a true empirical model because the source data were selected from periods of frequent substorm injection events but is useful for charging simulations. The model provides bi-Maxwellian descriptions of ions and electron distributions versus magnetic local time and A_p . This representation is convenient for input to a spacecraft charging code such as NASCAP [RD8.12].

The single Maxwellian distribution is:

$$f(v) = 4\pi n \left(\frac{m}{2\pi kT} \right)^{3/2} v^2 \exp(-v^2 m / 2kT)$$

where

n	is the density;
v	is the velocity;
k	is the Boltzmann constant;
T	is the temperature.

8.4.4 Typical and worst case parameters

Table 20 gives typical plasma parameters for the geostationary environment for quiet and substorm periods.

For assessment of surface charging, the following worst-case environment shall be used with the NASCAP [RD8.12] charging code or an equivalent code or calculations, applicable to the high altitude environment. It shall apply for all altitudes between the plasmopause and the magnetopause as defined in clause 5, i.e. between about $L = 4$ Earth-radii and $L = 10$ Earth-radii. This is listed in Table 21. This is a double-Maxwellian fit to an extremely severe event observed by the SCATHA spacecraft on 24 April 1979 [RD8.13], when the spacecraft charged to -8 kV in sunlight. It should be noted that although the listed ion and electron densities are not equal, electrical neutrality is maintained by less energetic plasma which is not involved in the charging process and so not listed.

Table 20: Typical plasma parameters at geostationary orbit

	Density (cm^{-3})	Ion temperature	Electron temperature	λ (m)
Quiet	10	1 eV-1 keV	1 eV-1 keV	50
Substorm	1	10 keV	10 keV	500

Table 21: Standard worst-case bi-Maxwellian environment

	Electron density (cm^{-3})	Electron temperature (keV)	Ion density (cm^{-3})	Ion temperature (keV)
Population 1	0,2	0,4	0,6	0,2
Population 2	1,2	27,5	1,3	28,0

8.5 The solar wind

8.5.1 Description

The solar wind is part of the Corona, the Sun's outer atmosphere. The high temperature of the plasma near the Sun causes it to expand outwards against gravity, carrying the solar magnetic field along with it. The solar wind starts at the Sun as a hot, dense, slowly moving plasma but accelerates outwards to become cool, rare and supersonic near the Earth. Most of the solar wind's acceleration takes place near the Sun and so Earth-orbiting satellites do not observe noticeable differences in velocity as their distance from the Sun varies.

The solar wind velocity typically lies in the range 300 km/s-800 km/s. It is most commonly around 400 km/s but there are frequent high-speed streams with velocities around 700 km/s. These streams are believed to originate from open magnetic field regions on the Sun, called coronal holes and are more commonly observed around solar minimum. They recur generally with a 27-day period as the coronal hole co-rotates with the solar surface. The strong variability of the solar wind is the driving force putting energy into the magnetosphere and ultimately causing surface charging and radiation effects. More severe but less frequent disturbances in the solar wind can be caused by coronal mass ejections.

At the Earth the presence of the magnetopause causes the supersonic solar wind to decelerate abruptly i.e. a shock wave is formed. At this "bow shock" the solar wind is slowed, compressed, heated and deflected. This shock typically lies 3 Earth-radii upstream of the magnetopause on the Earth-Sun line.

8.5.2 Effects

Although solar wind plasma is cold, the ions carry considerable kinetic energy, typically ~ 1 keV for protons and ~ 4 keV for He^{++} . This can result in sputtering

from surface materials. In the magnetosheath kinetic energy is lower, but temperature is higher, so sputtering still occurs. Because solar wind flow is highly directional, it acts as a very small non-gravitational perturbation to spacecraft trajectories but this effect is negligible compared to photon radiation pressure.

8.5.3 Models

Because the solar wind flows past the Earth with negligible modification, unless it encounters the bow shock, it can be considered spatially uniform in the vicinity of the Earth. For scoping studies of solar wind parameters, a flowing Maxwellian distribution shall be used, with density and temperature given in Table 22.

Table 22: Solar wind parameters (from RD8.14)

Parameter	Mean	5-95 % Range
Speed (km s^{-1})	468	320 - 710
Density (cm^{-3})	8,7	3,2 - 20
T_p (K)	$1,2 \times 10^5$	$1 \times 10^4 - 3 \times 10^5$
T_e (K)	$1,0 \times 10^5$	$9 \times 10^4 - 2 \times 10^5$
$N_{\alpha}/N_{\text{proton}}$	0,047	0,017 - 0,078

Average and extreme solar wind parameters are shown in Table 22.

Magnetosheath plasma parameters differ according to the latitude and local time of the observation. The highest density and temperature and the steepest velocity drop are observed at the subsolar point i.e. zero degrees latitude at local noon. Typical values for this region are given in Table 23.

Table 23: Typical magnetosheath plasma parameters (from RD8.14)

Local time	Speed (km/s)	T_p (K)	T_e (K)	Density (cm^{-3})
12 noon	50	2×10^6	2×10^6	35
06 hours	350	1×10^6	1×10^6	20

8.6 Induced environments

8.6.1 Description

The natural plasma environment can be augmented by a number of sources inside or on the satellite surface.

Under the influence of photoelectrons and secondary electrons, emitted due to impacting photons, electrons and, to a lesser extent, ions, many satellites charge a few volts positive. In this situation, the emitted electrons form a low-energy cloud which surrounds the spacecraft to a distance determined by the Debye length. The temperature of this population is determined by the secondary and photo-emission spectra and is typically 2 eV to 5 eV. The density is determined by the spacecraft potential. This population can obscure measurement of the natural low-energy electron population. Instruments looking at this population should be placed on booms.

High-energy electron and ion populations can be generated by active experiments, i.e. electron and ion guns. These can be used to control surface charging or as a probe of the magnetic field. An ion thruster is a particularly high-flux ion gun.

Low-energy ion populations can be generated by ionization of contaminant gasses i.e. those released from the spacecraft by “outgassing”, emitted by thrusters, including ion thrusters and sputtered off the surface due to ion impacts. These contamination processes are described in clause 11.

8.6.2 Effects

Once outside the spacecraft, neutral atoms produced by outgassing and sputtering can be ionized by sunlight or charge-exchange with other ions, to create a low-energy (<10 eV) ion population. These ions can be drawn to negatively charged surfaces and can adhere. This coating can alter optical properties e.g. of mirrors or solar panel covers, or change the secondary and photoemission yields and the susceptibility to surface charging. Within the spacecraft, e.g. in electronics boxes, residual gasses can facilitate electrostatic discharges from high voltage components.

8.6.3 Models

8.6.3.1 Photo- and secondary electrons

The electron density at the spacecraft surface shall be determined from the incident UV and primary electron fluxes, multiplied by the yield for the surface in question. Away from the emitting surface the density shall be calculated from the following [RD8.15]:

$$\frac{N}{N_0} = \left(1 + \frac{z}{\sqrt{2}\lambda_0} \right)^{-2}$$

where

- N is the density (cm^{-3});
- N_0 is the density at emitter (cm^{-3});
- z is the distance from surface;
- λ_0 is the shielding distance, calculated as the Debye length due to the emitted electrons.

8.6.3.2 Ionization of Contaminant Gasses

Once neutral gas is released into space by whatever mechanism, it becomes subject to photoionization and dissociation by solar UV and ionization by charge exchange with solar wind ions. Production of new ions can be calculated from the appropriate photoionization rates and charge exchange cross-sections.

$$Q = N_i(\nu + \sigma n_{sw} v_{sw})$$

from RD8.16 where

- Q is the production rate, ions s^{-1} ;
- N_i is the ion density;
- ν is the photoionization rate coefficient;
- n_{sw} and v_{sw} are the solar wind density and velocity;
- σ is the charge exchange coefficient.

Photoionisation rates depends on the atom or molecule concerned, and UV intensity and spectrum. Huebner and Giguere [RD8.17] have tabulated a number of rate coefficients for different species, for sunlight at 1 AU. As an example, some photoionization rates for common gasses are listed in Table 24.

Table 24: Some solar UV photoionization rates at 1 AU (from RD8.17)

Species	Photoionization rate (s^{-1})
H_2O	$3,34 \times 10^{-7}$
O_2	$5,13 \times 10^{-7}$
N_2	$3,52 \times 10^{-7}$

For H_2O , where sigma is around $2,1 \times 10^{-19} \text{ m}^{-2}$ [RD8.16], photoionization and charge exchange are comparable processes. However, all species and dissociation products shall be considered to calculate the total production of emitted ions.

8.6.4 Typical parameters

Table 25 gives typical photoelectron sheath parameters [RD8.18].

Table 25: Photoelectron sheath parameters

Temperature (eV)	Photoelectron current (A m^{-2})	Surface electron density (m^{-3})
3	1×10^{-5}	1×10^8

8.7 Tailoring guidelines

Tailoring of this Standard to apply to specific missions shall be done by consideration of the different regions of space traversed by the spacecraft under consideration. Induced plasma can be seen in all orbits but the natural plasma populations depend strongly on orbit. Some typical examples of plasma regimes to be considered, are given in Table 26.

Table 26: Examples of appropriate plasma environments for different missions

Orbit	Regions encountered	Problems to be addressed
LEO e.g. Mir and Space station	Ionosphere excluding auroral zone.	Power leakage, high spacecraft "ground" potential, ram/wake effects.
Polar LEO	Ionosphere including auroral zone.	Power leakage, high spacecraft "ground" potential, ram/wake effects, surface charging.
Geostationary orbit	Outer magnetosphere, with rare occasions when the plasmasphere, magnetosheath and even solar wind are encountered.	Surface charging.
Geostationary transfer orbit	Ionosphere, excluding auroral zone, plasmasphere, outer magnetosphere, with rare occasions when magnetosheath and even solar wind are encountered.	Power leakage, high spacecraft "ground" potential, ram/wake effects, surface charging.
High altitude elliptical orbit	All regions can be encountered, depending on orbit.	Power leakage, high spacecraft "ground" potential, ram/wake effects, surface charging.

8.8 References

- RD8.1 NASA TM 4527, "Natural Orbital Environmental Guidelines for Use in Aerospace Vehicle Development", Eds. B.J. Anderson and R.E. Smith, 1994.
- RD8.2 Bilitza D, "International reference ionosphere - status 1995/96", *Advances in Space Research*, 20, 9, pp.1751-1754.
- RD8.3 "Space Environment for USAF Space Vehicles", MIL-STD-1809 (USAF), 15 Feb 1991.
- RD8.4 Yeh H.-C. and M.S. Gussenhoven, "The statistical Electron Environment for Defense Meteorological Satellite Program Eclipse Charging", *J. Geophys. Res.*, pp.7705-7715, 1987.
- RD8.5 Gussenhoven M.S, D.A. Hardy, F. Rich, W.J. Burke and H.-C. Yeh, "High-Level Spacecraft Charging in the Low-Altitude Polar Auroral Environment", *J. Geophys. Res.*, pp.11009-11023, 1985.
- RD8.6 Lilley J.R., D.L. Cooke, G.A. Jongeward and I. Katz, "POLAR User's Manual", AFGL-TR-85-0246.
- RD8.7 Carpenter D.L. and R.R. Anderson, "An ISEE/Whistler Model of Equatorial Electron Density in the Magnetosphere", *J. Geophys. Res.*, 97, p.1097, 1992.
- RD8.8 Burke W.J., D.A. Hardy and R.P. Vancour, "Magnetospheric and High Latitude Ionospheric Electrodynamics", Chapter 8 of "Handbook of Geophysics and the Space Environment", Ed. A. Uram, USAF, 1985.
- RD8.9 Grard R., K. Knott and A. Pedersen, "Spacecraft Charging Effects", *Space Sci. Rev.*, 34, p.289, 1983.
- RD8.10 Purvis C.K, H.B. Garrett, A.C. Whittlesey and N.J. Stevens, "Design Guidelines for Assessing and Controlling Spacecraft Charging Effects", NASA TP-2361, 1984.
- RD8.11 Garrett H.B. and S.E. DeForest, "An Analytical Simulation of the Geosynchronous Plasma Environment", *Planet. Space Sci.*, 27, p.1101, 1979.
- RD8.12 Katz I., J.J. Cassidy, M.J. Mandell, G.W. Schnuelle, P.G. Steen and J.C. Roche, "The Capabilities of the NASA Charging Analyzer Program", in "Spacecraft Charging Technology - 1978", Eds. R.C. Finke and C.P. Pike, NASA CP-2071/AFGL TR-79-0082, ADA045459, p.101, 1979.
- RD8.13 Gussenhoven M.S and E.G. Mullen, "Geosynchronous Environment for Severe Spacecraft Charging", *J. Spacecraft and Rockets* 20, p.26, 1988.
- RD8.14 Feynman J, "Solar Wind", Chapter 3 of "Handbook of Geophysics and the Space Environment", Ed. A. Uram, USAF, 1985.
- RD8.15 Grard R.J.L. and J.K.E. Tunaley, "Photo Electron Sheath Near a planar Probe in Interplanetary Space", *J. Geophys. Res.*, 76, p.2498, 1971.
- RD8.16 Huddleston D.E., A.D. Johnstone and A.J. Coates, "Determination of Comet Halley Gas Emission Characteristics from Mass Loading of the Solar Wind", *J. Geophys. Res.*, 95, p.21, 1990.
- RD8.17 Huebner W.F. and P.T. Giguere, "A Model of Comet Comae II. Effects of Solar Photodissociative Ionization", *Astrophys. J.*, 238, p.753, 1980.
- RD8.18 Scialdone J.J., "An Estimate of the Outgassing of Space Payloads and Its Gaseous Influence on the Environment", *J. Spacecraft and Rockets*, 23, p.373, 1986.

Energetic particle radiation

9.1 Introduction – Overview of energetic particle radiation environment and effects

9.1.1 General

Radiation environments and effects shall be considered early in the design cycle. Energetic charged particles with energies in the MeV range are encountered throughout the Earth magnetosphere, in inter-planetary space, and in the magnetospheres of other planets. At pre-phase A, radiation environments are an element in trade-offs for orbit selection. Effects on both the payload and on the spacecraft carrier shall be considered. A radiation environment specification for a mission shall be established wherein all types of radiation shall be considered, reflecting general and mission-specific radiation susceptibilities.

9.1.2 Environments

9.1.2.1 Radiation belts

Energetic electrons and ions are magnetically trapped around the Earth forming the radiation belts, also known as the Van Allen belts. The radiation belts are crossed by low altitude orbits as well as high altitude orbits (geostationary and beyond). The radiation belts consist principally of electrons of up to a few MeV energy and protons of up to several hundred MeV energy. The so-called South Atlantic anomaly is the inner edge of the inner radiation belt encountered in low altitude orbits. The offset, tilted geomagnetic field brings the inner belt to its lowest altitudes in the South Atlantic region. More information can be found in references RD9.1. and RD9.2.

9.1.2.2 Solar energetic particles

Energetic solar eruptions (Solar Particle Events, SPEs) produce large fluxes of Solar Energetic Particles (SEPs) which are encountered in interplanetary space and close to the Earth. The Earth magnetic field provides a varying degree of geomagnetic shielding of near-Earth locations from these particles.

9.1.2.3 Galactic cosmic rays

There is a continuous flux of Galactic Cosmic Ray (GCR) ions. Although the flux is low (a few particles/cm²/sec), GCRs include energetic heavy ions which can deposit significant amounts of energy in sensitive volumes and so cause problems.

9.1.2.4 Other planets

The above environments are common to planets other than the Earth. Jupiter and Saturn, in particular, have severe radiation environments. Mercury also has a small magnetosphere.

9.1.2.5 Secondary radiation

Secondary radiation is generated by the interaction of the above environmental components with materials of the spacecraft. A wide variety of secondary radiations are possible, of varying importance.

9.1.2.6 Other radiation sources

Other sources of radiation include neutrons resulting from energetic particle interactions with the upper atmosphere and emissions from on-board radioactive sources such as in Radioisotope Thermo-electric Generator (RTG) electrical power systems.

9.1.3 Effects survey

The above radiation environments represent important hazards to space missions. Energetic particles, particularly from the radiation belts and from solar particle events cause radiation damage to electronic components, solar cells and materials. They can easily penetrate typical spacecraft walls and deposit doses of hundreds of kilorads during missions in certain orbits.

Radiation is a concern for manned missions. Astronauts shall operate within defined limits of dose equivalent [RD9.3], determined to ensure as low as reasonably achievable long-term risk. There are many possible radiation effects to humans, beyond the scope of this document. These are described in RD9.4. To account for dependence of effects on particle species, energy and LET, dose is expressed as dose equivalent where energy, LET and species dependent factors are used to scale absorbed dose contributions. For example, heavy ions and neutrons are known to cause severe biological damage, and therefore these contributions receive a heavier weighting than gamma radiation. The “quality factors”, as they are called, are established by the International Commission on Radiological Protection [RD9.5].

Energetic ions, primarily from cosmic rays and solar particle events, lose energy rapidly in materials, mainly through ionization. This energy transfer can disrupt or damage targets such as a living cell, or a memory element, leading to Single-event Upset (SEU) of a component, or an element of a detector (radiation background).

SEUs and biological effects can also arise from nuclear interactions between very energetic trapped protons and materials (sensitive parts of components, biological experiments, detectors). Here, the proton breaks the nucleus apart and the fragments cause highly-localized ionization.

Energetic particles also interfere with payloads, most notably with detectors on astronomy and observation missions where they produce a “background” signal which are not distinguishable from the photon signal being counted, or which can overload the detector system.

Energetic electrons can penetrate thin shields and build up static charge in internal dielectric materials such as cable and other insulation, circuit boards, and on ungrounded metallic parts. These can subsequently discharge, generating electromagnetic interference.

Apart from ionizing dose, particles can lose energy through non-ionizing interactions with materials, particularly through “displacement damage”, or “bulk damage”, where atoms are displaced from their original sites. This can alter the electrical, mechanical or optical properties of materials and is an important damage mechanism for electro-optical components (e.g. solar cells and opto-couplers) and for detectors, such as CCDs.

9.2 Quantification of effects and related environments

Models of the radiation environment are needed to assist in orbit selection, component selection and shielding optimization. In engineering a space system to operate in the space environment, it is necessary to relate the environment to system degradation quantitatively. This also involves questions of testing systems and their components for verification that they meet the performance requirements in the presence of the space environment.

For example, testing with calibrated radioactive sources can establish the threshold for functional failure or degradation of an electronic component in terms of *total absorbed dose* (often referred to simply as “total dose”, or just “dose”). Radiation environment models, used together with mission orbital specifications can predict the dose and enable correct performance to be verified.

Table 27 gives the parameters which shall be used for quantification of the various radiation effects.

Although some of these parameters are readily derivable from a specification of the environment, others either need explicit consideration of test data (for example, SEU calculation) or the detailed consideration of interaction geometry and mechanisms (e.g. radiation background estimation).

In the following subclauses, the basic data on the environment are presented, along with models to be employed for deriving data beyond those presented. Effects and the specific methods for derivation of engineering quantities are presented.

Table 27: Parameters for quantification of radiation effects

Radiation effect	Parameter
Electronic component degradation	Total ionizing dose.
Material degradation	Total ionizing dose.
Material degradation (bulk damage)	Non-ionizing dose (NIEL).
CCD and sensor degradation	NIEL.
Solar cell degradation	NIEL and equivalent fluence.
SEU and latch-up	LET spectra (ions); proton energy spectra; explicit SEU/SEL rate of devices.
Sensor interference (background signals)	Flux above above energy threshold or flux threshold; explicit background rate.
Internal electrostatic charging	Electron flux and fluence; dielectric E-field.

9.3 Energetic particle radiation environment reference data, models and analysis methods

Figure 13 shows the ranges of electrons and protons in aluminium.

9.3.1 Trapped radiation belts

9.3.1.1 Basic data

Trapped radiation belt charged energetic particles gyrate in the geomagnetic field with a gyration period $t_c = 2\pi m/(eB)$ and a radius of gyration of $R_c = mv^2/(eB)$.

Table 28 gives typical characteristics of energetic particles.

Table 28: Characteristics of typical radiation belt particles

	Particle	
	1 MeV Electron	10 MeV Proton
Range in aluminium (mm)	2	0,4
Peak equatorial omni-directional flux ($\text{cm}^{-2} \text{s}^{-1}$)*	4×10^6	$3,4 \times 10^5$
Radial location (L) of peak flux (Earth-radii)*	4,4	1,7
Radius of gyration (km)		
@ 500 km	0,6	50
@ 20 000 km	10	880
Gyration period (s)		
@ 500 km	10^{-5}	7×10^{-3}
@ 20 000 km	2×10^{-4}	0,13
Bounce period (s)		
@ 500 km	0,1	0,65
@ 20 000 km	0,3	1,7
Longitudinal drift period (min)		
@ 500 km	10	3
@ 20 000 km	3,5	1,1

* derived from the models of subclause 9.3.1.2

9.3.1.2 Standard models

For trapped radiation, the standard models of radiation belt energetic particle shall be the AE-8 and AP-8 models for electrons [RD9.6] and protons [RD9.7], respectively. They were developed at the NSSDC at NASA/GSFC based on data from satellites flown in the 1960s and early 1970s. The models give omni-directional fluxes as functions of idealized geomagnetic dipole coordinates B/B_0 and L (see clause 5). This means that they shall be used together with an orbit generator and geomagnetic field computation to give instantaneous or orbit-averaged fluxes. The user shall define an orbit, generate a trajectory, transform it to geomagnetic coordinates and access the radiation belt models to compute flux spectra. Apart from separate versions for solar maximum and solar minimum, there is no description of the temporal behaviour of fluxes. At high altitudes in particular (e.g. around geostationary orbit) fluxes vary by orders of magnitude over short times and exhibit significant diurnal variations; the models do not describe these. In addition, the models do not contain any explicit flux directionality.

At low altitudes, on the inner edge of the radiation belts, particle fluxes rise very steeply with altitude and small errors in computing locations can give rise to large errors in particle fluxes. This is a problem since the geomagnetic field is shifting and decaying so that the situation is no longer the same as when the model data were acquired. Use of a geomagnetic field model other than the one used in generating the model can result in large flux errors at low altitude. The models shall only be used together with the geomagnetic field models shown in Table 29.

Table 29: Standard field models to be used with radiation-belt models

Radiation-belt model	Geomagnetic field model
AE-8-MIN	Jensen-Cain 1960
AE-8-MAX	Jensen-Cain 1960
AP-8-MIN	Jensen-Cain 1960
AP-8-MAX	GSFC 12/66 extrapolated to 1970

Although use of an old field model and epoch can reduce errors in the magnitudes of fluxes, it should be noted that it does not model the spatial locations of radiation-belt features (e.g. the position of the South Atlantic anomaly), or particle fluxes, as they are today.

The particle ranges shown in Figure 13 show that in order to penetrate typical spacecraft shielding of the order of millimetres, protons need tens of MeV energies and electrons need in excess of about 0,5 MeV. The AP-8 model for protons gives proton fluxes from 0,1 to 400 MeV while the AE-8 model for electrons covers electrons from 0,04 to 7 MeV. Figure 14 shows contour plots of AE-8 and AP-8 model omnidirectional, integral fluxes for energies above 1 MeV and 10 MeV, respectively, in idealized dipole space.

Figure 15 shows values of energetic electron and proton particle fluxes as stored in these models, for positions on the geomagnetic equator ($B=B_0$), as functions of L for both solar maximum and solar minimum. This shows that as far as the models are concerned, the solar activity only affects electron fluxes in the mid- L range and protons at low altitude where the higher neutral atmospheric density at solar maximum leads to reduced proton fluxes because of enhanced loss. Solar cycle effects on electrons appear to differ from this behaviour in reality [RD9.8].

9.3.1.3 The South Atlantic anomaly

The South Atlantic anomaly (see subclause 9.1.2.1) produces an “island” of radiation and provides the only significant radiation encountered on low Earth orbits with altitudes below about 800 km and inclinations below about 40°. Figure 16 shows the South Atlantic Anomaly at 400 km.

Anisotropy (the “East-West effect”)

Because of the inclination of geomagnetic field-lines with respect to the atmosphere here, particles reaching a point from the West have gyrated from higher altitude while those arriving from the East have gyrated from lower altitude. There are fewer coming from below because of atmospheric absorption and therefore an asymmetry in the fluxes results. This can be important in certain cases, including the International Space Station. The current standard AP-8 model does not treat this effect but models have been developed by NASA [RD9.9] and BIRA [RD9.10]. Figure 17, from the BIRA ANISO model, shows the integral orbit-averaged flux of 100 MeV protons in the horizontal plane as a function of look-direction relative to North. The East and West “lobes” are clear. The ratio of the East and West peak fluxes is about 4,6. Measurements from MIR are also available which are consistent with this ratio [RD9.11].

Location of the South Atlantic anomaly

The slow movement of the South Atlantic anomaly as a result of shifts in the geomagnetic field has been clearly observed and agrees with expectation. This shift is essentially westward at a rate of $0,3^\circ$ per year ($\sim 10^\circ$ since the models were created) and account shall be taken of this figure for low Earth orbits when planning operations which involve a sensitivity to radiation (payload radiation background, astronaut EVA). Models including this shift capability are available [RD9.12].

9.3.1.4 Dynamics of the outer radiation belt

The dynamic nature of the outer electron radiation belt, together with its diurnal variations mean that unless one is interested in long-term averages (such as provided by AE-8), some statistical description is desirable. This is especially true when deep dielectric charging and radiation background are of concern. No standard models for the variability are yet available, but for engineering purposes the CRRESELE model may be used [RD9.13]. An older version of the AE-8 electron model, AE-4 [RD9.14], included a statistical model giving standard deviations of the logarithm of electron fluxes (assumed to be normally-distributed). It also included a model for local time flux modulation. This was a sinusoidal model providing amplitudes of the variation, with a fixed maximum at 11:00 hours local time. These have been extended and applied to the AE-8 model [RD9.15], although this extension is unvalidated.

9.3.2 Solar particle event models

9.3.2.1 Standard model for mission-integrated fluences

During energetic events on the Sun, large fluxes of energetic protons are produced which can reach the Earth. Solar particle events, because of their unpredictability and large variability in magnitude, duration and spectral characteristics, have to be treated statistically. However, large events are confined to a 7-year period defined as solar maximum. Although large events are absent during the remaining 4 solar minimum years of the 11-year solar cycle (see clause 6) the occasional small event can still occur.

Figure 18, based on data from RD9.16, shows reference data for solar maximum solar proton fluences at various energy levels based on the JPL-1991 model. The data are also tabulated in Table 30.

This statistical model is based on data from 3 solar cycles. This shall be the standard model used for engineering consideration of time-integrated effects. Since this is a statistical model, a probability level shall be entered. On the basis of analysis of worst-case periods [RD9.17], the probability levels in Table 31 are recommended.

The JPL model provides data up to 60 MeV. For fluences at energies above this, an exponential fit to the rigidity spectrum shall be used, where rigidity is defined as:

$$P = \left(\frac{A}{Z}\right) \frac{(E^2 + 1862 E)^{1/2}}{10^3}$$

where

P is the rigidity, expressed in GV;

E is the energy, expressed in MeV.

Table 30: Fluence levels for energy, mission duration and confidence levels from the JPL-1991 model

Energy (MeV)	Probability (confidence) level (%)	1 year (/cm ²)	2 years (/cm ²)	3 years (/cm ²)	5 years (/cm ²)	7 years (/cm ²)
>1	50	$5,92 \times 10^{10}$	$1,16 \times 10^{11}$	$1,72 \times 10^{11}$	$3,15 \times 10^{11}$	$3,99 \times 10^{11}$
>1	75	$8,76 \times 10^{10}$	$1,74 \times 10^{11}$	$2,42 \times 10^{11}$	$3,87 \times 10^{11}$	$4,77 \times 10^{11}$
>1	90	$1,26 \times 10^{11}$	$2,39 \times 10^{11}$	$3,25 \times 10^{11}$	$4,79 \times 10^{11}$	$5,89 \times 10^{11}$
>1	95	$1,64 \times 10^{11}$	$2,92 \times 10^{11}$	$3,96 \times 10^{11}$	$5,55 \times 10^{11}$	$6,95 \times 10^{11}$
>1	99	$2,91 \times 10^{11}$	$4,52 \times 10^{11}$	$5,89 \times 10^{11}$	$7,68 \times 10^{11}$	$1,00 \times 10^{12}$
>4	50	$8,00 \times 10^9$	$2,02 \times 10^{10}$	$3,33 \times 10^{10}$	$5,75 \times 10^{10}$	$8,84 \times 10^{10}$
>4	75	$1,69 \times 10^{10}$	$3,58 \times 10^{10}$	$5,74 \times 10^{10}$	$9,28 \times 10^{10}$	$1,27 \times 10^{11}$
>4	90	$3,46 \times 10^{10}$	$6,42 \times 10^{10}$	$9,81 \times 10^{10}$	$1,49 \times 10^{11}$	$1,96 \times 10^{11}$
>4	95	$5,49 \times 10^{10}$	$9,54 \times 10^{10}$	$1,40 \times 10^{11}$	$2,09 \times 10^{11}$	$2,70 \times 10^{11}$
>4	99	$1,50 \times 10^{11}$	$2,28 \times 10^{11}$	$3,10 \times 10^{11}$	$4,45 \times 10^{11}$	$5,63 \times 10^{11}$
>10	50	$2,11 \times 10^9$	$5,59 \times 10^9$	$9,83 \times 10^9$	$1,79 \times 10^{10}$	$2,78 \times 10^{10}$
>10	75	$5,34 \times 10^9$	$1,18 \times 10^{10}$	$1,85 \times 10^{10}$	$3,16 \times 10^{10}$	$4,70 \times 10^{10}$
>10	90	$1,25 \times 10^{10}$	$2,42 \times 10^{10}$	$3,41 \times 10^{10}$	$5,28 \times 10^{10}$	$7,55 \times 10^{10}$
>10	95	$2,12 \times 10^{10}$	$3,79 \times 10^{10}$	$5,19 \times 10^{10}$	$7,51 \times 10^{10}$	$1,05 \times 10^{11}$
>10	99	$5,88 \times 10^{10}$	$1,02 \times 10^{11}$	$1,31 \times 10^{11}$	$1,86 \times 10^{11}$	$2,36 \times 10^{11}$
>30	50	$4,50 \times 10^8$	$1,28 \times 10^9$	$2,22 \times 10^9$	$4,56 \times 10^9$	$6,61 \times 10^9$
>30	75	$1,23 \times 10^9$	$2,94 \times 10^9$	$4,67 \times 10^9$	$8,33 \times 10^9$	$1,16 \times 10^{10}$
>30	90	$3,19 \times 10^9$	$6,71 \times 10^9$	$1,00 \times 10^{10}$	$1,66 \times 10^{10}$	$2,24 \times 10^{10}$
>30	95	$5,81 \times 10^9$	$1,13 \times 10^{10}$	$1,66 \times 10^{10}$	$2,63 \times 10^{10}$	$3,52 \times 10^{10}$
>30	99	$1,93 \times 10^{10}$	$3,49 \times 10^{10}$	$4,83 \times 10^{10}$	$6,96 \times 10^{10}$	$9,04 \times 10^{10}$
>60	50	$1,67 \times 10^8$	$4,92 \times 10^8$	$9,18 \times 10^8$	$1,73 \times 10^9$	$2,85 \times 10^9$
>60	75	$4,93 \times 10^8$	$1,24 \times 10^9$	$2,11 \times 10^9$	$3,52 \times 10^9$	$5,26 \times 10^9$
>60	90	$1,37 \times 10^9$	$2,83 \times 10^9$	$4,39 \times 10^9$	$7,00 \times 10^9$	$1,01 \times 10^{10}$
>60	95	$2,61 \times 10^9$	$4,92 \times 10^9$	$7,36 \times 10^9$	$1,12 \times 10^{10}$	$1,53 \times 10^{10}$
>60	99	$9,20 \times 10^9$	$1,62 \times 10^{10}$	$2,26 \times 10^{10}$	$3,27 \times 10^{10}$	$4,25 \times 10^{10}$

Table 31: Standard probability (confidence) levels to be applied for various mission durations

Number of years of exposure	Probability level (%)
1	97
2	95
3	95
4	90
5	90
6	90
7	90

9.3.2.2 Spectrum of individual events

The August 1972 event produced a peak flux near the Earth in excess of 10^6 protons $\text{cm}^{-2} \text{s}^{-1}$ above 10 MeV energy, while the October 1989 event produced a peak flux of about 10^5 protons $\text{cm}^{-2} \text{s}^{-1}$. A fluence spectrum which is often used to represent a worst case flare, classified as “anomalously large” is based on the very large August 1972 event:

$$J(E) = 7,9 \times 10^9 \exp\left\{\frac{30 - E}{26,5}\right\}$$

with energy E in MeV and fluence J in protons cm^{-2} . The October 1989 event was the largest seen since August 1972 but had lower fluences at the medium energies. A fit to its differential fluence spectrum is given by a three-part power law:

$$J(E) = \begin{cases} 1,2 \times 10^{11} E^{-1,7} & \text{for } E < 30\text{MeV} \\ 4,5 \times 10^{12} E^{-2,8} & \text{for } 30\text{MeV} < E < 150\text{MeV} \\ 5,5 \times 10^9 E^{-1,45} & \text{for } E > 150\text{MeV} \end{cases}$$

where E is in MeV and J is in protons $\text{cm}^{-2} \text{MeV}^{-1}$.

Comparison of these two spectra reveals important points. Since flare spectra are variable, the worst-case event at one energy is not necessarily worst-case at another. The August 1972 event yield worst-case doses at most typical spacecraft shielding (1-10 mm) where particles of energy 10-70 MeV are most important. The October 1989 flare is apparently more severe at lower and higher energies. Lower energies are important for surface material and solar cell effects and the higher energies more important for nuclear interactions giving rise to certain types of background and SEUs. So the term “worst-case” is application dependent.

9.3.2.3 Event probabilities

Burrell, as reported in RD9.18, developed a modified Poisson statistic to describe the probability p of a number of events n occurring during a time t , based on a previously observed frequency of N during time T :

$$p(n, t; N, T) = \frac{\{(n + N)! (t/T)^n\}}{\{n!N! (1 + t/T)^{N+n+1}\}}$$

In this equation, $N=1$ and $T=7$ for the anomalous class of flare, while for ordinary flares, $N=24$ and $T=7$. This is sometimes useful in considering numbers of events in contrast to the total fluence. Simple application of Poisson statistics is also useful.

9.3.2.4 Analysis of event records

The JPL-91 model provides data only for integrated effects analysis (e.g. dose, long-term degradation, total upset count). It is often necessary to consider instantaneous fluxes. For radiation background estimation for example, the fluxes are required above an energy threshold determined by sensor shielding and sensor sensitivity, and above a flux threshold determined by sensor signal-to-noise characteristics. Two reference environment data resources are available: the NASA OMNIWEB database [RD9.19], and the NOAA GOES [RD9.20] database. With these databases, the durations and magnitudes of events above energy and flux thresholds can be analysed. Both databases are available on the WWW and provide a comprehensive long-term database of measurements of the interplanetary environment. OMNIWEB contains a complete database of energetic proton data from the IMP series of spacecraft. The NOAA GOES satellites have returned energetic proton and electron data from geostationary orbit since January 1986. Further information is provided in annex G.

9.3.2.5 Solar particle event ions

For analysing single event upset rates during Solar Particle Events (SPEs), the CREME96 model shall be used. It can also be used for other applications where data on severe SPE conditions are needed, such as background estimation. CREME96 is described further in subclause 9.3.3. While the older CREME model contained models for the peak flux for various types of events, CREME96 contains models based on the October 1989 event. It provides models of energy spectrum, composition and LET spectrum for the worst week, worst day and peak 5 minutes. The older CREME model provided more choice of peak environments. However, some of the more severe options were unrealistic.

9.3.2.6 Other models

Other model developments, which can lead to updates of this Standard, are discussed in annex G. These developments relate to alternative statistical approaches and models for peak fluxes.

9.3.2.7 Directionality

Fluxes and fluences of solar energetic particles shall be assumed to be isotropic in interplanetary space. This is generally not true in near-Earth space due to geomagnetic shielding (see subclause 9.3.4).

9.3.3 Cosmic ray environment and effects models

9.3.3.1 General

Cosmic ray environment and effects models were originally created by Adams and co-workers at the U.S. Naval Research Laboratory [RD9.21], under the name CREME. They provided a comprehensive set of cosmic ray and flare ion LET and energy spectra, including treatment of geomagnetic shielding and material shielding. CREME also included upset rate computation based on the path-length distribution in a sensitive volume and also treated in a simple manner trapped proton-induced SEUs. CREME has been superseded by CREME96 [RD9.22]. The major differences are in the inclusion of a model of the cosmic ray environment and its solar-cycle modulation due to Nymmik et al. [RD9.23], improved geomagnetic shielding calculation, improved material shielding calculation and more realistic Solar Energetic Particle Event (SEPE) ion environments (see subclause 9.3.2.5). Cosmic ray fluxes are anti-correlated with solar activity so the highest cosmic ray fluxes occur at solar minimum. CREME96 shall be the standard model for cosmic ray environment assessment. It shall also be the standard for evaluation of single event effects from cosmic rays, from solar energetic particles and from energetic protons.

Figure 19 shows composite LET spectra for three CREME96 environments: the nominal solar minimum cosmic ray flux; the average flux for a “worst week” of a large SEPE; and the peak flux from a large SEPE. Three orbital situations, with different geomagnetic shielding, are shown: geostationary (which also applies to high altitudes and interplanetary), a polar orbit (900 km) and LEO (28°, 450 km). Ions from $Z = 1$ to $Z = 92$ shall be included and, in the absence of a reason to use another value, shielding of 1 g/cm^2 aluminium shall be assumed.

9.3.3.2 Directionality

Fluxes and fluences of solar energetic particles shall be assumed to be isotropic in interplanetary space. This is not true in near-Earth space due to geomagnetic shielding (see subclause 9.3.4).

9.3.4 Geomagnetic shielding

The Earth magnetic field partially shields near-Earth space from solar energetic particles and cosmic rays, an effect known as geomagnetic shielding. However, these particles can easily reach polar regions and high altitudes such as the geo-

stationary orbit. Geomagnetic shielding of protons is computed on the basis of the trajectory in geomagnetic B, L space (see clause 5).

At a given location in the field there are minimum cut-off energies necessary for ions to penetrate to that point. Størmer's theory gives a cut-off rigidity, P_c , for particle arrival at a point, depending on the point's geomagnetic R, λ coordinates and the angle of ion arrival from east, γ [RD9.24]:

$$P_c = \frac{\{M \cos^4 \lambda\}}{\{R^2[1 + (1 - \cos^3(\lambda) \cos(\gamma))^{1/2}]^2\}}$$

M is the normalized dipole moment of the Earth. From this equation, it can be seen that cosmic rays penetrate the geomagnetic field more easily from the west ($\gamma = 180^\circ$) than from the east ($\gamma = 0$). The R, λ coordinates can be computed from B and L according to the method of Roberts [RD9.25]. For vertical arrival, the expression simplifies to:

$$P_c \sim = \frac{16 \cos^4(\lambda)}{R^2} = \frac{16}{L^2} \text{ GV, since } \gamma = 90^\circ \text{ and } R = L \cos^2(\lambda)$$

An approximate value of 16 for the constant $M/4$ is used to fit with observed effective cut-offs. Magnetospheric disturbances, which often follow solar-flares or CMEs, can result in a lowering of cut-off; this has been described by Adams et al. [RD9.24] as:

$$\frac{\Delta P_c}{P_c} = 0,54 \exp\left(-\frac{P_c}{2,9}\right) \text{ with } P_c \text{ in units of GV.}$$

Stassinopoulos and King [RD9.26] developed a model which has total cut-off at $L = 5$. It assumes that no protons can penetrate to lower values. It can be shown that this model corresponds to a quiet magnetosphere vertical cut-off model excluding protons of $E < 200$ MeV from $L < 5$ Earth-radii. This model is adequate for most cases. However, in reality protons of lower energy can penetrate below $L = 5$ with non-vertical arrival directions, especially in a disturbed magnetosphere where the geomagnetic shielding is weakened. For westward arrival at the $L = 5$ geomagnetic equator in a disturbed magnetosphere, the energy cut-off can be as low 30 MeV.

For engineering purposes, geomagnetic cut-off shall not be applied to orbits spending more than 50 % of the orbit period above $L = 5$. Geomagnetic cut-off shall always be applied to orbits spending more than 75 % of their time below $L = 5$.

9.3.5 Spacecraft secondary radiation

For engineering purposes it is often only electron-induced bremsstrahlung radiation that is considered as a significant secondary source. In special cases other secondaries shall be considered.

In evaluating the radiation background effects in detector systems, it is often secondary radiation that is important. Because of heavy shielding removing primaries, veto systems which actively protect against counting primary-induced signals, or secondary radiation generated within the sensing band of an instrument. Most secondary radiation is emitted at the instant of interaction ("prompt") while some is emitted some time after a nucleus has been excited by an incoming particle (induced radioactivity).

In manned missions, secondary neutrons and other products can be important contributors to the radiological hazard.

By its nature, secondary radiation shall be analysed on a case-by-case basis, possibly through Monte-Carlo simulation. For engineering estimates of bremsstrahlung, the SHIELDOSE model shall be used (see subclause 9.4.2).

9.3.6 Neutrons

A low-level flux of neutrons of between $0,5 \text{ cm}^2 \text{ s}^{-1}$ and $4 \text{ cm}^2 \text{ s}^{-1}$ is present at low altitudes due to cosmic ray interactions with the atmosphere. Neutrons are also generated by energetic particles undergoing nuclear interactions with the material of spacecraft. These neutrons shall be considered for manned missions. They also play a role in generating background in sensitive detector systems.

9.4 Analysis methods for derived quantities

9.4.1 General

The following analysis methods shall be used.

The environment models specified in 9.3 shall be used to generate the primary data described in subclause 9.2. The secondary data shall be derived as specified below:

9.4.2 Ionizing dose

The ionizing dose environment is represented by the dose-depth curve. This can provide dose as a function of shield thickness in planar geometry or as a function of spherical shielding about a point. The planar model is appropriate for surface materials or for locations near to a planar surface. In general, electronic components are not in such locations and a spherical model is recommended for general specification.

The SHIELDOSE model shall be used [RD9.27] for ionizing doses. Alternatively, a method which has been validated with respect to SHIELDOSE may be used. This method uses a pre-computed dataset of doses from electrons, electron-induced bremsstrahlung and protons, as derived from Monte-Carlo analysis. The doses are provided as functions of material shielding and incident electron and proton energy. The actual spectrum is folded with this data-set to yield the dose at a given depth, d :

$$D(d) = \sum_E f(E) D(E, d) \Delta E$$

Figure 20 shows this data-set. A computerized version of this procedure is available as described in annex G.

The reference geometrical configuration for the dose-depth curve shall be a solid aluminium sphere. The SHIELDOSE dataset represents a planar medium and the conversion is performed as follows [RD9.27]:

$$D_{\text{sphere}} = 2D_{\text{plane}} \left\{ 1 - \frac{d(\log D_{\text{plane}})}{d(\log(d))} \right\}$$

This conversion is included in the computer version.

In cases where more careful analysis of the shielding of a component or other sensitive location is necessary, a sectoring calculation is often performed. This can be necessary if the doses computed from simple spherical shielding are incompatible with the specification of the allowable radiation dose. The sectoring method traces rays through the shielding in a large number of directions. Along each direction the derived shielding, together with the data on dose as a function of shielding depth, d , is used to find the omnidirectional 4π dose contribution, $D_i(d)$, from each direction, i . The contributions, weighted by the solid angle increment around the rays, Ω_i , are then summed:

$$D_{\text{tot}} = \sum_i \left(\frac{\Omega_i}{4\pi} \right) D_i(d)$$

If this procedure is used, it shall employ the spherical model for the dose-depth curve.

In some cases, it is efficient to derive a shielding distribution. This is the result of the ray-tracing described above and provides the distribution of encountered shielding $p(d)$. This distribution can be folded with the dose depth curve to derive the total dose. The advantage of this method is that various dose calculations can be efficiently performed for one geometry as represented by the shielding distribution.

It is important to recognize that a shielding analysis in the presence of significant anisotropies (e.g. as in 9.3.1.3) in the environment can result in serious error if the environment is assumed to be isotropic. This assumption is implicit in the sectoring method defined above since all directional contributions are derived from a common “omnidirectional” dose-depth curve.

9.4.3 Reference orbital dose data

Figure 21 shows a summary of expected doses on circular equatorial orbits as a function of the orbit altitude, based on the standard models described in subclause 9.3. A spherical shield of 4 mm aluminium is assumed.

Figure 22 shows a summary of the doses expected for a selection of common orbit types, based on the standard models. A 1-year mission and spherical aluminium shielding of 4 mm radius is assumed. Dose from one years’ accumulated solar energetic protons is also shown, with a confidence level of 95 % that a higher dose is not seen. More details of the doses are given in Figure 23 in the form of doses as functions of the radius of the aluminium shielding.

9.4.4 Single-event upset rate

The CREME/CREME96 method shall be used [RD9.21, RD9.22]. It is possible to make upset rate predictions only when details of the device under consideration are known, particularly the critical charge and the sensitive volume dimensions. If a device is uncharacterized, tests shall be performed.

The test data shall show the normalized upset rate as a function of ion LET in the range 1 MeV cm²/mg to 100 MeV cm²/mg and as a function of proton energy in the range 20–100 MeV. These data shall be used to make an estimate of the upset rate from trapped protons and solar protons using the two-parameter Bendel method [RD9.28], and of upsets due to galactic and solar ions using the method of CREME/CREME96. This latter shall be modified to account for the non-ideal upset rate as a function of ion LET derived from component test data [RD9.29] (the so-called “IRPP” method) as described below. This method has been implemented in CREME96. CREME96 also includes the two-parameter Bendel method. Alternative methods which have been thoroughly validated with respect to these methods may be applied.

To compute an upset rate for an electronic device or a detector from the predicted fluxes, device characteristics shall be specified, particularly the size of the sensitive volume and the critical charge, or equivalently, critical energy E_c , in the volume which results in upset or registers as a “count”.

For SEUs resulting from direct ionization the rate is found by integrating over the composite differential ion LET (L) spectrum, $f(L)$, and the distribution of path-lengths (l) for the sensitive volume, $p(l)$ [RD9.21, RD9.29]:

$$U = \frac{S}{4} \int_{E_c/L_{max}}^{l_{max}} p(l) \int_{E_c/l}^{L_{max}} f(L) dL dl$$

which approaches $FS/4$ in a very sensitive detector (where E_c is very small, so all particles cause upset). S is the total surface area of the sensitive volume and F is the integral omnidirectional flux. Normally, for electronic components, the limiting solution does not apply and the integral shall be evaluated. The integration limits are set by the sensitive volume dimensions and the critical energy E_c ; E_c/L_{max} is the shortest path capable of supporting upset, l_{max} is the maximum

path length, E_c/l is the minimum particle LET necessary to cause upset on a path length l and L_{max} is the maximum LET of the spectrum. Predicted upset rates are very sensitive to the integration limits which are established through testing. This sensitivity is a result of the fact that particle fluxes in the environment are strong functions of LET. This form for the upset calculation assumes that above a unique critical charge, all bits, of equal size, are upset. Testing shows that in general the upset cross-section (σ , rate \times fluence) rises more gradually to a saturation cross-section, σ_0 , and a method of calculation accounting for this is to sum a step-wise set of differential upset-rate calculations:

$$U = \sum_i \left(\frac{\sigma_i}{\sigma_0} \right) \left(\frac{\Delta U}{\Delta L} \right)_i \Delta L = \sum_i \left(\frac{\sigma_i}{\sigma_0} \right) \Delta U_i$$

where each U_i is calculated using the respective (σ_i and L_i).

An estimate of the upset rate from nuclear interactions of energetic protons can be obtained by integration of the product of the measured proton-induced upset cross section $\sigma(E)$ and the differential proton flux $f(E)$ over all energies. $\sigma(E)$ can be derived directly from the test data, or the two-parameter Bendel fit can be used. Simulations of proton nuclear interactions can also be used to derive $\sigma(E)$, when data from heavy-ion testing is available to provide the critical charge and sensitive volume dimensions [RD9.28].

9.4.5 Solar cell degradation

The EQFRUX-Si or EQFRUX-Ga models shall be used for silicon and gallium arsenide solar cell degradation calculations, respectively [RD9.30]. In the absence of other test data, it shall be assumed that 10 MeV protons cause equivalent damage to 3000 1 MeV electrons in silicon cells. Similarly it shall be assumed for gallium arsenide cells that the damage equivalence of a 10 MeV proton is 400, 1000 and 1400 1 MeV electrons for short-circuit current, maximum power and open-circuit voltage degradation, respectively. Since the default in these models is the assumption of infinite rear-side shielding of cells, this shall be the standard way of reporting results. However, account shall then be explicitly taken of radiation penetration though the rear-side of solar arrays.

9.4.6 Internal electrostatic charging

Engineering methods for specifying derived parameters related to internal electrostatic charging are currently under development and are described in annex G. The flux of energetic electrons is clearly important, as are the energy spectrum and the duration of high-flux conditions. In addition, the “target” material plays a role and shielding of the target material obviously has a large effect.

9.4.7 Dose-equivalent

Dose equivalent calculation, for astronaut hazard estimation shall employ the quality factors defined in document RD9.5. For ions, the quality factor, Q , depends on the ion LET, L , as shown in Figure 24. Dose-equivalent is derived from:

$$D_{eq} = \sum D Q(L)$$

where the sum is over all energies and radiation types. Electrons and gamma-rays have Q of 1. Protons have a Q of between 1 and 5 (the latter because of the nuclear interaction effects). Neutrons have Q between 5 and 20, depending on energy [RD9.5].

9.4.8 Non-ionizing dose

Damage to CCDs and other electro-optical components susceptible to displacement damage shall employ the NIEL function, $N(E)$ [RD9.31], shown in Figure 25, to derive a 10 MeV equivalent proton damage fluence F_D :

$$F_D = \sum_E f(E) N_{10}(E) \Delta E$$

or a non-ionizing dose, D_N :

$$D_N = \sum_E f(E) N(E) \Delta E$$

where

$f(E)$ is the differential fluence spectrum;

$N(E)$ is the NIEL function;

$N_{10}(E)$ is the NIEL function normalized to 10 MeV;

ΔE is the energy step of the sum.

9.5 Tailoring guidelines: Orbital and mission regimes

9.5.1 General

In the following subclauses, attention is drawn to special considerations for various orbit types.

9.5.2 Geostationary orbit

Geostationary orbit is a circular orbit usually encountering an environment dominated by energetic electrons. This environment is characterized by strong time variations with many extended quiet periods of low radiation levels and many episodes of intense injections of energetic electrons which increase e.g. dose, sensor interference and electrostatic charging. Solar protons and cosmic rays have unrestricted access to this orbit. Solar particles make short-lived but important contributions to the total dose, interference and single event effects. They do not directly participate in charging processes. Cosmic rays provide a continuous source of single-event effects and sensor interference.

9.5.3 MEO, HEO

These orbits encounter the electron-dominated environment mentioned above, but in addition, encounter the inner, proton radiation belt. In such orbits, single-event effects from protons and proton non-ionizing damage need to be considered. These orbits often encounter more severe electron environments, near the peak of the electron belt (the location of which is also variable) than geostationary orbit and so electrostatic charging can be a more serious threat.

9.5.4 LEO

Current technology limits manned activities to low (< 550 km) and medium-inclination ($\sim 55^\circ$) orbits, however, this can improve in the future. We refer to these orbital regimes as LEO. Missions in these orbits encounter the inner edge of the radiation belt. This region is dominated by the South Atlantic anomaly. Also important is the strong asymmetry in fluxes from East and West. The low-altitude environment is characterized by high-energy radiation-belt trapped protons. The deflection of charged particles from outside the magnetosphere by the Earth magnetic field (geomagnetic shielding) reduces the fluxes of cosmic rays and solar energetic particles, but the shielding is not total. Like polar orbits, LEO orbits also encounter outer-belt trapped electrons at high-latitudes.

9.5.5 Polar

Polar orbits are generally of less than 1000 km altitude with inclinations above 80°. They encounter the inner proton and electron belts in the form of the South Atlantic anomaly and also the outer electron belt where the geomagnetic field lines bring it to low altitudes at “auroral” latitudes above about 50°. On the high-latitude parts of the orbit a spacecraft is exposed to almost unattenuated fluxes of cosmic rays and solar energetic particles. At low latitudes, geomagnetic shielding considerably reduces these fluxes.

9.5.6 Interplanetary and planetary environments

The interplanetary environment is characterized by cosmic rays and occasional solar energetic particle events. The variations in particle intensities with heliocentric radius and solar cycle modulation shall be considered. Missions to the giant planets shall consider their intense magnetospheres. Mercury also has a small magnetosphere. Science missions also take place at the Lagrangian points of the Sun-Earth system or Earth-Moon system. These locations can also be considered interplanetary from the point of view of the radiation environment.

9.6 Preparation of a radiation environment specification

A specification of the expected radiation environment of a space system shall be established at Phase A. The specification shall include:

- a. Unshielded mission-average proton and electron energy spectra from trapped radiation.
- b. The unshielded fluence spectrum of solar protons for the complete mission. Appropriate geomagnetic shielding shall be applied.
- c. Unshielded worst-case instantaneous energy spectra of trapped electrons, trapped protons and solar energetic protons (geomagnetically shielded) for the mission, for internal charging and sensor interference analysis.
- d. The ion LET spectrum for the appropriate solar cycle phase, together with a 10 % worst-case LET spectrum. A LET spectrum from a 10 % worst-case solar particle event with mean composition shall be included. The LET spectra shall include contributions from all ions from $Z = 1$ to $Z = 92$. Appropriate geomagnetic shielding shall be applied. Appropriate material shielding shall be applied. If no justification is available for another value, 1 g/cm^2 of aluminium shielding shall be used.
- e. A mission dose vs. shielding depth curve or table for dose at the centre of a solid aluminium sphere, including contributions from trapped electrons and protons, solar energetic protons and electron-induced bremsstrahlung.
- f. For manned missions, the above environment shall also be transformed into dose-equivalent.
- g. Damage-equivalent fluences of 1 MeV electrons and 10 MeV protons for solar cell damage estimates; this is generally possible for silicon and gallium arsenide cells as a function of cover-glass thickness, but should be revised for other technologies as a result of cell selection.
- h. NIEL (non-ionizing energy loss) 10 MeV equivalent fluences for CCD, optoelectronic and optical components as a function of spherical shielding depth.
- i. Orbital time-behaviour of radiation-belt, cosmic ray and solar energetic particle fluxes if the mission has a susceptibility to radiation background in sensors.
- j. Additions to the above environments from on-board nuclear sources.

The specification shall take account of the evolution of the mission orbit, either naturally or deliberately. This can have significant effects on radiation-belt exposure (e.g. due to natural perigee rise and apogee fall).

Operations which result in geo-synchronization of the orbit shall be considered (e.g. geostationary, apogee longitude maintenance of near-synchronous HEO orbits). In such missions radiation belt exposures are not averaged out.

9.7 Figures

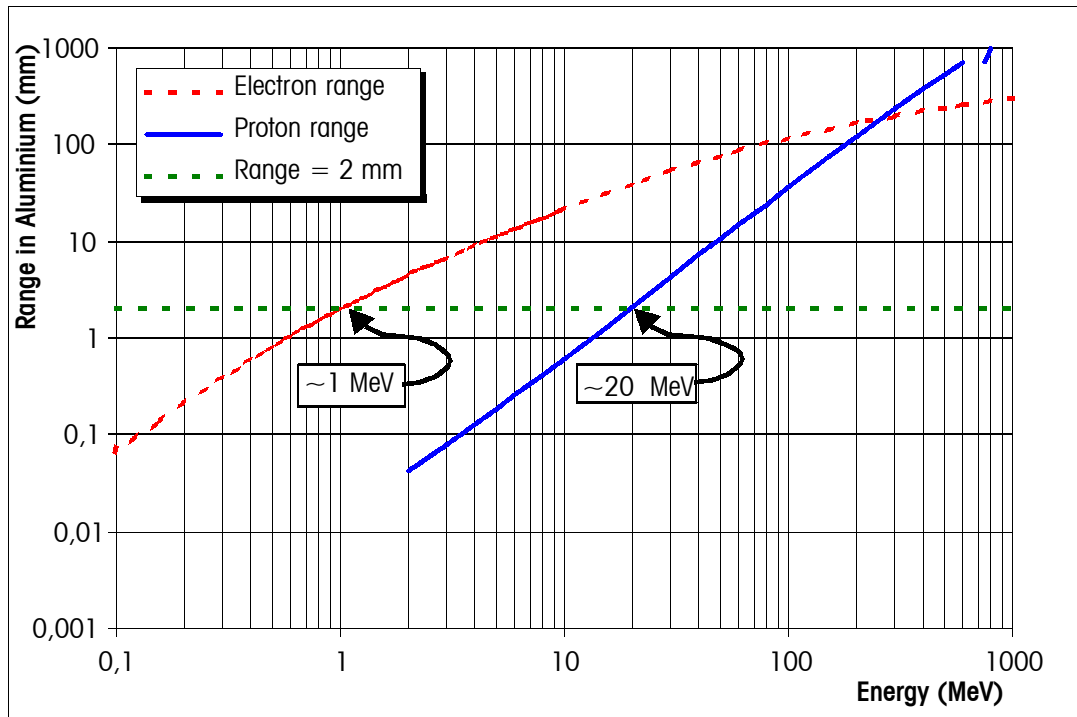
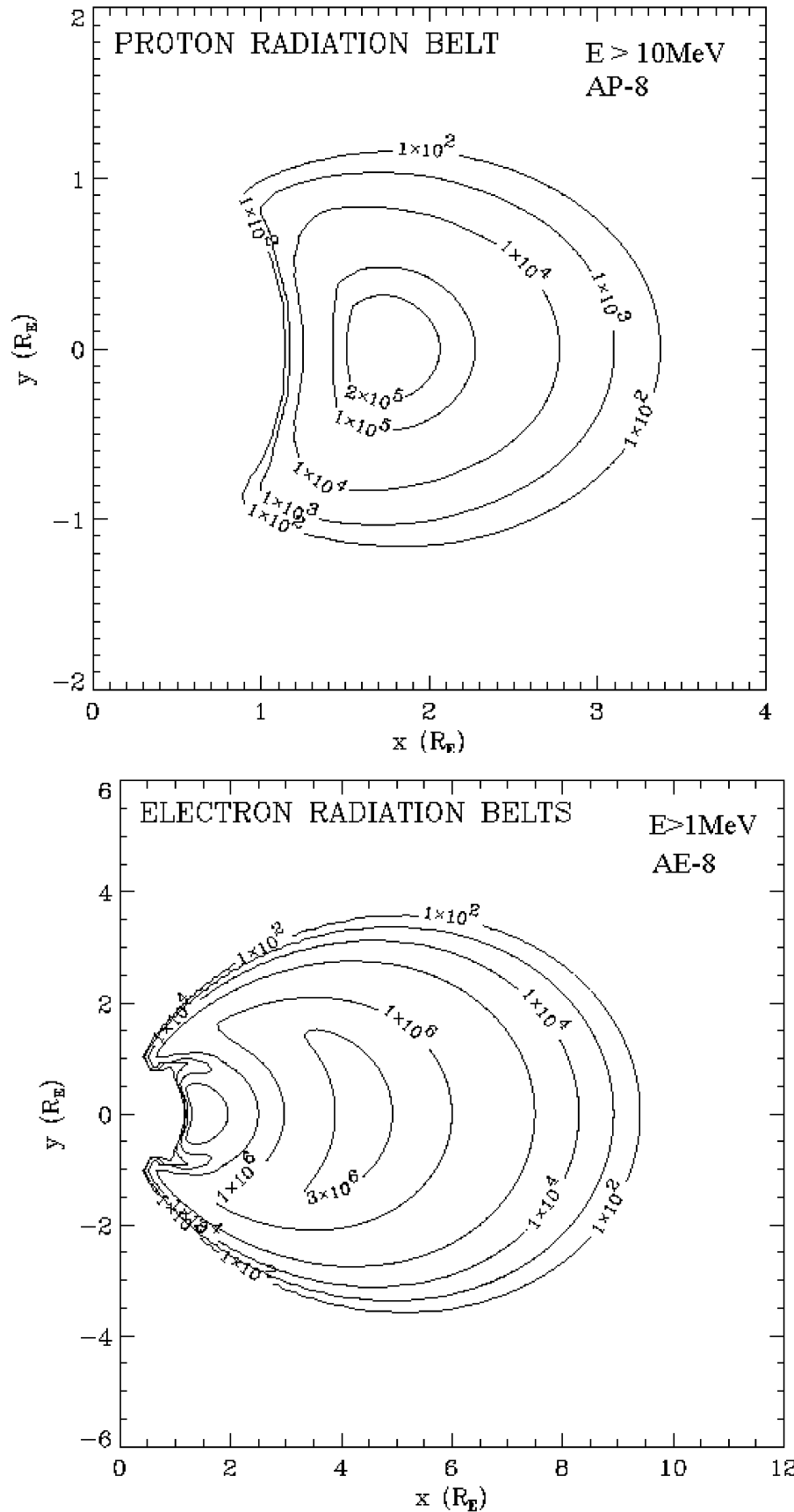


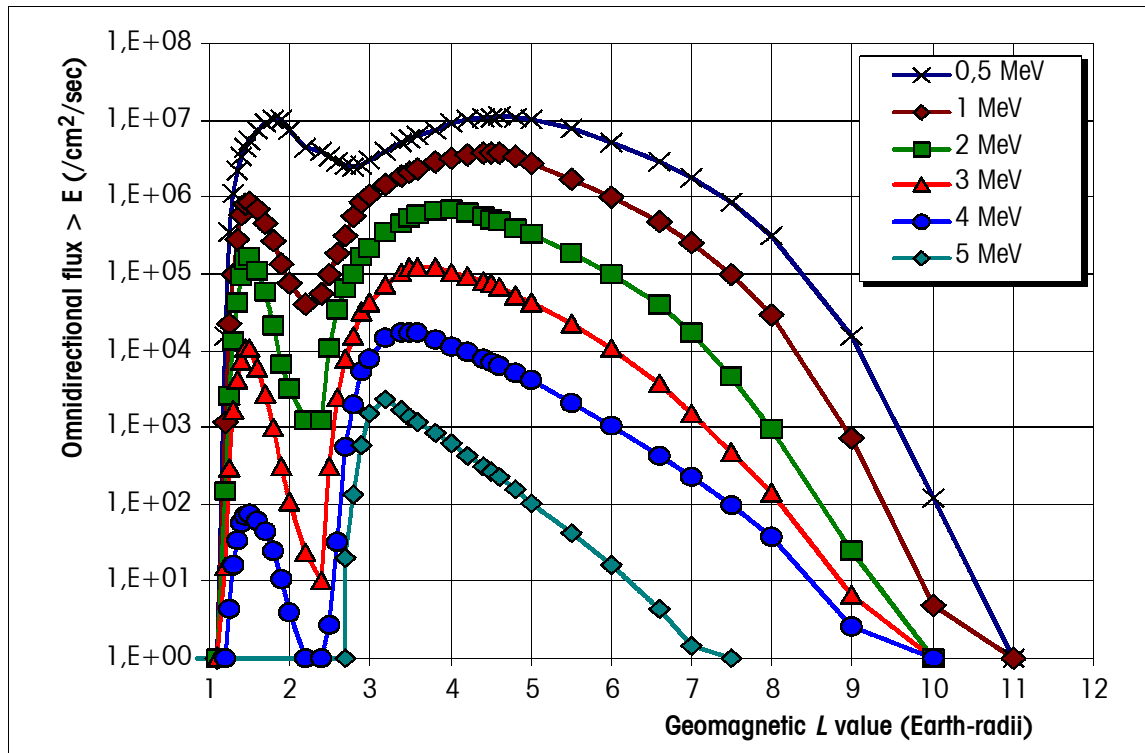
Figure 13: Mean ranges of protons and electrons in aluminium



Omnidirectional fluxes are for particles $>1 \text{ MeV}$ and $>10 \text{ MeV}$, respectively. The data are derived from the AE-8 and AP-8 models, respectively, and are shown in an ideal dipole representation of the Earth field.

Figure 14: Contour plots of the electron and proton radiation belts

(a) Electron



(b) Proton

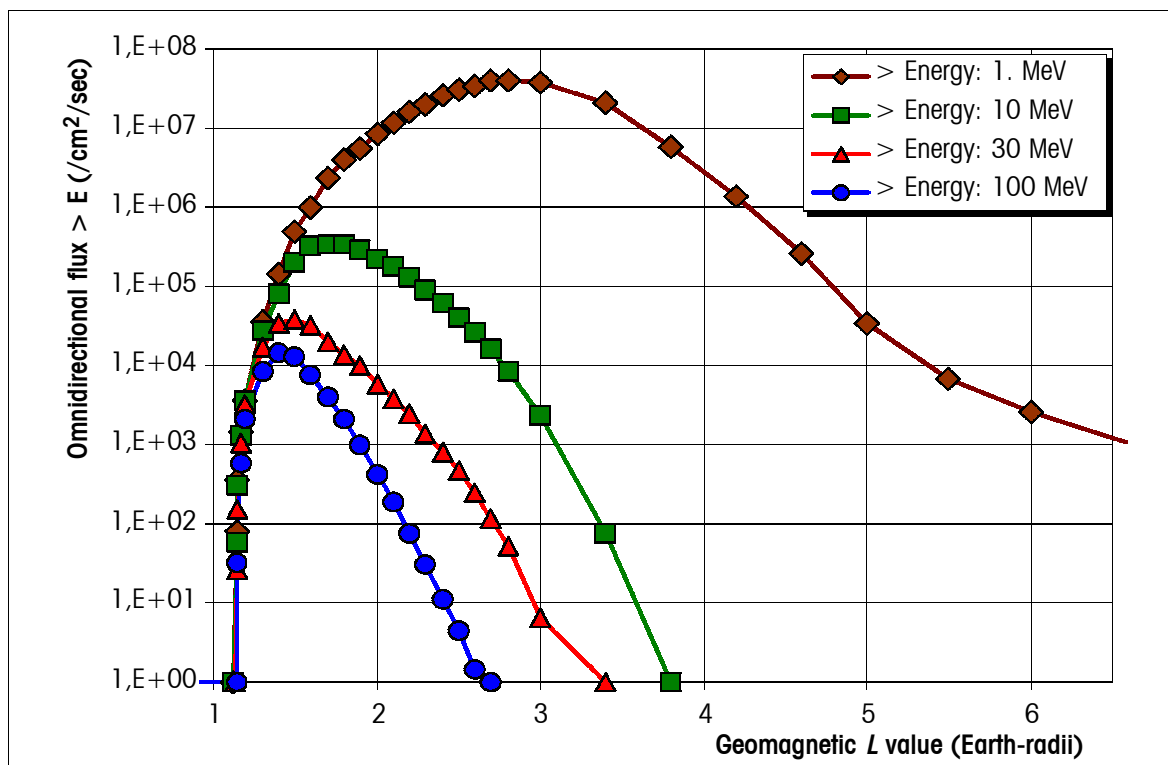


Figure 15: Electron (a) and proton (b) omnidirectional fluxes, integral in energy, on the geomagnetic equator for various energy thresholds

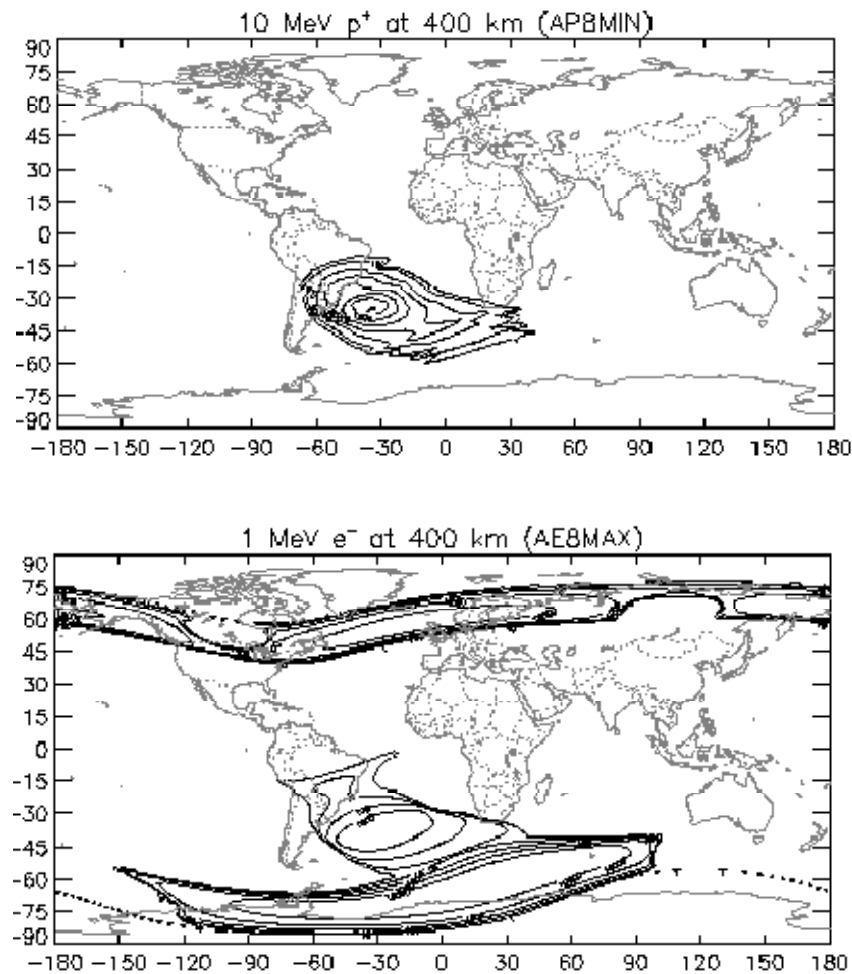
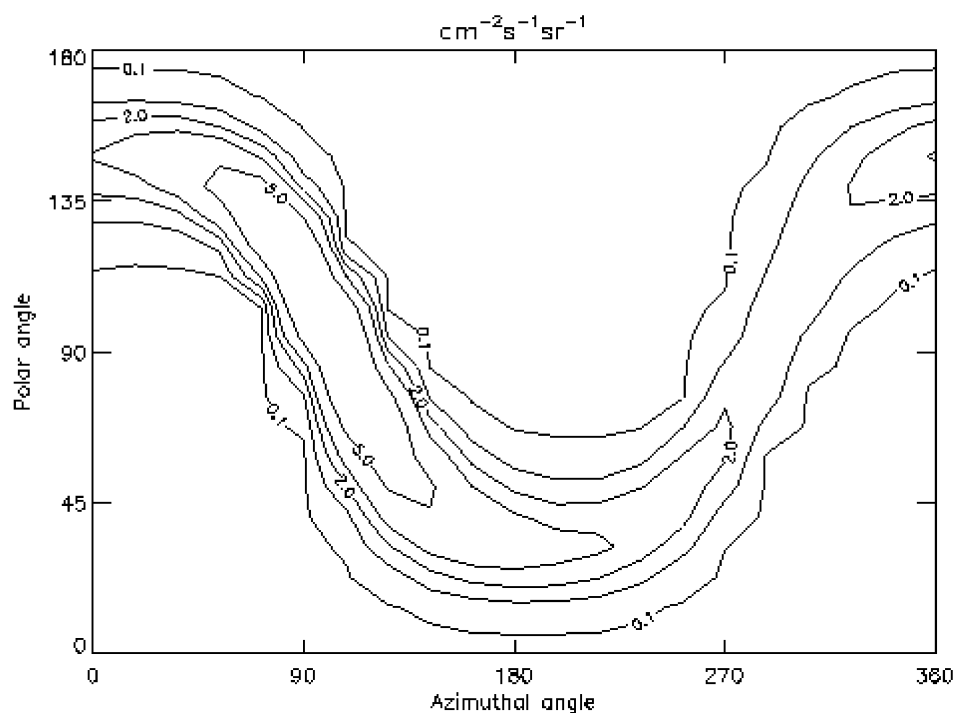


Figure 16: Integral omnidirectional fluxes of protons (>10 MeV) and electrons (>1 MeV) at 400 km altitude showing the inner radiation belt's "South Atlantic anomaly" and, in the case of electrons, the outer radiation belt encountered at high latitudes



Polar and azimuthal angles are with respect to Zenith and North respectively.
(Therefore the horizontal plane has polar angle 90°, and westward viewing
has azimuthal angle 90°.)

Figure 17: The flux anisotropy in low Earth orbit averaged over an orbit of the space station for protons >100 MeV energy

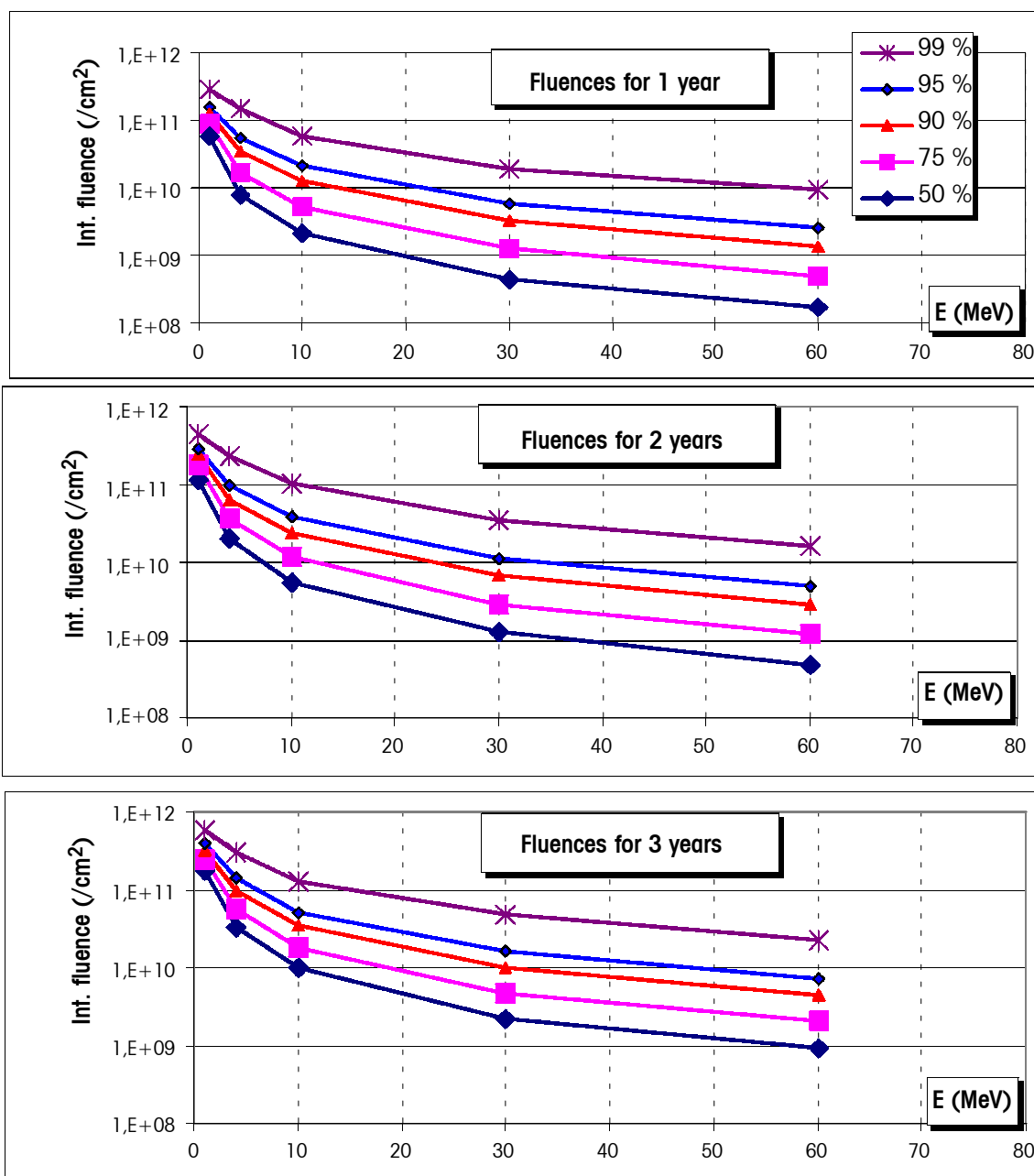


Figure 18: Solar proton fluence spectra for various statistical confidence levels (99 %, 95 %, 90 %, 75 % and 50 %, from top to bottom in each panel) for various mission durations (data from JPL-1991 Model)

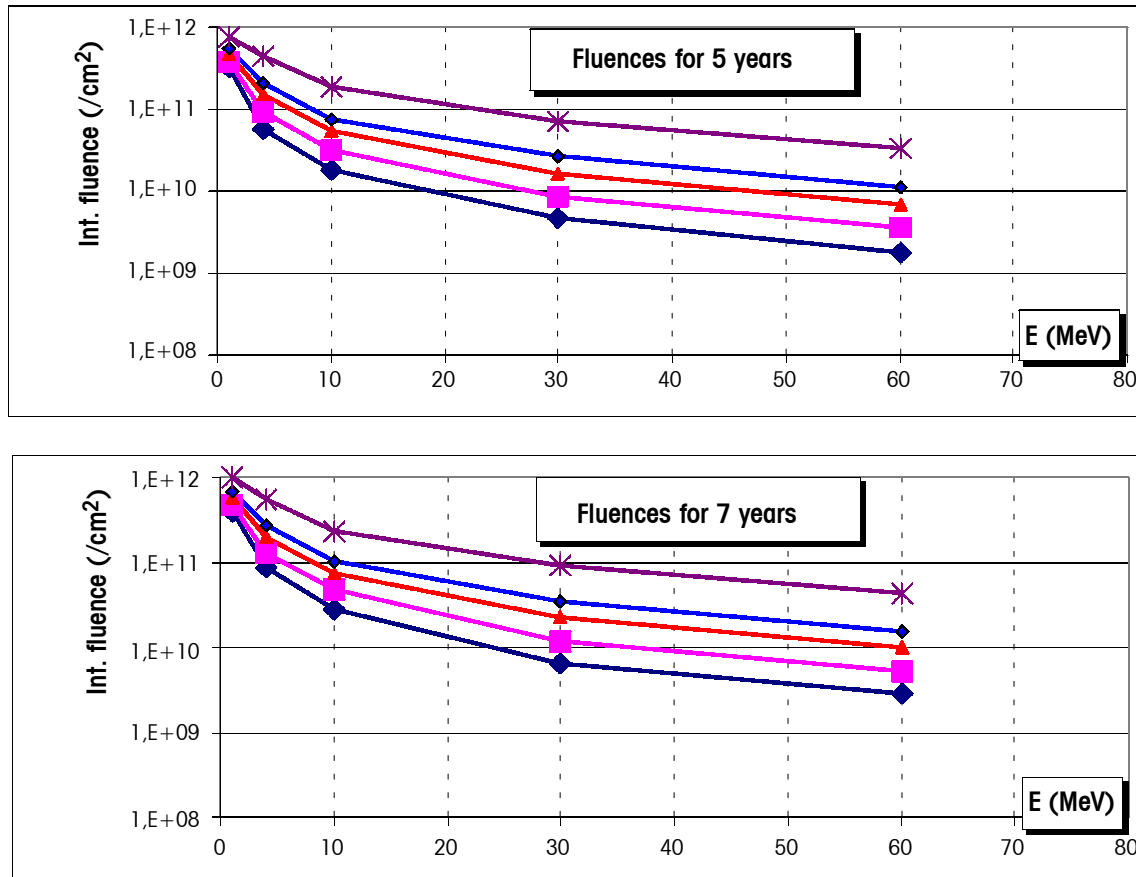


Figure 18: Solar proton fluence spectra for various statistical confidence levels (99 %, 95 %, 90 %, 75 % and 50 %, from top to bottom in each panel) for various mission durations (data from JPL-1991 Model) (*continued*)

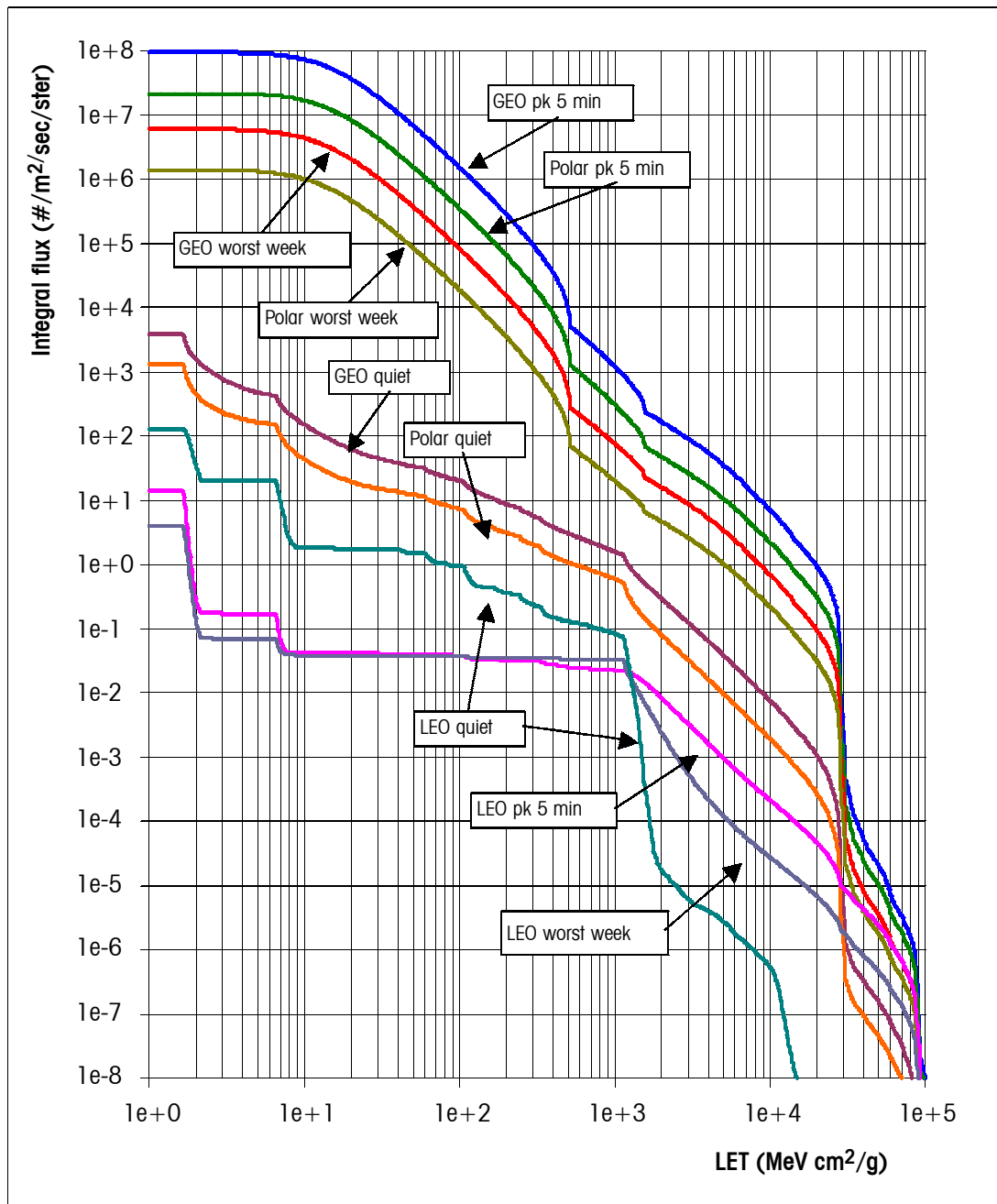


Figure 19: Cosmic ray LET spectra for typical missions

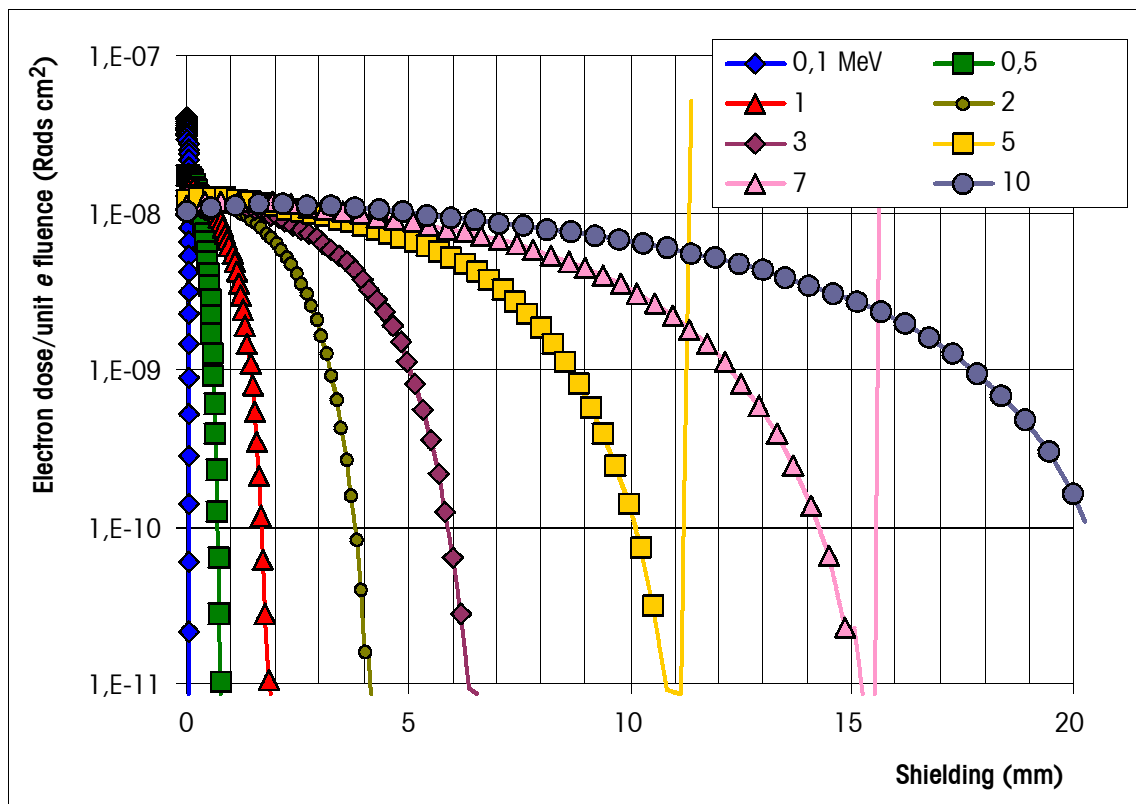
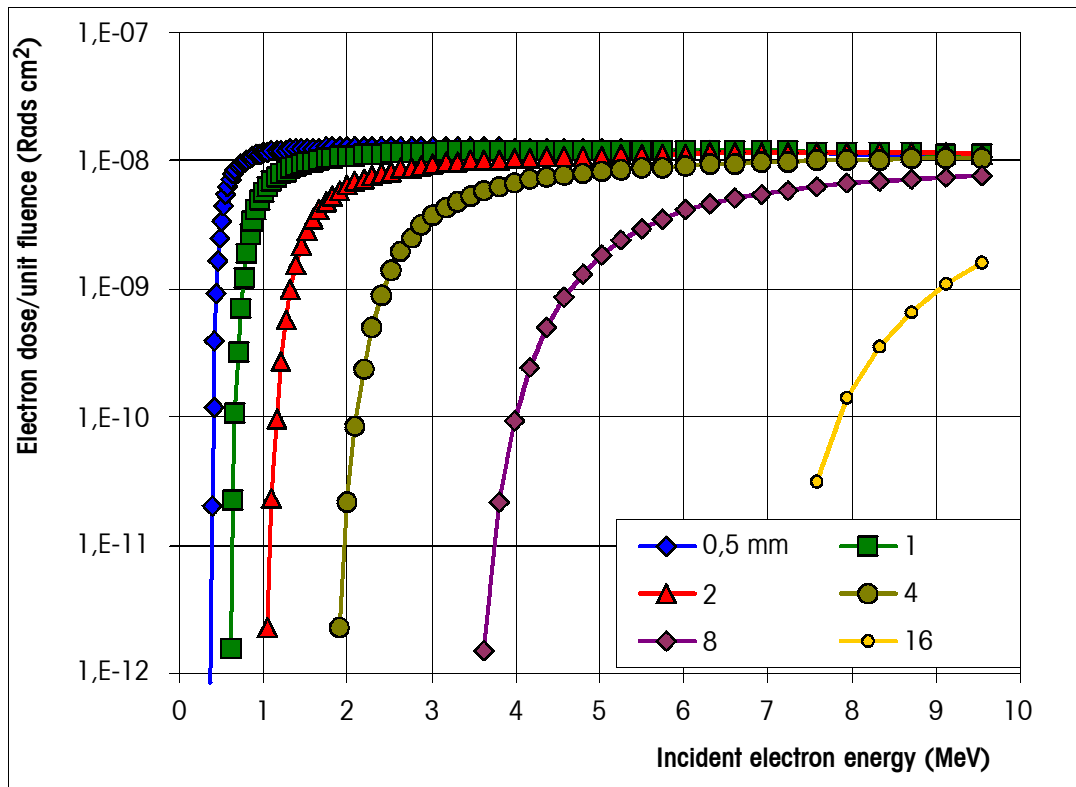


Figure 20: SHIELDOSE dataset for computing doses for arbitrary spectra:
(a) Electron doses as a function of energy and depth

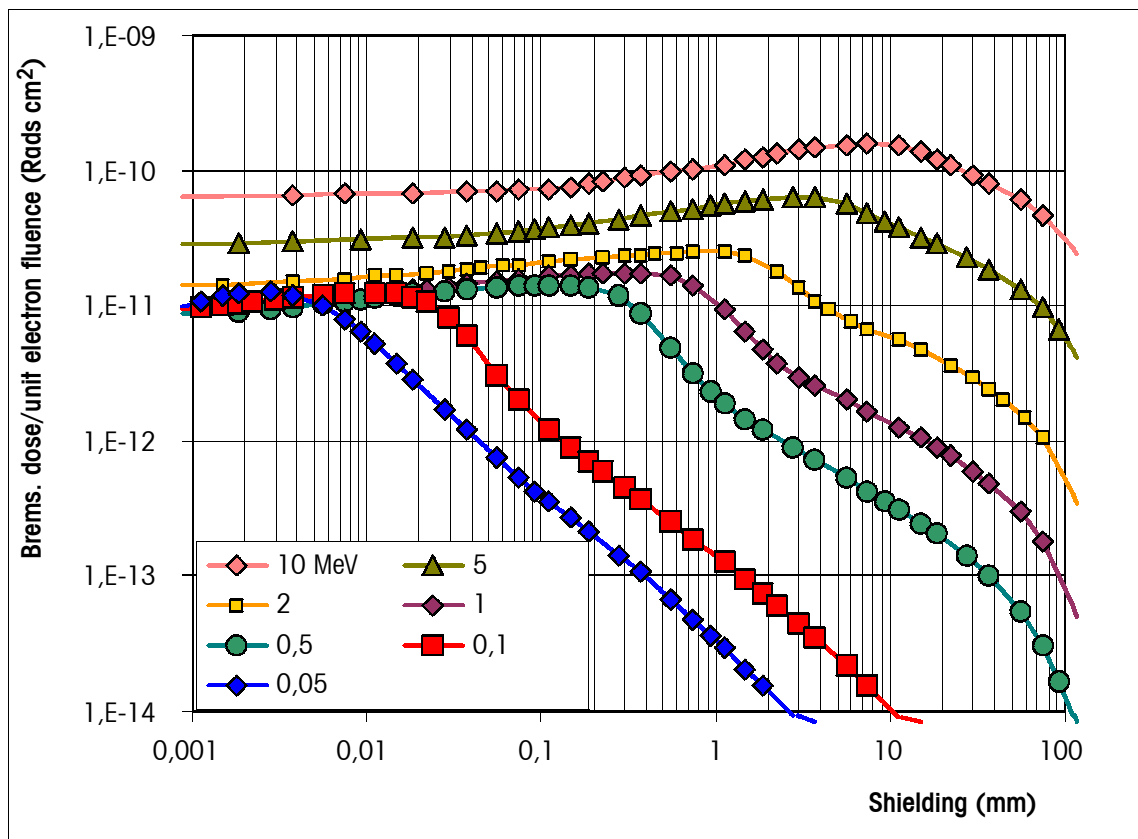
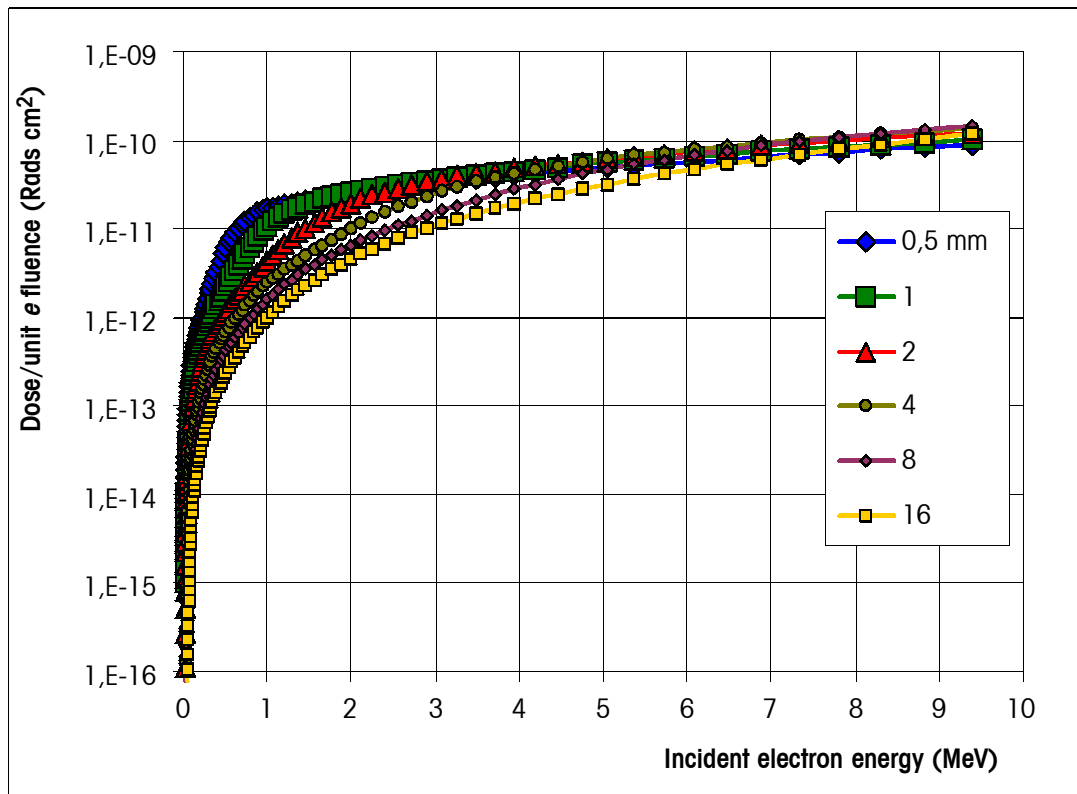


Figure 20 (continued): (b) Bremsstrahlung doses as a function of energy and depth

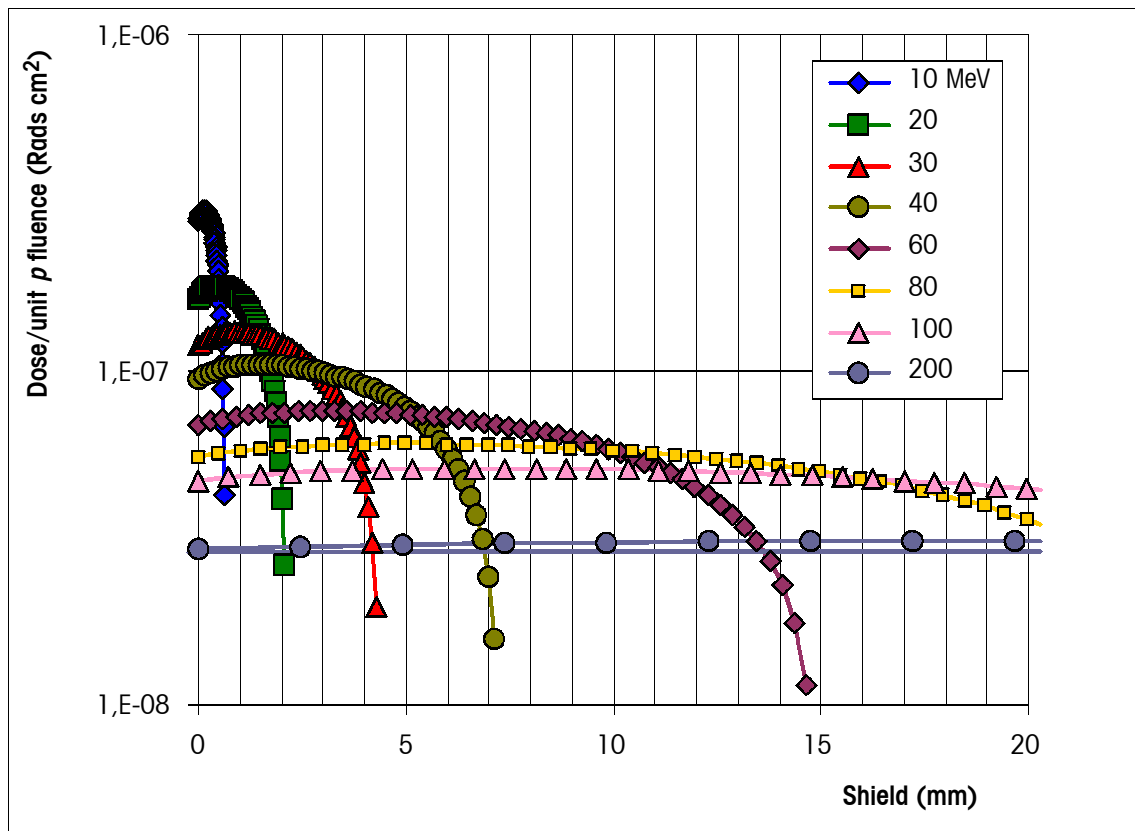
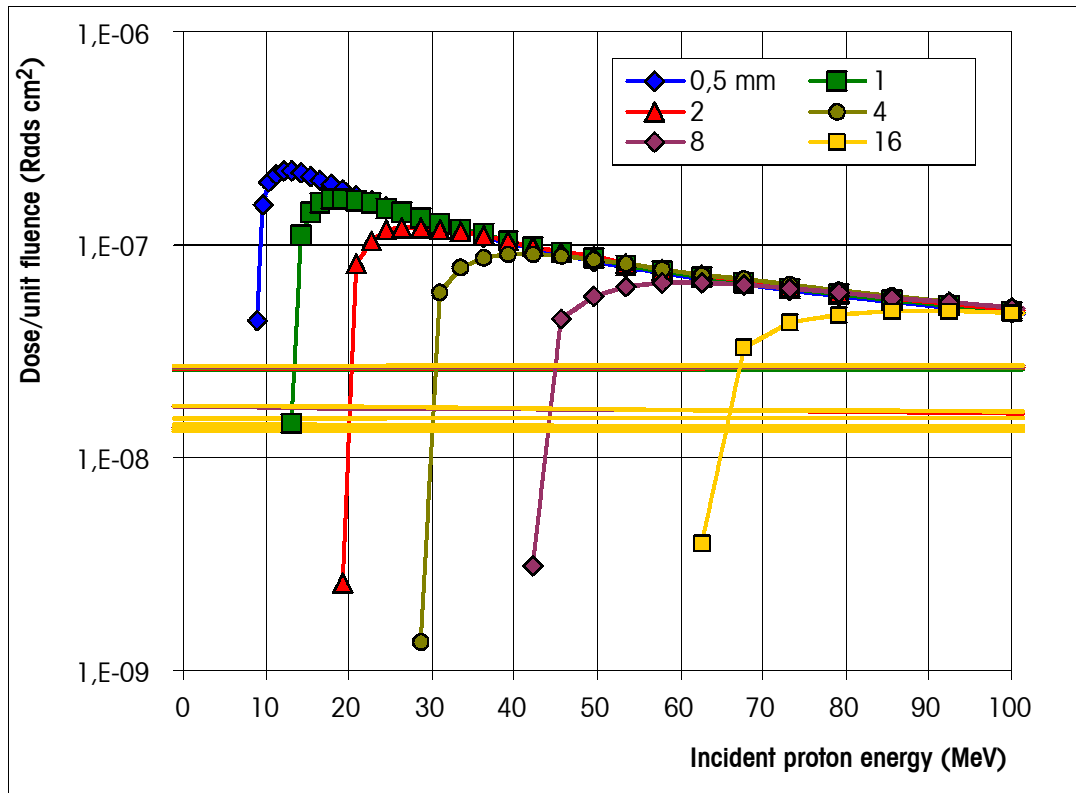


Figure 20 (continued): (c) Proton doses as a function of energy and depth

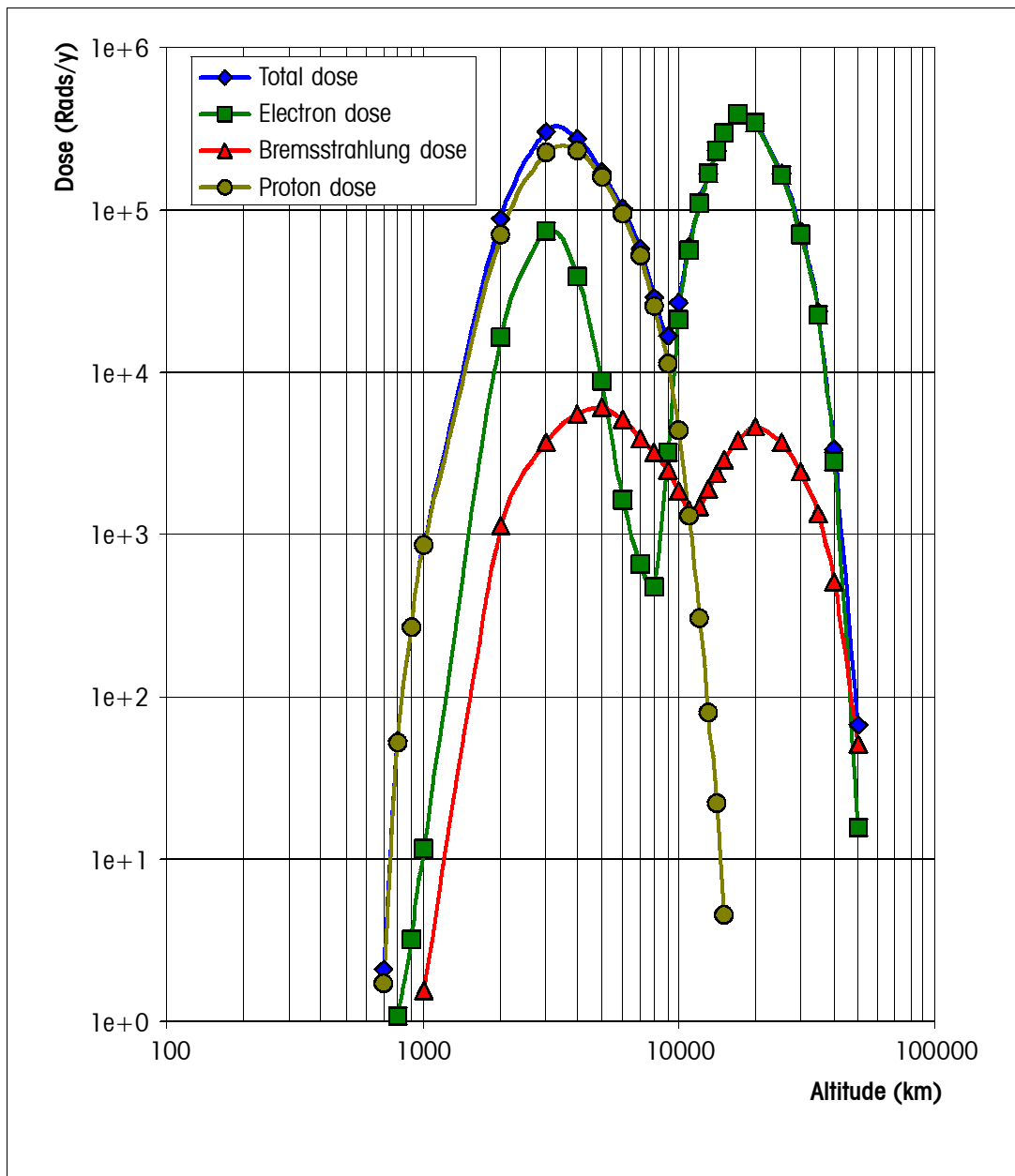


Figure 21: Annual doses behind 4 mm spherical shielding on circular equatorial orbits in the radiation belts, as a function of orbit height

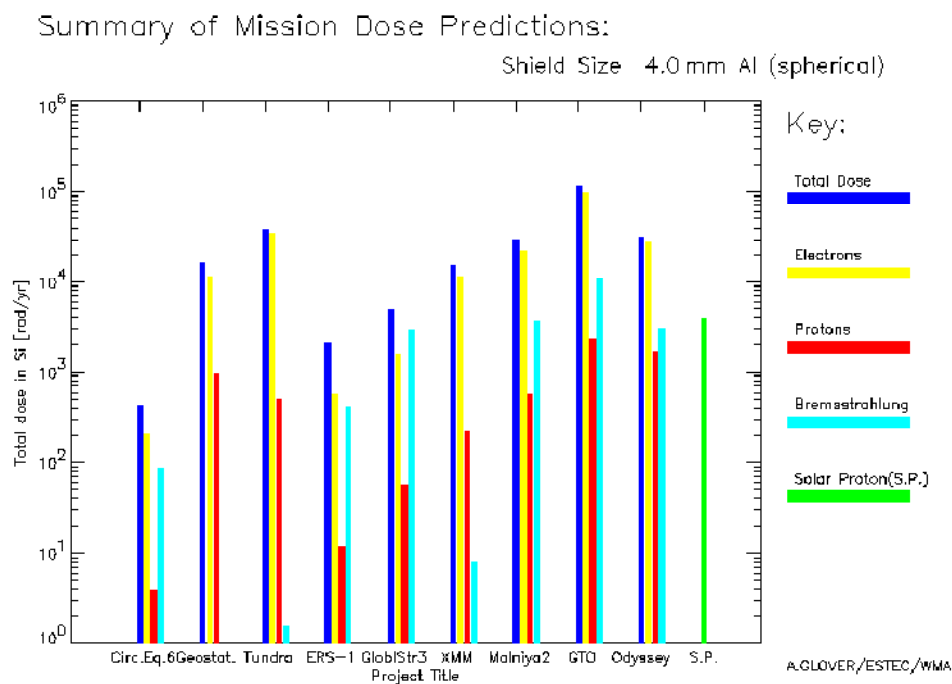
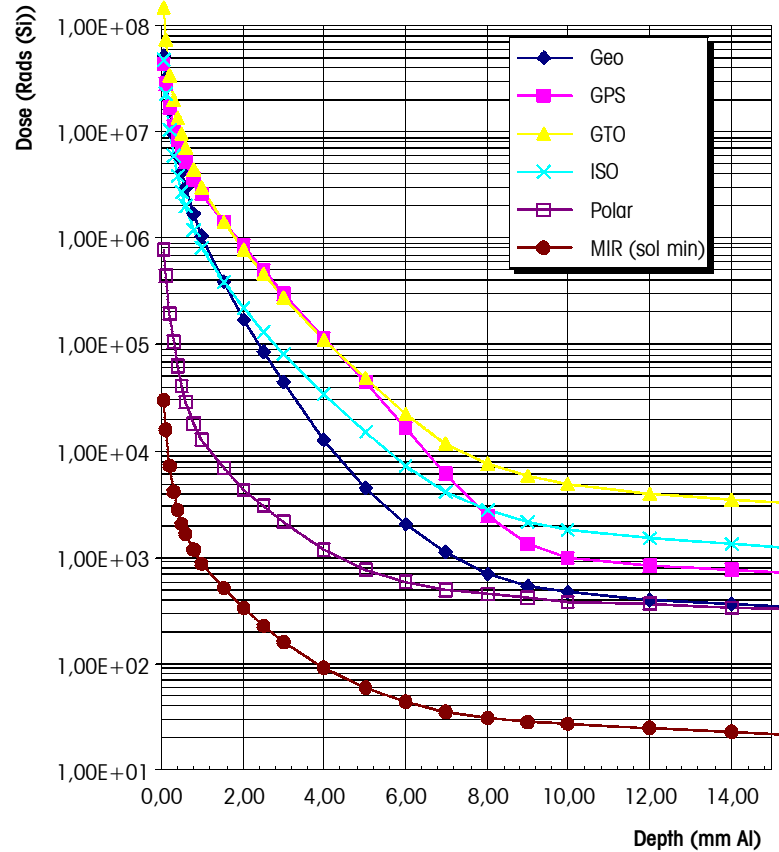


Figure 22: Typical doses predicted for typical missions

Typical annual mission doses (spherical Al shield)



Solar proton doses (1 y, 95 %)

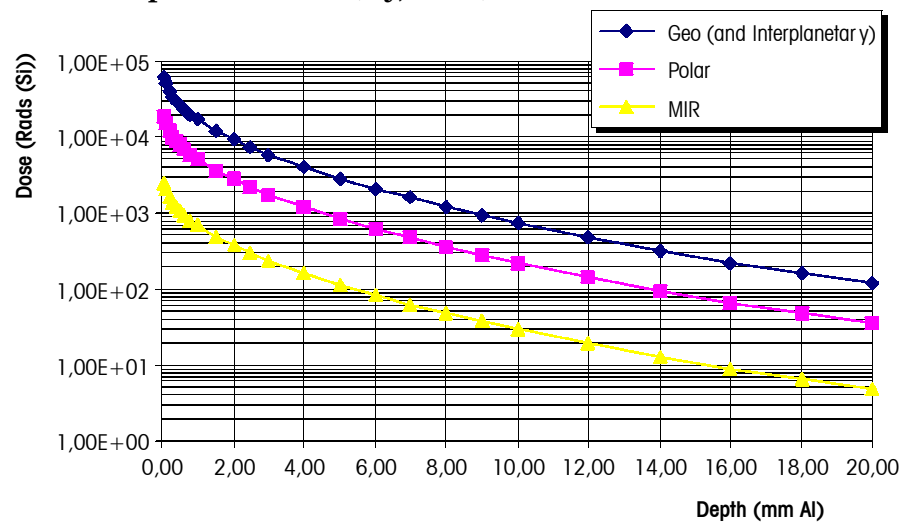


Figure 23: Typical dose-depth curves for Earth-orbits

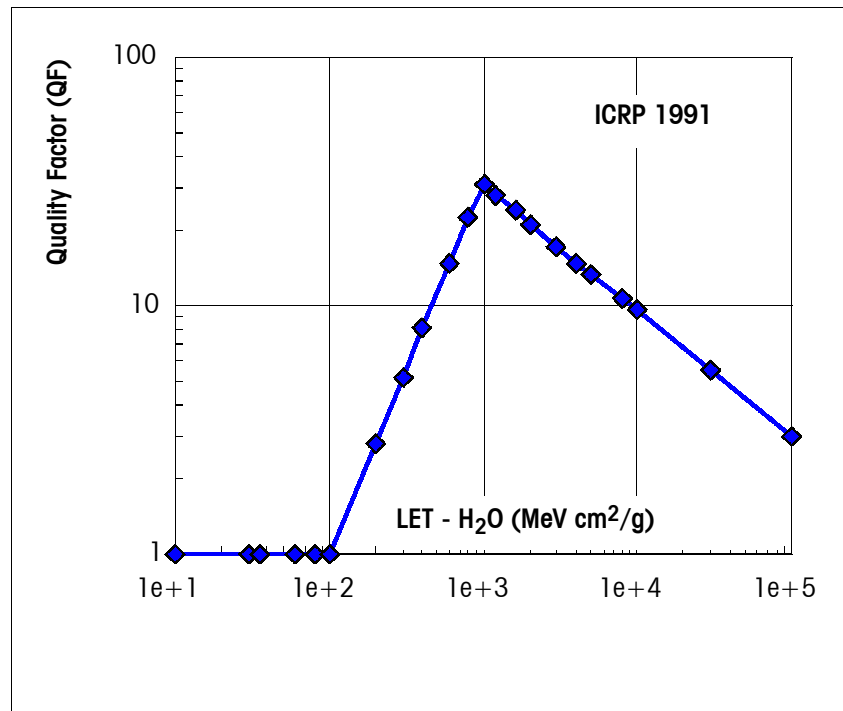


Figure 24: Quality factors for use in dose equivalent calculations for radio-biological effect purposes, as defined by the *ICRP*

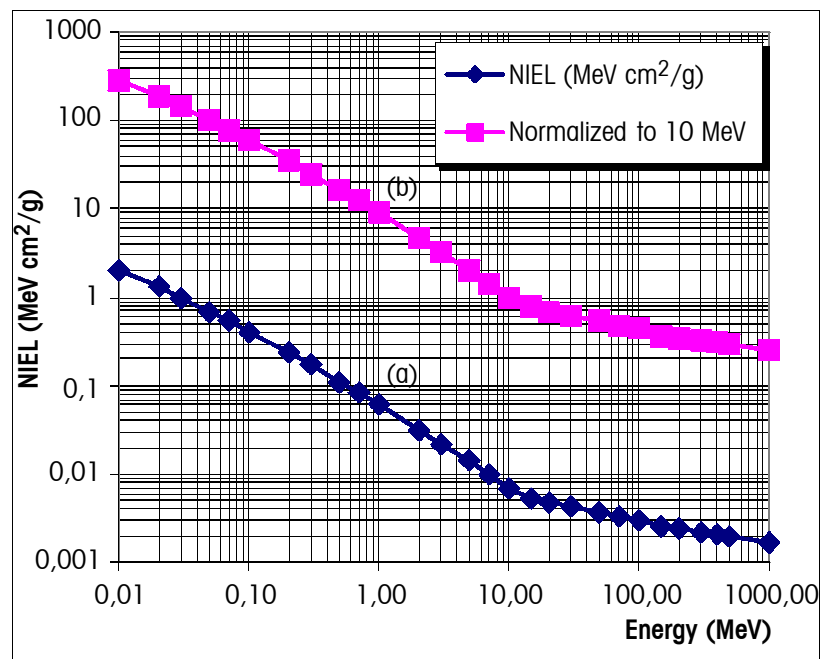


Figure 25: The NIEL curve: (a) energy lost by protons in non-ionizing interactions (bulk, displacement damage); (b) NIEL relative to 10 MeV giving damage-equivalence of other energies

9.8 References

- RD9.1 Hess W.N., "The Radiation Belt and Magnetosphere", Blaisdell Publ. Co., 1968.
- RD9.2 Daly, E.J., "The Radiation Belts", Radiation Physics and Chemistry 43, 1, pp.1-18 (in Special Issue on Space Radiation Environment and Effects), 1994.
- RD9.3 NCRP, "Guidance on Radiation Received in Space Activities", Report NCRP-98, National Council on Radiation Protection and Measurements, ISBN 0-929600-04-5, July 1989.
- RD9.4 ECSS, "Human Factors Standard", ECSS-E-TBD.
- RD9.5 ICRP, "1990 Recommendations of the International Commission on Radiological Protection", ICRP Publication 60, Annals of the ICRP 21, 1-3 ISBN: 0-08-041144-4, Pergamon Press, NY and Oxford, 1991.
- RD9.6 Vette J.I., "The AE-8 Trapped Electron Model Environment", NSSDC/WDC-A-R&S Report 91-24, NASA-GSFC, 1991.
- RD9.7 Sawyer D.M. and J.I. Vette, "AP8 Trapped Proton Environment For Solar Maximum and Solar Minimum", NSSDC WDC-A-R&S 76-06, NASA-GSFC, 1976.
- RD9.8 Belian, R.D., T.E. Cayton, R.A. Christensen, J.C. Ingraham, M.M. Meier, G.D. Reeves and A.J. Lazarus, "Relativistic electrons in the outer-zone: An 11-year cycle; their relation to the solar wind", Proceedings of the Taos Workshop on the Earth's Trapped Particle Environment, Ed, G.D. Reeves, AIP Conference Proceedings 383, 13-18, ISBN 1-56396-540-2, 1986.
- RD9.9 Watts J.W., T.A. Parnell and H.H. Heckman, "Approximate Angular Distribution and Spectra for Geomagnetically Trapped Protons in Low-Earth Orbit", in "High-Energy Radiation Background in Space", AIP Conference Proceedings 186, AIP, NewYork, 1989.
- RD9.10 Kruglanski M. and J. Lemaire, "Trapped Proton Anisotropy at Low Altitude", Technical Note 6, ESA/ESTEC/WMA Contr. 10725, Institut d'Aeronomie Spatiale de Belgique, 1996.
- RD9.11 Bühler P., A. Zehnder, E. Daly and L. Adams, "REM Measurements on-Board MIR in 1995", Cospar General Assembly 1996, to appear in Adv. Sp. Res., 1997-1998.
- RD9.12 Lemaire J., A.D. Johnstone, D. Heynderickx, D.J. Rodgers, S. Szita and V. Pierrard, "Trapped Radiation Environment Model Development (TREND-2)" Final Report of ESA Contr. 9828, Aeronomica Acta 393-1995, Institut d'Aeronomie Spatiale de Belgique/Belgisch Instituut voor Ruimte-Aeonomie, ISSN 0065-3713, 1995.
- RD9.13 Brautigam D.H., M.S. Gussenhoven and E.G. Mullen, "Quasi-Static Model of Outer Zone Electrons", IEEE Trans. Nucl. Sci. NS-39, 1797, 1992.
- RD9.14 Singley G.W. and I. Vette J.I., "The AE-4 Model of the Outer Radiation Zone Electron Environment", NSSDC/WDC-A-R&S 72-06, NASA-GSFC, 1972.
- RD9.15 Tranquille C, "Extension to AE-4 Local Time and Statistical Models for Application to AE-8", ESTEC/WMA Internal Memorandum, 1986.
- RD9.16 Feynman J., G. Spitale, J. Wang and S. Gabriel, "Interplanetary Proton Fluence Model: JPL 1991", J. Geophys. Res. 98, A8, 13281-13294, 1993.
- RD9.17 Tranquille C. and E.J. Daly, "An Evaluation of Solar Proton Event Models for ESA Missions", ESA J. 16, 275, 1992.
- RD9.18 King, J.H., "Solar Proton Fluences for 1977-1983 Space Missions", J. Spacecrafts and Rockets, 11, 401, 1974.
- RD9.19 Mathews J. and S. Towheed, OMNIWeb, <http://nssdc.gsfc.nasa.gov/omniweb/> mathews@nssdc.gsfc.nasa.gov, Code 633, NASA GSFC, Greenbelt, MD 20771, USA.

- RD9.20 National Geophysical Data Center, "Space Environment Data from NOAA's GOES Satellites", National Geophysical Data Center, Code E/GC2, Dept. 946 325 Broadway Boulder Co 80303 3328 USA., also Space Physics Interactive Data Resource at <http://www.ngdc.noaa.gov:8080/>.
- RD9.21 Adams, J.H., "Cosmic Ray Effects on MicroElectronics, Part IV", NRL Memorandum Report 5901, Naval Research Laboratory, Washington DC 20375-5000, USA, 1986.
- RD9.22 Tylka, A.J., et al., "CREME96: A Revision of the Cosmic Ray Effects on Micro-Electronics Code", IEEE Trans. Nucl. Sci. NS-44, 2150-2160, 1997.
- RD9.23 Nymmik, R.A., M.I. Panasyuk, T. I. Pervaja, and A.A. Suslov, "A Model of Galactic Cosmic Ray Fluxes", by, Nucl. Tracks & Radiat. Meas, 20, 427-429, 1992.
- RD9.24 Adams J.H., R. Silberberg and C.H. Tsao, "Cosmic Ray Effects on Microelectronics, Part I: The Near-Earth Particle Environment", NRL Memorandum Report 4506, Naval Research Laboratory, Washington DC 20375-5000, USA, 1981.
- RD9.25 Roberts C.S., "Co-ordinates for the Study of Particles Trapped in the Earth's Magnetic Field: A Method of Converting from B, L to R, λ Co-ordinates", J. Geophys. Res. 69, 5089, 1964.
- RD9.26 Stassinopoulos E.G. and J.H. King, "Empirical Solar Proton Model For Orbiting Spacecraft Applications", IEEE Trans. on Aerosp. and Elect. Systems AES-10, 442, 1973.
- RD9.27 Seltzer S., "SHIELDOSE: A Computer Code For Space Shielding Radiation Dose Calculations", NBS Technical Note 1116, National Bureau of Standards, May 1980.
- RD9.28 Petersen E.L., "Approaches to Proton Single-Event-Rate Calculation", IEEE Trans. Nucl. Sci. NS-43, 2 (special issue on Single Event Effects and the Space Environment), 496, 1996.
- RD9.29 Pickel J.C. "Single-Event Effects Rate Prediction", IEEE Trans. Nucl. Sci. NS-43, 2 (special issue on Single Event Effects and the Space Environment), 483, 1996.
- RD9.30 Tada H.Y., J.R. Carter, B.E. Anspaugh and R.G. Downing, "Solar Cell Radiation Handbook", 3rd Edition, JPL Publ. 82-69 (1982); B.E.Anspaugh, "GaAs Solar Cell Radiation Handbook", JPL Publ. 96-9, 1996.
- RD9.31 Hopkinson G.R., C.J. Dale and P.W. Marshall, "Proton Effects in Charge-Coupled Devices", IEEE Trans. Nucl. Sci. NS-43, 2 (special issue on Single Event Effects and the Space Environment), 614, 1996.

Particulates

10.1 Introduction

Every spacecraft in Earth orbit is exposed to a certain flux of micrometeoroids and man-made space debris. Collisions with these particles takes place with hypervelocity speed.

Meteoroids are particles of natural origin. Nearly all meteoroids originate from asteroids or comets. The natural meteoroid flux represents, at any instant, a total of about 200 kg of mass within 2000 km of the Earth surface [RD10.1].

Meteoroids that retain the orbit of their parent body can create periods of high flux and are called streams. Random fluxes with no apparent pattern are called sporadic.

Space debris is man-made. Since 1957, more than 3500 launches have led to a current (1996) population of approximately 8000 trackable objects (i.e. larger than about 10 cm in Low Earth Orbits (LEO)) in space. More than 90 % of these objects are space debris, i.e., man made objects that do not serve any useful purpose. About half of the trackable objects are fragments from explosions or from the break up of satellites or rocket bodies. It is expected that there is a much greater number of objects in orbit that cannot be operationally tracked. The number of space debris objects larger than 1 cm is estimated to between 30000 and 130000. Smaller particles are far more abundant still.

The damage caused by collisions with meteoroids and space debris depends on the size, density, speed and direction of the impacting particle and on the shielding of the spacecraft.

Submillimeter sized particles can cause pitting and cratering of outer surfaces and lead to degradation of optical, electrical, thermal, sealing or other properties.

Larger particles can puncture outer surfaces and can cause damage to structure or equipment by penetration and spallation.

Flux models have been developed for both micrometeoroids and space debris. The resulting damage can be assessed through empirically derived design equations which give e.g. penetration capabilities and crater sizes as function of the particle parameters and target properties.

All operational and mitigation aspects related to space debris are not covered within this document. This includes topics like lifetime and re-entry aspects, spacecraft passivation and other debris prevention measures, end-of-life de- or re-orbiting, collision avoidance.

10.2 Analysis techniques

Impact analysis techniques fall naturally into two different categories: larger, trackable pieces and smaller, non-trackable particles.

Objects larger than about 10 cm in LEO and larger than about 1 m in GEO are regularly tracked by Radar.

Trackable orbiting objects, whose orbital elements are known, can be propagated along their orbit and their chance of a future collision with another spacecraft or fragment can be assessed. This deterministic approach provides at the same time all relevant parameters of such a potential collision, like the respective object sizes, impact velocity and direction.

Several data sources of satellites and fragments and some analysis tools for trackable objects have been combined in the European DISCOS tool [RD10.2].

For meteoroids and the abundant smaller space debris particles which cannot be tracked, statistical flux models shall be used.

The meteoroid and debris fluxes are usually specified as a time-averaged flux, F_r , against a single sided, randomly tumbling surface. Flux is defined as number of intercepted objects per unit time and area.

The relevant area for F_r is the actual outer surface area of the spacecraft. One can also define a "cross sectional area flux", F_c , for a randomly tumbling satellite, where the relevant area is the time averaged cross sectional area. For objects with no concave surfaces (no self-shielding): $F_c = 4 F_r$.

For spacecraft which fly with a fixed orientation, the meteoroid and orbital debris fluxes shall be treated as vector quantities and the effects of directionality shall be carefully evaluated. Most impacts from both, meteoroids and space debris occur on forward facing surfaces.

The number of impacts, N , increases linearly with exposed area and with exposure time:

$$N = F \times A \times T$$

where

F is the number of impacts per unit area;

A is the total exposed area;

T is the exposure time.

The numbers of impacts from meteoroids and space debris can be summed to obtain the total number of impacts:

$$N_{tot} = N_{met} + N_{deb}$$

Once N has been determined, the probability of exactly n impacts occurring in the corresponding time interval is given by Poisson statistics:

$$P_n = \left(\frac{N^n}{n!} \right) \times e^{-N}$$

The probability for no impacts, P_0 is thus given by:

$$P_0 = e^{-N}$$

For values of $N \ll 1$ the probability, Q , for at least one impact ($Q = 1 - P_0$) is equal to N :

$$Q = 1 - e^{-N} \approx 1 - (1 - N) = N$$

10.3 Model presentation

10.3.1 Meteoroids

The isotropic meteoroid flux model given in RD10.3 or the new interplanetary flux model presented in RD10.4 and enhanced in RD10.5 shall be used depending on the analysis requirements and the applicable regimes for each model.

10.3.1.1 Flux model

The isotropic meteoroid model from RD10.3 is described below.

The total average meteoroid flux (sporadic + stream average) can be given in terms of the integral flux $F_{met,0}$ which is the number of particles with mass m or larger per m^2 per year impacting a randomly-oriented flat plate under a viewing angle of 2π . The unshielded interplanetary flux at 1 AU distance from the Sun can be described analytically [RD10.3] as:

$$F_{met,0}(m) = 3,15576 \times 10^7 (F_1(m) + F_2(m) + F_3(m))$$

where

$$\begin{aligned} F_1(m) &= (2,2 \times 10^3 m^{0,306} + 15)^{-4,38}, \\ F_2(m) &= 1,3 \times 10^{-9} (m + 10^{11} m^2 + 10^{27} m^4)^{-0,36}, \\ F_3(m) &= (1,3 \times 10^{-16} (m + 10^6 m^2))^{-0,85}, \end{aligned}$$

with m in g.

10.3.1.2 Velocity distribution

Meteoroid velocities near Earth can range from 11 km/s to 72 km/s.

The velocity distribution with respect to Earth to be used with the isotropic reference flux model given in RD10.3 is (number per km/s):

$$g(v) = \begin{cases} 0,112 & \text{if } 11,1 \leq v < 16,3 \text{ km/s} \\ 3,328 \times 10^5 v^{-5,34} & \text{if } 16,3 \leq v < 55,0 \text{ km/s} \\ 1,695 \times 10^{-4} & \text{if } 55,0 \leq v < 72,2 \text{ km/s} \end{cases}$$

The average velocity of this distribution is close to 17 km/s.

The average impact velocity to an orbiting spacecraft in LEO is 19 km/s.

10.3.1.3 Earth attraction and shielding

The unshielded flux $F_{met,0}$ shall be modified to account for the gravitational attraction (which enhances the meteoroid flux in the Earth proximity) and the geometrical shielding of the Earth (which reduces the flux). The gravitational enhancement factor G_e for the velocity distribution given above is defined as [RD10.1]:

$$G_e = 1 + \frac{R_E}{r}$$

where

R_E is the mean Earth radius;
 r is the orbit radius.

The Earth shielding factor, s_f , for a given surface depends on the spacecraft altitude above the Earth surface and on the relative orientation of the surface normal with respect to the Earth direction.

The average Earth shielding factor is given by:

$$s_f = \frac{(1 + \cos \eta)}{2}$$

with:

$$\sin \eta = \frac{(R_E + 100)}{(R_E + h)}$$

where

R_E is the Earth radius = 6378 km;

h is the spacecraft altitude in km; 100 km accounts for the atmosphere.

The meteoroid flux to an Earth orbiting spacecraft is then given by:

$$F_{met} = F_{met,0} \times G_e \times s_f$$

10.3.1.4 Mass density

The mass density of meteoroids varies widely from about 0,15 g/cm³ to 8 g/cm³. According to reference RD10.1 the average density of micrometeoroids larger than 0,01 g is assumed to be 0,5 g/cm³. Meteoroids smaller than 10⁻⁶ g are thought to have a higher mean density of 2 g/cm³. The recommended value for masses between 10⁻⁶ g and 0,01 g is 1 g/cm³. However, there is still a considerable uncertainty about these densities. The reference mass density values to be used for design are given in 10.3.1.9.

10.3.1.5 Directional distribution

The annual average meteoroid flux is usually considered to be omnidirectional with respect to the Earth surface. Relative to an orbiting spacecraft with fixed orientation with respect to the flight direction the meteoroid flux has a directional dependence, introduced by the spacecraft motion, in addition to the Earth shielding effect defined in 10.3.1.3.

The directional dependence of meteoroids shall be calculated numerically by converting the omnidirectional flux to the flux on a spacecraft surface with given surface orientation and spacecraft velocity vector.

10.3.1.6 Meteoroid streams

The meteoroid flux model of sections 10.3.1.1 – 10.3.1.5 gives a yearly average.

Meteoroid streams are accumulations of meteoroids with nearly identical heliocentric orbits. Relative to Earth all particles of a given meteoroid stream have nearly identical impact directions and velocities. Encounters with meteoroid streams typically lasts from a few hours to several days.

At peak activity stream fluxes can exceed the sporadic background fluxes by a factor five or more. Occasionally, very high fluxes (meteoroid storms, the visible meteor background flux can be exceeded by a factor 10000 or more) can be encountered for short periods (1–2 hours). Such a storm is predicted for the Leonid stream in 1998, 1999 or 2000.

Meteoroid streams are believed to consist of relative large particles only (mass > 10⁻⁸–10⁻⁶ g) with low density (0,5–1,0 g/cm³).

Activity ratios for the major yearly meteoroid streams are given in 10.4.2.2.

Reference meteoroid stream flux models are given in RD10.6 and RD10.7.

10.3.1.7 Interplanetary meteoroid model

A new interplanetary meteoroid flux model was presented in RD10.4 and enhanced in RD10.5. This model is based on five different types of meteoroid populations whose relative contributions depend on the particle size range and the distance from the Sun.

The model includes directional distributions of the populations.

For Earth orbits the meteoroid model predicts similar total fluxes as the reference model in subclause 10.3.1. In addition it includes directional effects.

A drawback for engineering applications is the higher complexity of the model.

10.3.1.8 Regime of applicability

The isotropic meteoroid model given in subclauses 10.3.1.1. – 10.3.1.5. is applicable for all Earth orbits and for interplanetary space at distances around 1 AU from the Sun.

The interplanetary meteoroid model in 10.3.1.7. is applicable for all Earth orbits and for interplanetary orbits.

10.3.1.9 Tailoring guidelines

Values for average mass densities of meteoroids are:

- low: 1,0 g/cm³
- nominal: 2,0 g/cm³
- high: 4,0 g/cm³.

For analysis of effects the nominal value of 2,0 g/cm³ shall be used.

For the assessment of impact effects the full velocity distribution of meteoroids should be used.

The distribution given in 10.3.1.2. is valid for LEO but can be used for all Earth orbits.

For a preliminary analysis a constant meteoroid impact velocity of 20 km/s shall be used.

A spherical shape shall be assumed to convert particle masses and diameters.

For meteoroid stream fluxes either the model in RD10.6 or in RD10.7 can be used.

For each meteoroid stream the specific particle velocity shall be considered.

For short duration missions (less than about 3 weeks), the contributions of meteoroid streams shall be considered. For longer missions the yearly average model can be used.

10.3.2 Space debris

Due to ongoing updates and extensions of existing space debris environment models no particular standard is defined yet.

As interim solution for space debris, the ESA MASTER-97 [RD10.8] model or the NASA ORDEM-96 model [RD10.9] shall be used, depending on the analysis requirements and depending on the areas of applicability for each model, as defined in annex H.

10.3.3 Dust

10.3.3.1 Lunar dust

From Surveyor and Apollo missions, a large amount of information has been gathered about the lunar dust environment.

This information, along with its engineering implications, is summarized in RD10.10.

Approximately 70 % weight of the lunar regolith (i.e. the blanket of rocks and soil, 3 m to 20 m thick that covers the Moon's surface) is composed of particles smaller than 1 mm. 50 % weight of that soil is in turn composed of particles smaller than 50 µm. This dust is abrasive and sticky due to the high vacuum that allows Van der Waals forces to weld dust grains to surfaces. Therefore dust represents a threat to any functional surface that, once contaminated, cannot be decontaminated.

For details on grain sizes, one should refer to RD10.11.

The models given in RD10.10 and RD10.11 shall be used as reference for Lunar dust.

10.3.3.2 Martian dust

A comprehensive description of the Martian environment can be found in RD10.12. This reference based on the results of the Mariner and Viking missions, contains information about the distribution and optical properties of dust in the atmosphere, the description of e.g. dust storms, as well as a surface model based on information gathered by the Viking Landers. This model includes physical description, chemical properties, physical properties, average bulk density, dielectric constants of surface material.

Recent estimates [RD10.13, RD10.14] place the likelihood of a global dust storm occurring in any one Martian year at about one in three, though with a large variance. In addition, observations made during the Phobos mission in 1989 indicate that the atmosphere can be clearer than the clearest seen by Viking in 1977-78 [RD10.15]. For engineering applications, it is recommended that atmospheric conditions similar to those observed during the Phobos mission are included.

A recent update on wind speed thresholds for dust lifting is given in RD10.16. The threshold friction velocity for 100 μm particles is 1,5 m/s. Higher winds are needed to lift smaller particles, but once lifted much lower winds can maintain them aloft.

The model given in RD10.12 shall be used as reference model for the Martian dust environment, together with the more recent data given in RD10.13 - RD10.15.

It shall be assumed that, in any Martian year, the probability of a global dust storm is 1/3.

10.3.3.3 Cometary dust

The available information on cometary dust is still seen as insufficient to define a general standard model. Two overviews of cometary gas and dust models are given in RD10.17 and RD10.18.

These documents are given for information only. New cometary dust models are presently being developed.

10.4 Reference data

10.4.1 Trackable space debris

The following information on the catalogued space debris population was obtained from the DISCOS [RD10.2] database. The figures show the situation of mid-1996.

The time evolution of the number of trackable objects in orbit is shown in Figure 26.

The altitude dependence for the lower altitudes is given in Figure 27.

The object distribution as function of their inclination is plotted in Figure 28. A concentration at certain inclinations is clearly visible.

10.4.2 Statistical flux models

10.4.2.1 Random plate

Cumulative meteoroid and space debris fluxes (i.e. fluxes of particles of given size or larger) can be obtained directly from the flux models. Table 32 gives the number of impacts / m^2 /year from one side to a randomly oriented plate for a range of minimum particle sizes. The ORDEM-96 model [RD10.9] was used for the debris fluxes. The results are for an altitude $h = 400$ km, inclination $i = 51,6^\circ$, year 2000, ratio of future to historic debris production rate, $N = 0,2$, and solar activity $S = 140$. The meteoroid fluxes are from the model given in 10.3.1. For meteoroids

a density of $\rho = 2,0 \text{ g/cm}^3$ and the assumption of spherical shape were used to convert masses to diameters.

Table 33 gives the same results for a polar reference orbit ($h = 800 \text{ km}$, $i = 98^\circ$, all other parameters are as for Table 32).

Table 34 gives the number of impacts at the geostationary altitude ($h = 36000 \text{ km}$). The space debris fluxes are obtained from the MASTER-97 model [RD10.8]. The model is applicable for sizes of 0,1 mm or larger.

In Figure 29 cumulative meteoroid and space debris fluxes are plotted as function of diameter for $h = 400 \text{ km}$ and $i = 51,6^\circ$ (all fluxes and model parameters are as in Table 32).

Table 32: Cumulative number of impacts, N , from one side to a randomly oriented plate for a range of minimum particle sizes using the ORDEM 96 debris model

Diameter (cm)	N_{deb} (/m ² /year)	N_{met} (/m ² /year)	N_{tot} (/m ² /year)
0,0001	1,23E+4	1,35E+3	1,37E+4
0,0002	3,28E+3	6,38E+2	3,92E+3
0,0003	1,53E+3	4,02E+2	1,93E+3
0,0005	5,92E+2	2,33E+2	8,25E+2
0,0007	3,18E+2	1,68E+2	4,86E+2
0,001	1,64E+2	1,18E+2	2,82E+2
0,002	4,27E+1	5,15E+1	9,42E+1
0,003	1,81E+1	2,70E+1	4,51E+1
0,005	6,31E+0	9,98E+0	1,63E+1
0,007	3,34E+0	4,58E+0	7,92E+0
0,01	1,64E+0	1,81E+0	3,45E+0
0,02	2,31E-1	2,25E-1	4,56E-1
0,03	5,56E-2	5,79E-2	1,14E-1
0,05	1,02E-2	9,46E-3	1,97E-2
0,07	3,56E-3	2,74E-3	6,30E-3
0,1	1,21E-3	7,12E-4	1,92E-3
0,2	1,53E-4	4,90E-5	2,02E-4
0,3	4,63E-5	9,98E-6	5,63E-5
0,5	1,04E-5	1,32E-6	1,17E-5
0,7	4,07E-6	3,47E-7	4,42E-6
1,0	1,60E-6	8,36E-8	1,68E-6
2,0	3,57E-7	5,22E-9	3,62E-7
3,0	1,90E-7	1,03E-9	1,91E-7
5,0	1,08E-7	1,32E-10	1,08E-7
10,0	6,48E-8	8,17E-12	6,48E-8

The results are for an altitude $h = 400 \text{ km}$, inclination $i = 51,6^\circ$, year 2000, ratio of future to historic debris production rate, $N = 0,2$, and solar activity $S = 140$. For meteoroids a density of $\rho = 2,0 \text{ g/cm}^3$ and spherical shape were used to convert masses to diameters.

Table 33: Cumulative number of impacts, N , from one side to a randomly oriented plate for a range of minimum particle sizes using the ORDEM 96 model

Diameter (cm)	N_{deb} (/m ² /year)	N_{met} (/m ² /year)	N_{tot} (/m ² /year)
0,0001	2,93E+4	1,46E+3	3,08E+4
0,0002	8,28E+3	6,86E+2	8,97E+3
0,0003	4,00E+3	4,32E+2	4,43E+3
0,0005	1,62E+3	2,51E+2	1,87E+3
0,0007	8,97E+2	1,81E+2	1,08E+3
0,001	4,81E+2	1,27E+2	6,08E+2
0,002	1,38E+2	5,54E+1	1,93E+2
0,003	6,40E+1	2,91E+1	9,31E+1
0,005	2,46E+1	1,07E+1	3,53E+1
0,007	1,33E+1	4,93E+0	1,82E+1
0,01	6,66E+0	1,94E+0	8,60E+0
0,02	1,25E+0	2,41E-1	1,49E+0
0,03	4,11E-1	6,23E-2	4,73E-1
0,05	9,85E-2	1,02E-2	1,09E-1
0,07	3,78E-2	2,94E-3	4,07E-2
0,1	1,35E-2	7,66E-4	1,43E-2
0,2	1,80E-3	5,27E-5	1,85E-3
0,3	5,56E-4	1,07E-5	5,67E-4
0,5	1,17E-4	1,42E-6	1,18E-4
0,7	3,95E-5	3,73E-7	3,99E-5
1,0	1,86E-5	8,99E-8	1,87E-5
2,0	7,02E-6	5,61E-9	7,03E-6
3,0	4,57E-6	1,10E-9	4,57E-6
5,0	2,92E-6	1,42E-10	2,92E-6
10,0	1,80E-6	8,79E-12	1,80E-6

The results are for an altitude $h = 800$ km, inclination $i = 98^\circ$, year 2000, ratio of future to historic debris production rate, $N = 0,2$, and solar activity $S = 140$. For meteoroids a density of $\rho = 2,0$ g/cm³ and spherical shape were used to convert masses to diameters.

Table 34: Cumulative number of impacts, N , from 1 side to a randomly oriented plate for a range of minimum particle sizes using the MASTER debris model

Diameter (cm)	N_{deb} (*) (/m ² /year)	N_{met} (/m ² /year)	N_{tot} (/m ² /year)
0,0001		1,23E+3	1,23E+3
0,0002		5,77E+2	5,77E+2
0,0003		3,64E+2	3,64E+2
0,0005		2,11E+2	2,11E+2
0,0007		1,52E+2	1,52E+2
0,001		1,07E+2	1,07E+2
0,002		4,67E+1	4,67E+1
0,003		2,45E+1	2,45E+1
0,005		9,04E+0	9,04E+0
0,007		4,15E+0	4,15E+0
0,01	2,08E-3	1,64E+0	1,64E+0
0,02	3,05E-4	2,03E-1	2,03E-1
0,03	1,14E-4	5,24E-2	5,25E-2
0,05	2,47E-5	8,57E-3	8,59E-3
0,07	9,09E-6	2,48E-3	2,49E-3
0,1	3,23E-6	6,45E-4	6,48E-4
0,2	3,87E-7	4,44E-5	4,48E-5
0,3	1,23E-7	9,04E-6	9,16E-6
0,5	3,09E-8	1,20E-6	1,23E-6
0,7	1,99E-8	3,14E-7	3,34E-7
1,0	1,51E-8	7,57E-8	9,08E-8
2,0	1,10E-8	4,73E-9	1,57E-8
3,0	1,03E-8	9,30E-10	1,12E-8
5,0	9,75E-9	1,20E-10	9,87E-9
10,0	9,35E-9	7,40E-12	9,36E-9

(*) The MASTER model is only applicable for sizes of 0,01 cm or larger.

The results are for an altitude $h = 35786$ km, inclination $i = 0,5^\circ$, and year 2000. For meteoroids a density of $r = 2,0$ g/cm³ and spherical shape were used to convert masses to diameters.

10.4.2.2 Meteoroid streams

The ratio, F , of the cumulative meteoroid stream flux to the average sporadic flux is shown in Figures 30a and 30b for the major yearly streams (taken from RD10.6). Plotted is the activity ratio versus the period of activity based on photographic meteors with mass, $m > 0,1$ g.

When impact fluxes are derived from these activity ratios the different stream velocities (also given in RD10.6) have to be considered.

10.4.2.3 Meteoroids directionality

The present meteoroid flux model assumes an isotropic flux with respect to the Earth surface. For an orbiting spacecraft the Earth shielding and the spacecraft motion both introduce a directional dependence.

The Earth shielding factor is defined in 10.3.1.3.

For a surface with normal pointing towards Earth the flux is reduced by an Earth shielding factor $s_f = \cos^2 \gamma$ relative to a surface pointing exactly away from Earth. The Earth shielding factor for a surface with normal perpendicular to the Earth direction is given by:

$$s_f = 1 - \frac{1}{\pi}(\eta - 0,5 \sin 2\eta)$$

For other fixed orientations the shielding factor can be obtained by interpolation. The directionality caused by the spacecraft motion leads to increased fluxes on forward facing surfaces and to reduced fluxes on trailing surfaces.

Combining the two factors the following flux ratios for meteoroids are found for 400 km and 800 km altitudes (using the velocity distribution from 10.3.1.2):

	400 km	800 km
Front/random	$\approx 2,2$	$\approx 2,0$
Front/rear	≈ 7	≈ 6
Space face/Earth face	≈ 11	$\approx 5,4$

As resulting effects such as penetration depth or impact plasma generation also depend on parameters such as impact velocity and angle, the directional ratios for these effects can be considerably different from those given above.

10.4.2.4 Debris directionality

For an oriented spacecraft surface the debris fluxes are different for the various surfaces.

The highest space debris fluxes are encountered by forward (ram) facing surfaces. Surfaces on spacecraft in circular Earth orbits which point towards Earth, space or the rear direction can only be impacted by space debris particles in eccentric orbits.

The flux ratio oriented/random surface depends on the particle size and the orbit. For higher inclination orbits impacting fluxes become more peaked towards the flight direction.

10.5 Figures

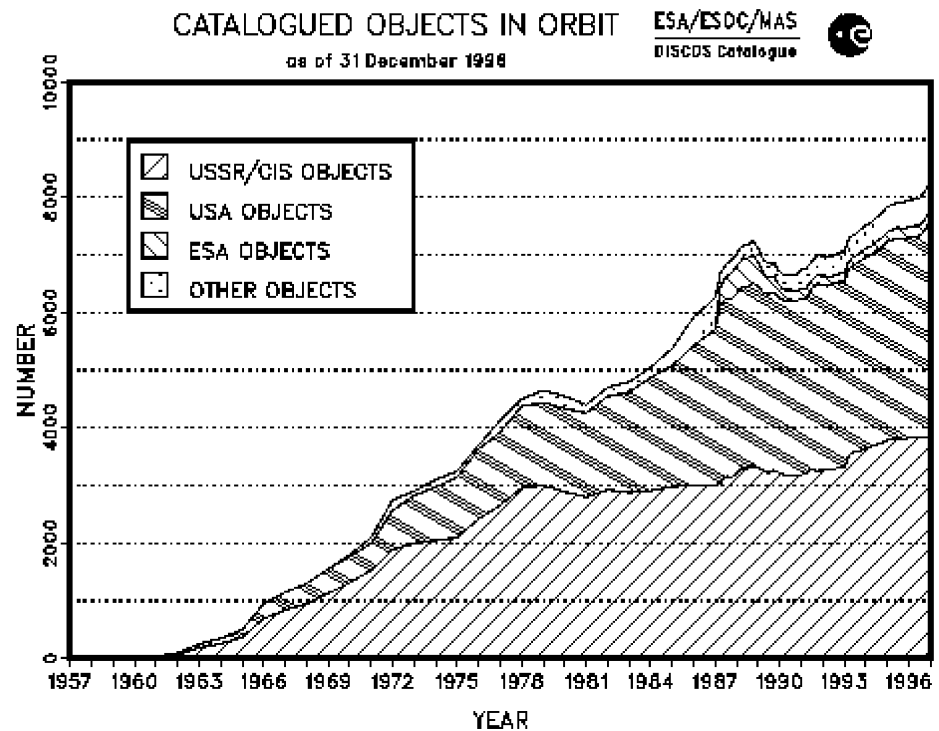


Figure 26: Time evolution of the number of trackable objects in orbit

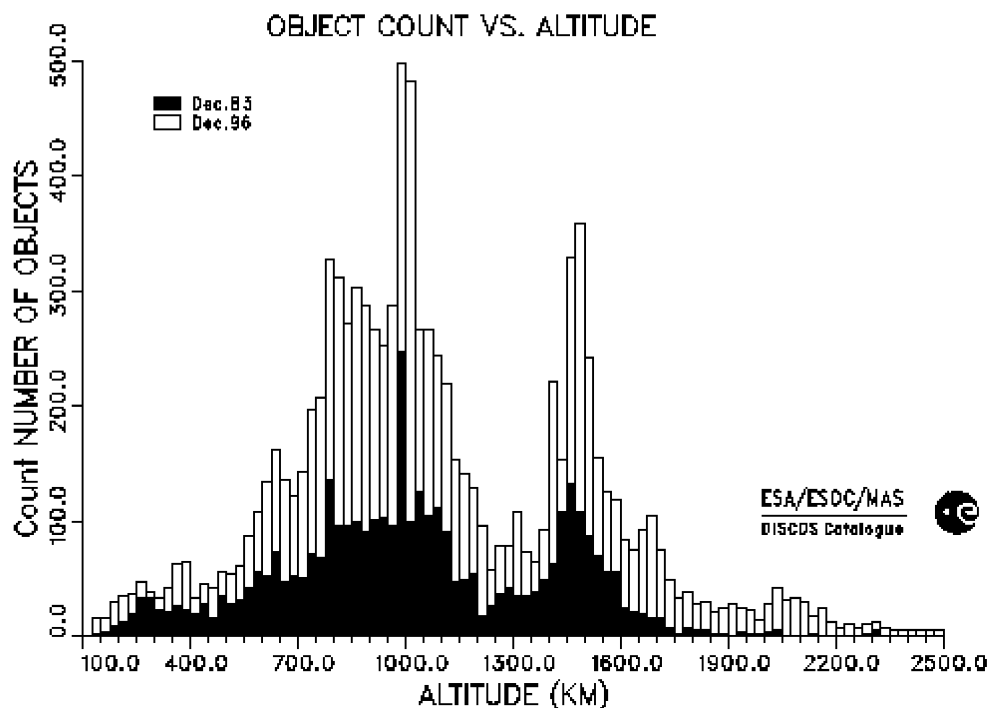


Figure 27: Altitude distribution of trackable objects in LEO orbits

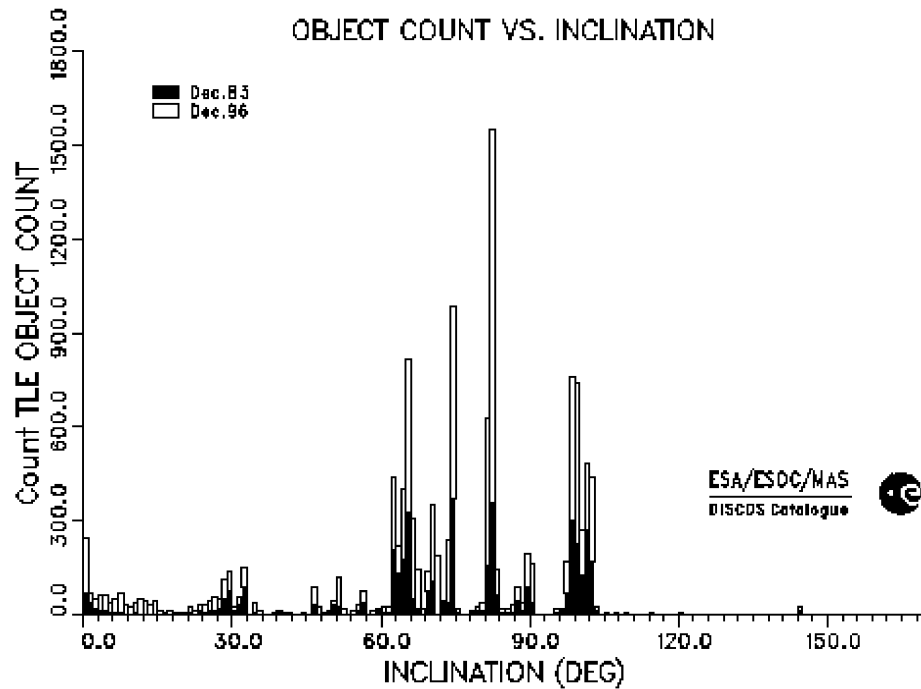
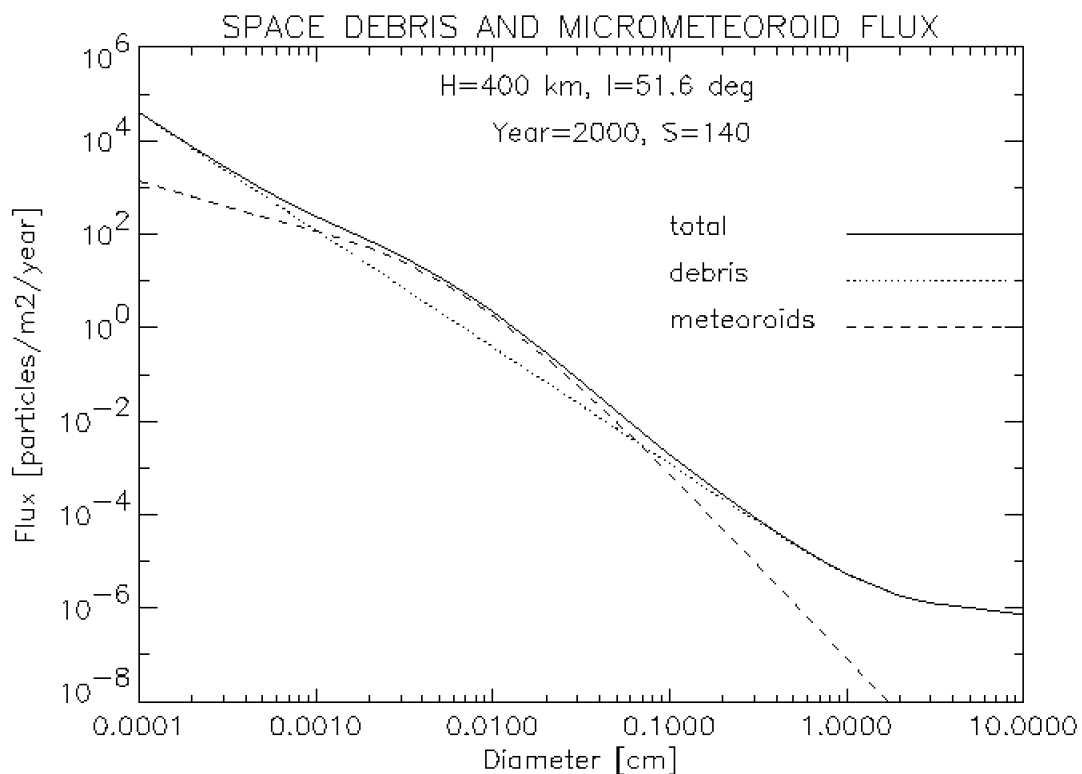


Figure 28: Distribution of trackable objects as function of their inclination



The ORDEM 96 debris model was used. The results are for an altitude $h = 400$ km, inclination $i = 51,6^\circ$, year 2000, ratio of future to historic debris production rate, $N = 0,2$, and solar activity $S = 140$. For meteoroids a density of $r = 2,0 \text{ g/cm}^3$ and spherical shape were used to convert masses to diameters.

Figure 29: Cumulative number of impacts, N from 1 side to a randomly oriented plate for a range of minimum particle sizes

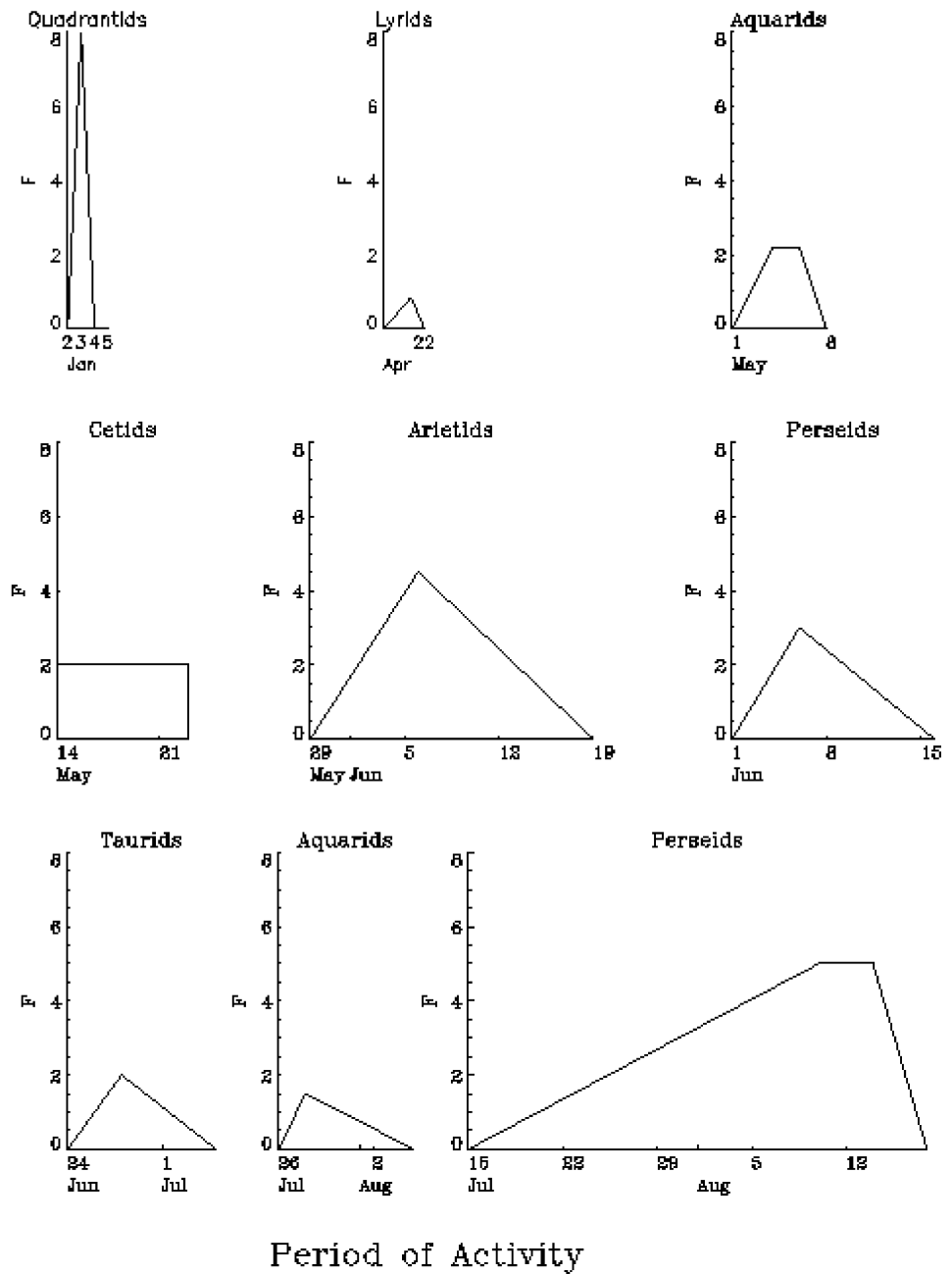
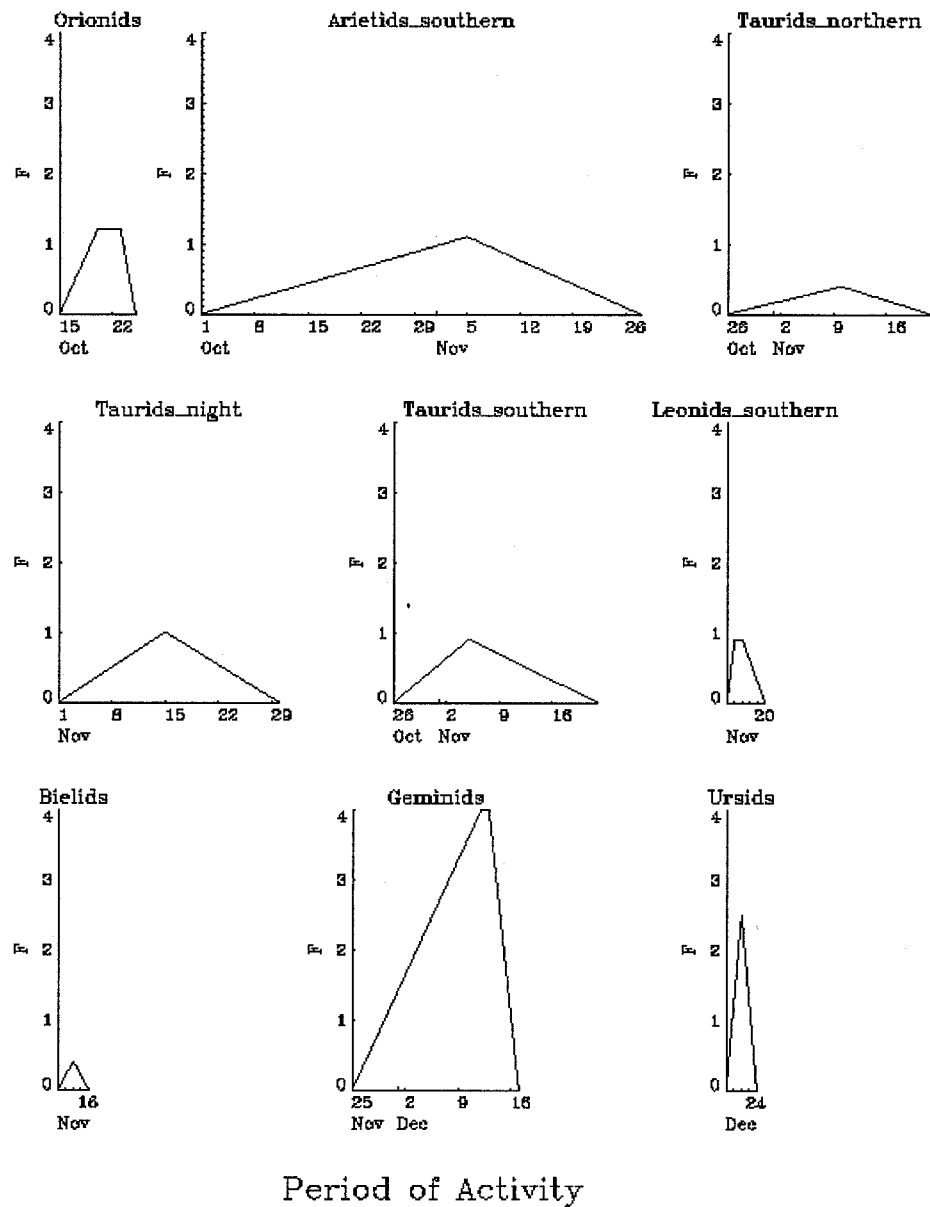


Figure 30: Activity ratio factor versus period of activity for major meteoroid streams

(a) January - August



$$F = \frac{\text{Cumulative Flux of Stream}}{\text{Average Cumulative Sporadic Flux}}$$

Figure 30: Activity ratio factor versus period of activity for major meteoroid streams (*continued*)

(b) September - December

10.6 References

- RD10.1 “Natural Orbital Environment Guidelines for Use in Aerospace Vehicle Development”, B.J. Anderson, Ed. and R.E. Smith, compiler, NASA TM 4527, chapter 7, June 1994.
- RD10.2 Klinkrad H., U. Fuller and J.C. Zarnecki, “Retrieval of Space Debris Information from ESA’s DISCOS Catalogue”, Proc. ESA Workshop on Space Environment Analysis, Noordwijk, 9-12 October 1990 (ESA WPP-23).
- RD10.3 Grün E., H.A. Zook, H. Fechtig and R.H. Giese, “Collisional Balance of the Meteoritic Complex”, *Icarus*, Vol. 62, p.244, 1985.
- RD10.4 Divine N., “Five Populations of Interplanetary Meteoroids”, *J. Geophys. Res.*, Vol. 98, No. E9, 1993.
- RD10.5 Staubach P., E. Grün and R. Jehn, “The meteoroid environment of the Earth”, 31th COSPAR Sci. Assembly, Birmingham/UK, July, 1996.
- RD10.6 Cour-Palais B.G., “Meteoroid Environment Model - 1969. (Near Earth to Lunar Surface)”, NASA SP-8013, 1969.
- RD10.7 Jenniskens P., “Meteor Stream Activity”, *Astron. Astrophys.* Vol. 287, pp 990-1013, 1994.
- RD10.8 Klinkrad H., J. Bendisch, H. Sdunnus, P. Wegener, R. Westerkamp, “An Introduction to the 1997 ESA MASTER Model”, Proc. of the Second European Conf. on Space Debris, pp. 217-224, ESA SP-393, May 1997.
- RD10.9 Kessler D.J., J. Zhang, M.J. Matney, P. Eichler, R.C. Reynolds, P.D. Anz-Meador and E.G. Stansbery, “A Computer Based Orbital Debris Environment Model for Spacecraft Design and Observations in Low Earth Orbit”, NASA TM 104825, November 1996.
- RD10.10 Katzan C.M., “Lunar dust transport and potential interactions with power system components”, NASA CR 4404, 1991.
- RD10.11 Graf J., “Lunar soils grain size catalog”, NASA RP 1265, 1993.
- RD10.12 Kaplan D., “Environment of Mars”, NASA TM 100470, 1988.
- RD10.13 Martin L.J. and R.W. Zurek, “An analysis of the history of dust activity on Mars”, *J. Geophys. Res.*, 98, 3221-3246, 1993.
- RD10.14 Zurek R.W. and L.J. Martin, “Interannual variability of planet-en-circling dust storms on Mars”, *J. Geophys. Res.*, 98, 3247-3259, 1993.
- RD10.15 Chassefiere E., P. Drossart and O. Korablev, “Post-Phobos model for the altitude and size distribution of dust in the low Martian atmosphere”, *J. Geophys. Res.*, 100, 5525-5539, 1995.
- RD10.16 Greeley R., M. Lacchia, B. White, J. Inversen and J.B. Pollack, “Dust on Mars: new values for wind threshold”, In XXV Lunar Planet. Sci. Conf., 467-468, 1994.
- RD10.17 Divine N. et al., “The comet Halley dust and gas environment, *Space Sci. Rev.*, Vol. 43, 1-104, 1986.
- RD10.18 Massone L., J. Fertig, E. Grün and G. Schwehm, “A cometary dust environment model for the generation of synthetic images”, in “Asteroids, Comets, Meteors II”, Conf. Proceedings, Univ. Uppsala, 407-410, 1985.

(This page is intentionally left blank)

Contamination

11.1 Introduction

This clause deals with the induced molecular and particulate environment in the vicinity of and created by the presence of a spacecraft in space. It is meant mainly to aid in the definition of the contamination environment of a satellite. The relevant computer models and tools are presented in annex I.

The quantitative modelling of this contamination environment is very complex. This is due to the high number of materials involved, with a variability of outgassing characteristics. Furthermore, there are interactions of the outgassing products with surfaces, residual gas and with other environmental parameters such as solar radiation and atomic oxygen.

The contamination analysis, which necessarily is very much dependent of a specific project/application, cannot be more detailed in this standard. ECSS-Q-70-01 [RD11.3] defines amongst others the requirements to be followed and guidelines to be taken into account in order to control the particulate and molecular contamination within the specified limits during mission.

The user shall:

- estimate the sensitivity of his system or equipment with regard to contamination;
- identify the contamination sources on-board;
- evaluate with all appropriate means the expected contamination levels or quantities present in critical areas, taking into account the mechanisms of transport and fixation of contaminants.

11.2 Molecular contamination

11.2.1 Sources of molecular contamination

11.2.1.1 Primary sources

11.2.1.1.1 Outgassing of organic materials

Outgassing of organic materials can be approached as a surface evaporation combined with a diffusion for bulk contaminant species. These species can be either initially present components, or decomposition products.

Initially present outgassing species can be:

- water;
- solvents;
- additives;
- uncured monomeric material;
- lubricants;
- ground contamination species, due to e.g. processes, test, storage, handling, pre-launch and launch.

The decomposition products are due to exposure of molecular materials to other environments, such as:

- thermal;
- solar radiation, electromagnetic and charged particles;
- atomic oxygen;
- impacts by micrometeoroids or debris;
- electrical discharges and arcing.

These products consist of lower molecular weight (higher volatility) species than the original species.

11.2.1.1.2 Plumes

Plume species can result from combustion, unburned propellant vapours, incomplete combustion products, sputtered material and other degradation products from a propulsion or attitude control system and its surroundings swept along with the jet.

Plumes can also be produced by dumps of gaseous and liquid waste materials of the environment control and life support systems in manned spacecraft or by leaks in systems or internal payloads. Overboard disposal of materials cause increased molecular column densities and can cause molecular deposition. Plumes can consist of gaseous (molecular) species, liquid droplets and solid particles. Particles can also be formed due to icing or presence of inorganic material during water dumps.

Return flux or back flow is possible due to ambient scattering, self scattering or diffusion processes.

11.2.1.1.3 Pyrotechnics and release mechanisms

During operation of pyrotechnics or other release mechanisms gases can evolve.

11.2.1.2 Secondary sources

A surface can act as a secondary source if an incoming contaminant molecule reflects (not accommodate, stick or condense on the surface) or if it has a limited residence time on that surface. Secondary sources can for example be solar panels having a higher temperature than the surrounding surfaces.

11.2.2 Transport mechanisms

11.2.2.1 Reflection on surface

A molecule reflects on a surface when the accommodation coefficient during a collision is zero, i.e. when there is no energy transfer between the molecule and the surface during that collision. A reflection of a molecule is always specular, although this is dependent on surface roughness, r.m.s.

11.2.2.2 Re-evaporation from surface

A molecule having a non-zero residence time can re-evaporate from a surface. Re-evaporation is diffuse, i.e. the molecule is leaving the surface following a Lambertian distribution law.

11.2.2.3 Migration on surface

A molecule accommodated on a surface can migrate over that surface.

11.2.2.4 Collision with residual (natural) atmosphere

The contamination environment shall take into account the collision between the contamination species and the residual atmosphere. This interaction results in an ambient scattering of the contamination species, and can sometimes lead to an increase in the local pressure.

11.2.2.5 Collision with other outgassed molecules

The contamination environment shall take into account the collision between two contamination molecules. This interaction results in self-scattering of the contamination species.

11.2.2.6 Ionization by other environmental parameters

A molecule can be ionized due to interaction with (V)UV or charged particles (electrons, protons, ions) and subsequently be attracted by a charged surface.

11.3 Particulate contamination

11.3.1 Sources of particulate contamination

11.3.1.1 Sources inherent to materials

- Particles originating from manufacturing (machining, sawing), handling (e.g. for brittle materials such as certain paints) or wear (friction).
- Degradation of binder under different environments (e.g. AO, UV) resulting in loose filler.
- Crack formation and subsequent flaking as a result of thermal cycling.
- Formation of particles due to oxidation in an atomic oxygen environment.

11.3.1.2 Sources external to materials

- Dust particles can be caused by atmospheric fall-out (dust) during assembly, integration and storage or by human sources during such activities (e.g. hair, skin flakes, lint or fibres from garments).
- Particles can be produced during spacecraft propulsion or attitude control operations, the functioning of moving parts (such as shutters), and water dumps.
- Particles can result from micrometeoroid or debris impacts on materials.

11.3.2 Transport mechanisms

11.3.2.1 (Acoustic) vibrations

Vibrations due to launch, (attitude control) manoeuvring and docking. Pyro-technic shocks can cause particles to migrate from one surface to another.

11.3.2.2 Electrostatic attraction

Particles can be charged due to their interaction with ambient plasma, or photo emission and subsequently attracted by electrically-charged surfaces.

11.3.2.3 Other mechanisms

For specific missions other mechanisms can have an effect on the particles, such as:

- drag, due to the residual atmosphere in the lowest Earth orbits;
- radiation pressure due to solar radiation;
- gravitational tide, e.g. re-attraction to spacecraft.

11.4 Effect of contamination

The primary concerns of contamination are related to the degradation of spacecraft system or sub-system performances due to the presence of:

- Deposited species onto a critical surface:
 - (thermo-)optical properties, such as transmission, reflection, absorption, scattering;
 - tribological properties, outgassing of lubricant, friction due to particles;
 - electrical properties, such as surface conductivity, secondary emission and photo-emission.
- Glow or other surface/gas reactions.
- Free flying species in the field of view of sensors:
 - light scattering (star trackers);
 - light absorption;
 - background increase (natural environment analysis).

The effect of a contamination can be altered by the exposure to other environmental parameters, e.g. UV can increase the absorption due to photo-degradation (darkening) of the deposited contaminant, atomic oxygen can have a cleaning-up effect on hydrocarbon material, but can also form non-volatile SiO_x that can further trap other contaminants.

11.5 Models

11.5.1 General

(Worst case) outgassing modelling can be based on VCM-test results, differentiating between CVCM (low vapour pressure, condensable material) and TML (sum of condensable and non-condensable material).

More sophisticated outgassing/condensation models takes into account the data of outgassing or mass flow rates, surface accommodation and sticking coefficients as obtained by e.g. the VBQC-test [RD11.4] or the ASTM E1559 test [RD11.5].

11.5.2 Sources

11.5.2.1 Outgassing

For a material that outgasses at a constant rate, independently of the quantity present, such as e.g. during evaporation or sublimation from a bulk, the process can be described as a zero order reaction.

$$\frac{dm}{dt} = k$$

where

$\frac{dm}{dt}$ is the outgassing rate ($\text{g cm}^{-2} \text{s}^{-1}$);

k is the reaction constant.

The weight-loss through evaporation, at a temperature T is given by RD11.6

$$\frac{dm}{dt} = 0,04375 \times P_s \times \left(\frac{M}{T}\right)^{1/2}$$

where

P_s is the vapour pressure in hPa;

$\frac{dm}{dt}$ is the weight loss per unit area in $\text{g cm}^{-2} \text{s}^{-1}$;

M is the molecular mass;

T is the temperature in K.

The outgassing is often described as a first order reaction [RD11.7], i.e. the material outgasses at a rate that is proportional to the mass available, and using Arrhenius law temperature dependency. Important parameters for the outgassing rate are temperature, exposed surface area (or the surface available for evaporation), surface morphology, dimensions of the material (characteristic dimension, thickness).

$$\frac{dm}{dt} = -km$$

The factor k can be seen as a measure for the temperature dependent time constant (τ) of the outgassing phenomenon.

$$k = \frac{1}{\tau}$$

Integration of

$$\frac{dm}{dt} = \frac{m}{\tau}$$

gives

$$m = m_0 \exp(-t/\tau)$$

Assuming the Arrhenius relation to be valid

$$\tau = \tau_0 \exp(-E/RT)$$

it is possible to determine the outgassing as function of temperature.

The mass loss can be expressed as

$$m_{\text{loss}} = m_0 - m = m_0 (1 - \exp(-t/\tau))$$

11.5.2.2 Plumes

Evaluation of plumes of thrusters or vents is often described by specific application related models. Parametric descriptions of plumes constitute an interesting alternative to spacecraft designers.

The mass flux Φ of a plume can be expressed in the most generic form

$$\Phi(r, \Theta) = f\left(r, \Theta, \frac{dm}{dt}\right)$$

where

$\Phi(r, \Theta)$ is the flux at a given position from the vent;

r is the radial distance from the vent;

Θ is the angle from the centerline of the vent;

dm/dt is the mass flow from the vent;

where, moreover, the function f depends on the plume type. However this formula can in general be reduced in a good approximation to the product

$$\Phi(r, \Theta) = A \left(\frac{dm}{dt}\right) f_1(\Theta) r^{-2}$$

where

A is a normalization coefficient.

For a thruster, the function f_1 is peaked around $\Theta = 0$ and can be expressed as a sum of decreasing exponentials [RD11.8] or as a (high) power law of $\cos(\Theta)$ or both [RD11.9]. It is in some extent specific of each thruster.

Plumes from vents are more standard and the f_1 function can consequently be fixed: the mass flux is approximated by the following engineering model:

$$\Phi(r, \Theta) = \left[\frac{(n+1)}{(2\pi)} \right] \left(\frac{dm}{dt}\right) \cos^n(\Theta) r^{-2}$$

where $1 \leq n \leq 2$ is used for space station design. The divergence is larger than the one of thrusters.

11.5.3 Transport of molecular contaminants

11.5.3.1 Transport between surfaces

11.5.3.1.1 General

The following subclauses only deal with the methods and models for transport of neutral molecules (11.2.2.4 and 11.2.2.5). There is no available model of ion transport devoted to contamination (11.2.2.6).

Three levels of complexity and accuracy in modelling the transport of neutral molecular contaminants can be distinguished.

11.5.3.1.2 Simplest view factors

This model simulates collisionless transport. In such a case the fraction of contaminants coming from surface j to surface i is given by the view factor V_{ij} of surface i seen from surface j (including the cosine factor coming from the Lambertian emission law). These view factors are similar to the ones of radiative thermal analysis. They can be computed geometrically or by Monte-Carlo ray tracing. The incident mass on a surface i is then given by

$$S_i V_{ij} \frac{dm_j}{dt}$$

where j runs over all surfaces and dm_j/dt denotes the outgassing mass rate of surface j .

11.5.3.1.3 Simplified Monte-Carlo

Collisions of contaminants are simulated in a simplified way, the density and speed of possible partners for molecular collisions are given a priori:

- for ambient scatter, the ambient density and speed are easily known, but wakes (or “shades”) are usually not treated;
- for self-scatter, the contaminant density is very simplified and usually taken proportional to $1/r^2$ and with spherical symmetry.

This simplifying assumption has a consequence: the fraction of contaminants coming onto surface i from surface j is still a constant (depending on assumed densities) that can be called an effective view factor. It results from the view factor (11.5.3.1.2) for collisionless processes diminished by the fraction of scattered molecules and increased by molecules outgassed in other directions but redirected to surface j due to collisions. The deposition rate is then computed similarly to the case in 11.5.3.1.2.

This method is usually limited to one collision per molecule because the uncertainties due to the densities given a priori increase with collision number. This effective view factors can conveniently be computed by Monte-Carlo ray-tracing method.

Both methods 11.5.3.1.2 and 11.5.3.1.3 can include other contaminant sources such as vents and plumes. The view factors are then replaced by interception factors.

11.5.3.1.4 True Monte-Carlo (Direct Simulation Monte-Carlo, DSMC)

This computes multiple collisions in a realistic way. The collision probabilities are computed auto-coherently from the densities given by the simulation. This method is more time consuming and requires more work for programming (in particular, contrarily to 11.5.3.1.2 and 11.5.3.1.3., it requires a meshing of volume and not only of spacecraft surfaces).

Either method can be better suited, depending on the spacecraft configuration. A potential contamination of a sensitive protected surface through multiple collisions shall require a precise DSMC simulation. In simpler cases, when contamination essentially happens in line-of-sight, it shall be more appropriate to use the less time-consuming and more widespread methods of 11.5.3.1.2 and 11.5.3.1.3.

11.5.3.2 Surface transport

Reflections on surfaces (11.2.2.1) and re-evaporation (11.2.2.2) are easy to implement and are usually included in models, the latter (re-evaporation) often as part of the outgassing process. Migrations on surfaces on the contrary are complex processes and there is no commercial available model.

11.5.3.3 Transport of particles

As mentioned in 11.3.2 particulate transport is governed by several phenomena:

- a. atmospheric drag
- b. solar radiation pressure
- c. differential gravitational effects (with respect to spacecraft) which result in tide effects
- d. particulate charging and subsequent electrostatic effects

among which the first three may be computed by methods similar to spacecraft orbit computing, whereas point d. requires specific modelling to access particulate charging in a plasma and potential map around spacecraft. The dominant phenomena are most commonly modelled: point a. atmospheric drag, first, and also point d. that gets important in GEO. Points b. and c. can become dominant in cases when points a. and d. become small (high altitude and no charging).

A last aspect of particulate transport is their interaction with walls. Sticking and accommodation coefficients are, however, very difficult to assess.

Most particulate contamination models remain in the field of research. Very few of them seem to be transferable to other users (only code described here in informative annex I.10: OPT).

11.6 References

- RD11.1 ECSS-Q-70-04, Space product assurance: A thermal vacuum test for the screening of space materials (former ESA PSS-01-702).
- RD11.2 ASTM E-595, Method for Total Mass Loss and Collected Volatile Condensable Materials from outgassing in a vacuum environment.
- RD11.3 ECSS-Q-70-01, Space product assurance: Contamination and cleanliness control (former ESA PSS-01-201).
- RD11.4 Van Eesbeek M. and A. Zwaal, "Outgassing and contamination model based on residence time", ESA SP232, Proc. of the 3rd European Symp. on spacecraft materials in a space environment, Noordwijk, The Netherlands, 1-4 Oct 1985.
- RD11.5 ASTM E-1559, Method for contamination outgassing characteristics of space materials.
- RD11.6 Dushman S., "Scientific Foundations of Vacuum Technique", Wiley & Sons, Inc, New York-London.
- RD11.7 Scialdone J., "Characterisation of the outgassing of spacecraft materials", SPIE Vol. 287 Shuttle Optical Environment, 1981.
- RD11.8 Trinks H., "Exhaust Plume Databook Update Version No. 3 / ESA/ ESTEC Contract 7590/87/NL/TP".
- RD11.9 Simons G.A., "Effect of Nozzle Boundary Layers on Rocket Exhaust Plumes", AIAA Journal, Tech. Notes, vol. 10, No. 11, pp. 1534-1535, 1972.

Annex A (informative)

It is the purpose of these informative annexes to provide supplementary information to the main text. All these annexes are called up in the main text. There is a one-to-one correspondence between the sections in the body of the document. Therefore, the main body section number is mentioned in each informative annex section title.

In several areas of natural and induced environments, models and tools are undergoing rapid evolution and development. Therefore, where appropriate, likely or possible future models are indicated. It is expected that in future revisions of this Standard, models which are outlined in the informative annexes become the standards referenced in the main body.

(This page is intentionally left blank)

Annex B (informative)

Gravitation

B.1 Related tools

The GRIM4 series of European global Earth gravity field modes has been developed through cooperation between GeoForschungs-Zentrum Potsdam (GFZ, Germany) and Groupe de Geodesie Spatiale (GRGS, France). The GRIM4 model exists as a satellite only version GRIM4-S and a combined solution GRIM4-C. The GRIM4-S series of satellites is derived from optical, laser and Doppler tracking and is complete up to degree and order 50. Combination with gravity anomaly and altimetry data provides the GRIM4-C solution with coefficients complete up to degree and order 60.

The United States Department of Defense Mapping Agency (DMA) has produced the World Geodetic System (WGS) Earth gravitation models, the most recent of which WGS-84 provides harmonic coefficients to degree and order 180. The model is based on Doppler tracking data of near-Earth satellites, laser-ranging data on LAGEOS and STARLETTE, satellite altimetry data over the oceans and mean gravity anomalies derived from surface observations.

The new EGM96 model, developed jointly by NASA Goddard Space Flight Center (GSFC), the National Imagery and Mapping Agency (NIMA, formerly DMA) and The Ohio State University, provides a more accurate reference surface for the topography, improves models of the ocean circulation, improves orbit determination for low-orbiting satellites, and contributes to global and regional studies in tectonics and geodynamics. The new spherical harmonic model, is complete to degree 360, corresponding to a global resolution of about 55 km. EGM96 incorporates newly released surface gravity data from around the globe, over three decades of precise satellite tracking data and altimeter measurements of the ocean surface from the TOPEX/POSEIDON, ERS-1 and GEOSAT satellites.

B.2 Effects

A number of simple analytic expressions [RDB.1] exist which provide approximate engineering solutions for perturbations to a satellite orbit about the Earth.

The Earth is appreciably oblate, the equatorial diameter being 42,77 km greater than the polar diameter. Changes in the gravity field caused by this oblateness lead to the major perturbations to a satellite orbit. First, the orbital plane of the satellite rotates about the Earth axis in a direction opposite to the satellite motion; and secondly, the major axis of the orbit rotates in the orbital plane. A number of simple analytic expressions exist which assume that the Earth is sym-

metric about its polar axis and also consider only the dominant terms in the harmonic expansions.

The rate of nodal regression is given to first order by:

$$\dot{\Omega} = - \frac{3nC_{20}R_E^2 \cos i}{2a^2(1 - e^2)}$$

The rate of precession of the line of apsides is given to first order by:

$$\dot{\omega} = \frac{3nC_{20}R_E^2(4 - 5 \sin^2 i)}{4a^2(1 - e^2)}$$

where

a is the semimajor axis of the satellite orbit;

e is the eccentricity of the orbit;

i is the inclination of the satellite orbit;

Ω is the right ascension of ascending node of the orbit;

ω is the argument of perigee of the orbit;

$$n = \sqrt{\frac{GM_{\oplus}}{a^3}}$$

C_{20} is the spherical harmonic coefficient representing the flattening of the Earth.

These perturbations to the satellite trajectory are exploited by mission designers to achieve preferred orbital configurations optimized to a particular application.

A Sun-synchronous orbit (one where the orbital plane remains nominally fixed relative to the Sun) can be achieved by matching the nodal regression rate $\dot{\Omega}$ to the average rotation rate of the Earth around the Sun. Thus by setting $\dot{\Omega}$ to 0,9856 °/day and substituting in the appropriate values of a , e , R_E , and C_{20} , we see that Sun-synchronicity is only possible for retrograde ($i > 90^\circ$) orbits.

The precession of the line of apsides $\dot{\omega}$ is zero when the orbital inclination is set to 63,4°. This characteristic is exploited in the so-called Molniya orbit which employs a highly eccentric orbit and a frozen perigee in the southern hemisphere to provide communication coverage to high northern latitudes.

A geosynchronous orbit (one where the period of the orbit of a satellite matches the daily rotation of the Earth on its axis) can be achieved by matching the period of the orbit T to 1436 min by varying the semimajor axis of the orbit ($a_{geos} = 42\,164,5$ km) where:

$$T = \frac{2\pi}{n}$$

The longitudinal variation of the Earth gravitational field has a significant influence on geostationary orbits. The terms representing the ellipticity of the Earth's equatorial section (C_{22} and S_{22}) and oblateness (C_{20}) combine to provide the so-called triaxiality perturbation resulting in a longitudinal drift from the stable points (105,3° W and 75,1° E) of the Earth's potential field which represents an East-West station-keeping problem for a geostationary satellite.

Flury [RDB.2] provides an expression for the longitudinal acceleration:

$$\ddot{\Lambda} = k^2 \sin 2(\Lambda - \Lambda_0)$$

$\Lambda - \Lambda_0$ is the departure from the stable point

and where

$$k^2 = -18 \sqrt{C_{22}^2 + S_{22}^2} \omega_{\oplus} \frac{a_{\oplus}^2}{a_s^2} = 1,7 \times 10^{-3} \text{ °/day}^2$$

ω_{\oplus} is the sidereal rotation rate of the Earth;

a_{\oplus} is the mean equatorial radius of the Earth;

a_s is the semimajor axis of the synchronous orbit.

For satellites at low altitude (<1 000 km), the orbital perturbation due to aerodynamic forces can be significant. The passage of a satellite through an atmosphere can induce drag and lift forces. The drag force acts in the opposite direction to the satellite velocity vector relative to the atmosphere, the lift force acting perpendicular to this velocity vector. Lift forces can normally be neglected for most satellites except when precise orbit determination is required. The drag force has the dominant influence on the satellite trajectory and acts to reduce the semimajor axis and eccentricity of the orbit, and thus in turn the orbital lifetime. King-Hele has developed simple analytic expressions relating the change in a satellite orbit to the aerodynamic forces acting on it. For a circular orbit the orbital lifetime is given by:

$$L = \frac{Hm}{\sqrt{GM_{\oplus}} a \rho S C_D}$$

where

H is the density scale height of the atmosphere (see clause 7);

ρ is the atmospheric density at distance from Earth a (see clause 8);

S is the profile area of the satellite;

C_D is the drag coefficient of the satellite (see clause 7).

The gravitational attraction of the Moon and Sun influences the orbit of a satellite about the Earth. The major influence is a cyclic variation in the inclination and eccentricity of the orbit. This manifests in geosynchronous orbit as a periodic variation in the orbital inclination requiring North-South station keeping to maintain a nominally geostationary orbit. Cook [RDB.3] has derived expressions for the average rates of change of orbital elements due to the gravitational attraction of a third body.

Solar radiation pressure can also perturb a satellite trajectory from the nominal Keplerian orbit. The major influence of solar radiation pressure (see clause 6) is an increase in orbital eccentricity. At geosynchronous altitudes this can be significant and leading to active stationkeeping while at lower altitudes the effect can be neglected.

The relative magnitudes of the accelerations due to each of the perturbing sources are compared in Table B-1.

B.3 Gravitational field at the surface of a planet

The gravitational accelerations F/m at the surface of the planets given below are derived from their respective masses M and equatorial radii R .

Table B-1: Planetary gravitational characteristics

Planet	Equatorial radius, R (km)	Mass, M (kg)	GM (km ³ s ⁻²)	F/m (ms ⁻²)
Mercury	2420	$3,345 \times 10^{23}$	22 322	3,5
Venus	6200	$4,881 \times 10^{24}$	325 657	8,5
Earth	6378	$5,974 \times 10^{24}$	398 600	9,8
Mars	3400	$6,452 \times 10^{23}$	43 049	3,7
Jupiter	71 370	$1,900 \times 10^{27}$	126 754 940	25,9
Saturn	60 400	$5,687 \times 10^{26}$	37 946 762	11,1
Uranus	23 530	$8,722 \times 10^{25}$	58 195 66	10,5
Neptune	22 300	$1,033 \times 10^{26}$	68 95 788	13,8

B.4 Uncertainties

The 1σ errors associated with the spherical harmonic coefficients for JGM-2 given in Table 2 for \bar{C}_{nm} and Table 3 for \bar{S}_{nm} are given below in Table B-2 and Table B-3, respectively. The errors should be interpreted with caution as many of the coefficients have highly correlated errors, especially for higher degree terms and the zonal coefficients.

Table B-2: Covariance errors in normalized coefficients \bar{C}_{nm} (units of 10^{-6}) from JGM-2 model to degree (n) and order (m) 9

		n							
		2	3	4	5	6	7	8	9
m	0	0,0001090	0,0000261	0,0002600	0,0001570	0,0003540	0,0003620	0,0005210	0,0005730
	1		0,0004170	0,0002350	0,0008440	0,0004870	0,0012000	0,0009020	0,0013500
	2	0,0001240	0,0002660	0,0004270	0,0006760	0,0008020	0,0012400	0,0011400	0,0016000
	3		0,0002010	0,0002290	0,0003910	0,0006450	0,0008340	0,0011500	0,0013200
	4			0,0002100	0,0002510	0,0003700	0,0005470	0,0007900	0,0010100
	5				0,0002490	0,0001980	0,0003580	0,0004520	0,0007230
	6					0,0002440	0,0001630	0,0003520	0,0004600
	7						0,0003130	0,0002032	0,0003780
	8							0,0003820	0,0002840
	9								0,0004780

Table B-3: Covariance errors in normalized coefficients \bar{S}_{nm} (units of 10^{-6}) from JGM-2 model to degree (n) and order (m) 9

		n							
		2	3	4	5	6	7	8	9
m	1		0,0004160	0,0002280	0,0008490	0,0004880	0,0011800	0,0008910	0,0012700
	2	0,0001240	0,0002920	0,0004390	0,0007060	0,0008380	0,0012700	0,0012100	0,0015900
	3		0,0001970	0,0002210	0,0003840	0,0006160	0,0008390	0,0010900	0,0013300
	4			0,0002120	0,0002450	0,0003710	0,0005310	0,0007880	0,0009880
	5				0,0002480	0,0002000	0,0003680	0,0004490	0,0007310
	6					0,0002460	0,0001630	0,0003460	0,0004740
	7						0,0003090	0,0002070	0,0003690
	8							0,0003880	0,0002840
	9								0,0004750

B.5 References

- RDB.1 Fortescue P. and J. Stark, "Spacecraft Systems Engineering", ISBN 0471 95220 6, 1995.
- RDB.2 Flury W., "ELDO", ESRO Scientific and Technical Review, Vol. 5, 1973.
- RDB.3 Cook G.E., Geophysics Journal, Vol. 6, p.271, 1962.

(This page is intentionally left blank)

Annex C (informative)

Geomagnetic field

C.1 Description of magnetosphere

Figure C-1 shows a schematic of the magnetosphere, including representative field lines and the main “external” current systems. The impinging solar wind compresses the Earth’s field on the day side and elongates it on the night side, making a bow-wave and wake type structure. Although the main Earth field is relatively stable, the external currents are highly variable and affected by solar wind and interplanetary magnetic field effects resulting from solar events such as high speed streams, coronal mass ejections and shocks.

The main external current systems are:

- the ring current, flowing azimuthally around the Earth in the plasmasphere ($L \lesssim 4$);
- the cross-tail current;
- magnetopause boundary currents.

C.2 Derivation of dipole strength from field model coefficients

Considering the centred dipole terms ($n = 1, m = 0, 1$), equation 5.1 then becomes:

$$V = \frac{1}{r^2} \{ g_1^0 a^3 \cos(\theta) + g_1^1 a^3 \cos(\phi) \sin(\theta) + h_1^1 a^3 \sin(\phi) \sin(\theta) \}$$

Each of the terms represents the contribution to the total dipolar potential from dipoles aligned with the three geocentric Cartesian axes. This is easily seen since the scalar potential due to a dipole whose strength and orientation are given by a moment \mathbf{m} is:

$$V = \frac{(\mathbf{m} \cdot \mathbf{r})}{r^3} = \frac{1}{r^2} \{ m_z \cos(\theta) + m_x \cos(\phi) \sin(\theta) + m_y \sin(\phi) \sin(\theta) \}$$

Comparing these equations it is clear that the total dipole strength (moment) is therefore:

$$M = a^3 \left[(g_1^0)^2 + (g_1^1)^2 + (h_1^1)^2 \right]^{1/2}$$

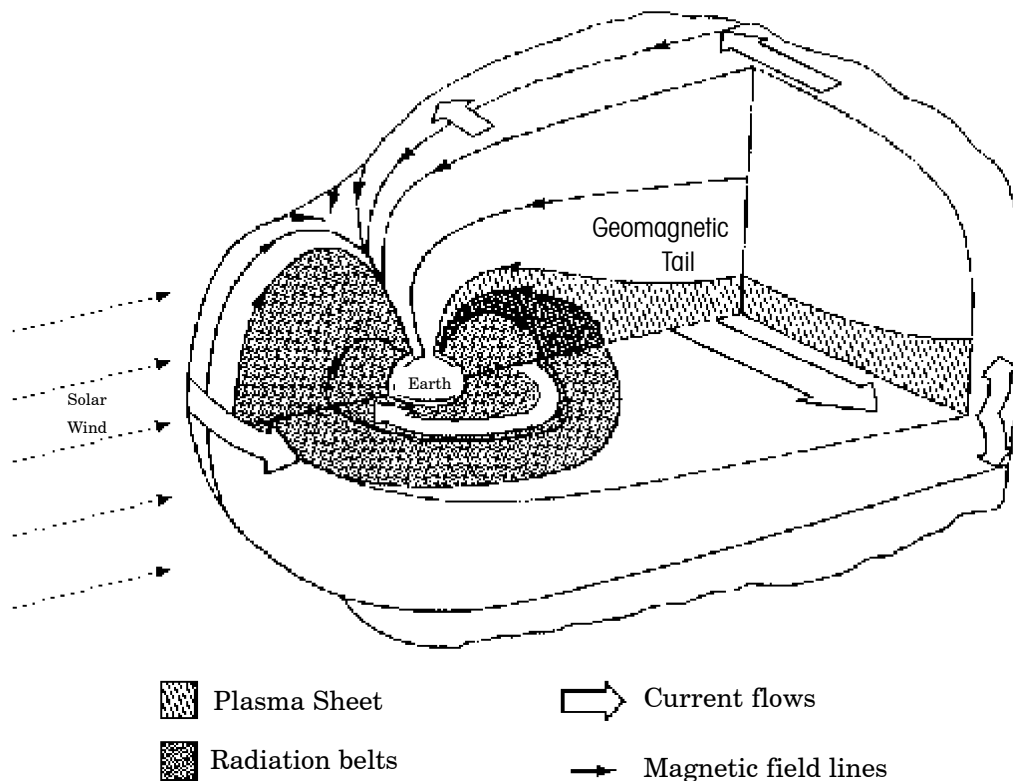


Figure C-1: Schematic of the magnetosphere showing the current flows and magnetic field lines

C.3 Incompatibilities and inconsistencies

McIlwain first established the B, L coordinate system in 1961 with a dipole moment of $31\,165,3 \text{ nT} \cdot R_E^3$ [RD C.1]. This raises an important problem. Although changes to the geomagnetic field are small, they can have a large effect if applied to radiation environment models which have large gradients of particle flux as a function of altitudes, at their lowest altitudes [RD C.2] and so are highly susceptible to error. It is therefore important when computing B, L coordinates for accessing radiation environment models to use precisely the same definition of L (and therefore value for M in equation 5.2), together with the geomagnetic field model and epoch, as were used in the production of the model in the first place.

Vette [RD C.3] indicates that the Jensen and Cain model (epoch 1960) was used throughout this modelling. However, even this subsequently appears to be wrong [RD C.2]. Therefore, use of the models defined in clause 9, together with $M=31\,165,3$, shall be regarded as the standard for computing B, L for radiation environment models until provisions for employing more recent models can be made.

C.4 IGRF model details and availability

The formal contact point for the IGRF series models is:

IGRF Secretariat, NASA/GSFC, Code 921

Greenbelt, Maryland 20771

langel@geomag.gsfc.nasa.gov

However, the model is available via WWW or FTP at:

<ftp://nssdc.gsfc.nasa.gov/pub/models/>

and more information is available at:

<http://nssdc.gsfc.nasa.gov/space/model/magnetos/>

The IGRF-95 model consists of coefficient sets for the epochs 1945 to 1995 in steps of five years and the first time derivatives of the coefficients for the time period 1995 to 2000. During the 5-year intervals between consecutive models, linear interpolation is recommended. The IGRF coefficients for 1945, 1950, ... 1985, 1990 are definitive coefficient sets, referred to by the title DGRF.

In combination with the IGRF coefficient sets different subroutines have been used to determine the components of the magnetic field vector and the L -value at a given location. The standard version uses the subroutines FELDG (magnetic field vector) and SHELLG (L shell) developed by G. Kluge (ESA/ESOC). His use of inverse Cartesian coordinates simplifies the computation. The IGRF subroutines were developed by A. Zunde of the U.S. Geological Survey (USGS). The program BILCAL produces tables of the geomagnetic field strength, vector components ($B_{abs.}$, B_{north} , B_{east} , B_{down} , declination, inclination), equatorial/minimum field strength (B_0), dipole moment, and L -value in latitude, longitude (geodetic), altitude, or year (decimal).

Models referred to in clause 5 for the perturbations to the Earth field from external sources are available from the NSSDC www site (<http://nssdc.gsfc.nasa.gov/space/model/>).

Models and access routines are also available in Europe from BIRA/IASB (B) and via the WWW at <http://www.spenvis.oma.be/spenvis>, the Space Environment Information System.

C.5 References

- RDC.1 McIlwain C.E., "Coordinates for Mapping the Distribution of Geomagnetically Trapped Particles", J. Geophys. Res. 66, 3681 (1961).
- RDC.2 Lemaire J., E.J. Daly, J.I. Vette, C.E. McIlwain and S. McKenna-Lawlor, "Secular Variations in the Geomagnetic Field and Calculations of Future Low Altitude Radiation Environments", Proceedings of the ESA Workshop on Space Environment Analysis, ESA WPP-23, ESTEC/WMA, Noordwijk, The Netherlands, October 1990.
- RDC.3 Vette J.I., "The NASA/National Space Science Data Center Trapped Radiation Environment Model Program (1964-1991)", NSSDC WDC-R&S Report 91-29, p.21, NASA-GSFC-NSSDC, November 1991.

(This page is intentionally left blank)

Annex D (informative)

Solar and Earth electromagnetic radiation and indices

D.1 Solar spectrum details

Figure D-1 shows the solar irradiation spectrum at sea level and outside the Earth atmosphere.

Solar irradiance values (in photons/cm² s⁻¹) and energy fluxes (in W/cm²) for the wavelength range 175,439 nm to 852,5 nm, split into small intervals, are given in [RDD.1] and reproduced in [RDD.2].

The ASTM standard [RDD.3] defines a solar spectral irradiance curve for the wavelength range 115 nm to 400000 nm.

D.2 Albedo and infrared variability

Information on the variability of the albedo and the Earth infrared radiation can be found in [RDD.2].

As an example, Table D-1 gives the mean albedo data for 30°, 60° and 90° inclination orbits. These are average values taken from [RDD.2]. The average albedo from Table D-1 (and also the average from other, more extensive data, given in [RDD.2]) appears to be somewhat below the standard average value of 0,3.

The values are the reflected fraction. The given percentile is the probability that the indicated albedo value is not exceeded. The albedo values are corrected to zero zenith angle.

Table D-1: Running mean (averaged over 90 minutes) albedo percentile data

Orbit Incl.	3 %	50 %	97 %
30°	0,14	0,18	0,22
60°	0,17	0,23	0,32
90°	0,18	0,25	0,34

A value of 0,3 and the same spectrum as the Sun were specified as standard for the Earth albedo. On a short time scale, albedo can be very variable and range from about 0,05 to 0,6.

In addition, the albedo spectrum can change, depending on properties of the surface and atmosphere. Ground vegetation and atmospheric water and dust can lead to absorption in certain wavelength bands and result in a highly variable albedo spectrum.

Table D-2 gives running mean values for the Earth emitted infrared radiation for 30°, 60° and 90° inclination orbits. These are average values taken from [RDD.2]. The given percentile is the probability that the indicated infrared radiation value is not exceeded.

Table D-2: Running mean (averaged over 90 minutes) Earth infrared radiation percentile values in units of W/m²

Orbit Incl.	3 %	50 %	97 %
30°	227	246	265
60°	211	233	255
90°	205	227	250

D.3 Activity indices information

Figures D-2 and D-3 show the $F_{10,7}$, Sunspot Number (SSN) and A_p indices over the last two solar cycles. Figure D-2 gives the daily and Figure D-3 the monthly mean values. The large fluctuations in the daily values are averaged out in the monthly mean values (please note the different scale of the figures). The short term A_p spikes are important for density variations and this is not well reflected in the long term high values.

The long term predictions of average solar activity, as given in Table 11 (see clause 6) can bias by mild cycles. The solar activity of the last two cycles clearly exceeded the long term average.

Regular updates of measured and predicted activity values are provided by the Marshall Space Flight Center [RDD.4a] and the National Geophysical Data Center [RDD.4b]. Indices are available via the World Wide Web:

<http://www.ngdc.noaa.gov/>

D.4 Radio noise

The magnetosphere-ionosphere system is filled with natural plasma emission sources. Fig. D.4 presents an overview of the natural plasma noise levels from near-Earth, solar and some cosmic sources (taken from [RDD.2]).

Electromagnetic radiation with frequencies below the peak plasma frequency of 1 MHz to 10 MHz is most likely negligible for spacecraft if the source is below about 200 km. The main near-Earth noise sources above that altitude are auroral arcs and ionospheric irregularities.

Man-made narrow band sources from 1 MHz to 300 GHz can be important for orbiting spacecraft.

D.5 Solar radiation pressure

A spacecraft moving within the solar system experiences a perturbation to its trajectory due to the incidence of solar radiation upon its illuminated surfaces. Electromagnetic radiation carries momentum and the reflection of incident radiation at a surface represents an exchange of momentum. The solar radiation exerts a small pressure, SRP, on a spacecraft given by:

$$SRP = \frac{F}{c}$$

where F is the solar energy flux at the spacecraft and c is the speed of light.

The effect of this solar radiation pressure as a force acting upon the vehicle is dependent upon the reflective characteristics of the spacecraft surfaces.

The perturbing effect upon a spacecraft's trajectory is directly dependent upon the vehicle's area to mass ratio and inversely proportional to the square of its distance from the Sun.

Hence the disturbing acceleration due to solar radiation F_{SRP} , acting along the Sun-spacecraft line, can be expressed as:

$$F_{SRP} = R \frac{A}{m} SRP \left(\frac{a_s}{r_s} \right)^2$$

where

R is a constant whose value depends upon the reflective properties of the surface;

r_s is the distance of the satellite from the Sun;

a_s is the mean distance of the Earth from the Sun;

A is the area of the satellite;

m is the mass of the satellite.

D.6 Figures

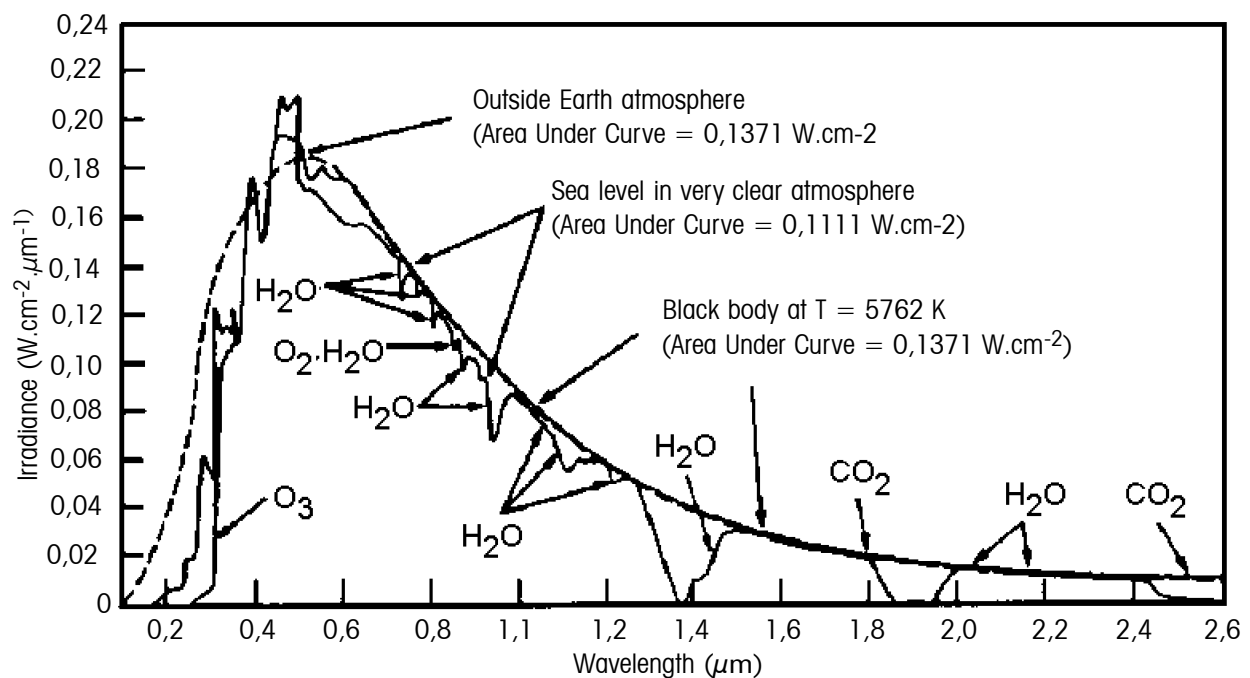


Figure D-1: Normally incident solar radiation at sea level on very clear days, solar spectral irradiance outside the Earth atmosphere at 1 AU, and black body spectral irradiance curve at T=5762 K.

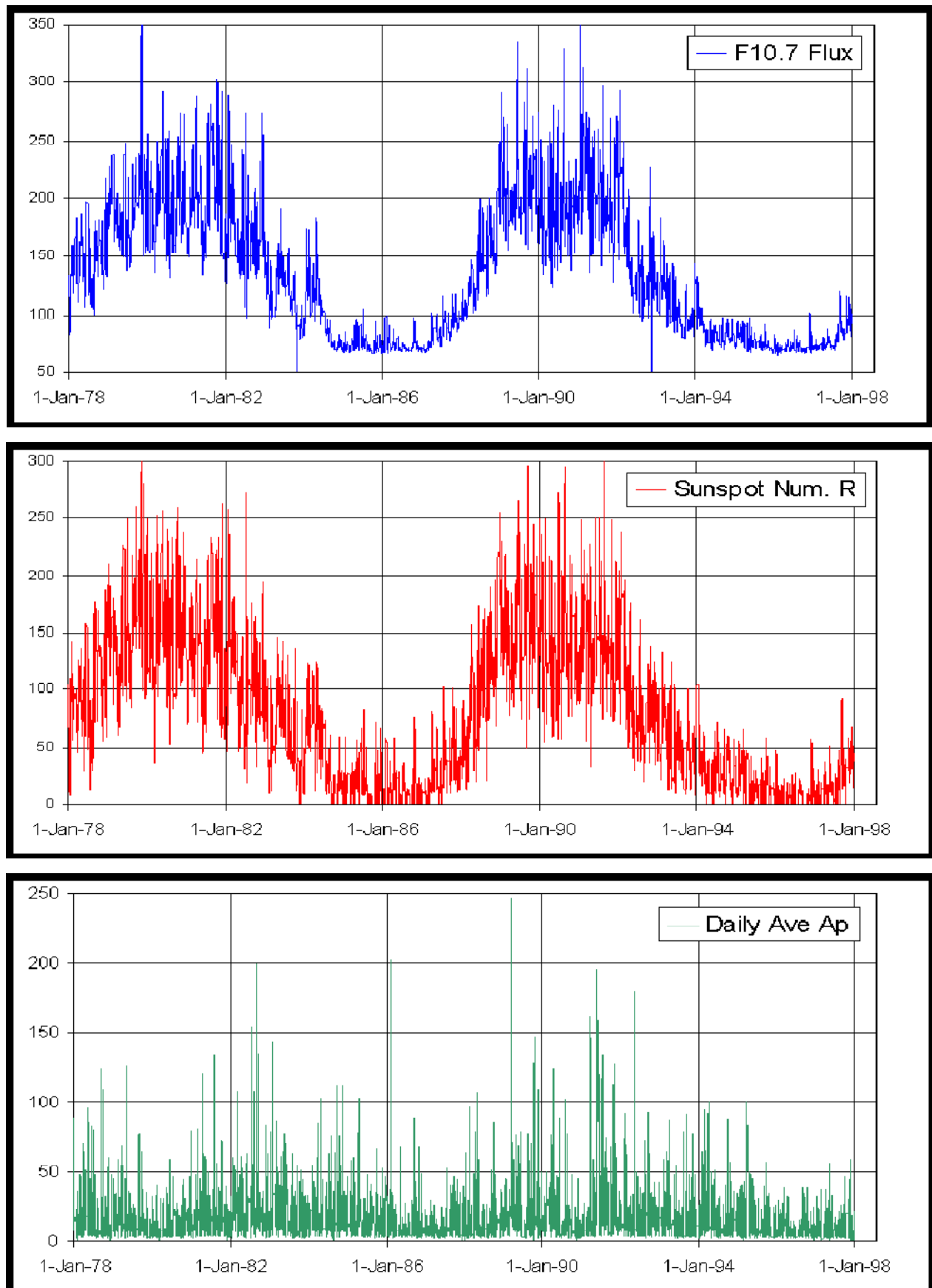


Figure D-2: Daily solar and geomagnetic activity indices over the last two solar cycles.

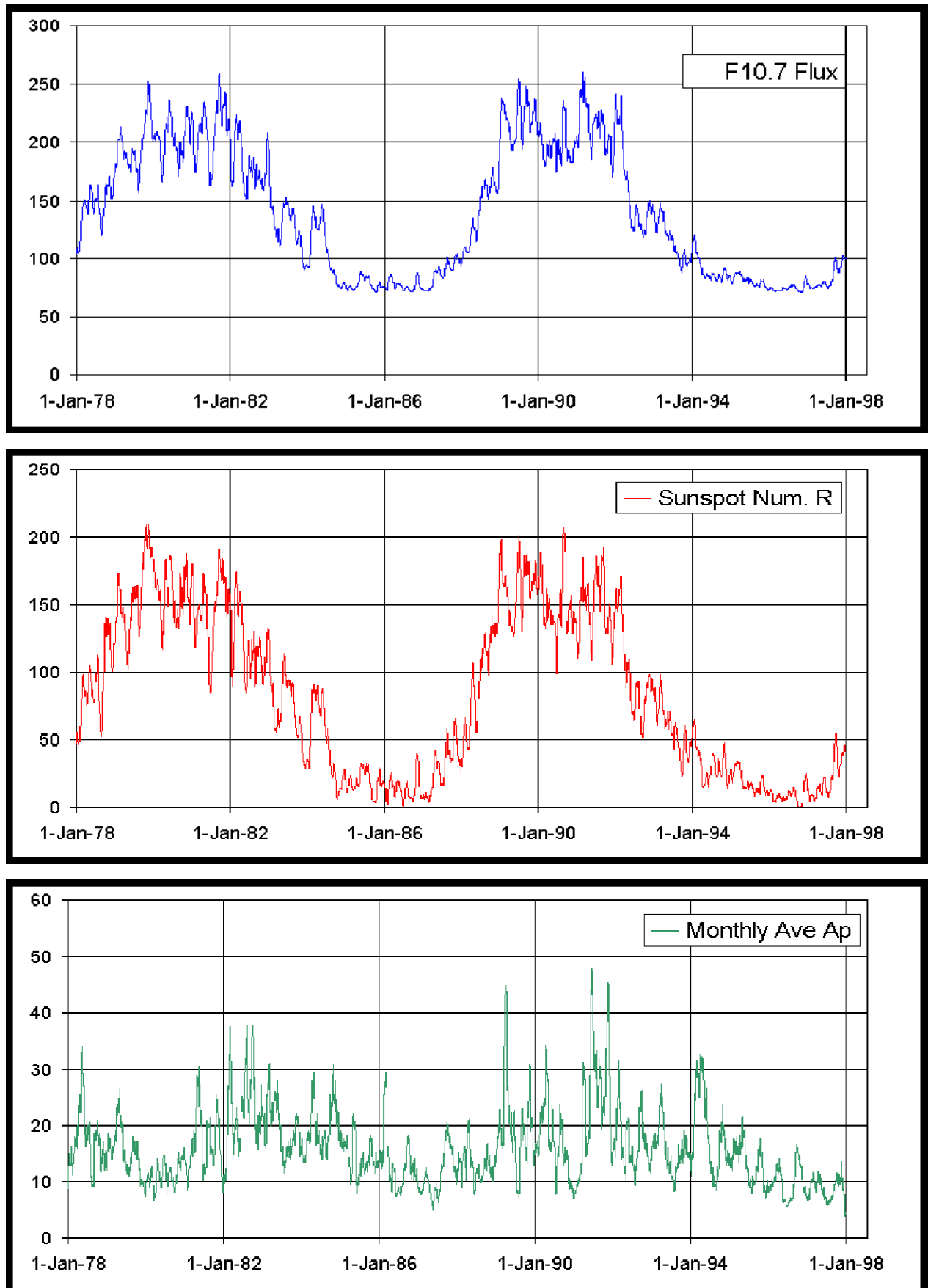


Figure D-3: Monthly mean solar and geomagnetic activity indices over the last two solar cycles.

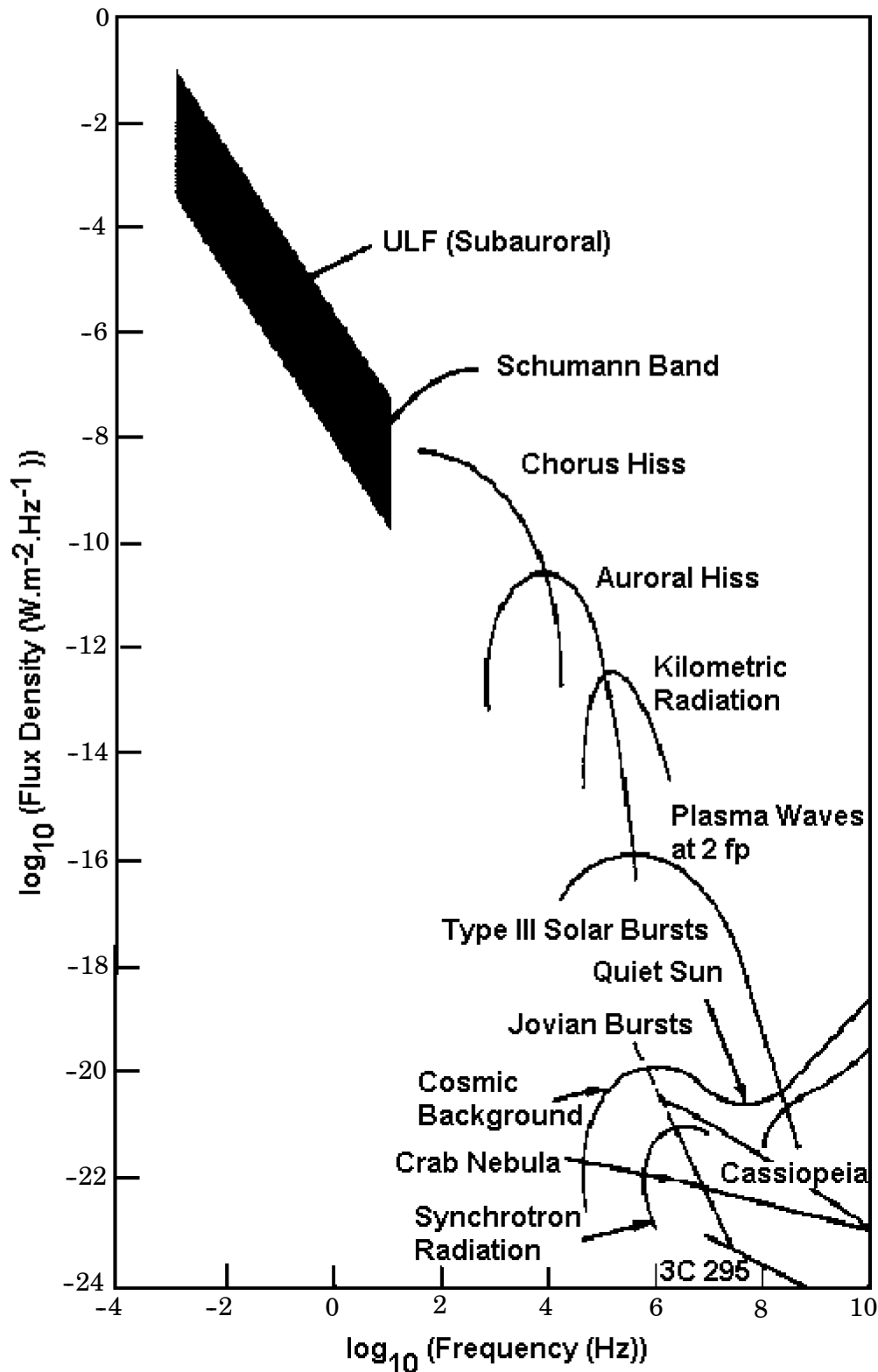


Figure D-4: Power flux levels for various frequency ranges of naturally occurring electromagnetic and plasma waves (from [RDD.2]).

D.7 References

- RDD.1 World Meteorological Organization, Compiler: "Atmospheric Ozone 1985, Assessment of Our Understanding of the Processes Controlling Its Present Distribution and Change", World Meteorological Organization Report, No. 16, Vol.1 Chapter 7, 1985.
- RDD.2 "Natural Orbital Environment Guidelines for Use in Aerospace Vehicle Development", B.J. Anderson, editor and R.E. Smith, compiler; NASA TM 4527, Chapters 6 and 9, June 1994.
- RDD.3 "Standard Solar Constant and Air Mass Zero Solar Spectral Irradiance Tables", American Society for Testing and Materials, ASTM standard E 490-73a (Reapproved 1992).
- RDD.4
 - a) "Solar Activity Inputs for Upper Atmospheric Models", George C. Marshall Space Flight Center, Updates of measured and predicted activities are distributed monthly.
 - b) Weekly measurements of solar and geomagnetic activity levels are published by the National Geophysical Data Center, Boulder.

(This page is intentionally left blank)

Annex E (informative)

The neutral Earth atmosphere

E.1 Overview of atmosphere models

Early models of the thermosphere emerged around 1965 (e.g. Harris-Priester, Jacchia-65). These, as well as their descendants Jacchia-71 [RDE.1], CIRA-72 [RDE.2], and Jacchia-77 [RDE.3], were based on a numerical quadrature of the species-wise diffusion equations. In these models the altitude profile of the number densities n_i is largely determined by the magnitude of the exospheric temperature T_∞ . This quantity is used to accommodate all activity related and diurnal effects, while semi-annual variations are introduced via empirical correction functions. In the Jacchia-77 model species-wise corrections are also introduced for diurnal, seasonal/latitudinal, and geomagnetic effects. The numerical quadrature can be very CPU demanding in orbit predictions. To improve the turn around time for calls to such routines, Mueller [RDE.4] implemented the Jacchia-Lineberry algorithm for the Jacchia-71 [RDE.1] model, and Lafontaine [RDE.5] developed an equally efficient method to approximate the Jacchia-77 model. The MET-87 model (Marshall Engineering Thermosphere Model, [RDE.6]) is also based on the early Jacchia-71 atmosphere, but it extends the range of output quantities, including pressure, pressure scale height, and ratio of specific heats.

Another line of atmosphere models directly applies analytical solutions of simplified diffusion equations to derive concentration profiles. The most prominent class of these models is called MSIS (Mass Spectrometer and Incoherent Scatter, [RDE.7, RDE.8, RDE.9]).

The MSIS models were continuously improved in 1977, 1983, and 1986 as new measurement data and new analysis results became available. MSIS-86 also became the CIRA-86 reference atmosphere for thermospheric altitudes. Recently, MSIS 86 has been upgraded to MSISE-90 by a continuation to ground level with smooth density and temperature profiles. The DTM-77 model (Density and Temperature Model) by Barlier et al. has a similar structure as MSIS-77 but limits itself to the constituents N_2 , O_2 , O , and He [RDE.10, RDE.11]. Hydrogen, which becomes dominant at high altitudes especially for low activity levels, is not taken into account. The C model by Proelss et al. [RDE.12] also has a MSIS-77 structure with modified correction functions. The advantage of MSIS, DTM, and C lies in their model flexibility to account for observed changes, and in their comprehensive range of output results (including number densities).

A third class of thermosphere models only aims at total densities as output result. The underlying data of the Russian GOST-84 model [RDE.13] are solely derived from satellite drag analysis. Total density is computed from a reference altitude profile which is adjusted by four factors accounting for (1) diurnal, (2) seasonal/latitudinal, (3) solar activity, and (4) geomagnetic activity effects. An updated set of model coefficients has been published in 1990. The TD-88 model by Sehnal et al. [RDE.14] is more flexible in its formulation, since TD-88 does not assume a rigorous separation of perturbing effects (factorization of corrections) as is done by GOST-84. The TD-88 model, however, should only be applied to altitudes from 150 km to 750 km.

E.2 Accessibility of the MSISE-90 model

The MSISE-90 model can be obtained via “<ftp://nssdc.gsfc.nasa.gov/pub/models/msise90>” from the NSSDC Web homepage. In applications which require a smooth, continuous density profile with altitude the “departure from diffusive equilibrium” option in MSISE-90 should be switched off (corresponding to switch setting SW(15) = 0,0).

E.3 References

- RDE.1 Jacchia L.G., “Revised Static Models of the Thermosphere and Exosphere with Empirical Temperature Profiles”, SAO Report No. 332, May 5, 1971.
- RDE.2 anon., “CIRA-72 (COSPAR International Reference Atmosphere 1972)”, Akademie Verlag, Berlin, 1972.
- RDE.3 Jacchia L.G., “Thermospheric Temperature, Density, and Composition – New Models”, SAO Report No. 375, March 15, 1977.
- RDE.4 Mueller A., “Jacchia-Lineberry Upper Atmosphere Density Model”, NASA Report 82-FM-52/JSC-18507, Oct. 1982.
- RDE.5 Lafontaine J. de and P. Hughes, “An Analytic Version of Jacchia’s 1977 Model Atmosphere”, *Celestial Mechanics* 29 (1983), pp 3–26, 1983.
- RDE.6 Hickey M.P., “The NASA Marshall Engineering Thermospheric Model”, NASA CR-179359, July 1988.
- RDE.7 Hedin A.E., “MSIS-86 Thermospheric Model”, *J. Geophys. Res.*, Vol. 92, No. A5, pp 4649–4662, May 1, 1987.
- RDE.8 Hedin A.E., “Extension of the MSIS Thermosphere Model into the Middle and Lower Atmosphere”, *J. Geophys. Res.*, Vol. 96, No. A2, pp. 1159–1172, Feb. 1, 1991
- RDE.9 Hedin A.E. et al., “Revised Global Model of Thermosphere Winds Using Satellite and Ground-Based Observations”, *J. Geophys. Res.*, Vol. 96, No. A5, pp. 7657–7688, May 1, 1991
- RDE.10 Barlier F., C. Berger, J.L. Falin, G. Kocharts and G. Thuiller, “A Thermospheric Model Based on Satellite Drag Data”, *Aeronomica Acta A-No. 185*, 1977.
- RDE.11 Koehnlein W. et al., “A Thermospheric Model of the Annual Variations of He, N, O, N₂ and Ar from AEROS Nims Data”, *J. Geophys. Res.*, Vol. 84, pp. 4355–4362, 1979.
- RDE.12 Proelss G.W. and Blum P.W., “Comparison of Recent Empirical Models of the Thermosphere”, in *Proceedings of ESA workshop on Re-Entry of Space Debris*, Darmstadt, 24–25 September 1985 (ESA SP-245)
- RDE.13 anon., “Density Model for Satellite Orbit Predictions”, GOST 25645–84, Standards Editing House, Moscow, 1984.
- RDE.14 Sehnal L. and L. Pospisilova, “Thermospheric Model TD 88”, Pre-print No. 67, Observatory Ondrejov, 1988.

Annex F (informative)

Plasma

F.1 Surface charging

This is principally a phenomenon that occurs in the outer magnetosphere, where plasma temperatures are high, but can also occur in the auroral zone, due to high fluxes of precipitating energetic electrons. High-level electrostatic charging results from the tendency for surfaces to achieve an equilibrium where there is a balance of the currents to them:

$$I_e + I_p + I_{se} + I_{be} + I_{sp} + I_{ph} + I_{cond} = 0$$

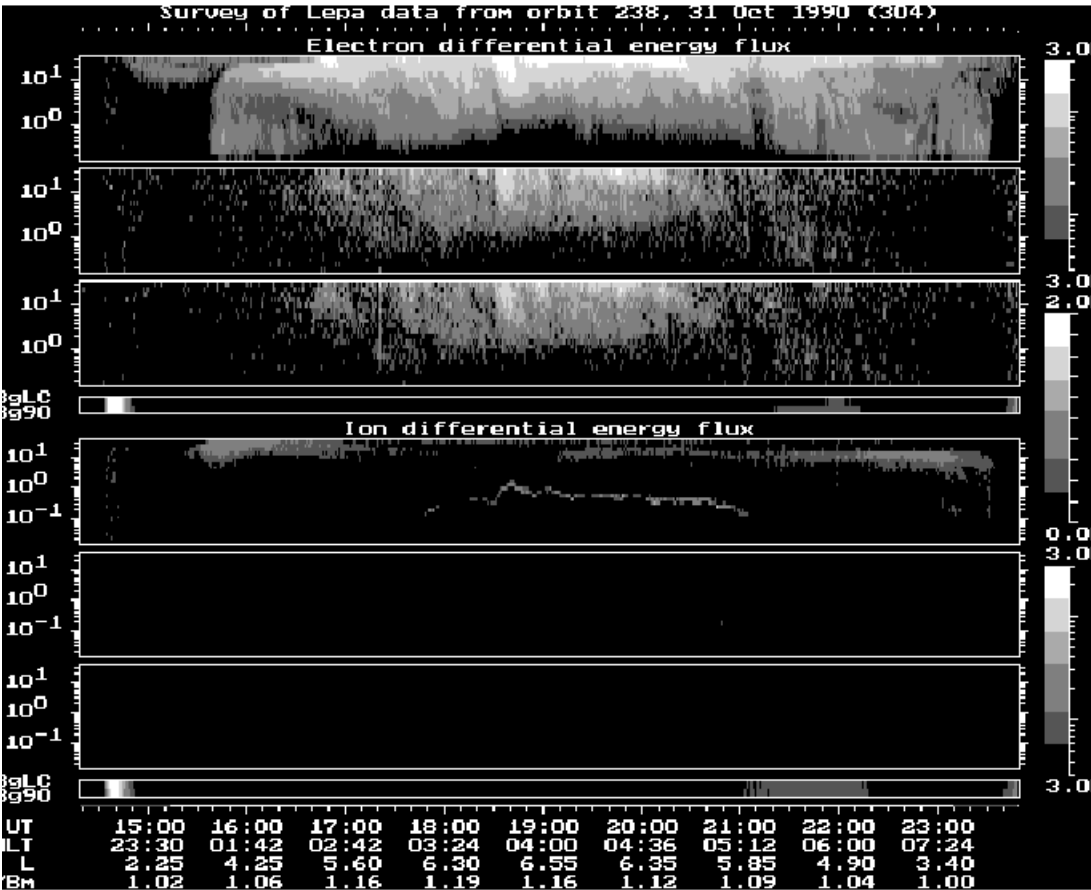
where

I_e	is the electron ambient current. This is the driver of high-level charging to negative potential;
I_p	is the ion ambient current. This counters negative charging but is weaker than electron current, since flux is proportional to $(KT/M)^{1/2}$;
I_{se}	is the low-energy secondary electrons resulting from electron impact. This is strongly material-dependent. Yield can be > 1 for low-energy impacting electrons;
I_{be}	is the back-scattered primary electrons;
I_{sp}	is the low-energy secondary electrons resulting from ion impact;
I_{ph}	is the low-energy photoemitted electrons due to solar UV. This is usually the dominant counter-charging current in sunlight;
I_{cond}	is the current between spacecraft surfaces, via material resistivity.

Charging occurs when I_e dominates the other currents. The surface potential becomes increasingly negative until this current becomes diminished by the potential barrier and equality with the other currents is achieved. Because secondary emission, back-scatter, photoemission and conductivity all depend on material properties, the flux and spectrum of the incident electrons, required to cause charging, depend on the material. The secondary emission coefficient (σ) is crucial, peaking usually for incident electrons of energy $< 1,5$ keV. If σ is greater than one, the net electron current opposes charging. At higher-energy the yield falls and as a result, the higher-energy component of the environment is important in driving charging. In sunlight, a surface emits a high flux of low-energy electrons which opposes charging. Darkness, due to satellite eclipse or self-shadowing, removes this photoelectron emission and high-level charging is more likely in these conditions.

Charging of a whole spacecraft is not usually hazardous, although it can interfere with the operation of scientific instruments. Danger to the spacecraft itself usually results from differential charging i.e. where different parts of the spacecraft are charged to different levels. This occurs because of the different material characteristics and orientation of different surfaces. The resulting electrostatic discharges between adjacent surfaces or between surfaces and ground can cause current spikes in sensitive electronic circuitry.

Figure F-1 shows a charging event as detected by the Low Energy Plasma Analyser on CRRES. The narrow band in the top ion spectrogram, between 18 UT and 21 UT, corresponds to cold ions that are accelerated into the detector by the spacecraft potential. On this occasion, the spacecraft potential reached more than 1 kV. This occurred when electron fluxes above 10 keV were most enhanced.



The three frames for each species correspond to look directions perpendicular to the field, field-aligned (looking equator-ward) and field-aligned (looking Earth-ward). (Courtesy of MSSL/UCL)

Figure F-1: Spectrograms showing electron and ion fluxes during a charging event

F.2 Charging in LEO

Charging in LEO occurs for the same reasons as charging elsewhere, i.e. due to high fluxes of electrons with energy a few kilo electron-volts or higher. This limits LEO charging to the auroral zone. However, at low altitudes, there is a substantial cold ion population which tends to neutralize negative potentials. Hence charging occurs less readily, and preferentially on wake surfaces, where ion densities are reduced. It rarely achieves the potentials seen in the outer magnetosphere but causes a greater amount of sputtering due to the high ion density.

Figure F-2 shows the charging potential seen during an auroral crossing by DMSP F6 in November 1983. The spacecraft potential showed little correlation with electron total flux but peaked when electron fluxes above 14 keV were high.

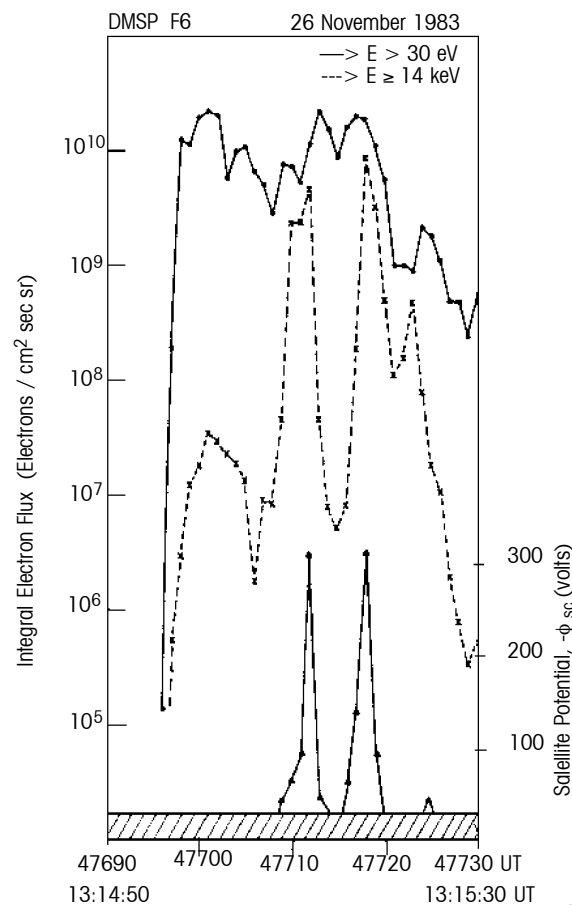


Figure F-2: Satellite potential and electron integral number flux above 30 eV and 14 keV [RDF.1]

Yeh and Gussenhoven [RDF.2] performed a statistical survey of environments seen by the DMSP satellite and their relationship with LEO charging levels. Various models are given, corresponding to different observed spectral shapes and reflecting the origin of the electrons:

- Type 1: low-energy Maxwellian + accelerated Maxwellian;
- Type 2: constant at low-energy + accelerated Maxwellian;
- Type 3: double-exponential + accelerated Maxwellian.

About 50 % of the >100 V charging events corresponded to type 2 and this is the type of spectrum adopted by MIL-STD-1809 [RDF.3] and used in this Standard. The transition between low and high-energy parts is at energies in the range 12–18 keV and the accelerated Maxwellian has temperatures of 4–7 keV.

F.3 NASCAP charging code

The most commonly used code in the West, for simulating surface charging in the outer magnetosphere, is NASCAP or NASCAP-GEO [RDF.4]. This calculates the total current, due to all the current contributions, for each surface on a numerically modelled 3-D spacecraft, using a two Maxwellian environment for both ions and electrons. From these currents, the change in potential at each surface is calculated. The current and potential calculations can be performed iteratively until an equilibrium charging state is achieved. Where spacecraft geometry is

unimportant because all that is required is the susceptibility of a particular material to charging in a particular environment, then a simple 1-D code, MATCHG [RDF.4], based on a subset of NASCAP subroutines, can be used. Current collection in both codes is determined using the “thick sheath” approximation i.e. assuming that the Debye length is long compared to the spacecraft dimensions. This approach is valid at GEO but for charging in low-altitude auroral conditions a different approach is needed.

In Figure F-3, MATCHG has been used to show the different charging responses to changing electron temperature of a number of typical materials found in space. Each is for a single Maxwellian distribution with density 1 cm^{-3} , in eclipse. For each material, the potential rises with electron temperature but the different secondary emission characteristics means that there is a wide difference between different materials.

Ion and electron density of 1 cm^{-3} is assumed and an ion temperature of 10 keV. For each material the secondary yield maximum and the energy at which it occurs is given.

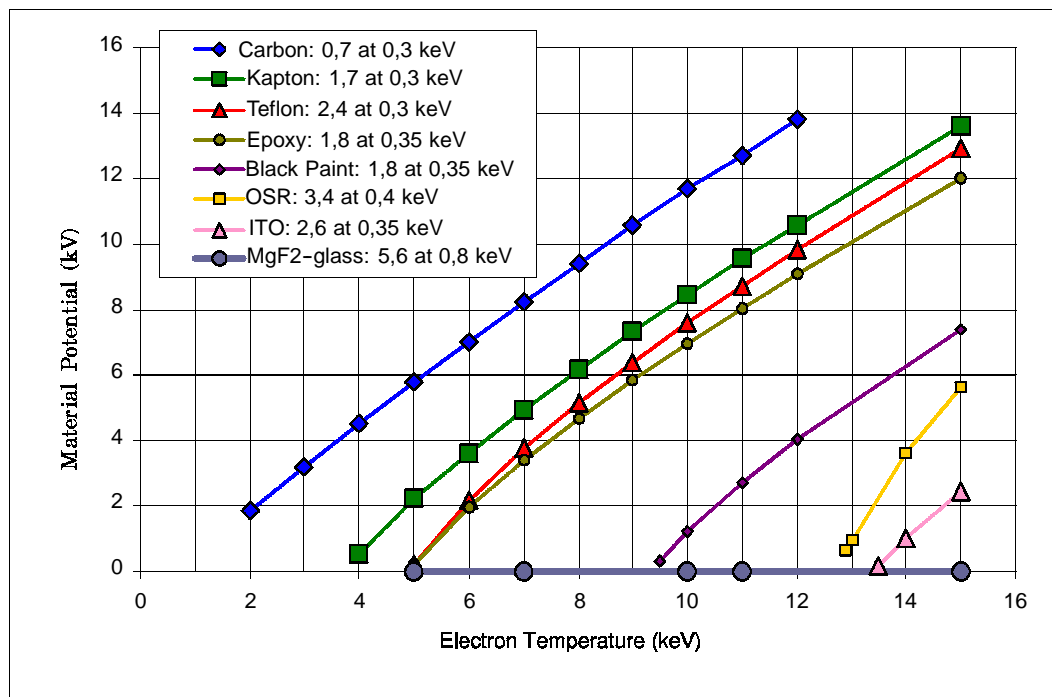


Figure F-3: Surface potential vs. electron temperature for a number of materials

F.4 POLAR charging code

The main problem with computing charging in LEO is computing effects associated with the spacecraft sheath. The most notable computational tool for assessing interactions and charging at low altitudes is the 3-D POLAR code [RDF.5]. This uses numerical techniques to track ambient ions inwards from the electrostatic sheath surrounding a negatively charged spacecraft, onto the spacecraft surface. Spacecraft velocity is included as an input and ram and wake effects are simulated. One or two Maxwellian components may be used to define the ambient plasma. The electron population in POLAR is a superposition of power-law, Maxwellian, and Gaussian components. Once the surface currents have been found, POLAR calculates potentials and equilibrium charging state in a similar way to NASCAP.

F.5 Other charging codes

There are a number of other codes available to simulate surface charging. Two Russian codes ECO-M [RDF.6] and COULOMB [RDF.7] perform a very similar function to NASCAP and POLAR and a LEO version of NASCAP, called NASCAP-LEO [RDF.8] also exists. A 1-D charging code, called EQUIPOT [RDF.9] performs computations assuming either thick-sheath or thin-sheath current collection and is thus applicable to GEO and LEO charging.

This code is available in the Space Environment Information System (Spennis) at <http://www.spennis.oma.be/spennis/>.

Whilst charging codes are usually a good indicator of whether a spacecraft design is susceptible to charging or not, it is very difficult to quantitatively calculate charging potentials. The main reason for this is that the equilibrium potential is highly sensitive on material properties, such as secondary emission coefficient. These properties are very difficult to measure on the ground and, in any case, frequently change in orbit.

F.6 NASA worst case charging environment

The NASA worst case charging environment for the outer magnetosphere [RDF.10] is widely used in spacecraft charging assessment and is different from the one defined in this standard. NASA chose a worst case charging event derived from the 90th percentile ion and electron environments.

Table F-1: NASA worst-case environment

Ne (cm ⁻³)	Te (KeV)	Ni (cm ⁻³)	Ti (KeV)
1,12	12	0,236	29,5

Since severe ion and electron environments do not necessarily happen at the same time it is felt that this environment is overly severe. Hence in this standard, an extreme environment, known to produce severe charging has been specified.

F.7 Ram and wake effects

When a spacecraft velocity is higher than or comparable to the ion acoustic velocity, it distorts the plasma environment it experiences, creating a void of particles behind it and often a build-up of particles before it. These effects are seen principally in the ionosphere. The ion acoustic velocity is the speed at which pressure differences are transmitted through a plasma and is defined as:

$$V_s = \left(\frac{KT_e + \gamma kT_i}{M} \right)^{1/2}$$

where

V_s is the acoustic velocity in m s⁻¹;

k is the Boltzmann constant;

T_e and T_i are the electron and ion temperatures, respectively, in K;

M is the ion mass in kg;

γ is a constant, usually 3.

Taking typical parameters for the 300 km ionosphere ($T_e = T_i = 1000$ K, Composition 77 % O⁺, 20 % H⁺, 3 % He⁺) this velocity is 1,5 km/s. A spacecraft in a circular orbit at this altitude has a velocity V of 7,7 km/s. Hence the spacecraft motion is supersonic. As the spacecraft moves through the plasma it sweeps up particles ahead of it and the plasma is too slow to fill in the void behind it as soon as it passes by. The result is that there is a wake behind the spacecraft with essentially none of the local cold plasma in it. The length of the wake depends on the Mach number

V/V_s of the spacecraft and its width. In the ram direction, density can be enhanced by back-scattering of ions from the front of the spacecraft.

Wake creation can be used to create an extremely pure vacuum for materials processing in space. It is also a means for creating charging conditions in low Earth orbit because potentials created by energetic auroral electrons are not neutralized by the ambient ions. Under these conditions the wake can become very complex because ion trajectories can be bent and accelerated by the potential, partially filling the wake. The resulting intense flux of ions can increase erosion by sputtering.

F.8 Current collection effects

In the ionosphere, the intense plasma density means there is an ample supply of ions and electrons which tend to neutralize high potential surfaces on spacecraft. However, on solar panels, high potentials are maintained by the action of sunlight on photovoltaic cells. In this case, the incident ions and electrons, collected on the negative and positive ends of the solar array respectively, act as a current travelling through the ionospheric plasma. This current is hence not available to drive spacecraft systems and so the efficiency of the solar panels is effectively diminished.

The different mobilities of the ions and electrons means that electrons are collected more easily than ions. This drives the positive end of the array towards space potential and leaves the negative end at high negative potential. The precise potentials at equilibrium depend on the exposed areas on the array and on the rest of the spacecraft. The grounding strategy of a spacecraft can be very important in determining spacecraft potential under these circumstances. If spacecraft ground is attached to the positive end of the array, it floats at a small positive potential. If it is attached to the negative end, it floats at a negative potential, which depends on the collecting area but which is generally a high fraction of the total potential across the solar array. This situation can be quite hazardous, as it increases the possibility of arcing between ground and insulated surfaces and leads to enhanced sputtering by impacting ions. A study of grounding strategy on Space Station Freedom [RDF.11] showed that a total array potential difference of 160 V results in structure ground being between -115 V and -150 V, if the structure were negatively grounded. The study showed that this situation can be corrected by use of a plasma contactor, emitting a sufficiently high current of electrons.

F.9 Sputtering

Sputtering is the removal of surface material by the impact of ions. Where thin surface coatings are used, this can significantly alter surface characteristics over time and produces a contaminant population which may adhere to other surfaces. The overwhelming majority of sputtered products are neutral atoms, although 2 %-4 % may be emitted as ions. In the ionosphere, the spacecraft ram velocity can cause significant sputtering due to the dense ion and neutral population, even though the yield per impact can be very low (around 10^{-6} [RDF.12]). Sputtering is expected to be considerably enhanced when high spacecraft potential, caused by spacecraft charging or an inappropriate grounding strategy, causes cold ionospheric ions to be accelerated onto the spacecraft surface. Peak yields are generally higher for higher atomic number ions and occur at higher energies. For He^+ on Al, the yield peaks just below 1, at 1 keV [RDF.13].

In the outer magnetosphere, where charging events are more common, sputtering has been observed to produce a small contaminant ion population [RDF.14]. The high flow velocity of the solar wind gives a proton a kinetic energy of typically 1,5 keV, is expected to give significant sputtering rates in this region too. A comprehensive theory for how sputtering occurs is given by Sigmund [RDF.15] and

Thompson [RDF.16]. Irrespective of the incident ion species or energy, the sputtered atoms have energies of about 10 eV [RDF.13].

F.10 Ionospheric propagation effects

The most significant propagation effect of the ionosphere is the reflection of waves below a critical frequency, called the plasma frequency, so that communications between ground-stations and spacecraft shall take place at higher frequencies. The plasma frequency is a function of electron density, as described below and is typically between 1 MHz and 9 MHz.

$$f_p = \frac{1}{2\pi} \left(\frac{N_e e^2}{\epsilon_0 m_e} \right)^{1/2} \quad \text{or} \quad f_p = 9 N_e^{1/2}$$

where

f_p is the plasma frequency in s^{-1} ;

N_e is the electron density in m^{-3} ;

ϵ_0 and m_e are natural constants.

For high-accuracy positioning of radio beacons by range or range rate measurement between a satellite and a ground-based beacon and for radar altimetry, the propagation delay caused by ionospheric plasma density shall be considered to achieve accurate range measurements. This delay can be expressed as:

$$\Delta T = - \frac{4,03 \times 10^3 N}{c f^2}$$

where

ΔT is the propagation delay in seconds;

N is the electron column density along the path in m^{-2} ;

c is the velocity of light;

f is the frequency in s^{-1} .

Since the models described in this Standard do not reflect time variations in ionospheric density, altitude corrections for radar altimetry purposes are, in practice, usually made by comparing radio propagation delays at two frequencies. The change in propagation speed of radio waves also means that refraction needs to be considered when calculating satellite orbits by radio tracking.

Below 300 MHz degradation of radio signals can occur, principally due to scintillation caused by ionospheric irregularities. Other propagation effects are dispersion, absorption and Faraday rotation.

F.11 Availability of the IRI95 model

The International Reference Ionosphere 95 [RDF.17, RDF.18] can be obtained via the World-Wide Web at:

<ftp://nssdc.gsfc.nasa.gov/pub/models/ionospheric/iri/iri95/>

It can also be obtained on 2 floppy disks from the National Space Science Data Center request office by sending a request to:

request@nssdca.gsfc.nasa.gov

or by contacting:

NSSDC
 COSPAR/ URSI Working Group on IRI
 NASA/GSFC
 Code 933
 Greenbelt MD 20771
 U.S.A.

IRI facilities are also available through the Space Environment Information System (Spenvis) at <http://www.spenvis.oma.be/spenvis>

F.12 References

- RDF.1 Gussenhoven, D.A. Hardy, F. Rich, W.J. Burke and H.C. Yeh "High-Level Spacecraft Charging in the Low-Altitude Polar Auroral Environment" *J. Geophys. Res.*, pp.110099-11023, 1985.
- RDF.2 Yeh H.C. and M.S. Gussenhoven "The statistical Electron Environment for Defence Meteorological Satellite Program Eclipse Charging", *J. Geophys. Res.*, pp. 7705-7715, 1987.
- RDF.3 "Space Environment for USAF Space Vehicles", MIL-STD-1809 (USAF), 15 Feb 1991.
- RDF.4 Katz I., J.J. Cassidy, M.J. Mandell, G.W. Schnuelle, P.G. Steen and J.C. Roche, "The Capabilities of the NASA Charging Analyzer Program", in "Spacecraft Charging Technology - 1978", Ed. R.C. Finke and C.P. Pike, NASA CP-2071/AFGL TR-79-0082, ADA045459, p. 101, 1979.
- RDF.5 Lilley J.R., Cooke D.L., G.A. Jongeward and I. Katz "POLAR User's Manual", AFGL-TR-85-0246.
- RDF.6 Vasilyev Ju.V, V.V. Danilov, V.M. Dvoryashin, A.M. Kramrenko and V.S. Sokolv, "Computer Modeling of Spacecraft Charging Using ECM", *Proc. International Conference of Problems of Spacecraft/Environment Interactions*, June 15-19, 1992 Novosibirsk, Russia, p.187, 1993.
- RDF.7 Krupnikov K.K, V.N. Mileev, L.S. Novikov and G.V. Babkin, "Mathematical Modelling of High Altitude Spacecraft Charging", *Proc. International Conference of Problems of Spacecraft/Environment Interactions*, June 15-19, 1992 Novosibirsk, Russia, p.167, 1993.
- RDF.8 Mandell M.J, I. Katz and D.L. Cooke, "Potentials on large spacecraft in LEO", *IEEE Trans. Nucl. Sci.* NS-29, p.1584, 1982.
- RDF.9 Wrenn G.L. and A.J. Sims, "Surface Potentials of Spacecraft Materials", *Proc. ESA Workshop on Space Environment Analysis*, p.4.15, ESA WPP-23, 1990.
- RDF.10 NASA TM 4527 "Natural Orbital Environmental Guidelines for Use in Aerospace Vehicle Development", Eds. B.J. Anderson and R.E. Smith, 1994.
- RDF.11 Hastings D.E., M. Cho and J. Wang, "Space Station Freedom Structure Floating Potential and the Probability of Arcing", *J. Spacecraft and Rockets*, vol.29, p.830, 1992.
- RDF.12 Hanson W.B., S. Santoni and J.H. Hoffman, "Ion Sputtering from Satellite Surfaces", *J. Geophys. Res.*, 86, p.11350, 1981.
- RDF.13 Olsen R.C. and C.W. Norwood, "Spacecraft-Generated Ions", *J. Geophys. Res.*, 96, 15951-15962, 1991.
- RDF.14 Olsen R.C. and E.C. Whipple, "An unusual charging event on ISEE1", *J. Geophys. Res.*, 93, p.5568, 1988.
- RDF.15 Sigmund P., "Theory of Sputtering", *Phys. Rev. Lett.*, 184, 383-416, 1969.
- RDF.16 Thompson M.W., "The energy spectrum of atoms during the high energy sputtering of gold", *Philos. Mag.*, 18, 377-414, 1968.
- RDF.17 Bilitza D, "International Reference Ionosphere 1990", NSSDC/WDC-A-R&S 90-22, 1990.
- RDF.18 <http://nssdc.gsfc.nasa.gov/space/model/ionos/iri.html>

Annex G (informative)

Radiation

G.1 Links with radiation testing

Table G-1 below recalls the parameter used for quantification of various radiation effects, and for illustration purposes, lists the types of testing which shall be done to verify compatibility with the effects. See ECSS-E-20 for further details.

Table G-1: Radiation tests

Radiation effect	Parameter	Test means
Electronic component degradation	Total ionizing dose	Radioactive sources (e.g. ^{60}Co), particle beams (e^- , p^+)
Material degradation	Total ionizing dose	Radioactive sources (e.g. ^{60}Co), particle beams (e^- , p^+)
Material degradation (bulk damage)	Non-ionizing dose (NIEL)	Proton beams
CCD and sensor degradation	Non-ionizing dose (NIEL)	Proton beams
Solar cell degradation	Non-ionizing dose (NIEL) and equivalent fluence	Proton beams (~ low energy)
Single-event upset or latch-up for example	LET spectra (ions) Proton energy spectra, explicit SEU/L rate	Heavy ion particle beams Proton particle beams ⇐
Sensor interference (background signals)	Flux above energy threshold, flux threshold Explicit background rate	Radioactive sources, particle beams ⇐
Internal electrostatic charging	Electron flux and fluence Dielectric E-field.	Electron beams ⇐ Discharge characterization

⇐ = test data feedback to calculation

e , p = electron, protons

G.2 Future models

There are several efforts underway relating to radiation belt, solar particle and cosmic ray environment and interaction models which will probably lead to future internationally-acceptable standards.

Many of these models are available in the Space Environment Information System (Spenvis) at <http://www.spenvis.oma.be/spenvis/>.

TREND project (ESA-funded):

- BIRA/IASB development of empirical models of the low altitude environment derived from AZUR, SAMPEX and UARS, especially relating to energetic protons and their directionality. The measurements from MIR reported by PSI are also of interest in this context [RDG.1].
- MSSL (UK), development of models based on the Meteosat (geostationary) environment monitor and, together with A. Vampola, a CRRES-based model.
- MPAe (D) and MSSL (UK), development of a medium-energy electron model at high altitudes based on ISEE data.

CERT/DERTS

A French-funded consortium are developing techniques for deriving transient radiation belt morphologies and empirical models from physical principals via computer simulations of magnetospheric disturbances and injection events.

US efforts

CRRES-related efforts:

- Phillips Lab. Geophysics Directorate are developing a series of engineering radiation-belt models based on the CRRES mission; a proton model (CRRES-PRO), an electron model (CRRESELE), and a total dose model (CRRESRAD) have been released.
- A. Vampola: using CRRES data, development of MEA model and an outer-zone model based on a neural network analysis of CRRES data, its link with geomagnetic indices, and the historic record of these indices.
- CHIME is a cosmic ray environment model developed by the USAF Phillips Laboratory on the basis of CRRES measurements.

Other US efforts

- Boeing are developing models of the low altitude environment based on NOAA particle environment monitor data. Solar cycle variations and links with atmospheric density variations are being modelled.
- Naval Research Laboratories have developed but not generally released, an update of the CREME model, CREME96, including an improved model of the solar cycle modulation, improved physical and geomagnetic shielding models, and a worst-case solar particle event based on the October 1989 event. This effort was a collaboration with Moscow State University. A WWW-site has been established (<http://crsp3.nrl.navy.mil/creme96/>).

Russian efforts

Moscow State University are developing:

- A low altitude electron environment model;
- A cosmic ray model (in collaboration with NRL);
- Solar particle environment models;
- Models of heliospheric modulation of cosmic and solar energetic particles.

COSPAR task group

With IASB as convenor (D. Heynderickx, Belgisch Instituut voor Ruimte-Aeronomie, Ringlaan 3, B-1180 Brussel; <http://www.magnet.oma.be/>), a special task group has been established by COSPAR with a view to coordinating the various radiation belt modelling efforts in order to eventually produce international consensus standard radiation belt models.

ISO standard efforts

ISO TC10/SC14/WG4 on space environment models are overseeing the development of various environment models, with Russia as convenor. It is intended that this ECSS Standard stays harmonized with ISO standards but new models are not expected in the near future.

G.3 Sources of models

AE-8, AP-8	NSSDC, NASA-Goddard Space Flight Center. Models can be downloaded from the FTP address: nssdc.gsfc.nasa.gov/pub/models/radbelt . Models can be accessed via www: http://nssdc.gsfc.nasa.gov/space/model/ , and are available in Europe via D. Heynderickx, Belgisch Instituut voor Ruimte-Aeronomie, Ringlaan 3, B-1180, Brussel; (http://www.magnet.oma.be/ as part of UNIRAD and Spenvis.
SHIELDOSE	Stephen M. Seltzer, Ionizing Radiation Division, National Institute of Standards and Technology, Gaithersburg MD 20899, USA; seltzer@enh.nist.gov ; also available through NEA library, CCC-379 and available in Europe via D. Heynderickx, Belgisch Institute voor Ruimte-Aeronomie, Ringlaan 3, B-1180, Brussel; http://www.magnet.oma.be/ as part of UNIRAD and Spenvis.
CREME	National Geophysical Data Center, Code E/GC2, Dept. 946 325 Broadway Boulder Co 80303 3328 USA (Although developed by NRL, NOAA act as distribution agents).
CREME-96	Naval Research Laboratory Department of the Navy Code 7654 Washington, DC 20375 USA http://crsp3.nrl.navy.mil/creme96/
JPL-1991	J. Feynman, JPL, 4800 Oak Drive, Pasadena, Ca 91109, USA.
CRRESELE, CRRESPRO, CRRESRAD	USAF Phillips Lab, Geophysics Directorate PL/GPS, Hanscom AFB Ma.01731 USA
EQFRUX, EQGAFLUX	B. E. Anspaugh, JPL, 4800 Oak Drive, Pasadena, Ca 91109, USA

G.4 Internal electrostatic charging analysis tools

Internal electrostatic charging (or deep-dielectric charging) results from the build-up over a period of up to several days of electrostatic charge. For hazardous levels to be reached, the environment normally shall be characterized by high levels of energetic electron flux. The charge build-up depends on:

- the severity of the environment and its duration;
- the dielectric resistivity of the susceptible part (or lack of grounding of floating metalization);
- effects such as radiation induced conductivity.

While discharge can also depend on properties such as geometry and material condition. Charge build-up can therefore be mitigated by choice of material and grounding, but also by employing shielding to reduce the severity of the environment.

Tools are available to address these issues, such as ESADDC [RDG.2] which employs a Monte-Carlo radiation transport method to compute the charge buildup

in a dielectric material behind specified shielding in a certain input environment. Efforts in tool development seek to simplify this approach into a robust engineering tool. ESA's effort, by means of sponsoring a collaboration between DERA(UK) and DERTS(F), removing especially the need for Monte-Carlo analysis and introducing a method to specify the hazard, has resulted in computational tools which have been incorporated in the Space Environment Information System <http://www.spennis.oma.be/spennis/>.

G.5 Further information

Further information on analysis of space radiation environments and effects can be found on various WWW sites:

ESTEC Space Systems Environment Analysis Site	http://www.estec.esa.nl/wmwww/wma
ESA/IASB Space Environment Information System	http://www.spennis.oma.be/spennis/
NASA Space Environment and Effects Site	http://see.msfc.nasa.gov/

G.6 References

- RDG.1 Bühler P., L. Desorgher, A. Zender and E. Daly, "Observation of the Radiation Belts with REM", Proceeding of the ESA Workshop on Space Weather, ESA-WPP-155 (1998).
- RDG.2 Sorensen, J., "An Engineering Specification of the Internal Charging" Proceeding of the Symposium on Environment Modelling for Space-Based Applications, ESA-SP-392, December 1996.

Annex H (informative)

Particulates

H.1 Space debris flux models

H.1.1 General

Two developed space debris population models are the Meteoroid And Space Debris Terrestrial Environment Reference Model (MASTER-97) [RDH.1] and a NASA engineering model, ORDEM-96 [RDH.2]. These models can be used as interim solution for impact risk assessments and shielding design purposes until a specific standard for the space debris environment is defined.

H.1.2 MASTER-97

MASTER-97 uses a semi-deterministic approach which represents the debris environment by modelling its history from the beginning of spaceflight to present. It uses three source terms for the debris population: launches, explosions and collisions and follows their orbital evolutions. The space debris population at an epoch of 31 March 1996 is derived from 132 low and high intensity on-orbit break-ups.

A linear growth rate of 2 percent (uniform for all sizes) is applied for other years. Solar cycle effects on cleansing rate are included as for the NASA engineering model given in [RDH.3].

Mass (or diameter) dependent binning is used to assign weights to a condensed population of about 240 000 objects larger than 0,1 mm.

An Analyst application allows to interrogate the spatial debris distribution to determine collision fluxes for an arbitrary target orbit passing through the control volume. Flux results can be analysed with respect to collision velocity magnitude, its direction (azimuth and elevation), the orbit location, and the 3D position where the flux was encountered.

MASTER is provided on a CD-ROM containing the stored, binned data together with some processing software.

A simplified version, called the MASTER engineering model, is available as well. This version is applicable for target orbits with small eccentricities.

H.1.3 ORDEM-96

The NASA engineering model, ORDEM-96, analytically represents similar sources to MASTER plus additional non-fragmentation source distributions like

paint flakes, Aluminium Oxide particles from solid rocket motor burns and Sodium/Potassium droplets. These non-fragmentation sources mainly contribute to the small size population. The model is also derived from recent radar measurements and impact data from retrieved surfaces. The debris environment distribution is approximated with six different inclination bands. Each band has a unique distribution of semi-major axis, for circular orbits, and a unique perigee distribution for highly elliptical orbits. In addition, each inclination band has a unique, analytically defined size distribution which depend on the source of debris.

Collision probability equations are used to relate the orbital element distributions of the population to the flux measured on a spacecraft or to the flux measured through the field of view of a ground sensor. It provides directional information of the impacting flux. The model is computer based.

H.1.4 Velocity distribution

Impact velocities can range from 0 to about 15,5 km/s with an average velocity of 10 km/s for low inclination and of 12 km/s for high inclination orbits.

H.1.5 Mass density

According to [RDH.3], the average density of particles larger than 0,62 cm in diameter is assumed to be:

$$\rho = 2,8d^{-0,74} \text{ g/cm}^3.$$

The average density of smaller space debris particles is thought to be in the range 2,8 - 4,7 g/cm³. The values to be used for design are given in H.1.6.

H.1.6 Regime of applicability

The MASTER-97 space debris model [RDH.1] is applicable for particle sizes larger than 0,1 mm and for circular and elliptical Earth orbits up to geostationary altitudes.

The ORDEM-96 space debris model [RDH.2] is applicable for particle sizes larger than 1 micron and for circular and elliptical Earth orbits up to altitudes of 2000 km.

H.1.7 Tailoring guidelines

Nominal and worst case debris model parameters and mass densities are:

Table H-1: Nominal and worst case debris model parameters and mass densities

Parameter	Nominal	Worst case
solar activity, S	140	70
ref. mission year, t	middle	last
debris density ρ [g/cm ³]	4,0	8,0

For design purposes the nominal parameter values shall be used. A spherical shape shall be assumed to convert particle masses and diameters. Values for the solar activity, S, at specific times within a solar cycle can be found in clause 6. The default growth rates for the respective models shall be used. For the assessment of impact effects the full velocity distribution of space debris should be used. For a preliminary analysis a constant debris impact velocity of 10 km/s shall be used. Uncertainty factors for space debris fluxes (see H.2) shall not be applied.

H.1.8 Other debris models

Several other space debris models are in use or under development. These models can be used in special cases for impact analyses or risk assessments if the user

is familiar with the features and range of validity of the models. Two of these models are mentioned below.

H.1.8.1 NASA-90 model

From about 1990 until 1996 the NASA space debris engineering model defined in [RDH.3] has been most widely used for design applications. This model is given in terms of simple analytical expressions. It is relatively easy to use and widely distributed. However, it has some known shortcomings of which the assumption of spherical orbits for all debris particles is probably the most severe. The model can still be used for some initial risk assessments, however, the user should be aware of its shortcomings.

H.1.8.2 IDES

The Integrated Debris Evolution Suite (IDES) [RDH.4] space debris model uses a deterministic representation of individual objects > 10 cm and a statistical representation of the populations between $10 \mu\text{m}$ and 10 cm (by fragment orbit discretization in dimensions of perigee, radius, eccentricity, inclination and mass).

Considered debris source terms include launch related objects, high and low intensity explosions, collisions, paint flaking and secondary ejecta. These sources are modelled and evolved from the beginning of the space age to the present day and into the long term future. For impact risk assessments the directional and velocity distribution of the encountered flux is included. Circular and elliptical target orbits can be analysed. IDES is applicable to LEO altitudes and for particle sizes larger than $10 \mu\text{m}$. The tool also allows to study the long term evolution of the debris population and the long term impact risk to target orbits under different traffic scenarios, and the effectiveness of different mitigation measures.

H.2 Model uncertainties

H.2.1 General

The meteoroid and space debris environment flux models given above contain several known approximations and other uncertainties.

H.2.2 Meteoroids

According to [RDH.3] uncertainties in the meteoroid models mainly result from uncertainties in particle densities and masses. Fluxes for meteoroids larger than 10^{-6} g are well defined, but the associated masses are quite uncertain. The mass density of meteoroids spans a wide range, from about $0,15 \text{ g/cm}^3$ to values as large as 8 g/cm^3 . At a set mass this implies an uncertainty in the flux of a factor 0,1 to 10. For meteoroids smaller than 10^{-6} g flux uncertainties at a given mass are estimated to be a factor of 0,33 to 3.

H.2.3 Space debris

The space debris flux models were developed as a best estimate rather than a conservative one. In [RDH.3] uncertainties for debris fluxes in different size regimes are quoted. These factors give the 90 % confidence level that the real debris flux is within a bandwidth defined by the model flux multiplied by the uncertainty factors.

**Table H-2: Uncertainty of 90 % confidence level
for debris flux**

Particle size	Uncertainty factor
d > 10 cm	0,5 to 1,5
0,05 cm < d < 10 cm	0,33 to 3,0
d < 0,05 cm	0,5 to 2,0

Other uncertainties of the debris model include

- the debris density,
- the debris shape,
- the annual growth rates,
- the altitude dependence, especially for altitudes above 800 km,
- the velocity distribution, especially for low impact velocities, and
- the dependence on solar activity.

A more detailed discussion of model uncertainties is given in [RDH.3 and RDH.2].

H.3 Damage assessment

In this clause a brief general overview of damage assessment criteria and procedures is given.

For each individual project the damage assessment shall be tailored according to the specific conditions and requirements (e.g. orbit, shielding, damage criteria, required reliability).

Any damage assessment depends to a large extend on the relevant failure criteria. Possible failure criteria include:

- cratering (sensor degradation, window blinding, surface erosion);
- larger craters (sealing problems, short circuits on solar arrays);
- impact generated plasma (interference, discharge triggering);
- impulse transfer (attitude problems);
- spallation from inner wall (equipment damage, crew injury);
- wall penetration (damage, injury, loss of liquid or air);
- burst, rupture (pressurized parts);
- structural damage.

For a quantitative damage and risk assessment so called damage or design equations for the given shielding configuration are needed. They give shielding thresholds or hole sizes for given impacting particle parameters and failure mode.

One of the most widely used damage equation gives the threshold thickness for penetration of single metal plates (thin plate formula):

$$t = k_m m^{0,352} \rho^{0,167} v^{0,875}$$

where

- t is the threshold thickness for penetration;
- k_m is the material constant, 0,55 for Aluminium;
- m is the mass of projectile (g);
- ρ is the density of projectile (g/cm³);
- v is the normal impact velocity component of projectile (km/s).

A puncture occurs whenever the threshold thickness for an impacting particle with given mass, density and velocity exceeds the shielding thickness of the surface under consideration.

Finding a realistic damage equation for a given shielding configuration can be problematic.

The translation of a failure mode to a damage equation can be difficult. Many damage equations for different types of shields and for different velocity regimes have been developed. However, for most materials, compounds, and shielding concepts no specific damage equation is available.

Sometimes scaled effective thicknesses in combination with known damage equations can be used for a first assessment.

For impact damage and risk assessments secondary ejecta should be considered as well. Every hypervelocity impact leads to the ejection of secondary particles which can impact other surfaces (depending on the spacecraft geometry). The total mass of the ejected particles can exceed the mass of the primary impactor by orders of magnitude. Secondary particles will be typically ejected within a cone around the impact direction. Their velocities are typically below 2 km/s.

At present, quantitative models of secondary ejecta are not mature enough to be used as standard.

H.4 Analysis tools

H.4.1 General

Several numerical tools have been developed to perform impact and impact risk analyses. The following tools are mentioned for information only. Other tools can be used as well if they are based on the reference flux models.

H.4.2 Deterministic analysis

For information and analysis of the deterministic, trackable space objects, the DISCOS database was developed [RDH.5]. DISCOS (ESA's Database and Information System Characterising Objects in Space) is a catalogue on Earth orbiting space objects and debris.

DISCOS can be used to extract detailed data on all the tracked objects and it also provides facilities to manipulate those data (forward propagation, data presentation). DISCOS is implemented at and maintained by ESA/ESOC. It is accessible for registered users only.

H.4.3 Statistical analysis

A statistical tool, ESABASE/DEBRIS, was developed for a detailed impact risk assessment of smaller, non-trackable particles [RDH.6]. ESABASE/DEBRIS is a fully three dimensional numerical analysis tool including directional and geometrical effects and spacecraft shielding considerations. It is based on environment and particle/wall interaction models and includes the reference meteoroid and space debris flux models defined in this document.

The user specifies the mission, spacecraft geometry, attitude and shielding as well as the particle type, size and velocity range to be analysed. The computed output includes:

- the number of impacts;
- the resulting number of damaging impacts taking into account the spacecraft shielding and damage assessment equations;
- the mean particle impact velocity (amplitude and direction);
- the numbers of craters of specified size;
- the probability of no failure.

ESABASE/DEBRIS allows the optional use of several meteoroid and debris flux models.

H.5 Lunar dust simulant

Various simulants have been prepared in the laboratory to mimic the properties of lunar dust. One well-known simulate is the Minnesota Lunar dust simulate that can be obtained from:

Space Science Centre,
University of Minnesota,
Minneapolis.

This simulate reproduces the chemical composition of lunar dust as well as its microscopic morphology. It does not reproduce well the mechanical properties of in situ lunar dust, due to the absence of Van der Waals forces between grains at ambient pressure.

H.6 References

- RDH.1 Klinkrad H., J. Bendisch, H. Sdunnus, P. Wegener, R. Westerkamp, "An Introduction to the 1997 ESA MASTER Model", Proc. of the Second European Conf. on Space Debris, pp. 217-224, ESA SP-393, May 1997.
- RDH.2 Kessler D.J., J. Zhang, M.J. Matney, P. Eichler, R.C. Reynolds, P.D. Anz-Meador and E.G. Stansbery, "A Computer Based Orbital Debris Environment Model for Spacecraft Design and Observations in Low Earth Orbit"; NASA TM 104825, November 1996.
- RDH.3 Anderson B.J., "Natural Orbital Environment Guidelines for Use in Aerospace Vehicle Development", by:, editor and R.E. Smith, compiler; NASA TM 4527, chapter 7, June 1994.
- RDH.4 Walker R., S. Hauptmann, R. Crowther, H. Stokes and A. Cant, "Introducing IDES: Characterising the Orbital Debris Environment in the Past, Present and Future", Paper AAS 96-113, Advances in the Astronautical Sciences, Vol. 93 Part I, 201-220, 1996.
- RDH.5 Klinkrad H., U. Fuller, J.C. Zarnecki, "Retrieval of Space Debris Information from ESA's DISCOS Catalogue", Proc. ESA Workshop on Space Environment Analysis, Noordwijk, 9-12 October 1990.
- RDH.6 Drolshagen G. and J. Borde, "ESABASE/DEBRIS, Meteoroid/Debris Impact Analysis, Technical Description", ref. ESABASE-GD-01/1, 1992.

Annex I (informative)

Contamination

I.1 Existing Tools

The computer codes dedicated to spacecraft contamination are presented here in clauses I.2 to I.11 from information available in literature. All of them are simulation tools at system level, except the CONTAM III code, clause I.4, that is devoted to thruster plume modelling. The clause I.12 presents identified data bases, although some of the simulation codes also contain integrated (limited) data bases. When available, the integration in a global tool that allows to automatically take into account parameters, such as surface temperatures (from thermal models), mission description and atmospheric models, is also mentioned.

The main field of applicability of the codes is external contamination either in LEO or GEO. However, some of the programs, as described in each section, have limited transport modelling capabilities (simple or improved view factors only), and gives poor results in cases when return-flux through ambient-scatter and self-scatter is important, i.e. essentially in “lowest LEO” (at altitudes below 500 km-700 km or even more at lower altitudes typical of Shuttle, MIR or ISS). At such altitudes, pressure increase due to ram flux can go as high as 10^{-5} hPa - 10^{-4} hPa, resulting in decametric to metric mean free path, which makes collisions really not negligible and collisional return-flux important (typically of the order of the percent).

The capability to model semi-enclosed systems is not often reported in literature. However, provided these can be modelled, which seems to be possible for most of the codes, semi-enclosed systems can be modelled as well. Here again, some codes can be limited due to too poor transport modelling in case of high pressures. A difference with external contamination computing for which collisional return flux may often be the main contamination process (for surfaces not in direct view), is that in closed systems direct surface to surface collisionless transport (with possible surface reflections) is most of the time the dominant process. Except for high pressures such as 10^{-3} hPa (and thus decimetric mean free path), which can be found in semi enclosed systems yet.

I.2 ESABASE: OUTGASSING, PLUME-PLUMFLOW and CONTAMINE modules

ESABASE is a general spacecraft modelling tool including several modules developed by several parties under ESA sponsorship, and now supported by GEC ALSTHOM, UK.

In its currently available version, ESABASE essentially deals with contamination through its OUTGASSING module, developed by Matra Marconi Space (MMS). It allows to compute contaminant deposit on spacecraft by numerical integration:

- sources: material outgassing by standard laws (see 11.5.1.1), the surface temperatures being obtained by the thermal analysis module;
- transport: by mass-transport factors computed from view factors (collisionless transport) improved by adding the possibility of one collision per particle trajectory with background densities (i.e. fixed, not self-consistent) of ambient and outgassed species, as described in 11.5.2.1.2;
- deposition on surfaces: deposited mass computed, reemission or immediate reflection allowed.

The PLUME module currently implemented in ESABASE simulates thruster plume expansion. It was derived from CONTAM code and does not correctly model plume backflow (see the section about CONTAM for details). It is thus essentially used for forces and torques, and thermal analysis.

As a conclusion, the current version of ESABASE is consequently rather limited in two major aspects of contamination:

- contamination by thruster backflow (and droplets);
- more collisional transport mechanisms in case of particularly sensitive surfaces (e.g. cooled optics) that are baffled and can only be reached after some collisions, or even one collision, which is crudely modelled by OUTGASSING through very approximate background densities (not modified by spacecraft for ambient density, and with spherical symmetry for outgassed density [RDI.1]).

Yet, several improvements or new modules have been developed recently by MMS [RDI.2] under CNES sponsorship, and the new improved version is available in ESABASE.

First, the PLUME module has been improved:

- Its PLUMFLOW sub-module, modelling the dynamics of the thruster itself, has been added a two-dimensional multi-species DSMC model of nozzle lip region, in order to describe thruster backflow correctly now.
- Droplets produced by bi-propellant thrusters have been included. Their distribution is taken from experiments, and their trajectories are followed in straight lines until possible surface impingement.

Secondly, a new module called CONTAMINE has been added. It computes surface interactions (adsorption, diffuse reflection, specular reflection) and above all surface effects: modification of thermo-optical, electrical and mechanical properties, or global output power reduction for solar cells. These property changes are either taken from data gathered in a data base included in CONTAMINE (with interpolation between available data, which are not always very numerous), or complex index computed. It can also be interfaced with the older OUTGASSING module to compute deposit thickness including re-emission.

This new contamination capability of ESABASE should now allow a good prediction of thruster contamination. It remains to be validated by comparison with experiments (see TRICONTAM experimental validation, which can be partially considered as validating ESABASE modules). The limited capability of the quasi-collisionless transport model, that was pointed out above, remains in this new version.

I.3 JMC3D

JMC3D is a tri-dimensional Monte-Carlo code developed by Aérospatiale, Les Mureaux, France. It seems to have been initially devoted to Hermes re-entry phase modelling, but has also been applied to Ariane 5 and spacecraft contamination simulation [RDI.3]. It exhibits the following features:

- molecular rotational degrees of freedom taken into account;
- specular/diffusive surface reflections, with possible accommodation;
- inclusion of thruster flow computed by Euler method (application to Shuttle);
- variable time step and weighting factors;
- un-structured objects and volume mesh;
- vectorized code (on CRAY computers).

The few data available indicate acceptable agreement with experiments: good accuracy for Hermes high densities and the order of magnitude for Shuttle back-flow.

It seems to be a rather high-standard model (molecular rotational degrees of freedom, un-structured mesh), although the small number of publications about it makes it difficult to know whether it includes the necessary “technical” features to be used for satellites (versatile geometry and thruster flow modelling, contaminant effects). JMC3D is an Aérospatiale developed model presently not diffused to other companies.

I.4 CONTAM 3.2 or CONTAM III

CONTAM has been developed from the late seventies to the mid eighties by Science Application International Corporation (SAIC) for the Air Force Rocket Propulsion Laboratory (AFRPL). It is one of the most well known and widely used computer code for computing the plume flowfields of monopropellant, bipropellant or solid rocket thrusters. Spacecraft contamination assessment thus requires this model to be included as a contaminant source in a contaminant transport/effects model, as it has been done in ESABASE (PLUMFLOW module developed by MMS but based on CONTAM) or in the TUHH contamination model TRICONTAM [RDI.4].

The computational methods and physics included are described in many references [RDI.5]. It computes both steady state and transient combustion processes. Computed gaseous outflow includes unburned propellant, unburned droplet or solid particles, and liquid wall film. The two-phase fluid dynamics is treated by the method of characteristics, possibly including one shock or none (depending on the thruster). Non-equilibrium chemical kinetics is computed along streamlines in a one-dimensional model. The droplets (liquid engine) or solid particles (solid engine) dynamics is computed in the flowfield, including condensation/evaporation.

In such inviscid flow field computations, the boundary layers (along nozzle walls) shall be treated separately, as it is the case in CONTAM. Boundary layers are of prime importance for contamination because they determine the transition region around the nozzle lip and thus the backflow. Only thin turbulent boundary layers of large propellants were included in the first version of the code. Improvements have been implemented on the next version (CONTAM 3.2), including thicker viscous laminar boundary layers of smaller thrusters and the possibility for the user to define some parameters “by hand”. However, the modelling of the transition region around nozzle lip remains a simple Prandtl-Meyer expansion from the boundary layer at the lip. The backflow rate remains consequently approximate, and diffusion and species demixing at lip are not included. This makes the simple use of CONTAM for backflow contamination rather inaccurate. This is the reason why several people supplemented CONTAM with a DSMC model of nozzle lip flow (in the PLUMFLOW module to be included by MMS in ESABASE, and for a specific case in [RDI.6]).

Droplets are emitted at smaller angles, and the modelling of their dynamics seems more accurate. The reader can also look at the experimental validation of the TRICONTAM code derived from CONTAM in the section below.

I.5 TRICONTAM

TRICONTAM, a global contamination model developed at Technical University Hamburg Harburg (TUHH), Germany, has been developed under ESA/ESTEC contract. It seems to be essentially devoted to computing contamination from thruster plume exhausts. The plume flowfield is computed by an improved version of CONTAM III (essentially concerning transient combustion processes and chemistry), and the contaminant transport to spacecraft surfaces is assumed to be collisionless. An important part of the software is dedicated to forces, torques and thermal analysis.

The major interest of that code is that its results were compared to the numerous experimental measurements realized at TUHH [RDI.4]. As the plume model of TRICONTAM was improved with respect to CONTAM III, this very valuable experimental validation of the code can unfortunately not be considered as a full validation of CONTAM III (or other evolutions of CONTAM III, such as the one to be implemented in ESABASE/PLUMFLOW). The validation results can be sketched here (from [RDI.4]):

- Plume gas composition (module specific to TRICONTAM): good, to be supplemented with some rare species like HCN and NO.
- Gas streamlines up to 90° divergence (similar to CONTAM and certainly ESABASE/ PLUMFLOW): good.
- Gas backflow, divergence angle greater than 90° (similar to CONTAM III worse than ESABASE/PLUMFLOW which includes a DSMC model of nozzle lip): total flow not very good, and no mechanism included to account for species demixing.
- Droplets (module specific to TRICONTAM, modified from CONTAM III): good concerning droplet dynamics, even for pulsed firings, but not very good concerning droplet size and composition; possibility of droplet outflow from wall film towards backflow not modelled.

I.6 SOCRATES

The SOCRATES code (Spacecraft/Orbiter Contamination Representation Accounting for Transiently Emitted Species) was developed by Spectral Sciences for the Phillips Lab., Hanscom Air Force Base, Massachusetts.

It is one of the most elaborate contamination tools concerning collisional transport and gas-phase reactions [RDI.7]. It is a true DSMC (Direct Simulation Monte Carlo), which thus simulates realistically collisions, including reactions: any kind of bi-molecular collision, excitation, reaction, dissociation into several products, photon production. Molecular internal energy (vibrational) is taken into account (Borgnakke & Larsen model). A special treatment of highly collisional regions, where thermal equilibrium is reached, is implemented.

Two nested meshes, an inner and an outer one, are included one in the other, which allows to compute both short and long distance effects.

The contaminant sources are much simpler: standard outgassing sources and thrusters described by the analytical formula:

$$\phi(r, \theta) \propto \frac{e^{-C(1 - \cos(\theta))}}{r^2}$$

where

- | | |
|----------|--|
| r | is the distance to thruster exit; |
| θ | is the angle with respect to thruster axis; |
| ϕ | is the thruster efflux density at position r, θ ; |
| C | is a constant. |

Output quantities also aim at gas phase physics: return fluxes can be obtained, but much more gas phase data can be computed, such as species (relative) velocities, temperatures and collision or reaction rates.

I.7 SPACE II

The Shuttle or Payload Contamination Evaluation code (SPACE) was developed since the late seventies by Martin Marietta to predict the contamination of the Shuttle and Spacelab [RDI.8]. Only a reduced number of possible geometries have thus been included: Spacelab, the Shuttle with various possible payloads (IECM...).

Contaminant sources are:

- surfaces: early desorption, outgassing and also evaporation.
- specific parametric description of vents, leakages, Shuttle flash evaporators and thrusters (Simons' model [RDI.9] but with the possibility to include CONTAM plumflow model).

The transport model is of an hybrid type. First order transport is done by view factor computing. Surface reflections are also included. Second order transport through gas phase collisions is added following Bhatnager-Gross-Krook simplified method: it is in fact a Monte-Carlo ray-tracing technique (importantly) improved by considering "secondary emitters" accounting for collisions in the volume surrounding the Shuttle, with rates and distribution functions computed by BGK method [RDI.10]. A next improvement allows to also take into account third order effects: the attenuation of fluxes between these volumic "secondary emitters" and the impinged surfaces [RDI.10]. Column-density can be computed. Standard surface output is deposition thickness, but no contamination degradation effects routines are included.

I.8 MOLFLUX

MOLFLUX (MOlecular FLUX) was developed for NASA by Martin Marietta Aerospace and Lockheed Engineering & Sciences Company. It has been used for a long time in industry. It seems moreover to have been chosen by NASA as the model to be used by all American ISS participants to predict contamination [RDI.11].

Contaminant transport is computed at first order by view factors that shall be computed separately by thermal radiation program TRASYS. Similarly to SPACE II model, second order collisional transport is computed by an approximate BGK method [RDI.2], which certainly makes both models very close.

Global sticking coefficients S for contaminants coming from surface i to surface j are taken equal to [RDI.12]

$$S = \begin{cases} 0 & \text{for } T_i > T_j \\ \frac{T_j - T_i}{200} & \text{for } T_i < T_j \text{ and } T_i > T_j - 200 \\ 1 & \text{for } T_i < T_j - 200 \end{cases}$$

which seems to have been chosen more generally for ISS contamination modeling.

Program outputs are column densities and contaminant deposit thickness.

I.9 ISEM

The Integrated Spacecraft Environments Model (ISEM) is presented as the next generation of contamination models developed for NASA, following SPACE and MOLFLUX [RDI.13]. It has been delivered to NASA Goddard and Marshall Space Flight Center, but also JPL, Fairchild, Boeing and the Applied Physics Laboratory (APL).

The transport modelling technique seems to be the same as in SPACE and MOLFLUX, with some improvements [RDI.13]. It has the advantage to be quicker than DSMC but lacks of accuracy in case of high densities or multi-collisional transport.

The improvements with respect to SPACE or MOLFLUX are essentially in the possibility of modelling new phenomena:

- multiple surface reflections;
- atomic oxygen erosion as contaminant source;
- ion production by UV or charge exchange;
- UV emission from excited emitted N₂.

or doing things more conveniently:

- putting imaginary surfaces in the volume without re-running geometry model;
- modelling the inside of a vacuum chamber included;
- possibility to operate in atmospheres of Venus and Mars.

I.10 OPT

The Orbital Particulates Trajectory model (OPT) was developed by Applied Science Technologies, partially on NASA funding, partially on own funding [RD I.13]. It computes particulate transport on spacecraft.

Particulate sources shall be defined by the user, with a possibility to generate them at random with a specified distribution.

Particulate transport takes into account:

- gravitational effects (non-sphericity of the earth, lunar-solar effects);
- atmospheric drag;
- solar radiation pressure;

but nothing due to the presence of spacecraft itself (e.g. pressure increase and electrostatic effects), and OPT can be seen as a simple orbitography code applied to particulates.

I.11 CAP

Contamination Analysis Tool (CAP) developed by JPL for NASA (Goddard) is a basic tool, including standard first-order emission rate, collisionless transport with surface diffuse reflections and accommodation [RDI.14]. An example of application of CAP is described in [RDI.15].

I.12 Databases

Some of the tools described above include databases about contamination effects. References to two other important databases created independently of any model were found in literature. They can be used to assess contamination effects from contaminant deposit and column densities computed by these models.

A first database was created by Boeing Aerospace & Electronics in 1986-1988 for Air Force Wright Research and Development Center [RDI.16]. Its availability to non-Americans is not reported. It is a very important work resulting from the collection of over 3000 sources and covering most of contamination fields.

The Plume Contamination Database (PCD) was developed by MMS for ESTEC, using ORACLE [RDI.2]. It is anticipated that the database is progressively filled by ESTEC contractors and presently essentially contains measurements made at TUHH [RD I.17].

I.13 References

- RDI.1 Koeck C., Frezet M., Calculation of environmental effects on spacecraft surface using Monte-Carlo technique - application to contamination and atomic oxygen, Proceedings of the Fourth International Symposium on Materials in a Space Environment, Toulouse, France, Sept. 6-9, 1988, pp 263-273.
- RDI.2 Chéoux-Damas P., Thérode C., Castejon S., Hufenbach B., PCD: An interactive tool for archiving plume impingement and contamination data, to be published in The Proceedings of the Second European Spacecraft Propulsion Conference, ESTEC, Noordwijk, The Netherlands, May 27-29, 1997, p. 587-594.
- RDI.3 Delamare B., Dumas L., 3D Monte-Carlo simulation of contamination induced by shuttle RCS engines, Proceedings of the Sixth International Symposium on Materials in a Space Environment, Noordwijk, The Netherlands, Sept. 19-23, 1994, pp 39-44.
- RDI.4 Trinks H., Exhaust Plume Data Handbook (EPDH IV), Progress Report IV, ESA Contract No 7510/87/NL/PP, Sept. 1991a.
- RDI.5 Hoffman R. J., Kawasaki A., Trinks H., Bindemann I., Ewering W., The CONTAM 3.2 plume flowfield analysis and contamination prediction computer program: Analysis model and experimental verification, AIAA paper No 85-0928, AIAA 20th Thermophysics Conference, Williamsburg, VA, June 19-21 1985.
- RDI.6 Guernsey C. S., McGregor R. D., Bipropellant rocket exhaust plume analysis on the Galileo spacecraft, AIAA paper No 86-1488, AIAA/ASME/SAE/ASEE 22nd Joint Propulsion Conference, Huntsville, AL, June 16-18, 1986.
- RDI.7 Elgin J., Bernstein L. S., The theory behind the SOCRATES code, NASA STAR 93N24298, AD-A259987, Final Report, Aug. 1992.
- RDI.8 Jarossy F. J., Pizzicaroli L. C., Owen N. L., Shuttle/payload contamination evaluation (SPACE) program improvements, Shuttle optical environment; Proceedings of the Meeting, Washington, DC, April 23-24, 1981, pp 78-85.
- RDI.9 Simons G.A.: "Effect of Nozzle Boundary Layers on Rocket Exhaust Plumes", AIAA Journal, Tech. Notes, vol.10, Nø 11, 1972, pp. 1534-1535.
- RDI.10 Ehlers H. K. F., An analysis of return flux from the space shuttle orbiter RCS engines, AIAA paper No 84-0551, AIAA 22nd Aerospace Sciences Meeting, Reno NV, Jan. 9-12, 1984.
- RDI.11 Babel H, Hasegawa M., Jones C., Fussell J., The effects of contamination from silicones and a modified-Tefzel insulation, IAF Paper 96-I.5.08, 47th International Astronautical Congress, Beijing, China, Oct. 7-11, 1996.
- RDI.12 Cognion, R., MOLFLUX analysis of the SSF electrical power system contamination, AIAA paper 91-1328, AIAA 26th Thermophysics Conference, Honolulu, HI, June 24-26, 1991.
- RDI.13 Rantanen R., Gordon T., On-orbit transport of molecular and particulate contaminants, Optical system contamination V and stray light and system optimization; Proceedings of the Conference, Denver, CO, Aug. 5-7, 1996, (SPIE Proceedings. Vol. 2864), 1996, pp. 115-126.
- RDI.14 Millard J. M., Jet Propulsion Laboratory Contamination Analysis Program - Programmer and User Manual (with appendix), JPL report No 715-55, Prepared by the Jet Propulsion Laboratory for the Goddard Space Flight Center, 1980.

- RDI.15 Barengoltz J. B., Millard J. M., Jenkins T., Taylor D. M., Modeling of internal contaminant deposition on a cold instrument sensor, Optical system contamination: Effects, measurement, control II; Proceedings of the Meeting, San Diego, CA, July 10-12, 1990, pp 337-351.
- RDI.16 Thorton & Gilbert: "Spacecraft contamination database", SPIE Volume 13, 29; Optical System Contamination: Effects, Measurement and Control-2; 1990. pp 305-319.
- RDI.17 Trinks H., Surface Effect Data Handbook (SEDH III), Progress Report V, ESA Contract No 7510/87/NL/PH, Sept. 1991b.

ECSS Document Improvement Proposal		
1. Document I.D. ECSS-E-10-04A	2. Document date 21 January 2000	3. Document title Space environment
4. Recommended improvement (identify clauses, subclauses and include modified text or graphic, attach pages as necessary)		
5. Reason for recommendation		
6. Originator of recommendation		
Name:	Organization:	
Address:	Phone: Fax: e-mail:	7. Date of submission:
8. Send to ECSS Secretariat		
Name: W. Kriedte ESA-TOS/QR	Address: ESTEC, P.O. Box 299 2200 AG Noordwijk The Netherlands	Phone: +31-71-565-3952 Fax: +31-71-565-6839 e-mail: wkriedte@estec.esa.nl

Note: The originator of the submission should complete items 4, 5, 6 and 7.

This form is available as a Word and Wordperfect-Template on internet under
<http://www.estec.esa.nl/ecss/improve/>

(This page is intentionally left blank)